# The suspension systems of the interferometric gravitational-wave detector GEO 600

Vom Fachbereich Physik
der Universität Hannover
zur Erlangung des Grades

**Doktor der Naturwissenschaften**
**– Dr. rer. nat. –**

genehmigte Dissertation
von

**Dipl.-Phys. Stefan Goßler**

geboren am 4. Mai 1968 in Westerland/Sylt

2004

## Zusammenfassung

Die Existenz von Gravitationswellen wurde bereits von Albert Einstein, basierend auf seiner Allgemeinen Relativitätstheorie, vorhergesagt. Gemäß der Theorie werden Gravitationswellen durch die Beschleunigung von Massen erzeugt. Sie bewirken eine Änderung der lokalen Metrik der Raumzeit und rufen dadurch eine Änderung von Abständen hervor. Aufgrund der extrem schwachen Kopplung an Materie, kommen nur astrophysikalische und kosmologische Prozesse zur Erzeugung von Gravitationswellen mit nachweisbarer Signalstärke in Betracht. Die Suche nach diesen Wellen gehört zu den grössten und technisch anspruchsvollsten Herausforderungen der modernen Physik.

Ein weltweites Netzwerk von Gravitationswellendetektoren steht gegenwärtig am Beginn der Aufnahme kontinuierlicher Messungen. Ein Mitglied dieses Netzwerkes ist GEO 600, basierend auf einem Michelson Interferometer mit 600 m Armlänge. Jeder Interferometerarm ist einmal gefaltet, so dass die effektive Armlänge 1200 m beträgt. Zusätzlich wird die Empfindlichkeit von GEO 600 durch Dualrecycling, der Kombination von Power- und Signalrecycling, gesteigert.

Die durch die seismische Bodenbewegung verursachte Bewegung der Testmassen muss um mehr als zehn Grössenordungen reduziert werden um ein seismisch induziertes Positionsrauschen von $2.4 \cdot 10^{-20}\,\mathrm{m}/\sqrt{\mathrm{Hz}}$ bei einer Frequenz von $50\,\mathrm{Hz}$ erreichen zu können. Dieses Niveau entspricht einem Drittel des erwarteten Beitrags durch thermisches Rauschen der Testmassen. Die erforderliche Isolation der Testmassen und des Strahlteilers wird mit Hilfe von Dreifachpendeln verwirklicht, während alle anderen relevanten optischen Komponenten als Doppelpendel aufgehängt sind. Insgesamt sind 26 Doppel- oder Dreifachpendel in GEO 600 installiert.

Um eine Verbesserung der vertikalen Isolation zu erreichen, beinhaltet jedes Dreifachpendel zwei Blattfederstufen. Die relevanten Eigenmoden aller Pendel werden mittels Magnet-Spulen-Aktuatoren an der jeweiligen obersten Pendelstufe gedämpft. Die hierfür benötigten Informationen über die Pendelbewegung werden durch optische Sensoren an den obersten Pendelstufen erlangt. Die Feedbacksignale, mit denen GEO 600 am Arbeitspunkt gehalten wird, werden mit Hilfe von Reaktionspendeln auf die aufgehängten Spiegel übertragen. Diese Reaktionspendel stellen seismisch isolierte Plattformen zur Verfügung, an denen die Feedbackaktuatoren angebracht sind. Niedrigfrequentes longitudinales Feedback für das Michelson Interferometer wird durch Magnet-Spulen-Paare auf die vorletzte Pendelmasse ausgeübt, während höherfrequentes Feedback durch elektrostatische Aktuatoren auf die Testmassen selber ausgeübt wird. Die in GEO 600 installierten Aufhängungen sind die komplexesten Aufhängungen unter den bisher betriebsbereiten Detektoren.

Die unterste Aufhängungsstufe jedes Dreifachpendels besteht vollständig aus fused silica. Derartige monolithischen Aufhängungen werden bei GEO 600 eingesetzt um eine dissipationsarme Aufhängung der Testmassen und des Strahlteiler zu erreichen und dadurch das thermische Rauschen zu reduzieren. Zur Herstellung einer monolithischen Aufhängung werden silica Fasern an Aufnahmen aus fused silica geschweisst, die zuvor durch silicate bonding an den Mittelmassen und Testmassen angebracht wurden. GEO 600 ist der erste und bislang einzige Gravitationswellendetektor mit monolithischen Aufhängungen. Da thermisches Rauschen voraussichtlich die erreichbare Nachweisempfindlichkeit im empfindlichsten Frequenzbereich limitieren wird, werden die zukünftigen interferometrischen Detektoren vergleichbare Aufhängungen benötigen.

Um einen stabilen Betrieb von GEO 600 zu ermöglichen, wurden die Violinmoden aller Aufhängungsfasern gedämpft, wobei die Güte sowie die Eigenfrequenzen der ersten beiden Moden in einem eng vorgegebenen Rahmen liegen.

Im Rahmen dieser Arbeit wurden alle Aufhängungen von GEO 600 installiert. Im Anschluss an den mit Testoptiken durchgeführten, vorläufigen Betrieb von GEO 600, wurden die monolithischen Aufhängungen produziert und installiert. Dafür wurde eine Methode zum Dämpfen und Abstimmen der Violinmoden entwickelt und angewendet.

**Stichworte:** Gravitationswellendetektor, Monolithische Aufhängungen, Violinmoden

# Summary

The search for gravitational waves, as were predicted by Albert Einstein based on his theory of general relativity, is among the most ambitious challenges in modern physics. According to the theory, gravitational waves are generated by strong accelerations of massive objects as happen in certain astrophysical processes. Gravitational waves change the local metric of spacetime resulting in an alteration of distances. Due to the minuscule effects caused by gravitational waves, instruments of an unprecedented sensitivity are required to attempt a detection.

A world-wide network of gravitational-wave detectors is currently approaching the continuous observation mode. One member of this network is GEO 600, based on a Michelson interferometer with 600 m arm length. Each interferometer arm of GEO 600 is folded once to obtain an effective arm length of 1200 m. Dual-recycling, a combination of power- and signal-recycling is employed to enhance the sensitivity.

Due to the ambient seismic noise in the vicinity of GEO 600 an isolation of the test masses from the seismic by more than ten orders of magnitude is required to achieve a residual seismically-induced displacement noise of $2.4 \cdot 10^{-20}\,\mathrm{m}/\sqrt{\mathrm{Hz}}$ at 50 Hz. This level is a factor of three below the expected motion of the test masses due to internal thermal noise. The required seismic isolation of the test masses and the beamsplitter is accomplished by the use of triple cascaded pendulums. All other relevant optics are suspended as double pendulums. Altogether 26 double or triple pendulums are installed in GEO 600.

All pendulums are suspended from pre-isolated platforms. In order to further improve the vertical isolation, each triple pendulum includes two cantilever-spring stages. The relevant eigenmodes of all pendulums are damped via magnet-coil actuators at the respective uppermost pendulum stage. Optical sensors are co-located with the actuators to provide the required position and orientation information. The feedback signals required to maintain GEO 600 at its operating point are applied to the suspended mirrors from reaction pendulums. These pendulums provide seismically isolated platforms to support the feedback actuators. The low-frequency longitudinal feedback for the Michelson interferometer is applied via magnet-coil actuators at the penultimate pendulum mass, while the higher-frequency feedback is applied via electrostatic actuators at the test masses themselves. The GEO 600 test-mass suspensions are the most complex among the detectors so far working.

The last suspension stage of each triple pendulum is entirely made of fused silica. These monolithic suspensions are employed in GEO 600 to obtain a low dissipation support for the test masses and the beamsplitter, thus reducing the thermal noise. The monolithic stages are realized by welding flame-drawn silica fibers to silica pieces that were attached to the masses by silicate bonding prior to the welding. In GEO 600 the first-ever implementation of monolithic suspensions in an interferometric gravitational-wave detector was realized. Since thermal noise is expected to set a limit on the achievable detector sensitivity in the most sensitive frequency band, the future interferometric detectors will require such suspensions.

In order to allow for a stable operation of GEO 600, the suspension fiber violin modes are damped to obtain the required mechanical quality factors. This was done individually for the first two modes of each fiber. Furthermore the frequencies of the first two modes were individually tuned for each fiber to obtain a small overall spread centered around the respectively desired frequency.

During the work this thesis is based on, all suspension systems of GEO 600 were installed. Subsequent to a commissioning phase, during which GEO 600 was operated with test optics, the monolithic suspensions were produced and installed. A method to damp and tune the fiber violin modes was developed and applied to the monolithic suspensions.

**Keywords:** Gravitational-wave detector, Monolithic suspensions, Violin modes

# Contents

# Contents

# List of figures

# List of tables

# Glossary

| | | |
|---|---|---|
| $A$ | [m$^2$] | Area |
| $\alpha$ | [K$^{-1}$] | Coefficient of thermal expansion |
| $\beta$ | [K$^{-1}$] | Temperature dependence of the Young's modulus |
| $c$ | $3 \cdot 10^8$ m s$^{-1}$ | Vacuum speed of light |
| $C_v$ | [J K$^{-1}$ m$^{-3}$] | Coefficient of thermal diffusion |
| $D_n$ | [ ] | Loss dilution factor |
| $d_s$ | [m] | Dissipation depth |
| E | [J] | Energy |
| $E$ | [Pa] | Young's modulus |
| $f_n$ | [Hz] | Frequency of the $n$th mode |
| $g$ | $9.81$ m s$^{-2}$ | Acceleration due to gravity at the Earth's surface |
| $\gamma$ | [rad] | Angle of misalignment |
| $\hbar$ | $1.05 \cdot 10^{-34}$ Js | $h/2\pi$ Planck's constant |
| $I$ | [m$^4$] | Bending moment of inertia |
| $\kappa$ | [kg s$^{-2}$] | Spring constant |
| $k_B$ | $1.38 \cdot 10^{-23}$ J K$^{-1}$ | Boltzmann constant |
| $L$ | [m] | Length |
| $m$ | [kg] | Mass |
| n | [ ] | Index of refractivity |
| $\omega_n$ | [Hz] | $2\pi f_n$ |
| $P$ | [Pa] | Tension |
| $\phi$ | [ ] | Loss function |
| $Q$ | [ ] | Quality factor |
| $R$ | [m] | Radius |
| $\rho$ | [kg m$^{-3}$] | Mass density |
| $\rho_L$ | [kg m$^{-1}$] | Linear mass density |

| | | |
|---|---|---|
| $\sigma$ | [ ] | Poisson ratio |
| $\sigma_{\mathrm{B}}$ | [Pa] | Breaking stress |
| $T$ | [K] | Temperature |
| $\tau$ | [s] | 1/e amplitude decay time |
| $u_0$ | [ ] | Static strain |
| $w_0$ | [m] | Laser beam waist (1/e amplitude radius) |

| | |
|---|---|
| ACIGA | Australian Cosortium for Interferometric Gravitational Astronomy |
| **BD** | Beam director |
| **BS** | Beamsplitter |
| CAD | Computer-aided design |
| COM | Center of mass |
| **CP** | Compensation plate |
| CTE | Coeffiecient of thermal expansion |
| CTD | Coeffiecient of thermal diffusion |
| EOM | Electro-optic modulator |
| FEA | Finite elements analysis |
| FSR | Free spectral range |
| FWHM | Full width at half maximum |
| IC | Ion Chromatography |
| LIGO | Laser Interferometer Gravitational-wave Observatory |
| LISA | Laser Interferometer Space Antenna |
| **MC** | Modecleaner |
| **MCe** | East inboard mirror |
| **MCn** | North inboard mirror |
| **MFe** | Far east mirror |
| **MFn** | Far north mirror |
| **MMC 1,2** | Mirror of first or second modecleaner, respectively |
| **MMC 1a,b,c** | Mirror a,b, or c, respectively, of the first modecleaner |
| **MPR** | Power-recycling mirror |
| **MSR** | Signal-recycling mirror |

| | |
|---|---|
| **MU** | Mounting unit |
| NPRO | Nonplanar ring oscillator |
| **OMC** | Output modecleaner |
| **PD** | Photo diode |
| Pitch | Rotation of a mirror around a horizontal axis, perpendicular to the normal of the mirror surface |
| ppm | Parts per million |
| **RM** | Reaction mass |
| ROC | Radius of curvature |
| Roll | Rotation of a mirror around its normal |
| TAMA300 | Japanese interferometric gravitational-wave detector |
| **TCc** | Beamsplitter tank |
| **TCe** | East inboard tank |
| **TCn** | North inboard tank |
| $\mathrm{TEM}_{nm}$ | $nm$th transversal electromagnetic mode |
| **TFe** | Far east tank |
| **TFn** | Far north tank |
| UHV | Ultra-high vacuum |
| VI | LabVIEW$^{\textregistered}$ virtual instrument |
| Virgo | French–Italian interferometric gravitational-wave detector |
| Yaw | Rotation of a mirror around a vertical axis |

xx

# Chapter 1

# GEO 600

## 1.1 Introduction

The existence of gravitational waves was predicted by Albert Einstein, based on the theory of general relativity, which he had published in 1916. The equations predict that gravitational waves are emitted whenever a change in the quadrupole momentum of a given mass distribution occurs. Moreover, it can be shown that gravitational waves carry energy and obey a wave equation with the speed of light as the propagation velocity.

The disturbances of the spacetime caused by gravitational waves are, however, so small that Einstein himself was of the opinion that it might never be possible to perform a direct measurement. In fact, the interaction of matter with spacetime is so weak that only astrophysical processes can generate gravitational waves of amplitudes that are sufficiently large for a detection. This weak coupling allows, however, for an almost undiminished propagation of gravitational waves through the universe. Thus, the waves can carry almost undisturbed information about remote regions of the universe. So far, all knowledge of mankind about astrophysical and cosmological processes is solely based on the observation of electro-magnetic radiation and neutrino detection. Gravitational waves are generated, however, by the interaction of very massive objects, such as neutron stars or black holes that may neither emit electro-magnetic radiation nor neutrinos. Hence, the use of gravitational waves for astronomical observations can provide insight into processes that are not accessible by any other means. Regions that are obscured by interstellar clouds (e.g., the center of our own galaxy) as well as the inner dynamics of astrophysical processes (e.g., supernovae stellar collapses) may become directly observable via gravitational waves. Dark matter eventually neither emits neutrinos nor does it interact with electro-magnetic radiation at all. Thus, gravitational-wave astronomy will open a completely new and complementary window to the universe, which can be expected to be of deep impact on our existent perception of it.

A first proof of the existence of gravitational waves was found by Hulse and Taylor from the repeated observation of the binary system PSR 1913+16 over almost 20 years [Hulse '75, Taylor '82]. The observed decrease of the orbital period was found to be in perfect agreement with the predicted loss of energy due to the emittance of gravitational waves. In 1993, Hulse and Taylor were awarded the Nobel price for this indirect measurement of gravitational waves.

A brief overview of the most promising gravitational-wave sources will be given before current projects that are attempting the detection of gravitational waves with complex

new instruments such as GEO 600 are introduced. Since GEO 600 is part of a world-wide network of gravitational-wave detectors, the other relevant projects are briefly described to allow for a basic comparison of the different approaches. The GEO 600 project and its most relevant subsystems are presented in the subsequent sections to illustrate how this thesis is embedded in the project itself.

Since all interferometric gravitational-wave detectors employ suspension systems, a further integration of this thesis into the international context is provided in detail in the respective sections (please see, e.g., Section 3.12, Section 3.13, and Section 4.7).

## 1.2  Gravitational-wave sources

Although there is a wide variety of astrophysical gravitational-wave sources, not all of them emit waves of amplitude and frequency suitable for a detection. Listed below are the most promising sources for the earth-bound detection. For a detailed overview of these and further sources along with the expected event rates please see, e.g., [Cutler '02]. The candidate sources of gravitational waves are usually sorted according to the signal pattern associated. The signal patterns are divided into burst, chirp, periodic, or stochastic signals. This division is made due to the fact that the appropriate search algorithms differ substantially for the individual patterns.

Burst signals are generated by supernovae explosions. A red giant star may eventually collapse in a supernova, leaving either a neutron star or a black hole. Huge masses are subject to strong acceleration during this collapse. Thus, any deviation of the collapse evolution from spherical symmetry results in the generation of a burst of gravity waves.

Chirp patterns are expected from inspiraling binary systems. Such systems can be composed of either two neutron stars, two black holes, or a combination of both. In the final life phase of the system the binary partners eventually merge. The rapidly decreasing orbital period during this phase of coalescence results in a gravitational-wave signal that increases simultaneously in frequency and strength.

Periodic signals may be generated by deviations of rapidly spinning neutron stars from the perfectly spherical shape. Since pulsars are formed by such fast rotating neutron stars, they are promising candidate sources of periodic gravitational waves.

The stochastic gravitational-wave background originates in part from processes during the early universe and in part from unresolvable background noise. It is the analogue to the well known $2.73\,\mathrm{K}$ micro-wave background. A major difference arises, however, from the fact that the early universe became transparent for gravitational waves at about the Planck time (i.e., $\sim 5 \cdot 10^{-44}\,\mathrm{s}$ after the big bang), whereas electro-magnetic waves decoupled about 380000 years later [Bennett '04]. Thus, the observation of the stochastic background and thereby of the relic gravitational waves, yields information of the very early universe at a time, not accessible by any optical observation.

## 1.3  The effect of gravitational waves

A passing gravitational wave changes the local metric of spacetime and thus the distance between objects (in the following referred to as test masses). The expected relative
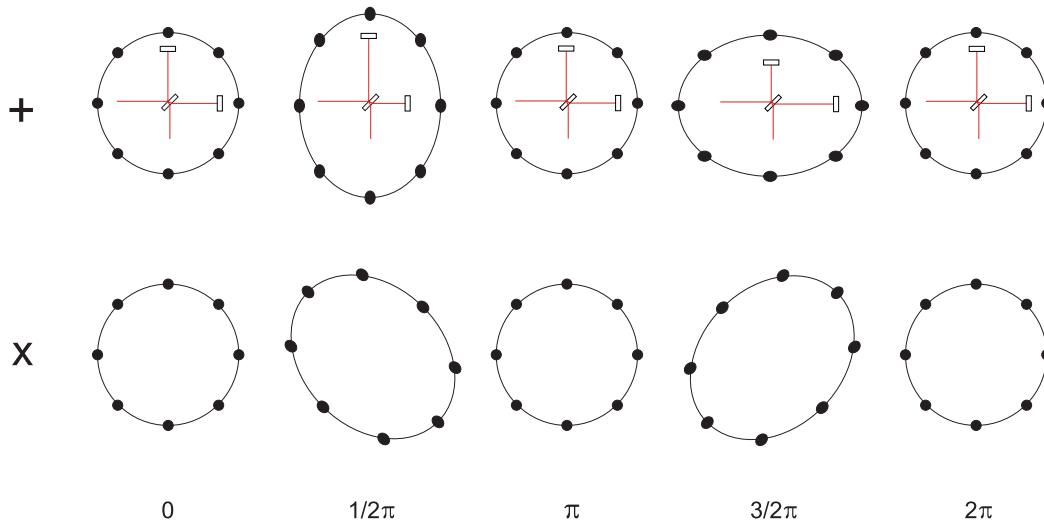
**Figure 1.1:** Effect of the two polarization states of a gravitational wave on a ring of free test masses. The propagation direction of the wave is perpendicular to the ring. In order to emphasize the capability of a Michelson interferometer to sense the apparent length changes, the according evolution of such an instrument is depicted inside the upper ring.

length changes are of order $10^{-21}/\sqrt{\text{Hz}}$ or even below. According to the orientation of the changing quadrupole momentum, two polarisations of gravitational waves exist, referred to as the + (plus) and the x (cross) polarisation. Figure 1.1 displays the effect of a gravitational wave on a ring of free falling test masses due to both polarisation states. It is evident that a Michelson interferometer is suited ideally to detect the apparent length changes for most orientations. However, due to the minuscule effects of gravitational waves on the detector, instruments of an unprecedented sensitivity are called for (see Section 1.5.8 for the design-sensitivity of GEO 600).

## 1.4 Gravitational-wave detectors

The detection of gravitational waves is among the most ambitious projects in modern physics. Basically two approaches to the detection of gravitational waves are followed: The detection via resonant-mass antennas, or via laser-interferometric detectors. The experimental field of detecting gravitational waves, was started in the early 1960's by Joseph Weber. By 1966 his setup included a room temperature aluminum bar of 1180 kg, vibrationally isolated inside a vacuum chamber.[1] The idea is that a passing gravitational wave that has a sufficiently strong spectral component at the resonance frequency of the bar, causes it to oscillate. The resulting oscillation amplitude adds to the thermally-driven oscillation of the bar. This change in the state of oscillation can in principle be detected. However, due to the minuscule effect of a gravitational wave on the detector, a highly sophisticated read-out system has to be employed to minimize the back action

---

[1]This bar is now presented to the public at the LIGO Hanford observatory.

on the bar due to read out process itself. Furthermore, the thermally-driven oscillations need to be decreased by means of cooling to obtain a sufficient signal-to-noise ratio.

Currently seven resonant antennas of either cylindrical or spherical symmetry are in operation or under construction around the world:

**ALLEGRO** is a 2300 kg Al bar antenna at 4.2 K in Baton Rouge, USA [Astone '02].

**AURIGA** is a 2230 kg Al bar detector at 200 mK located in Legnaro, Italy [Zendri '02].

**EXPLORER** is a 2270 kg Al bar at 2.6 K at CERN in Geneva, Switzerland [Astone '02].

**MARIO SCHENBERG** in Brasil is a spherical antenna of 1150 kg CuAl, which is still under construction. It is proposed to work at 20 mK [Aguiar '02].

**MiniGRAIL** in the Netherlands is a 1150 kg CuAl sphere still under construction. It is proposed to work below 1 K [de Waard '02].

**NAUTILUS** is a 2260 kg Al antenna at 130 mK located in Frascati, Italy [Astone '02].

**NIOBÉ** is a 1500 kg Nb bar antenna at 5 K in Perth, Australia [Coward '02].

While the resonant detectors provide a high sensitivity only within a comparatively narrow bandwidth of a few tens of Hz, the interferometric approach yields a broad bandwidth of up to a few kHz of high sensitivity. Since recently five interferometric gravitational-wave detectors are operating in a more or less continuous observation mode. Two further detectors are under construction, one of them close to first operation. Advanced detectors, employing next generation techniques, are already proposed [Weinstein '04, Uchiyama '04], and eventually there will even be a space-borne mission, designed to detect low frequency gravitational waves with a very long-baseline laser interferometer [Danzmann '03].

**AIGO** is the Australian project, under construction at Gingin near Perth [Ju '04]. Currently AIGO is operating a vacuum system with two 80 m long arms. The installation of first optics is under way.

The **LIGO** collaboration operates three interferometric gravitational-wave detectors in the USA [Abramovici, Sigg '04]. One Michelson interferometer with 4 km arm length is located in Livingston, Louisiana. Two Michelson interferometers with 4 km and 2 km arm length, respectively, are co-located in a common vacuum system in Hanford, Washington. All three interferometers follow the same scheme, having Fabry-Perot cavities in the arms with a finesse of 208 (220 for the 2 km interferometer), and using a power-recycling factor of 50. The test-mass suspensions of the LIGO interferometers are realized by single pendulums. A brief introduction to the LIGO suspensions is provided in Section 3.12.1. The LIGO collaboration has initiated and performed three scientific data taking runs, referred to as S1, S2, and S3, partly in coincidence with other detectors (resonant detectors as well as interferometers). LIGO will be upgraded to Advanced LIGO within this century. This upgrade will include, e.g., more complex suspension systems and higher optical power levels.

The Japanese **TAMA** project is operating a Michelson interferometer (referred to as TAMA300) with 300 m arm length, located near Tokyo [Tsubono, Takahashi '04]. TAMA300 has Fabry-Perot cavities in the interferometer arms with a finesse of 520 and employs a power recycling factor of 10. The test masses of TAMA300 are suspended as double pendulums from a pre-isolation stage (see Section 3.12.2). TAMA300 has participated in coincidence with the LIGO detectors in the scientific data taking runs S1, S2, and S3 (for S1 and S3 in a further coincidence with GEO 600).

**Virgo**, the French-Italian project, is building a Michelson interferometer with 3 km arm length near Pisa [Bradashia '90, Acernese '04]. The interferometer has Fabry-Perot cavities in the arms with a finesse of 50 and will, in the final configuration, use a power-recycling factor of about 100. The test masses of the Virgo interferometer are suspended from the so-called super attenuator (see Chapter 3.13.1). The super attenuator includes a multiple-cascaded pendulum, suspended from the top of a large inverted pendulum. It allows for the search for gravitational waves in the low frequency regime (the designed strain sensitivity of Virgo at 20 Hz is of remarkable $\sim 10^{-21} \, 1/\sqrt{\text{Hz}}$). Virgo is now close to its first data taking.

**LISA** eventually is the proposed space borne gravitational-wave detector [Vitale '02, Danzmann '03]. It is currently worked on with equal contributions from NASA and ESA. LISA will consist of three spacecraft, arranged in an equilateral triangle with $\sim 5 \cdot 10^7$ km side length. Thus, it will form three coupled interferometers with the side lengths of the triangle as the arm lengths. The three satellites will follow the earth on a heliocentric orbit at a distance of one astronomical unit (i.e., $1.5 \cdot 10^8$ km). LISA will explore the low frequency regime from 0.1 mHz to 100 mHz, which is due to the so-called seismic wall, not accessible with any earth bound detector. The launch date is scheduled to September 2012.

## 1.5 GEO 600

The British-German GEO 600 project [Danzmann '95, Hewitson '03, Willke '04] is located in Ruthe, near Hannover, Germany. It is based on a Michelson interferometer with arms of 600 m length, each folded once to obtain an effective arm lengths of 1200 m. Both techniques, power recycling and signal recycling are employed in GEO 600, as is illustrated in the simplified optical layout of GEO 600 shown in Figure 1.2. All relevant optics of GEO 600 are suspended as multiple pendulums that are enclosed in a common ultra-high vacuum system with a volume of 400 m³.

The light source of GEO 600 is a 14 W Nd:YAG laser system in a master-slave configuration. The laser light is passed through two consecutive modecleaner cavities before it enters the interferometer through the power-recycling mirror. At the beamsplitter it is split up and then send along the two interferometer arms (referred to as north and east arm, respectively). At each far mirror (**MFn** and **MFe**) the beams are reflected toward the corresponding inboard mirror (**MCn** and **MCe**). The inboard mirrors in turn send the beams back to the far mirrors, which now reflect them toward the beamsplitter where the two beams are eventually recombined. This scheme is realized by placing the inboard mirrors 25 cm above the beams that go toward or come from the beamsplitter. The light path is such that the beams are raised on the way to the far mirrors by 12.5 cm and by another 12.5 cm on the way to the inboard mirrors.

The Michelson interferometer is maintained on its nominal operating point by means of feedback actuation on the inboard mirrors. The feedback signals are applied from suspended reaction masses. With the currently used length-control servo, the inboard mirrors follow the differential motion of the far mirrors from 0 Hz to 100 Hz.
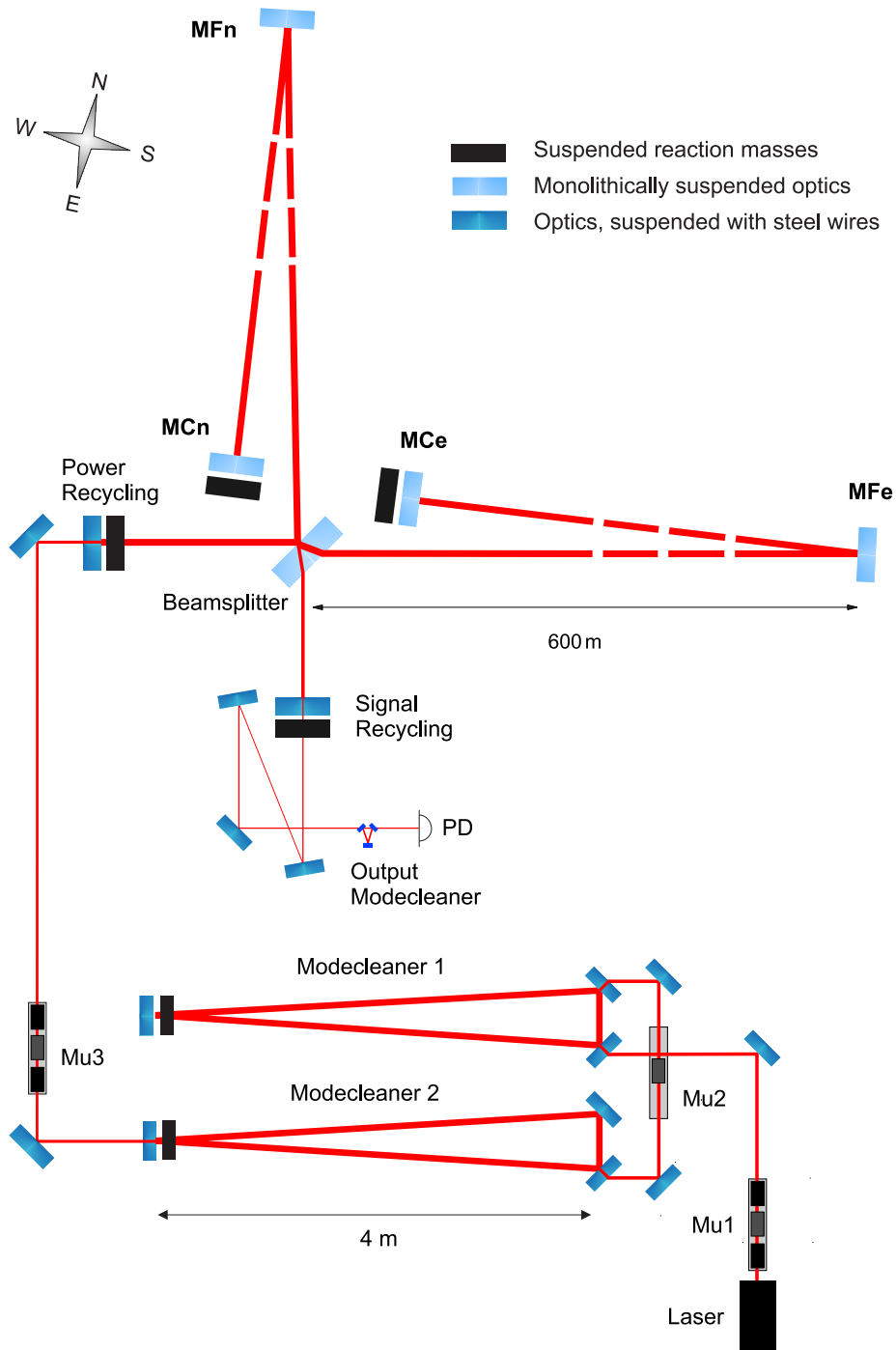
**Figure 1.2:** Simplified optical layout of GEO 600. It is a dual-recycled Michelson interferometer with 600 m arm length. Each arm is folded once, such that an effective arm length of 1200 m is obtained. Before the laser beam enters the interferometer it is passed through the two consecutive modecleaner cavities to obtain spatial and temporal filtering. In the final configuration a further modecleaner will be located at the output port of the interferometer to reject light in higher order modes.

The design of GEO 600 includes several specialities that are regarded as second generation techniques. Among these techniques are the use of signal recycling, low-noise electrostatic actuation at the test masses, and complex test-mass suspension systems. The test masses and the beamsplitter are suspended as triple-cascaded pendulums, including a last stage that is entirely made of fused silica.

## 1.5.1 The ultra-high vacuum system

All relevant optics of GEO 600 are enclosed in a common ultra-high vacuum (UHV) system to avoid contamination of the optics and to minimize both the influence of refractive index variations of the air and acoustic coupling to the optics. The system can be divided into individual sections by the operation of gate valves, thus allowing for maintenance or installation work in a certain section while the rest of the system remains evacuated. The overall enclosed volume is approximately $400 \, \mathrm{m}^3$, kept at a pressure in the low $10^{-6} \, \mathrm{Pa}$ ($10^{-8} \, \mathrm{mbar}$) region. For further information about the UHV system, please see Appendix D.

A second vacuum system that provides the evacuation of the pre-isolation system for the optics is built inside the UHV system. This second vacuum system has to be operated separately, since it contains non UHV compatible components. A description of the pre-isolation system can be found in Section 3.2.

## 1.5.2 Suspensions

For frequencies above $3 \, \mathrm{Hz}$ the ambient seismic noise in the vicinity of GEO 600 is roughly of the form $10^{-7} \, \mathrm{m}/\sqrt{\mathrm{Hz}} \cdot [1 \, \mathrm{Hz} \, / f \,]^2$. Hence, a strong isolation of more than ten orders of magnitude (at $50 \, \mathrm{Hz}$) is required for the test masses to obtain the design sensitivity of GEO 600, displayed in Figure 1.5 in Section 1.5.8. Evidently, the seismic isolation of the test masses is one of the key aspects of the earth bound interferometric gravitational-wave detectors.

The required isolation for GEO 600 is achieved by suspending the test masses from triple-cascaded pendulums [Plissi '00, Torrie '00, Goßler '02], damped at the uppermost stage by magnet-coil actuators. These pendulums include two additional cantilever-spring stages to improve the isolation in the vertical direction. The suspension point itself is pre-isolated by the use of stack isolators [Plissi '98], containing a passive and an active isolation stage. The test masses have a diameter of $180 \, \mathrm{mm}$, a thickness of $100 \, \mathrm{mm}$, and weigh $5.6 \, \mathrm{kg}$. The length of the triple pendulums is $920 \, \mathrm{mm}$. The test-mass suspensions include a monolithic last stage, to lower the thermal noise of the suspension and of the test mass itself [Barr '02, Goßler '04, Smith '04]. The beamsplitter ($9.3 \, \mathrm{kg}$, $260 \, \mathrm{mm}$ diameter, $80 \, \mathrm{mm}$ thickness) is suspended similar to the test masses by a triple pendulum with a monolithic last stage. Please see Chapter 4 for a detailed description of the production and installation of the monolithic suspension stages.

Besides the test masses and the beamsplitter, also the signal-recycling mirror is suspended from a triple-cascaded pendulum. All other relevant optics are suspended from individual double pendulums. Please see Chapter 3 for the full description of the different suspension types employed in GEO 600.

In order to apply the fast feedback signals required to maintain the interferometer at the operation point and the modecleaner cavities as well as the power- and signal-recycling cavity at resonance, reaction pendulums are suspended behind the respective optics. These reaction pendulums provide seismically-isolated platforms to support the feedback actuators. The feedback for the modecleaner cavities and for the power- and signal-recycling cavity is applied directly to the according mirrors via magnet-coil actuators. The length-control signals for the Michelson interferometer are applied by magnet-coil actuators at the penultimate masses of the inboard suspensions, and via electrostatic actuation at the inboard mirrors themselves. Section 3.9 provides the description of the reaction pendulums used for the control of the Michelson interferometer.

### 1.5.3 The light source

As the light source, GEO 600 employs a 14 W injection locked master-slave system with an 800 mW Nd:YAG non-planar ring oscillator (NPRO [Kane '85]) as the master laser [Zawischa '02]. The master laser has a high intrinsic temporal and spatial stability, while the free running slave laser has a high output power at moderate stability. By the appropriate injection of the master beam into the slave cavity and the according length control of the slave laser cavity, injection locking can be achieved. This techniques allows for a transfer of the master laser's stability to the high power output of the slave laser. The slave laser is a ring oscillator in bow-tie configuration, housed in an Invar spacer. The active media are two Nd:YAG rods, each pumped from one end by an individual fiber-coupled laser-diode array of 17 W output power.

For the commissioning phase and the first scientific data taking run S1, the laser power was attenuated to 1 W input power at the first modecleaner. After passing through both modecleaners and the required phase modulators for the modecleaner and interferometer control, about 0.5 W remained to illuminate the Michelson interferometer. The attenuation was done via a half-wave plate and a polarizing beamsplitter. Before the next data taking run in coincidence with the LIGO and TAMA detectors the light power was increased by a factor of two, such that currently 1 W of laser power is impinging at the interferometer. A further increase of light power is under way, aiming for 5 W at the interferometer input.

### 1.5.4 The modecleaners

The illuminating laser light must be very stable in power, frequency and geometry to achieve the GEO 600 strain sensitivity goal. Despite its already high beam quality, the light is required to be filtered temporally and spatially by a sequential two-cavity optical modecleaner system [Goßler '02, Goßler '03]. After passing the laser light through such a modecleaner system it has a much better stability in terms of geometrical fluctuations [Rüdiger '81], frequency fluctuations, and power fluctuations (the latter two are diminished at frequencies above the cavity pole frequency.).

Figure 1.3 provides the simplified optical layout of the modecleaner system employed in GEO 600. It consists of two high-finesse triangular ring cavities of 8 m optical path length each. The modecleaner system is housed in an individual section of the common
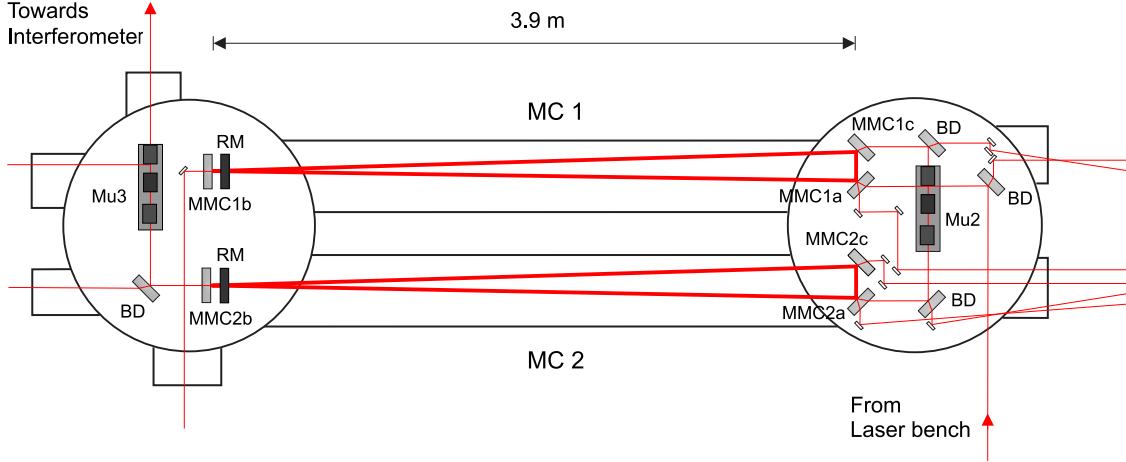
**Figure 1.3:** Simplified optical layout of the modecleaner system. In addition to the six cavity mirrors (**MMC1a, MMC1b, ...**) four beam-steering mirrors (**B**eam **D**irector) are suspended, one each at the input and output of each modecleaner cavity. Two reaction masses (**RM**) are suspended in front of **MMC1b** and **MMC2b**, to allow for the length control of the cavities. The electro-optic modulators for the second modecleaner and for the interferometer are mounted on suspended platforms, so-called mounting units (**MU**), after the first and after the second modecleaner. In addition to the modulators, the last mounting unit supports two Faraday isolators and a lens. Small pick-off mirrors (most of them have been omitted for clarity here) are mounted on the bottom plates of the vacuum chambers to direct the laser beams needed for the control of the cavities toward the respective photo diodes (not shown here) that are installed outside the vacuum system.

|                      | MC1        | MC2        |
| -------------------- | ---------- | ---------- |
| Optical path length  | 8.00 m     | 8.10 m     |
| FSR                  | 37.48 MHz  | 37.12 MHz  |
| $w_0$                | 1.05 mm    | 1.05 mm    |
| $z_R$                | 3.3 m      | 3.3 m      |
| Finesse              | 2700       | 1900       |
| Visibility           | 94%        | 92%        |
| Throughput           | 80%        | 72%        |

**Table 1.1:** Properties of the modecleaner cavities. The optical path length, the free spectral range FSR, the beam waist $w_0$ and the Rayleight range $z_R$ of each cavity are given. The finesse of the first modecleaner was measured both with a ring down and an amplitude transfer function method. The finesse of the second modecleaner is derived from the mirror specifications. Furthermore, the measured visibility and throughput of both modecleaners are given.

UHV system. All optical components of the two modecleaners are suspended as double pendulums to isolate the cavities from seismic noise. The pendulums are damped at their resonance frequencies at the upper pendulum stage with four magnet-coil actuators. A suspended reaction mass supports further three coils that match three magnets bonded onto the surface of one mirror of each cavity. These actuators are used for the length control of the modecleaner cavities to maintain resonance with the laser light. A detailed description of the modecleaner suspension systems and the employed active damping is given in Section 3.3. Table 1.1 provides the most relevant properties of the two modecleaner cavities.

Maintaining the two modecleaner cavities transparent for the laser light requires a hierarchical control structure. The fully automated control system employed in GEO 600 stabilizes the slave laser's frequency to that of the master laser, the master laser's frequency to the length of the first modecleaner and the length of the first to the length of the second modecleaner. Eventually the length of the power-recycling cavity is taken as the reference for the stabilization of the second modecleaner's length. The control system uses the Pound-Drever-Hall sideband technique [Drever '83] and operates autonomously over long time periods (i.e., many months) with only infrequent human interaction. Furthermore, the second modecleaner is kept resonant for modulation sidebands, phase locked to a Rb reference oscillator which tracks the Global Positioning System time standard, providing long term stability.

Table 1.2 provides a comparisson of the basic properties of the modecleaner cavities for GEO 600, LIGO, TAMA, and Virgo.

|                    | GEO 600        | LIGO     | TAMA     | Virgo    |
|--------------------|----------------|----------|----------|----------|
| Number of cavities | 2              | 1        | 1        | 1        |
| Length             | 8 m            | 24 m     | 9.75 m   | 143 m    |
| Finesse            | 2700 and 1900  | 1350     | 1700     | 1100     |
| Throughput         | 80% and 72%    | 64%      | 50%      | 40%      |
| Suspension type    | 2 stages       | 1 stage  | 2 stages | 1 stage  |

**Table 1.2:** Comparison of the basic properties of the modecleaner cavities employed for the different interferometric gravitational-wave detectors.

### 1.5.5  Power recycling

The nominal operating point of the GEO 600 interferometer is the so-called dark fringe at which, ideally, all of the ingoing light is reflected backward to the input port. Thus, the interferometer can be regarded as a high reflecting mirror. By placing a mirror in the input port of the interferometer the backward reflected light power can be "recycled" by reinserting it into the interferometer. The Michelson interferometer hence forms a Fabry-

Perot cavity (the power-recycling cavity) with the so-called power-recycling mirror (see Figure 1). This technique of power recycling allows maximization of the light power stored in the Michelson interferometer and thus improves the shot-noise limited sensitivity.

The stabilization of the GEO 600 power-recycling cavity is obtained by stabilizing the length of the second modecleaner to the length of the power-recycling cavity. As described in Section 1.5.4, the length of the first modecleaner and thus the laser frequency is stabilized to follow the length of the second modecleaner. An electro-optical modulator at the third mounting unit **MU3** is used as a fast phase shifter to increase the bandwidth of the power-recycling lock. The length noise of the power-recycling cavity is dominated by the motion of the power-recycling mirror itself due to the more powerful vibration isolation of the test masses and the beamsplitter. The design of the power-recycling suspension (described in detail in Section 3.5) leads, however, to a residual motion of the power-recycling mirror that provides a safety factor of three orders of magnitude in terms of the resulting length stability at frequencies above 100 Hz.

Currently, the power-recycling mirror used in GEO 600 has a transmissivity of 1.35%, leading to a power-recycling factor of about 300. [2] The final power-recycling mirror has a more than ten times higher reflectivity, leading to a power-recycling factor of about 2000. For an impinging laser power of 5 W, the light power stored inside the power-recycled Michelson interferometer will thus be of the order of 10 kW.

The power-recycling factors, laser power, and arm cavity finesse for the final configurations of the interferometric gravitational-wave detectors are provided in Table 1.3. Please note that the laser power is subject to a substantial reduction by passing through the required input optics. The input optics consist of the modecleaner cavities, electro-optical modulators, and optical isolators. The values for the throughput of the input optics given in the table reflect the actual status.

|  | GEO 600 | LIGO | TAMA | Virgo |
|---|---|---|---|---|
| Laser Power | 14 W | 10 W | 10 W | 22 W |
| Throughput input optics | 50% | 40% | 30% | 33% |
| Power-recycling factor | 2000 | 50 | 10 | 100 |
| Arm cavity finesse | — | 208 | 520 | 50 |

**Table 1.3:** The laser light power is diminished by the input optics before it impinges on the power-recycling mirror. The light power stored inside the interferometer is scaled by the power-recycling factor and arm-cavity finesse.

---

[2]The power-recycling factor relates the light power stored in the power-recycled Michelson interferometer to the incident light power.

### 1.5.6 Signal recycling

Placing also a mirror in the output port of the interferometer (see Figure 1), provides an enhancement of the phase modulation sidebands induced by gravitational waves. This technique is referred to as signal recycling. The combined use of power and signal recycling is called dual recycling [Strain '91, Heinzel '02, Grote '04].

The frequency response of a signal-recycled (or dual recycled) interferometer can be adjusted by changing the signal recycling mirror's reflectivity and/or position [Meers '88, Heinzel '98]. The response can either be set such that a wide-band sensitivity of the detector from about 50 Hz to a few kHz results, or such that a narrow frequency band of enhanced sensitivity is created. The latter case increases, however, the sensitivity at a given frequency band of choice at the expense of a deterioration of the sensitivity at other frequencies. Figure 1.5 displays the design sensitivity of GEO 600 for different tuning states of the signal-recycling cavity, and for different reflectivities of the signal-recycling mirror.

The modulation scheme used in GEO 600 to obtain control signals is known as frontal or Schnupp modulation [Schnupp '88]. The phase modulation is applied after the second modecleaner at the third mounting unit **MU3** (Section 3.3). A beam reflected at the anti-reflective coating of the beamsplitter is used to derive the control signal (beam on photo diode **PDBSe** in Figure 3.23).

### 1.5.7 Data acquisition

Besides monitoring the so-called $h$ channel, containing the potential gravitational-wave signal, more than 100 auxiliary channels are subject to surveillance. The effective bandwidth for these channels (referred to as fast channels) is 8 kHz. Further $\sim 1000$ signals (referred to as slow channels) are recorded by the LabVIEW® [3] control system. Among these are the channels for the drift control of the suspended optics as well as the local control channels, required for the damping of the pendulums. Moreover, the environmental channels, containing information about the seismic vibrations, temperature, magnetic fields, etc. are included in the slow channels. [Kötter '02]

The immense amount of data produced by GEO 600 at a rate of about $1\,\mathrm{Mbyte\,s^{-1}}$ is locally stored on a raid disc array and also sent via radio link to the Albert-Einstein-Institut in Hannover. In order to provide compatibility with the data acquired by other detectors, a common file format, the Frame format, is used in the gravitational-wave community to store and exchange data.

A further important requirement is the timing accuracy. Firstly, accurate time stamps are required for the search for coincident events in widely spaced detectors. This technique is used to identify the presence of burst signals in the data. Secondly, for continuous gravitational wave searches, a timing accuracy of $10\,\mu$s or better is required so that the phase of the gravitational waves can be properly taken into account when integrating over time periods of the order of several months. [Kötter '04]

---

[3] National Instruments http://www.ni.com/labview/
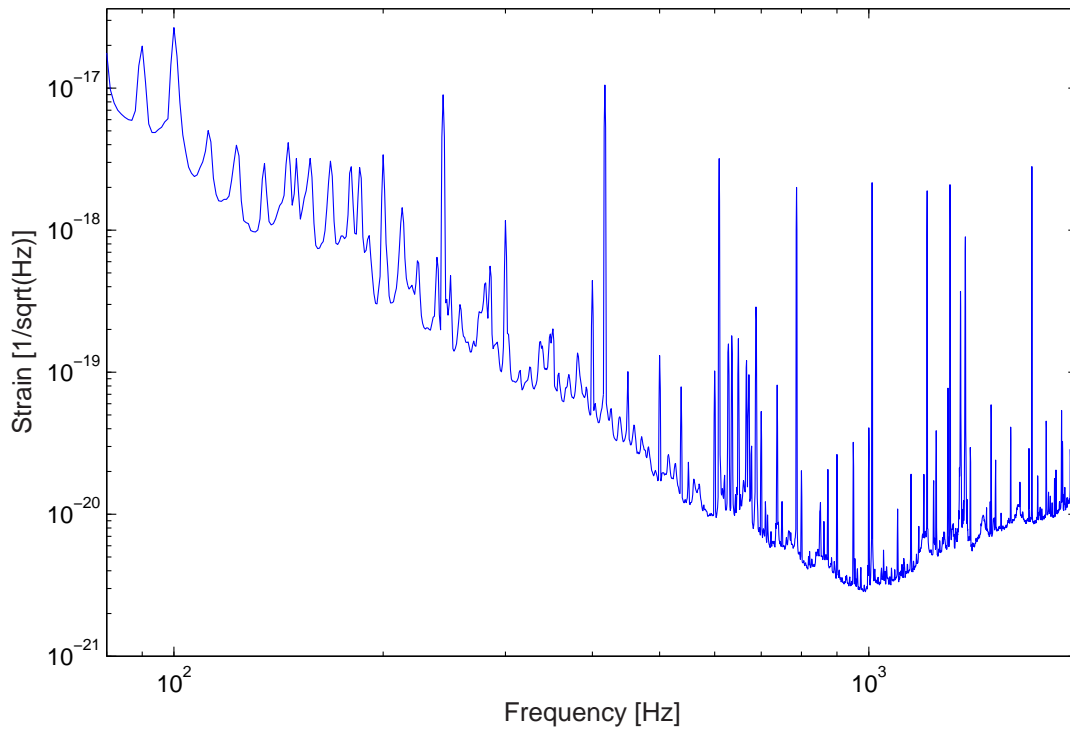
**Figure 1.4:** Strain sensitivity of GEO 600 during the second participation phase of the scientific data taking run S3.

### 1.5.8 Performance

The current performance of GEO 600 can be judged on the basis of the 14-day-long second participation phase of GEO 600 during the scientific data taking S3 run. GEO 600 was maintained in the observational mode during 98.8% of the time in this period. Losses of lock were due to, e.g., an earthquake of magnitude 6.4 in New Caledonia, or local events such as a truck passing nearby one of the end station of GEO 600.

The preliminary calibrated sensitivity of GEO 600 during the second part of S3 is displayed in Figure 1.4. The most sensitive region is around 1 kHz due to the employed signal-recycling tuning. The strain sensitivity at this frequency is $3 \cdot 10^{-21} \, 1/\sqrt{\mathrm{Hz}}$. The peaks at 417 Hz, 609 Hz, 787 Hz, 1011 Hz, 1213 Hz, 1309 Hz, and 1717 Hz are due to injected frequency lines that are used for the calibration of the detector sensitivity. The excess noise around 650 Hz is caused by the violin-mode oscillations of the suspension fibers. The corresponding high noise level is due to the fact that the according notch filter in the length-control servo was accidentally deadjusted at the time of the measurement. Chapter 5 describes in detail the effects of the violin-mode oscillations and the precaution that has been taken to allow for a stable operation of GEO 600 with the sensitivity deteriorated as little as possible.

As described in Section 1.5.6, the sensitivity of GEO 600 depends strongly on the signal-recycling state actually set. The upper graph in Figure 1.5 shows the design sensitivity of GEO 600 for the wide-band detection case, along with the projected noise budget

for the individual subsystems. Below 40 Hz, seismic noise is clearly dominating all noise contributions. Between 50 Hz and 400 Hz, the internal thermal noise of the test masses is the dominating noise source. Above 400 Hz, shot noise sets a limit to the sensitivity. The peak in the noise spectrum at 650 Hz represents the violin-mode oscillations of the suspension fibers. The lower graph in Figure 1.5 displays the associated design sensitivities for different tunings of the signal-recycling cavity and transmissivities of the signal-recycling mirror.
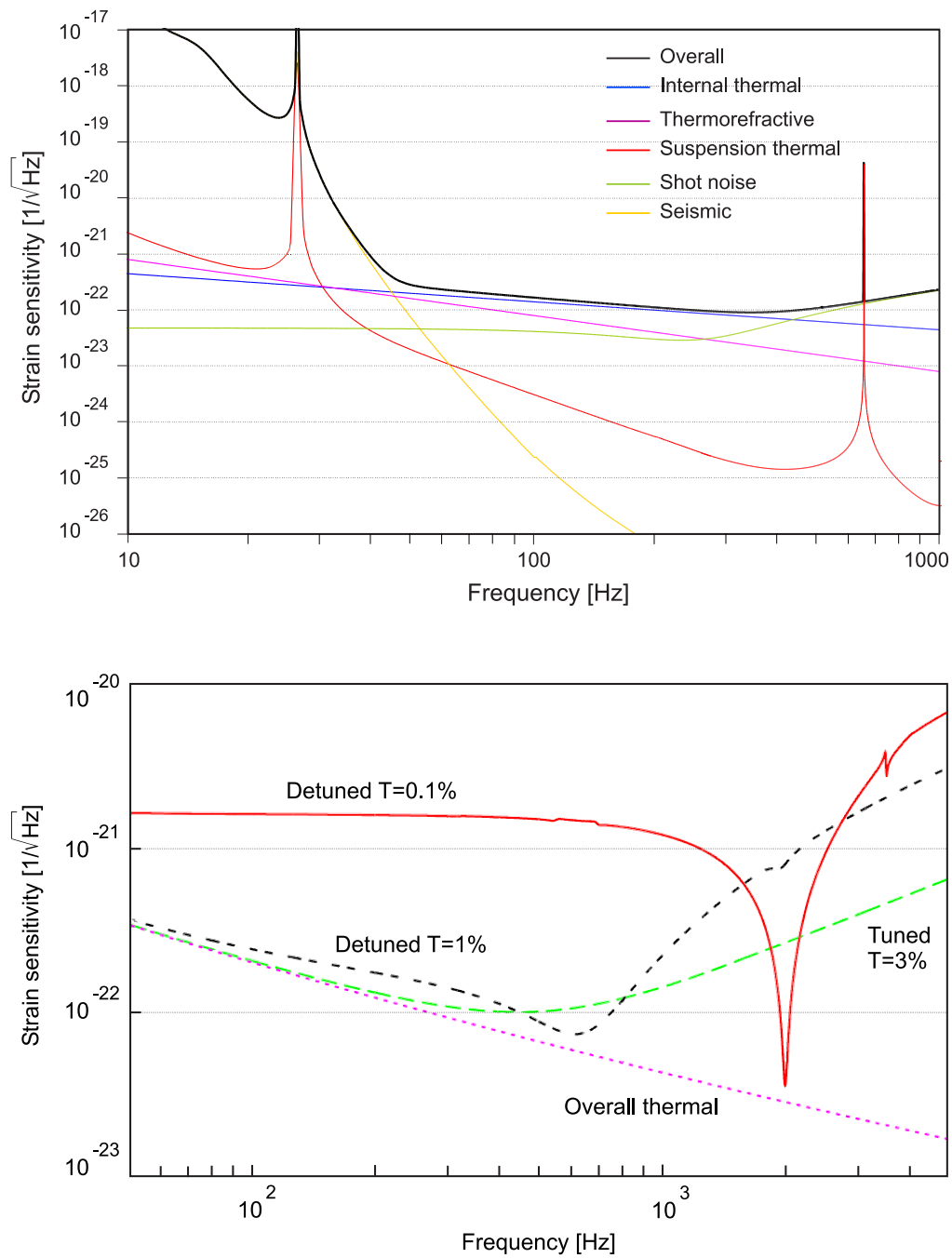
**Figure 1.5: Upper graph:** Design sensitivity of GEO 600 if operated in the broadband mode, along with the projected noise contributions.

**Lower graph:** Sensitivity of GEO 600 for different tunings of the signal-recycling cavity and different transmissivities T of the signal-recycling mirror. The suspension violin mode at 650 Hz has been omitted for clarity.

# Chapter 2

# Seismic and thermal noise

## 2.1 Introduction

In order to allow for measurements with the precision asked for in Chapter 1, the test masses of the interferometric gravitational-wave detectors require an isolation by many orders of magnitude from the ground motion. A spectrum of the horizontal seismic motion as acquired on the inner part of the split foundation in the central station of GEO 600, is shown in Figure 2.1. Above about $3\,\mathrm{Hz}$ the horizontal seismic motion is roughly of the form $10^{-7}\,\mathrm{m}/\sqrt{\mathrm{Hz}} \cdot [1\,\mathrm{Hz}\,/f\,]^2$. The resulting demands on the isolation performance can be fulfilled by suspending the test masses as (multiple cascaded) pendulums. The isolation achieved by suspending the test masses in this way is explained and quantified in the first part of this chapter. A detailed description of the GEO 600 test-mass suspensions is provided in Chapter 3. In order to allow for a direct comparison, the test-mass suspensions of the other interferometric gravitational-wave detectors are briefly introduced in Section 3.12 and Section 3.13.

Once the seismic noise has been sufficiently suppressed by the attenuation of the suspensions, the thermal noise of the test-masses and their suspensions becomes the limiting noise source. Thermal noise is among the major limitations to the sensitivity of the gravitational-wave detectors. Consequently, great effort is being carried out worldwide in order to develop novel suspension techniques that allow for a lowering of the thermal-noise floor. New materials are under investigation for the suspension filaments as well as for the test masses themselves. The most encouraging candidate materials among these are sapphire, silica, or silicon for the test masses, and sapphire or silica for the suspension filaments. By the use of new bonding and welding techniques, so called "monolithic" suspensions can be made, which are expected to lower the thermal noise substantially with respect to steel wire suspensions. Although monolithic suspensions will play a key role for all future earth-bound interferometric gravitational-wave detectors, so far these suspension types are solely employed in GEO 600. Chapter 4 gives a detailed description of the monolithic suspensions of GEO 600.

Since there is a wide variety of literature about the aspects of the different thermal noise contributions, the full derivation of the results and expressions is not provided here, but rather cited. However, the most relevant expressions for the work on which this thesis is based, are derived in the respective chapters. The second part of the current chapter hence provides an introduction to the underlying processes that cause the different thermal noise contributions. Thus, it provides the motivation for the inevitable need to
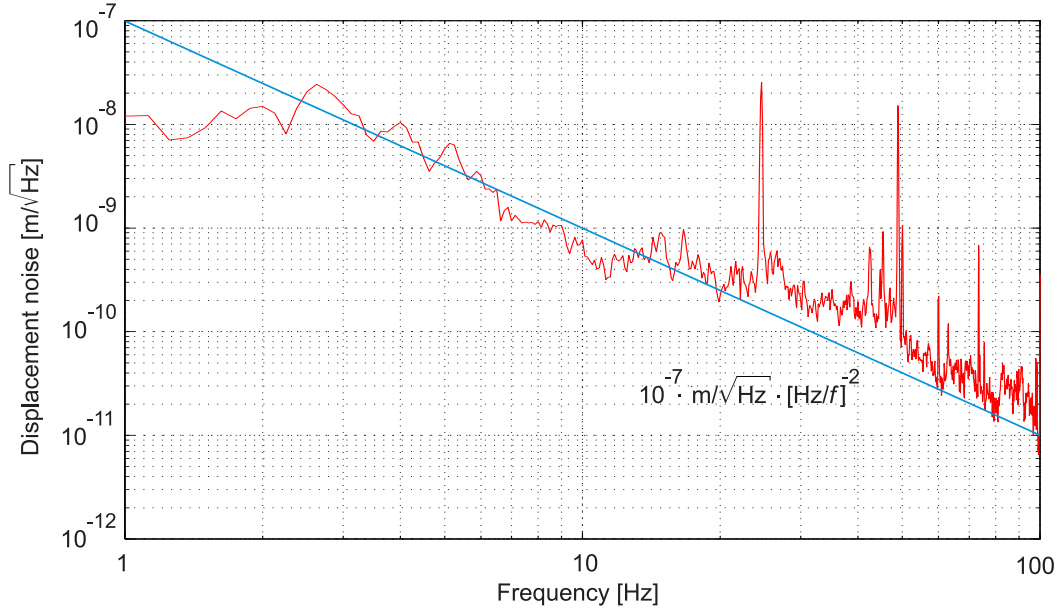
**Figure 2.1:** Horizontal seismic motion, measured on the inner part of the split foundation of the central station. The motion is roughly of the form $10^{-7}\,\mathrm{m}/\sqrt{\mathrm{Hz}}\cdot[1\,\mathrm{Hz}\,/\,f\,]^2$ above $3\,\mathrm{Hz}$. The sharp resonance at $23.5\,\mathrm{Hz}$ is caused by a scroll pump, which is now suspended from a coil spring.

utilize low dissipation, i.e., monolithic, suspension systems in the following generations of interferometric gravitational-wave detectors.

## 2.2 Vibration isolation

The first duty of the suspension systems is to provide sufficient vibration isolation. Above its resonance frequency the response of a single pendulum to a displacement of the suspension point scales with $1/f^2$. Thus, by suspending the optics one benefits from the mechanical low pass filtering of the pendulum. The resonance frequency $\omega_0 = 2\pi\,f_0$ of a single pendulum is given by

$$\omega_0 = \sqrt{\frac{\kappa}{m}} = \sqrt{\frac{g}{L}} \tag{2.1}$$

Here $\kappa$ denotes the spring constant, $m$ is the suspended mass, $g$ is the acceleration due to gravity at the earth's surface, and $L$ is the length of the pendulum. Below this frequency, the motion of the suspended mass follows any horizontal motion of the suspension point in phase and with equal magnitude. The result is simply a translation of the rest position of the pendulum. If the suspension point oscillates with the resonance frequency of the pendulum, the suspended mass oscillates around its rest position. The occurring oscillation amplitude of the suspended mass exceeds the motion of the suspension point by a certain amount, which is a characteristic value (the mechanical quality factor $Q$)

for a given pendulum. The phase of the suspended mass lags by 90 degree compared to the phase of the suspension point, when exactly on resonance. This phase lag leads to a continuous transfer of energy from the suspension point motion into the pendulum oscillation. The resulting pendulum amplitude increases to a level at which the rate of energy transfered into the oscillation and the rate of energy dissipated during the oscillation is in equilibrium. The dissipation of energy in the pendulum due to the oscillation is caused by a variety of mechanisms, which are discussed in the designated sections in the second part of this chapter.

Above the resonance frequency, the suspended mass lags 180 degree of phase. As a result, the mass follows the oscillation of the suspension point with an amplitude that decreases quadratically with increasing frequency. This becomes clear from a straightforward consideration of the energy stored in the oscillation. The energy is stored in the lossless gravitational field [1] at the extremes of the oscillation or manifests as kinetic energy when the pendulum swings through its rest position. The kinetic energy at this point is

$$\mathrm{E} = \frac{1}{2}mv^2 = \frac{1}{2}m\,C^2\,\omega^2 \tag{2.2}$$

where $v$ is the velocity and $C$ is the oscillation amplitude. Hence, the amplitude decreases with $1/f^2$ for a given energy.

The three cases discussed illustrate the response of a suspended mass, $x_{\mathrm{mass}}$, to the motion of its suspension point, $x_{\mathrm{susp}}$. In general, the response defines the transfer function of the pendulum. The transfer function is given by

$$\hat{x}(\omega) := \left| \frac{x_{\mathrm{mass}}}{x_{\mathrm{susp}}} \right| = \sqrt{\frac{(1 + \phi^2)\,\omega_0^4}{(\omega_0^2 - \omega^2)^2 + \phi^2\,\omega_0^4}} \tag{2.3}$$

while the respective phase is described by

$$\alpha = \arctan\frac{\phi\,\omega^2}{\omega^2 - \omega_0^2\,(1 + \phi^2)} \tag{2.4}$$

where $\phi$ describes the damping of the oscillation. If viscous damping is negligible, $\phi$ is independent of frequency and its inverse equals the mechanical quality factor $\phi^{-1} = Q$. The quality factor describes the ratio of energy stored in the oscillation to the energy dissipated per cycle.

$$Q = 2\pi \cdot \frac{\text{Energy stored}}{\text{Energy lost per cycle}} \tag{2.5}$$

Figure 2.2 illustrates the transfer function of a single pendulum with a resonance frequency of $f_0 = 2\pi \cdot \sqrt{9.81/0.28}\,\mathrm{Hz} = 0.94\,\mathrm{Hz}$, as for the lowest stage of a GEO 600 test-mass suspension. The damping term is assumed to be $\phi = 10^{-8}$.

---

[1] To be exact, a fraction of the energy is stored in elastic energy via the deformation of the suspension fibers. This deformation causes the energy dissipation during the oscillation. However, in calculating the overall energy stored in the oscillation, it needs not be accounted for.
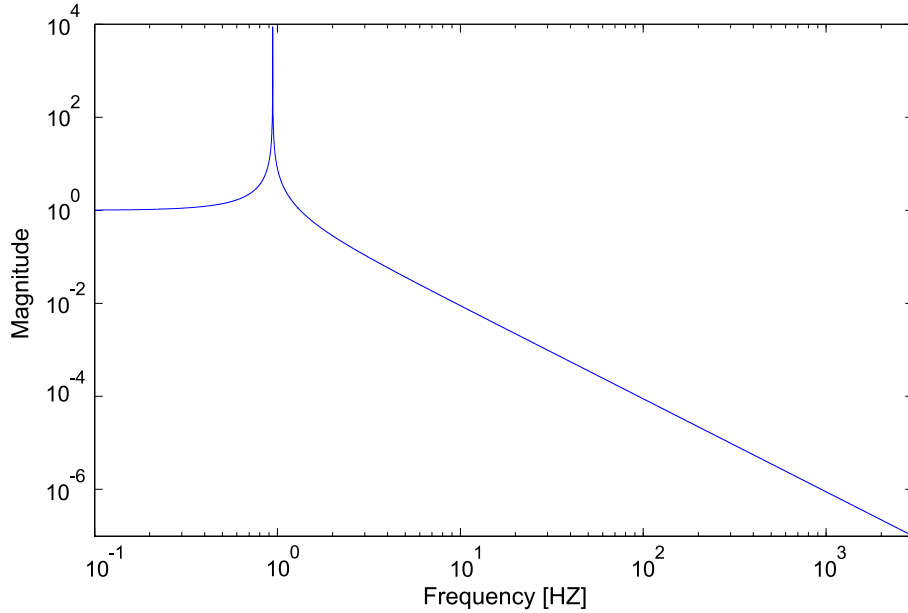
**Figure 2.2:** Longitudinal transfer function of a single pendulum with a resonance frequency of $f_0 = 2\pi \cdot \sqrt{9.81/0.28}\,\mathrm{Hz} = 0.94\,\mathrm{Hz}$ and a damping constant of $\phi = 10^{-8}$.

Referring to Equation (2.3), by suspending the interferometer mirrors one benefits from the $1/f^2$ isolation performance in terms of attenuation of the vibrational excitation of the suspended optics. However, a tribute has to be paid at the resonance frequency of the pendulum. The resonant enhancement of the motion nearby this frequency can lead to significant amplitudes of the pendulum. Thus, the pendulum needs to be damped in order to inhibit excessive amplitudes. As will be explained in Section 2.3, the damping of the pendulums for gravitational-wave detectors is required to be as low as can be achieved in the sensitive frequency band. Hence the damping has to be applied solely in a selected frequency region. For the GEO 600 suspensions, this is done via magnet-coil actuators with co-located optical position and orientation sensors at the uppermost pendulum stages. Please see Section 3.3.2 and Section 3.6.3 for further reading about the damping system employed in GEO 600.

## 2.2.1 Multiple pendulum suspensions

A cascade of $n$ similar pendulum stages allows, in principle, for an overall isolation, scaling with $1/f^{2n}$ above resonance. Thus, a strong decoupling of the suspended optics from the ground motion can be obtained. However, due to different noise sources, no multiple cascaded pendulum of comparable dimensions to the test-mass suspensions of the gravitational-wave detectors, has so far been proved to operate at the seismic limit at frequencies above some tens of Hz. Possible disturbances are due to the readout of the pendulum motion at these low frequencies, and to the damping of the pendulum. The strongest difficulties arise, however, from cross-coupling of the different degrees of freedom.
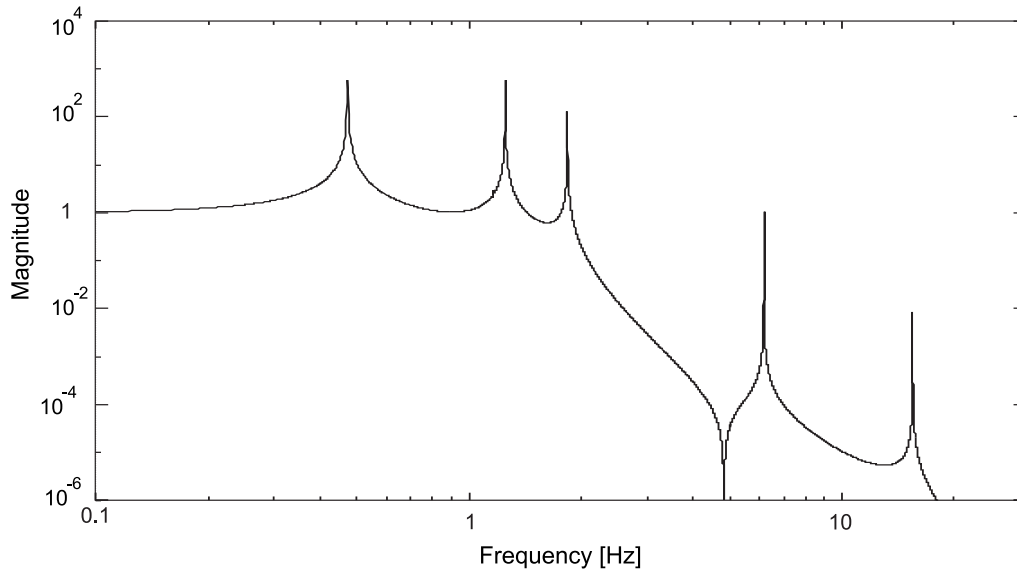
**Figure 2.3:** Longitudinal transfer function of a triple pendulum, including only the cross coupling between the longitudinal and pitch motion of the three suspended masses.

The transfer function of a real, multiple cascaded pendulum is far more complex than the curve for a simple pendulum displayed in Figure 2.2. The different stages form a system of coupled oscillators, which shows a variety of differential and common mode resonances. The individual pendulum stages of the GEO 600 suspensions are of slightly different length and shape and moreover, the masses are not suspended by a single wire, but by either two or four wires (please see Section 3.6 for a detailed description of the triple cascaded pendulums, employed in GEO 600 to suspend the test masses). Hence, not only the longitudinal motion of the pendulum, as was assumed so far, but furthermore "pitch" around a horizontal axis, perpendicular to the optical axis, "yaw" around the vertical axis, "roll" around the optical axis, sideways motion, and vertical motion have to be considered. Eventually the resonances of the suspension wires themselves, the so called "violin modes" have to be taken into account. In order to derive the transfer function for such a system, individual coupling coefficients have to be assigned to the different degrees of freedom. These coefficients translate any motion in a given degree of freedom into the resulting longitudinal displacement of the suspended mass. Figure 2.3 shows the longitudinal transfer function of a triple pendulum, referring to the longitudinal and pitch degrees of freedom. Please note that only these degrees of freedom are taken into account, no coupling from the other degrees of freedom is assumed.

## 2.3 Thermal noise

Thermal fluctuations of the test masses and of the suspension systems are expected to dominate the noise spectrum of the interferometric gravitational-wave detectors in their most sensitive frequency band. The off-resonant thermal noise is, however, so small that until recently no experiment was capable of measuring it directly. The following predictions of the level of the thermal noise due to the test masses are therefore derived from theoretical considerations, based on quality factor measurements of the relevant materials and systems.

### 2.3.1 Fluctuation-dissipation Theorem

The basis for the calculation of thermally-induced noise is the fluctuation-dissipation theorem [Callen '51, Callen '52]. The fluctuation-dissipation theorem relates the thermal fluctuations of a given system to the dissipation of energy. More precisely, it states that thermal fluctuations can only arise in the presence of a dissipation channel.

Dissipation may arise from different mechanisms as, e.g., viscous damping, internal friction, thermoelastic and nonlinear thermoelastic damping. Viscous damping arises from collisions with gas molecules. Since the suspension systems of the interferometric gravitational-wave detectors are enclosed in ultra-high vacuum systems, viscous damping can safely be neglected. Thus, the dominating thermal noise is due to damping related to the material itself. The following sections provide an introduction to the relevant processes that lead to dissipation and thus to thermal noise.

### 2.3.2 Bulk loss

The intrinsic loss of the material itself is referred to as the bulk loss. The bulk loss is generated by internal friction in the material and can be described by the imaginary part of the material's Young's modulus. Internal friction arises from anelasticity effects in the material. These effects are increased in the presence of, e.g., impurities, lattice imperfections, or internal stress. Materials with low bulk loss are therefore very pure materials with a low intrinsic anelasticity. In order to utilize a material as a suspension filament, a high breaking stress is required to benefit from the dilution factor (Section 2.4.3). Thus, materials with a high yield stress combined with a high breaking stress are asked for. Among these materials are fused silica and sapphire. Silicon is a further candidate material for the test masses, in particular if cooling of the test masses is intended (see Section 4.7.3).

The bulk loss of fused silica is about two orders of magnitude smaller than that of the steel typically used for steel-wire suspensions (like C 85 or C 70 steel).

### 2.3.3 Thermoelastic loss

At one extreme of an oscillation, a suspension filament (or a mirror) is compressed at one side while being extended on the other side, and vice versa at the other extreme of the

oscillation. Due to the nonzero coefficient of thermal expansion (CTE)

$$\alpha = \frac{dl/dT}{l} \neq 0 \tag{2.6}$$

any compression/expansion of the material raises/lowers the temperature of the respective section. The resulting heat flow across this gradient, due to the nonzero coefficient of thermal diffusion (CTD) $D \neq 0$, irreversibly deposits the thermal energy in the material. By this mechanism, referred to as thermoelastic loss, energy is removed from the oscillation with each cycle. In reverse, any thermal fluctuation of the material is via the expansion or contraction of the respective area, transferred into a displacement noise. The thermoelastic loss is described by [Gretarsson '00, Willems '02]

$$\phi_{\text{thermoel}} = \frac{E\,\alpha^2\,T}{C_v}\,\frac{\omega\,\tau_R}{1 + (\omega\,\tau_R)^2} \tag{2.7}$$

where $E$ is the Young's modulus of the material, $C_v$ denotes the materials heat capacity per unit volume, and

$$\tau_R = \frac{4\,R^2}{13.55\,D} \tag{2.8}$$

is a characteristic time constant for the given geometry and material. $R$ is the radius of the fiber and $D$ is the CTD of the fiber material. The loss function has its maximum when the oscillation frequency equals the inverse of the time constant (characteristic frequency)

$$\phi_{\text{thermoel}} = \frac{E\,\alpha^2\,T}{C_v}\,\frac{1}{2} \qquad \text{for} \quad \tau_R^{-1} = \omega \tag{2.9}$$

This maximum is referred to as the Debey peak.

The CTE of the relevant types of steel is of the order of $\alpha_{\text{steel}} \simeq 5 \cdot 10^{-5}$ while it is only about $\alpha_{\text{silica}} \simeq 5 \cdot 10^{-7}$ for fused silica.

### 2.3.4 Nonlinear thermoelastic loss

In order to benefit from the dilution factor, discussed in Section 2.4.3, the radius of the suspension fibers is reduced such that they are loaded to a significant fraction of the breaking stress. In the elastic limit the stress $\epsilon$ in the material is related to the strain $u$ by the Young's modulus, $E$ as follows

$$\epsilon = E\,u \tag{2.10}$$

Thus, a nonzero temperature dependence of the Young's modulus of the fiber material

$$\beta = \frac{(dE/dT)}{E} \neq 0 \tag{2.11}$$

leads to a change of the strain if the temperature changes. The result is that the wire material expands or contracts due to thermal fluctuations. These length changes must not be confused with the simple thermal expansion of the wire, responsible for the linear thermoelastic noise. The changes rather have to be added to the contribution of the linear thermoelastic loss.

In reverse, bending of a stressed wire causes temperature changes in the according sections of the wire due to the temperature dependence of the Young's modulus. The nonlinear thermoelastic loss, depending nonlinearly on the strain, is described by expanding Equation (2.7) to [Willems '02, Cagnoli '02]

$$\phi_{\mathrm{nonlin}} = \frac{E \, (\alpha - u_0 \beta)^2 \, T}{\rho \, C_v} \, \frac{\omega \, \tau_R}{1 + (\omega \, \tau_R)^2} \tag{2.12}$$

From Equation (2.12) it is evident that the effects from thermoelastic and nonlinear thermoelastic noise cancel out if the static strain $u_0$ equals $\alpha/\beta$

$$u_0 = \frac{P}{A \, E} = \frac{\alpha}{\beta} \tag{2.13}$$

This strain may be well below the breaking strength of a suspension fiber. In fact, the fibers used to suspend the GEO 600 test masses are loaded by a factor of 2.2 above this level due to the requirements described in Section 5.2 .

## 2.4 Suspension thermal noise

According to the great relevance of the suspension thermal noise for the performance of the interferometric gravitational-wave detectors, there exists a wide variety of literature covering the different aspects of this topic. Among the most fundamental are, e.g., [Braginsky '93, Gillespie '93, Gillespie '94, Braginsky '94, Gillespie '95, Braginsky '96, Cagnoli '96, Cagnoli '97, Bondu '98, Levin '98, Gretarsson '99, Cagnoli '99, Gretarsson '00]. The relevant results, referring to the pendulum mode and to the violin modes of the suspension fibers, are introduced in the following two sections.

### 2.4.1 Violin modes

The eigenmodes of the suspension filaments themselves, the violin modes, are of major relevance for this thesis. A detailed description of the direct influence of the violin modes on the detector performance is provided in Chapter 5 . The equations required for the calculation of the frequencies and the losses are derived in that chapter along with the discussion of the relevant parameters for GEO 600. In order to avoid redundancies, only the results required for a general understanding of the violin-mode related noise are provided here.

Figure 2.4 shows the fundamental violin mode of a single pendulum, compared to the
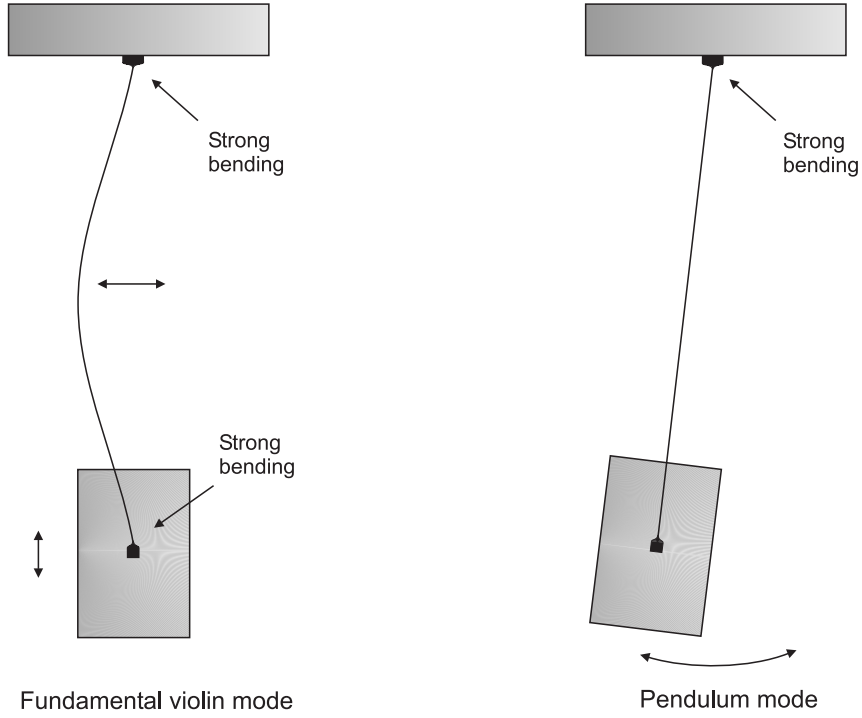
**Figure 2.4:** The fundamental violin mode and the pendulum mode of a single pendulum. For clarity only one suspension fiber is depicted. While for the case of the violin mode a strong bending of the fiber occurs at both the upper and the lower attachment points, the fiber is strongly bent at only the upper attachment point for the pendulum mode.

pendulum mode. The frequency of the $n$th violin-mode is derived in Section 5.1.1 to be

$$\omega_n = \frac{n\pi}{L} \sqrt{\frac{P}{\rho_L}} \left[ 1 + \frac{2}{L} \sqrt{\frac{E\,I}{P}} + \left( 4 + \frac{(n\pi)^2}{2} \right) \frac{2}{L^2} \frac{E\,I}{P} \right] \tag{2.14}$$

where $\rho_L = \rho\,\pi R^2$ is the linear mass density of the fiber, $P = mg$ is the tension, and

$$I = \frac{\pi}{4}\,R^4 \tag{2.15}$$

is the fiber's bending moment of inertia, also referred to as secondary moment of area. The first term on the right hand side of Equation (2.14)

$$\omega_n \simeq \frac{n\pi}{L} \sqrt{\frac{P}{\rho_L}} \tag{2.16}$$

reflects the violin mode frequencies of an ideal string. However, the stiffness $EI$ of the fiber generates a recoil that leads to the additional terms. These two terms are also closely related to the so called dilution factor of the violin-mode oscillation (Section 5.1.2).
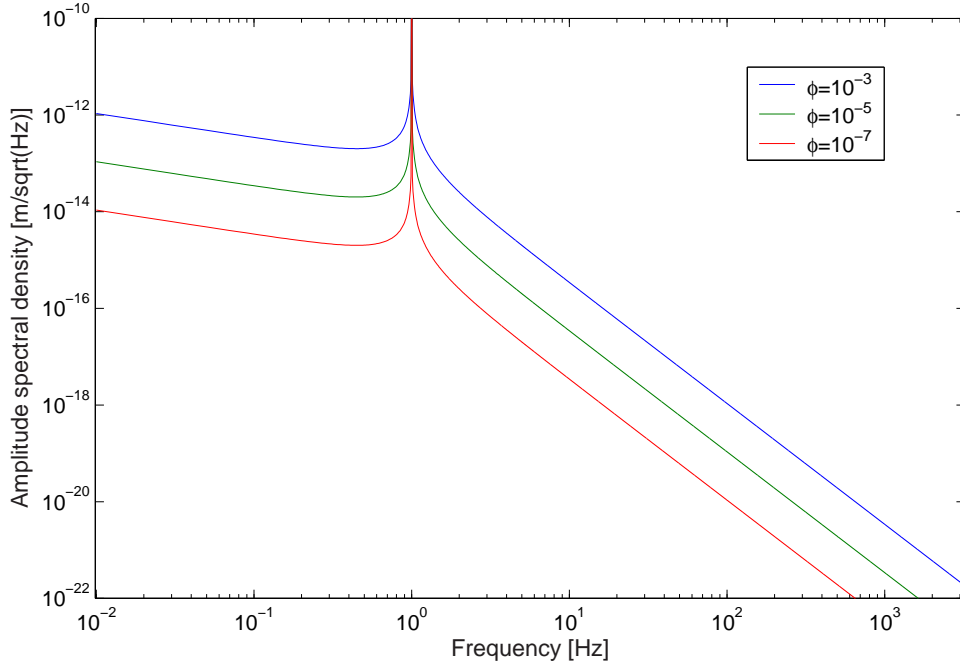
**Figure 2.5:** Amplitude spectral density of a thermally-driven pendulum for different damping strengths $\phi = 10^3 - 10^7$.

The loss $\phi_{\text{fiber}}$ of the fiber itself is not only composed of the aforementioned constituents, but furthermore by loss related to the surface quality (Section 2.5.1) and by recoil loss of the support structure (Section 2.5.2). The loss for the $n$th mode is given by

$$\phi_{\text{fiber}\,n} = D_n^{-1} \cdot \left[ \left( 1 + \frac{8\,d_{\text{s}}}{R} \right) \phi_{\text{bulk}} + \phi_{\text{nonlin}} \right] + \phi_{\text{recoil}} \tag{2.17}$$

where $d_{\text{s}}$ denotes the dissipation depth, the relevant measure of the surface quality and $D_n$ is the dilution factor. $\phi_{\text{recoil}}$ describes the loss due to the support structure, described in Section 2.5.2 .

The contribution of the $n$th violin mode to the power spectral density of the displacement noise of the test mass is given by

$$\hat{x}_n^2 = \frac{8\,k_{\text{B}}T\,\omega_0^2\,\phi_{\text{fiber}\,n}}{m\,\omega\,[(\omega_n^2 - \omega^2)^2 + \omega_n^4\,\phi_n^2]} \tag{2.18}$$

where $k_{\text{B}}$ is the Boltzmann constant. Figure 2.6 shows the amplitude-spectral density of a thermally driven pendulum including its violin modes.

## 2.4.2 Pendulum mode

The loss of the pendulum mode is caused by the same mechanisms that cause the violin mode loss. However, there is one significant difference. Referring to Figure 2.4 the
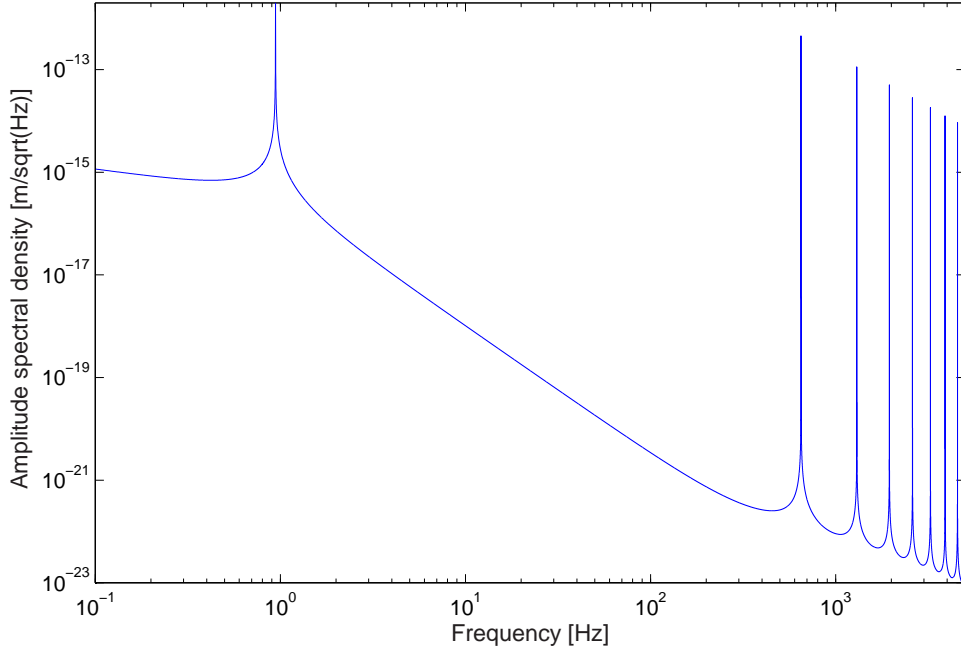
**Figure 2.6:** Amplitude spectral density of a thermally-driven pendulum including its violin modes. The parameters assumed for the pendulum are close to the parameters for the lowest stage of the GEO 600 triple pendulums.

strongest bending of the fiber, due to the violin modes, occurs at the two attachment points. The length of the bent section is given by the ratio of the fiber stiffness to the tension

$$\lambda \simeq \sqrt{\frac{E\,I}{P}} \tag{2.19}$$

Almost all the loss (except for the recoil loss) is generated at these sections. The pendulum-mode oscillation in contrast, causes the fiber only to bend at the upper attachment point. The result is that the loss of the pendulum mode can accurately be assumed to be half of the violin-mode loss [Logan '92], provided that the employed isolation allows the recoil loss to be neglected.

$$\phi_{\text{violin}} \simeq 2 \cdot \phi_{\text{pendulum}} \tag{2.20}$$

This relation can be used to experimentally derive the pendulum loss from violin-mode measurements. The violin-mode loss is much more easily accessible, since the loss is usually derived from the ring-down time of the oscillation amplitude. The 1/e amplitude decay time $\tau$ scales as

$$\tau = \frac{1}{\pi\,f\,\phi} \tag{2.21}$$

27

Since the frequency of the pendulum mode is usually of the order of one Hz while the loss for this mode can be as small as $\sim 10^{-9}$, the ring-down time of the pendulum mode can be a few tens of years. The violin-mode frequencies are almost three orders of magnitude (or even more for the higher-order modes) higher than the pendulum-mode frequency, leading to ring-down times of the order of some hours to a few days.

The thermal noise power spectral density for the pendulum mode is given by

$$\hat{x}^2_{\text{pendulum}} = \frac{4\,k_{\text{B}}T\omega_0^2\,\phi}{m\,\omega\,\left[(\omega_0^2 - \omega^2\,)^2\,+\,\omega_0^4\,\phi^2\,\right]} \tag{2.22}$$

Figure 2.5 shows the amplitude spectral density of the thermally-induced displacement for a single pendulum with the above used length of $0.28\,\text{m}$ for different $\phi$ s. The suspended mass is assumed to weigh $5.6\,\text{kg}$, as the GEO 600 test masses.

### 2.4.3 Dilution

Referring to the thermal noise of the pendulum mode and the violin modes, there is help in the fact that the oscillation energy is fractionally stored in the lossless gravitational field. Only the remaining fraction is stored in elastic energy and hence, is subject to the above discussed dissipation mechanisms. As a consequence, the loss of the fiber itself is diluted to a certain extent. This dilution of the loss is accounted for in Equation (2.17) by the introduction of the factor $D_n$.

The actual amount of dilution increases with the fiber stress. A reduction of the fiber radius leads thus to an increase of dilution for a given load. The dilution factor $D_n$ is given in Section 2.4.3 by the expression

$$D_n^{-1} = \frac{2/\,L}{\left(\frac{\sqrt{P^2+4E\,I\rho_L\,\omega^2}+P}{2E\,I}\right)^{1/2}} \left[1 + \left(4 + \frac{(n\pi)^2}{2}\right)\frac{1/\,L}{\left(\frac{\sqrt{P^2+4E\,I\rho_L\,\omega^2}+P}{2E\,I}\right)^{1/2}}\right] \tag{2.23}$$

The achievable quality factor $Q_{\text{violin}} = \phi_{\text{violin}}^{-1}$ for loaded steel wires is of the order of $Q_{\text{violin}} = 5 \cdot 10^5 - 10^6$ [Goßler '02, Goßler '03], whereas for silica fibers $Q$'s in excess of $5 \cdot 10^8$ can be achieved [Willems '02]. Even the artificially damped silica fibers of the far mirror suspensions of GEO 600 were measured to show $Q$'s in excess of $10^8$ [Goßler '04]. The measurements of the violin-mode $Q$'s of the GEO 600 suspensions are provided in Chapter 5 .

## 2.5 Other thermal noise sources

Besides the fundamental sources, attention has to be paid to other sources of thermal noise. The presence of an optical coating, absorption of photons, or imperfections of the relevant surfaces are among the most important of the non-fundamental thermal noise

sources. These aspects are discussed before the thermal noise estimate for a GEO 600 test mass is provided in the last section of this chapter.

### 2.5.1 Surface loss

The bulk loss of the test masses and of the suspension fibers is degraded at the surface due to the presence of micro cracks. Energy is dissipated by friction inside these cracks when the fiber or test mass is deformed due to an oscillation. A measure for the surface quality is the dissipation depth, which is related to the depth of the micro cracks. The typical dissipation depth for silica fibers is of the order of $100\,\mu$m [Gretarsson '00]. Since the surface-to-volume ratio differs substantially for a test mass or a suspension fiber, the surface quality is of different relevance for the two cases. While for the test-mass loss only a small correction may arise from the surface loss, the loss of a suspension fiber may be dominated by the same mechanism. Due to the fiber production, however, the fiber surface is melted and thereby cured. Rather the opposite applies to the treatment of the test masses: There is a strong indication that polishing or even super-polishing of the barrel of the test masses further deteriorates the surface quality, referring to the micro cracks and thus to the loss.

The mathematical formalism appropriate to derive the displacement noise of a test mass due to surface loss follows the same approach as is applied to derive the coating loss (Section 2.5.3).

#### 2.5.1.1 Flame polishing

If the surface of the sample is carefully melted with a flame, the surface quality can be improved to a certain extent. The loss of thin super-polished disks was demonstrated to be lowered by about one order of magnitude by flame polishing of their surface [Ageev '03]. The thermal stress induced by the local heating during the flame polishing may require however, a subsequent annealing of the sample.

#### 2.5.1.2 Mechanical annealing

By heating the material and subsequently allowing for a very slow cool down, a relaxation of inherent mechanical strain can be achieved. While being well known in metallurgy, this technique can also be applied to the test masses and suspension fibers. Already a low temperature annealing at $600°$C can yield up to a factor of ten decrease of the loss. By higher temperature annealing at $950°$C$-1100°$C with a cool down time of about two weeks, a reduction of the loss by up to a factor of 25 can be achieved for silica fibers [Ageev '03]. As the annealing is performed at temperatures well below the melting point of fused silica ($T_{\mathrm{melt}} \simeq 1650°$C), the surface quality of the sample is not enhanced.

### 2.5.2 Recoil loss

The support structure from which to suspend the pendulum forms another dissipation channel. The pendulum or violin-mode oscillation exerts a certain recoil force on the support structure. As a result, the support structure oscillates itself. The thereby generated

loss is referred to as recoil loss. The coupling of the suspension oscillation to the support structure scales with the ratio of the resonance frequencies and the ratio of the masses. The recoil loss for the $n$th violin mode oscillation is given by

$$\phi_{\text{recoil}\,n} = \frac{m_{\text{fiber}}/2}{m_{\text{support}}} \frac{\omega_n \, \omega_{\text{support}}^2}{(\omega_n^2 - \omega_{\text{support}}^2)^2} \cdot \phi_{\text{support}} \tag{2.24}$$

While $\phi_{\text{support}}$ will usually be comparatively low, the mass of the structure can be made very big in comparison to the fiber mass. The same argument applies to the difference of the resonance frequencies, which is usually very high for a violin mode. Hence, the recoil loss for a violin mode is a relatively small contribution.

In order to derive the recoil loss for the pendulum mode, the effective mass of the fiber $m_{\text{fiber}}/2$ ($\simeq 12\,\text{mg}$ for a GEO 600 suspension fiber) has to be replaced by the suspended mass (5.6 kg for a GEO 600 test mass). Moreover, the resonance frequency of the pendulum mode ($\sim 1\,\text{Hz}$) is much lower than the violin mode frequency ($\sim 650\,\text{Hz}$). Thus, the recoil loss for the pendulum mode exceeds the recoil loss for the violin modes by many orders of magnitude. In order to lower this contribution, it is advisable to suspend the pendulum from a massive structure with low intrinsic loss. Cascading of multiple pendulum stages is, however, the most appropriate way to isolate the lowest, and most relevant, stage from recoil loss by the support structure.

### 2.5.3 Coating loss

While in the last two decades the optical quality of the mirror coatings has dramatically increased, the mechanical properties have, until recently, not been accounted for. With the increasing sensitivity of the proposed detectors the demands on the thermal noise performance related to the test masses are increasing as well. Since the coating is in direct interaction with the laser beam (in contrast to to, e.g., the bonds, described in Section 2.5.6) it becomes one of the main limitations. Hence, great effort is being carried out in order to get a better understanding of the loss generated by the coating. The influence due to the number of coating layers, the thickness of the individual layers, as well as the coating materials themselves are under investigation [Harry '02, Penn '03, Crooks '04]. While silica ($SiO_2$) is of sufficient optical and mechanical quality to realize the low refractive-index constituent of the coating, the high refractive-index constituent is the main subject of the ongoing investigations. Besides the photon thermal noise, which is related to the optical quality (see next section), two contributions to the displacement noise have to be taken into account. Firstly the displacement noise due to dissipation by internal friction, and secondly the thermoelastic noise. In order to reduce the thermoelastic noise, it would be desirable to have a common CTE of the mirror material and the coating material. The candidate materials to form the high refractive-index constituent are tantala ($Ta_2O_5$), as used for the GEO 600 mirrors, or alternatively alumina ($Al_2O_3$, which has a lower internal loss). Experiments suggest, however, that the addition of a dopant to the tantala (which has the better thermoelastic noise performance) in the coating may reduce the internal dissipation [Crooks '04].

The derivation of the equivalent displacement noise of the test mass due to the coating follows the so called Levin pressure formalism. In contrast to the previously applied normal-mode decomposition, the Levin pressure formalism is capable of accounting for inhomogeneously distributed loss, as generated by a comparatively thin coating layer on a real-size test mass. The rather complex equations, describing the thermal noise of a test mass due to its coating can be found in [Levin '98, Braginsky '03, Crooks '04]. An estimate for the loss of the GEO 600 test masses is provided in Section 2.6 .

### 2.5.4 Photon thermal noise

Despite the progress that has been made in the optical quality of the mirror coatings available these days, still a nonzero residual absorptions remains. Due to the high level of light power, stored in either the arm cavities (up to 0.8 MW for Advanced LIGO) or the power-recycling cavity (10 kW for GEO 600), even a low absorption can lead to a substantial deposition of energy in the coating. The resulting heating of the material leads not only to a static overall deformation of the coating, but moreover it causes the so called photon thermal noise. Following the description of the thermoelastic noise, it is evident that thermal fluctuations in the material convert into displacement noise via the nonzero CTE. The absorption of a single photon leads to the heating of only a small volume of the coating, which in turn expands. Thus, the coating is subject to a random thickness noise on small length scales. The power spectral density of the equivalent displacement noise is given by [Braginsky '99]

$$\hat{x}^2_{\mathrm{photon\,thermal}} = \alpha^2 \left(1 + \sigma\right)^2 \frac{\hbar\,\omega_{\mathrm{light}}\,P_{\mathrm{abs}}}{(\pi\,\omega\,C_v\,w^2\,)^2} \tag{2.25}$$

where $\omega_{\mathrm{light}}$ is the frequency of the laser light and $w$ is the 1/e amplitude radius of the laser beam at the mirror surface. The scaling with $w^4$ is due to the optical averaging of the beam over the reflecting area.

Additional noise arises from the absorption of photons inside the beamsplitter substrate. Since the laser beam has to pass through the substrate, also effects inside the beamsplitter have to be accounted for. By the absorption of a photon a small volume inside the substrate is heated. On average the absorption of laser light inside the beamsplitter substrate generates a thermal lens, whereas the random fluctuations on small length scales disturb the phase front of the laser beam by changing the path length due to the expansion of the material.

### 2.5.5 Thermorefractive noise

A further effect related to the absorption of photons in the coatings or in the beamsplitter substrate, is the thermorefractive noise. The nonzero temperature dependence of the index of refraction

$$\frac{dn}{dT} \neq 0 \tag{2.26}$$

causes the optical path length to change due to the temperature changes from the absorption of photons.

The comparatively high power-recycling factor used for GEO 600 leads to a relatively high intra-cavity light power. The requirements on the residual absorption inside the beamsplitter substrate are therefore more stringently for GEO 600 than for the other interferometric gravitational-wave detectors. The absorption inside the beamsplitter used for GEO 600 has been measured to be smaller than $0.5\,\mathrm{ppm\,cm^{-1}}$.

The power spectral density of the equivalent displacement noise due to the thermorefractive effects is given by [Braginsky '00]

$$\hat{x}_{\mathrm{thermorefractive}} = \frac{\sqrt{2}\,\beta^2 D\,k_{\mathrm{B}}\,T^2}{\pi\,w^2\sqrt{\omega\,C_v\,D}} \tag{2.27}$$

For the case of absorption in the optical coating, the substrate's $\beta$ has to be replaced by an effective value representing the coating layers of two different materials. The effective $\beta_{\mathrm{eff}}$ is given by

$$\beta_{\mathrm{eff}} = \frac{n_1^2\,\beta_2\,+\,n_2^2\,\beta_1}{4(n_1^2\,-\,n_2^2)} \tag{2.28}$$

where the subscripts refer to the two different materials and $n_i$ gives the refractive index of the respective material.

### 2.5.6 Loss due to the bonds

One of the major advantages of monolithic suspensions over steel wire suspensions, is the possibility to circumvent the clamping of the suspension wires. Clamping of wires is well known to cause dissipation from creep and slippage [Cagnoli '96, Cagnoli '97, Dawid '97, Huang '98]. The fibers of monolithic suspensions are, however, attached to the test mass and the penultimate pendulum mass by welding and hydroxy-catalyzed silicate bonding [Gwo '98, Sneddon '03, Smith '03], thereby preventing these effects.

As is described in Chapter 4, the fibers are welded to stand-off plates that are bonded to the sides of the masses. Due to the high ratio of substrate volume to bond volume, the appropriate way to calculate the thermal noise related to the bonds, is the Levin pressure formalism. For the GEO 600 test masses this loss was estimated based on previous experiments, and consequently accounted for in the estimation of the internal thermal noise, given below.

## 2.6 Internal thermal noise of the test masses

The resulting power spectral density of the displacement noise due to internal thermal noise of a GEO 600 test mass is given by

$$\hat{x}^2_{\mathrm{internal}} = \frac{4\,k_{\mathrm{B}}\,T}{\omega}\,\frac{1-\sigma^2}{\sqrt{\pi}\,E\,w}\cdot\phi_{\mathrm{internal}} \tag{2.29}$$
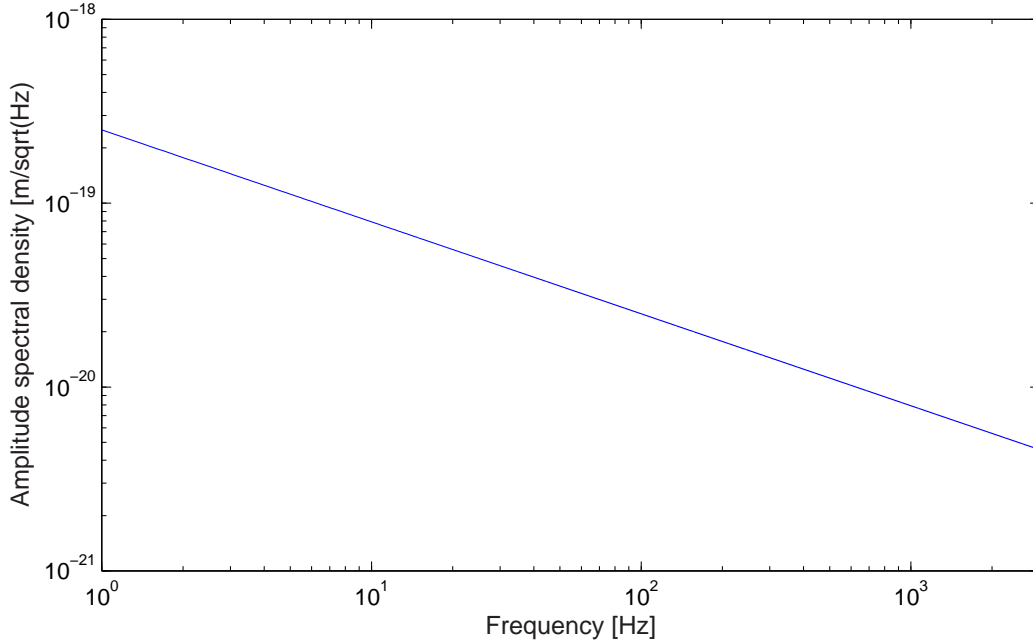
**Figure 2.7:** Amplitude spectral density of the predicted internal thermal noise of a GEO 600 test mass, if used as a far mirror.

where $\sigma$ denotes the Poisson ratio of the mirror material ($\sigma = 0.17$ for fused silica). The $1/e$ amplitude radius, $w$, of the laser beam at the far mirrors is 24.7 mm, while it is 9.7 mm at the inboard mirrors. $\phi_{\text{internal}}$ is composed of the aforementioned loss sources.

$$\phi_{\text{internal}} \simeq \phi_{\text{bulk}} + \phi_{\text{bond}} + \phi_{\text{coating}} + \phi_{\text{surface}} \tag{2.30}$$

The bulk loss of the test masses can be assumed to be $\phi_{\text{bulk}} \simeq 1.8 \cdot 10^{-8}$. The relative energy loss in the bonded area can be estimated to be $\phi_{\text{bond}} = 4.2 \cdot 10^{-9} - 1.3 \cdot 10^{-8}$. The relative coating loss for a GEO 600 test mass has been modeled to be $\phi_{\text{coating}} \simeq 5 \cdot 10^{-8}$. Thus, by neglecting the surface loss, the overall loss can be estimated to be of the order of [Smith '04]

$$\phi_{\text{internal}} \simeq 8 \cdot 10^{-8} \tag{2.31}$$

Figure 2.7 displays the thermal noise prediction for a GEO 600 test mass if used as a far mirror, based on the estimated $\phi_{\text{internal}}$.

In order to derive the corresponding limit to the detector sensitivity, one has to account for each individual mirror separately. Referring to Figure 1.2 the laser beam is reflected twice at the far mirrors before it is recombined at the beamsplitter. Hence, the motion of these mirrors has to be weighted by a factor of two with respect to the motion of the inboard mirrors, which are only hit once by the beam. Longitudinal motion of the beamsplitter shortens or lengthens the north arm. The length change has to be scaled by a factor of $\sqrt{2}$, since the beamsplitter is installed under an angle of nearly 45 degrees.

Noise from the power-recycling mirror and from the signal-recycling mirror causes no differential length change in the interferometer. Accordingly, the requirements on the thermal noise performance of the associated suspensions are not as stringent as for the test masses and the beamsplitter.

Provided the test masses are at the same temperature, the motion of the individual mirrors therefore adds up to a differential change of the interferometer arm length of

$$\delta L = \left( \frac{1}{2}\, \hat{x}^2_{\mathbf{MCn}} \,+\, \hat{x}^2_{\mathbf{MFn}} \,+\, \frac{1}{2}\, \hat{x}^2_{\mathbf{BS}} \right)^{1/2} \tag{2.32}$$

The mirrors **MCn** and **MFn** are arbitrarily chosen to represent the inboard mirrors or the far mirrors, respectively. Inserting the relevant values for the GEO 600 test-mass suspensions eventually yields the corresponding sensitivity limit of the Michelson interferometer [Smith '04]

$$h(f) := \frac{2\,\delta L}{L} \simeq \frac{1.16 \cdot 10^{-21}}{\sqrt{f}} \left[ \frac{1}{\sqrt{\mathrm{Hz}}} \right] \tag{2.33}$$

where $L = 1200\,\mathrm{m}$ is the effective arm length of GEO 600.

# Chapter 3

# The suspension systems

## 3.1 Introduction

The test masses of the interferometric gravitational-wave detectors need powerful isolation from the ground motion to allow for length measurements of the predicted precision. Referring to Figure 2.1 the seismic noise in the vicinity of the GEO 600 detector site in Ruthe is above $3\,\mathrm{Hz}$ roughly of the form $10^{-7}\,\mathrm{m}/\sqrt{\mathrm{Hz}} \cdot [1\,\mathrm{Hz}\,/f\,]^2$. Hence, an isolation of the test masses from the seismic by a factor of about $10^{10}$ is required to obtain a residual seismically induced motion of $2.4 \cdot 10^{-20}\,\mathrm{m}/\sqrt{\mathrm{Hz}}$ at $50\,\mathrm{Hz}$, which is a factor of three below the expected displacement noise due to internal thermal noise of the test masses themselves. While the isolation of the optics from the seismic noise is the major issue of the suspension systems, simultaneously minimizing the thermal noise of the test masses and the suspensions themselves is the other main objective. Since thermal noise will be a limiting factor in the most sensitive frequency band of the interferometric gravitational-wave detectors, the suspension systems are among the most crucial key elements of these instruments. The mechanical isolation performance of multiple pendulum suspensions is discussed in Section 2.2.1. The thermal noise relations for suspensions and suspended test masses can be found in Section 2.4 and Section 2.6.

The current chapter describes the eleven different types of multiple-pendulum suspensions installed in GEO 600. It covers the individual installation and alignment procedures and it provides measurements of the obtained performance. Topic of the 'main suspension' sections are the steel wire suspensions for the test optics, used for the first commissioning phase of the power-recycled Michelson interferometer. The test-optics suspensions were eventually exchanged by the final monolithic suspensions described in the next chapter (Chapter 4). Since this change affected only the last suspension stage, the major part of the mechanical and electronic setup remained as built for the test phase. During that time of commissioning, the complex mechanical and electronical systems were debugged and optimized to prepare a well tested environment for the delicate final suspensions.

All suspension systems of GEO 600 are enclosed in one large ultra-high vacuum (UHV) system to avoid contamination of the mirrors and to reduce the effect of fluctuations of the refractive index of the air. Furthermore, both acoustic coupling and frictional damping of the suspensions and mirrors are thereby reduced. The overall volume of the UHV system is approximately $360\,\mathrm{m}^3$ at a pressure of about $10^{-6}\,\mathrm{Pa}$ ($10^{-8}\,\mathrm{mbar}$), dominated by water vapor [Lück '98]. As a consequence, only ultra-high vacuum compatible materials could be used for the construction of the suspension systems and furthermore, all components

had to be UHV compatibly cleaned before the installation. During the installation work on a particular suspension, the relevant vacuum section is separated by gate valves from the rest of the system. Appendix D gives an overview of the GEO 600 ultra-high vacuum system, Section 3.6.1 provides a short description of the cleaning procedure for the suspension components.

The inner part of the central station and of the end stations is build to form a class 2000 compatible cleanroom [1]. By the utilization of mobile cleanroom tents with a class 100 compatible internal space, a non-contaminating environment is ensured during the installation of the delicate optics. These tents are positioned over the vacuum tank that is actually worked in. Working inside the cleanroom requires full body protection by compatible clothing (abrasion-proof overall, overshoes, and full head cover). A face mask is required for the installation as well as abrasion-resistant gloves. Laser safety goggles complete the clothing by covering the last square centimeters of bare skin. Despite all precaution, the last step before closing a tank after an installation or maintenance phase, is to blow across the optics with a so-called deionization gun. Thereby light adherent dust particles are reliably removed. Section 3.6 gives a description of the mirror cleaning and the subsequent discharging.

Starting this chapter with the first suspended optics in the light path of GEO 600 means also to start with the most simple type of suspension used in GEO 600: The double pendulums used to suspend the mirrors of the modecleaner cavities. As some principal features are common to all suspension types, these shall be explained at this most straightforward approach. The use of local control of the pendulums at the uppermost mass is one aspect common to all suspension types, the application of feedback signals, where needed, from a seismically isolated reaction mass is another one. The variation of these and other common aspects with the respective type of suspension will be discussed in detail in the designated sections.

## 3.2 The stacks

All types of suspensions that are described in this chapter are mounted on top of a pre-isolation system, accomplished by the so called stacks. Three of these stack isolators are set up in each vacuum tank to support the so called top plates from which all pendulums in one tank are suspended (e.g., eight pendulums are suspended in the first modecleaner tank **TCMa**). Two-stage passive stacks are used to support the top plates in the two modecleaner tanks. The first stage consists of a steel base mass, followed by a layer of three rubber [2] cylinders (40 mm diameter, 25 mm height) and another steel mass. A second layer of three rubber cylinders (33 mm diameter, 25 mm height) and a third steel mass form the second stage. The stacks are encapsulated with corrugated stainless-steel bellows in order to obtain ultra-high vacuum compatibility. The bellows are damped from the inside with silicone grease [3] to reduce their mechanical quality factor to $Q \simeq 8$. The resonance frequency of the bellows is 70 Hz. The lower passive stack layer is replaced by

---

[1] Less than 2000 particles of 0.3 μm per cubic foot.
[2] RTV 615 A, loaded with synthetic powdered graphite.
[3] Dow Corning type DC4
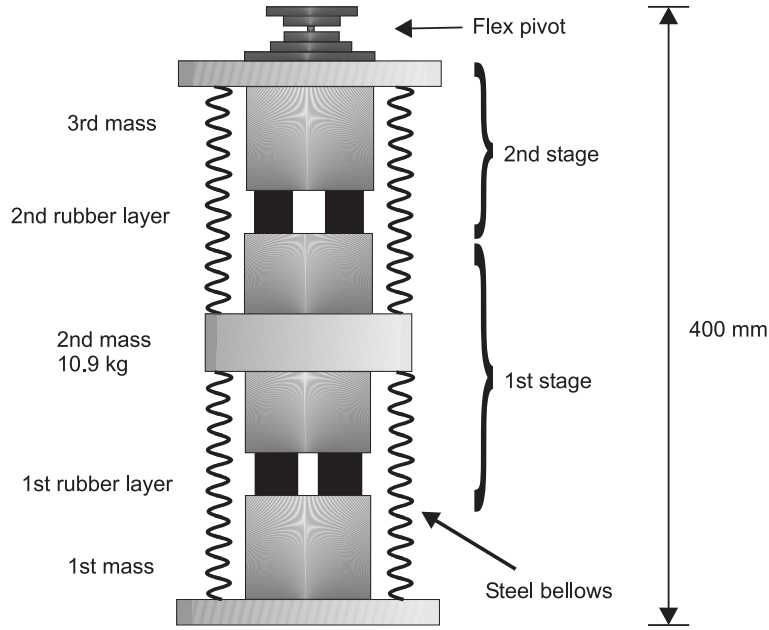
**Figure 3.1:** Drawing of a passive stack as used in the modecleaner tanks.

an active stage for the main interferometer. For a short description of the active stage and its utilization see Section 3.6 and Section 4.4. A drawing of a passive stack is displayed in Figure 3.1.

In order to meet the specification for the vertical isolation, the vertical resonance frequency of the stacks is required to be 15 Hz or below [Plissi '98]. This is the uncoupled load requirement, which means that the load due to the pendulum itself does not contribute to the stacks' resonance frequency (although it causes the rubber to become more compressed). The pendulum is decoupled from the dynamic behavior of the stacks because it is suspended from soft cantilever springs (Section 3.6.4). Thus, in the following the term uncoupled frequency refers to the frequency observed for a spring in a particular stage supporting only the mass of that stage. The vertical mode quality factor of the stacks is $Q \simeq 12$.

In the longitudinal direction the specification is more relaxed because the pendulum already provides a large amount of isolation and besides that the stacks are softer in this direction. The horizontal resonance frequency of the stack is 9 Hz.

The vertical spring constant of the stacks is $\kappa = 1.25 \cdot 10^5 \, \mathrm{N\,m^{-1}}$. Using the formula for the resonance frequency

$$f_0 = \frac{1}{2\pi} \cdot \sqrt{\frac{\kappa}{m}} \tag{3.1}$$

one obtains that each stack needs to be loaded with 14 kg to obtain the frequency asked for. The mass that does contribute belongs to the suspension support structures and the coil holders for the local-control actuators (Section 3.6). Since the inboard mirrors have two coil holders while the far mirrors have only one, the stacks would be differently

loaded from 9.5 kg to 12.5 kg per stack for the respective suspensions. This would lead to resonance frequencies of $f_0$=18.3 to $f_0$=15.9 Hz. In order to compensate for the different weights and for the missing weight, additional load was put on the stacks to obtain the desired 14 kg.

The bellows of the stacks are soft in all degrees of freedom, except for rotation around the cylindrical axis. In order to decouple the suspension from the rotational vibration, rotational flexures were mounted on top of each stack. These so called "flex pivots" are soft in only the rotational degree of freedom and can support large weights. The resulting rotational resonance frequency is 2 Hz.

The stacks are required to be evacuated to sustain a pressure difference below $10^4$ Pa (100 mbar) between the inside and the outside of the steel bellows encapsulation. Since the inner components of the stacks are not UHV compatible, the stacks require to have a vacuum system on their own. In order to avoid any hazardous expansion or compression of the stacks due to a failure of either the stack vacuum system or the UHV system, the stacks have adjustable end stops in both directions. These end stops are set to allow for a $\pm 3$ mm compression/inflation of the stacks. By tightening the end stops in both directions they were also used as a transportation lock for the transport of the stacks from Hannover to the 25 km distant detector site.

## 3.3 The modecleaner suspension

A brief introduction to the modecleaner system along with its optical layout is given in Section 1.5.4. Since the modecleaners are used for the temporal and spatial stabilization of the GEO 600 laser source, the motion of the modecleaner mirrors should not exceed a limit of $\delta x \simeq 6.3 \cdot 10^{-15}$ m/$\sqrt{\text{Hz}}$ at 100 Hz, set by the Doppler-induced frequency shift of the light. Hence, all relevant components of the modecleaner system (six cavity mirrors, four beam steering mirrors, two mounting units and two reaction masses) are suspended as the lower stage of a double-pendulum, to provide sufficient seismic isolation (see Figure 3.2). Optical sensors and magnet-coil actuators at the upper pendulum stage allow position and alignment control of each mirror, and provide local damping of the relevant mechanical eigenmodes of the suspensions.

The upper suspension wires of the pendulums are attached to a top plate common to all pendulums in one vacuum chamber. The top plate is a hollow stainless steel structure damped from the inside with graphite loaded silicone rubber. As described above, the top plate is supported via flex pivots on three passive stack isolators.

The upper stage of a double pendulum is formed by an aluminum block of 0.86 kg (the intermediate mass, $85 \cdot 75 \cdot 50$ mm$^3$), suspended by two 290 mm long steel wires. The wire material is high-tensile stainless steel with a breaking stress of $\sigma_\mathrm{B} \simeq 1.5 \cdot 10^9$ Pa. The properties of suspension wires of different materials like titanium, tungsten, niobium, molybdenum, tantalum, and steel are discussed in, e.g., [Dawid '97, Cagnoli '99]. The upper wires have a diameter of 128 μm, which means they are loaded to 44 % of the breaking load. These wires are clamped to a block at the top plate (the so called slider) and to the intermediate mass, using small stainless steel blocks. Previous investigations by [Dawid '97] on the influence of the clamping material on the mechanical quality factors
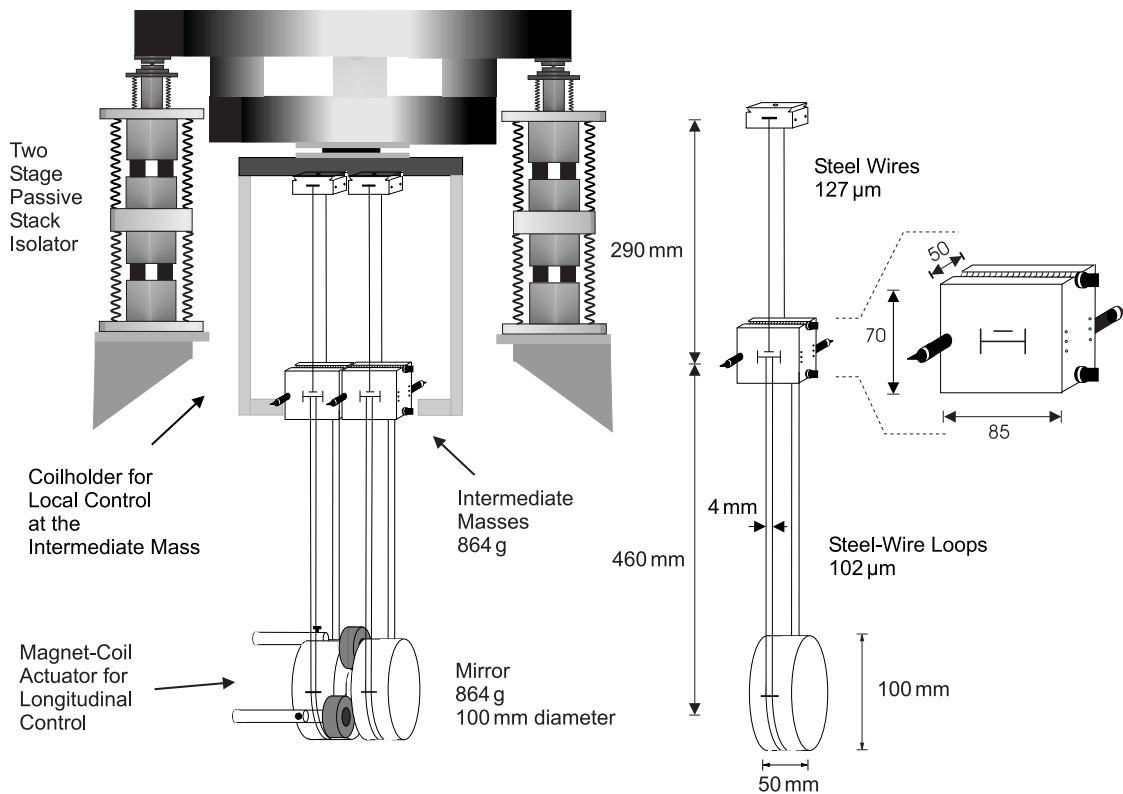
**Figure 3.2:** Schematic drawing of the modecleaner suspension: **Left:** The whole suspension system is pre-isolated by three double-layer passive stack isolators (for clarity only two are shown in this schematic sketch). The double pendulums themselves are suspended by steel wires from a common top plate. The length control signals for the stabilization of the cavities are applied from a second pendulum that carries a reaction mass **Right:** The damping and steering of the pendulums is done via magnet-coil actuators at the intermediate stage in four degrees of freedom. Magnets for the feedback actuators and flags for optical position sensors are attached to the aluminum intermediate masses.

of the suspension modes revealed that stainless steel and titanium yield the best results. Aluminum for example proved to be too soft to allow for a slip-free suspension. The energy dissipated at the clamps by friction, creep, or slip of the wires can easily dominate the dissipation of a high $Q$ suspension stage if the clamps are not well designed or the clamp material is not properly chosen. Please see Section 3.3.5 for $Q$ measurements of a GEO 600 modecleaner pendulum.

The four ends of two further steel wires are clamped to each intermediate mass to suspend the optics. The upper/lower wires break off the intermediate mass at 5 mm above/below the center of mass (COM). The lower wires form two loops and pass over break-off-position defining bars (2 mm above the COM) on each side of the cylindrical mirror. The mirrors have a diameter of 100 mm, are 50 mm thick and weigh 864 g. The diameter of the lower wires is 102 μm, which means the wires are loaded to 17 % of the breaking load. The lower stage has a length of 460 mm. Table 3.1 gives the first few

| Mode | Resonance frequency [Hz] |
|------|--------------------------|
| Longitudinal, pitch | 0.6, 1.3, 1.6, 2.3 |
| Sideways, roll | 0.6, 1.5, 15, 34.5 |
| Yaw | 0.7, 2.0 |
| Vertical | 11.8, 30.1 |

**Table 3.1:** The calculated values of the relevant resonance frequencies of the double pendulums. The lower frequencies belong to the common-mode motion of the two pendulum stages, while the higher frequencies are caused by the differential-mode motion of the two stages.

resonance frequencies of the double pendulums, as calculated by the MATLAB$^{\circledR}$[4] code written by C. I. Torrie [Torrie '00].

In order to suspend a pendulum the slider, the intermediate mass and a mirror-sized aluminum block are fixed in a 'jig' that gives the right separations of the masses. Then the wires are positioned at the masses with a precision of about 0.1 mm, using a positioning jig. This second jig ensures as well that the wires are running rectangular with respect to their clamps, to provide a well defined break-off position without bending of the wires. One end of each wire is then clamped to the intermediate mass. All this is done horizontally on a bench. The other end runs over a pulley and is loaded via a weight to provide similar tension of the two wires within each pendulum stage. While the wires are loaded, the clamps are tightened. The pendulum can then be installed inside the tank without the lowest mass, which is inserted later. The attachment of the suspension to the top plate is done via a revolvable table, allowing the rotational pre-alignment of the mirrors, while the tilt pre-alignment is done via a small balancing weight on top of the intermediate mass. The final alignment is done via bias currents through the local-control actuator coils.

### 3.3.1 Mounting-unit suspensions

In order to provide seismical isolation for the phase modulators required for the second modecleaner, the power-recycling cavity, the Michelson interferometer, and the signal-recycling cavity, they are as well suspended as double pendulums. The modulators are mounted on platforms, the so called "mounting units", that form the lower pendulum stage. The modulation frequency for the second modecleaner (13 MHz) and for the power-recycling cavity (37.19 MHz) are applied at the second mounting unit (**MU2** in Figure 1.3), while the modulation frequency for the Michelson interferometer (14.9 MHz) and the Schnupp modulation (9 MHz) are supplied at the third mounting unit (**MU3**). In addition to the modulator two Faraday isolators and a lens are located on the third mounting unit. Figure 3.3 displays a schematic drawing of the third mounting unit.

---

[4]http://www.mathworks.com/products/matlab/
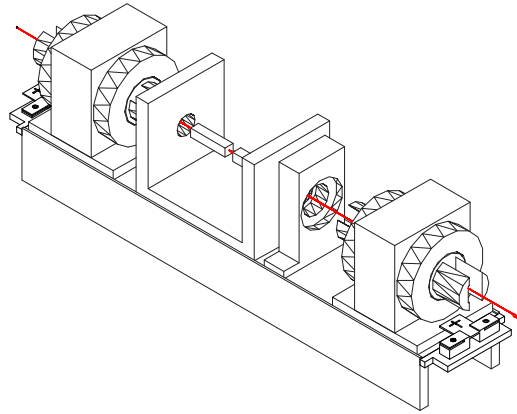
**Figure 3.3:** Schematic drawing of the third mounting unit **MU3**. The suspended platform supports two Faraday isolators with the Li:Nb phase modulators in between.

### 3.3.2 Local control

The position and orientation of the intermediate mass, and as a result of the suspended optics, is controlled in four degrees of freedom, using four magnet-coil actuators (see Figure 3.2). The Nd:Fe:B magnets (3 mm thick and 10 mm in diameter) are bonded with Ceramabond 571 VFG [5] onto spacers attached to the intermediate mass. Table 3.2 provides the properties of the UHV compatible ceramic bonding agent. Despite the fact that a curing bake at 100 °C for two hours is recommended, the bonds were not baked at all. Instead they were left to cure under normal conditions for at least 24 h. This is due to the fact that the bonds were used to attach the magnets. Baking test performed beforehand proved that a considerable degradation of the magnetic strength occurs already at baking temperatures clearly below 75 °C.

The coefficient of thermal expansion (CTE) of Ceramabond 571 VFG is similar to the CTE of the type of stainless steel used for the 600 m long vacuum tubes of GEO 600 (CTE of V4A stainless steel: $1.4 \cdot 10^{-5}$ K$^{-1}$). Hence, it could also be used to seal small leaks in the two 600 m vacuum tubes, which are at outside temperature.

| No. of components | Main constituent | CTE | Viscosity | Air set | Bake |
|---|---|---|---|---|---|
| 2 | Magnesium oxyde | $1.26 \cdot 10^{-5}$ K$^{-1}$ | Semifluid | 4 h | 2 h at 100 °C |

**Table 3.2:** Properties of the two-component ceramic bonding agent Ceramabond 571 VFG used to attach the magnets for local control to aluminum spacers. The same bond was used to attach the magnets for the longitudinal control to the relevant mirrors.

---

[5]http://www.aremco.com/a2.html

The actuator coils are mounted on a rigid frame extending down from the top-plate. In order to provide ultra-high vacuum compatibility of the actuators, the coils had to be encapsulated in glass housings. Simple optical sensors, so-called shadow sensors, are co-located with the actuators within the glass encapsulations. These shadow sensors sense the position of a metal flag bonded onto each magnet, by measuring the degree to which it blocks a beam emitted by an infrared emitter from reaching a silicon photo detector. The sensors allow a position/orientation control at low frequencies, and simultaneously provide a signal that is used for active damping of the relevant mechanical eigenmodes of the suspension. The four sensors and actuators are positioned to sense and control the position in the two horizontal degrees of freedom (referred to as longitudinal and sideways) and in the rotational degree around the vertical and the horizontal axis parallel to the reflective surface of a mirror (referred to as pitch and yaw). There is neither control in the vertical direction nor of roll motion around the normal to the reflective surface of the mirrors.

The control algorithm used to damp the normal modes of the suspension is derived from velocity feedback, optimized for the double-pendulum configuration. The control law used gives better damping of the lowest frequency modes, and includes low pass filtering to exclude sensor noise above its active band (of approx. 3 Hz). The objective is to provide a short settling time without adding significant noise in the gravitational wave signal band. This so-called local-control circuit has more than one unity gain frequency, the lowest at 0.3 Hz and the highest at 3 Hz. The fact that there is no gain at very low frequencies allows the application of offset currents to the coils for alignment purposes [Grote]. The analog local control servo is digitally supervised and can be controlled/adjusted from a PC using LabVIEW® [Casey '00].
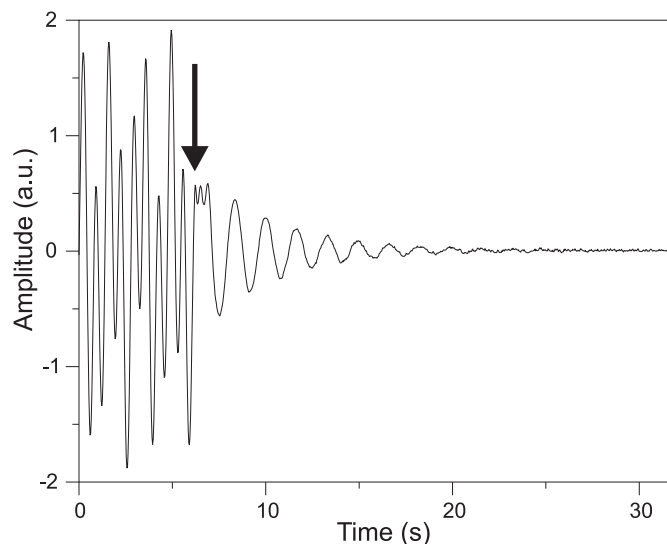


**Figure 3.4:** Performance of the local control by damping the free longitudinal oscillation of a double pendulum. The arrow marks the moment when the damping was activated. A quality factor of 3.5 for the damped oscillation can be calculated from the decay curve.

In order to measure the performance of the local control the damping of a modecleaner-mirror pendulum was deactivated. Then a step function in the longitudinal direction was applied to the undamped pendulum. After one step the excitation was turned off and after some seconds of free pendulum oscillation the local control servo was reactivated. The measured performance of the active damping is displayed in Figure 3.4. While the quality factor of the undamped motion is of the order $Q \geq 5 \cdot 10^5$, derived from the measurements of the violin modes presented in Section 3.3.5, a quality factor of $Q \simeq 3.5$ is obtained for the damped oscillation.

### 3.3.3 Length control

The control scheme of the modecleaners necessitates the possibility to apply feedback at one mirror of each cavity. In order to avoid the coupling of seismic noise to the cavity through the length control actuators, two reaction pendulums were suspended. Each of the mirror pendulums (**MMC1b** and **MMC2b**) is faced by one of these reaction pendulums. Such a reaction pendulum is made in the same way as the mirror pendulums but instead of a mirror it contains a reaction mass (**RM**), that supports three actuator coils. The intermediate masses of the reaction pendulum and the mirror pendulum are separated by about 5 mm. With the reaction mass, as well as the mirror, being 35 mm thinner than the intermediate mass, this results in a separation of the lower masses of about 40 mm. The coils protrude from the reaction mass in order to coincide with three magnets (3 mm thick and 10 mm in diameter, made of Nd:Fe:B), bonded onto the mirror's surface. Ceramabond 571 VFG was used for these bonds. Since the bonds seem
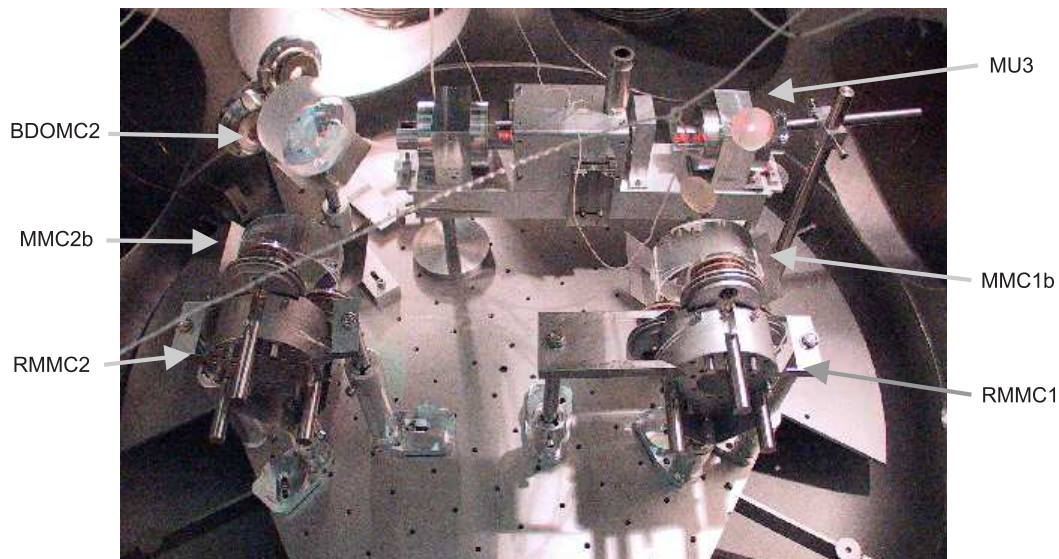


**Figure 3.5:** Suspended optics in the second modecleaner tank **TCMb**: The two end mirrors (**MMC1b** and **MMC2b**) of the two modecleaner cavities are suspended together with their reaction masses (**RMMC1** and **RMMC2**). In the background the beam steering mirror **BDOMC2** and the third mounting unit (**MU3**) are to be seen.

to get weakened under vacuum conditions, Vacseal®, a silicon based two-component UHV compatible leak sealant, was later on used for bonding magnets onto the signal-recycling mirror and onto the intermediate-reaction masses of the main suspensions. The reaction masses have an aperture of 43 mm in diameter to provide enough clearance for the through-going beam.

### 3.3.4 Residual length noise

The residual motion of the suspended mirrors was measured by locking both the laser frequency and the second modecleaner's length to the length of the first modecleaner. In this configuration the feedback spectrum of the second modecleaner reveals the differential motion of the two cavities (see Figure 3.6).

In the low frequency regime up to 1 Hz the spectrum is dominated by seismically induced motion. The bump at 2.3 Hz is caused by the pendulums' well damped longitudinal and tilt modes. The multiple peak structure at 10 Hz to 12 Hz corresponds to the mechanical resonances of the two tubes that are connecting the modecleaner vacuum chambers (11.4 Hz, $Q = 41$ and 13.2 Hz, $Q = 50$) and of the tube that connects the modecleaner vacuum chambers to the power-recycling tank (10 Hz, $Q = 110$). The tubes
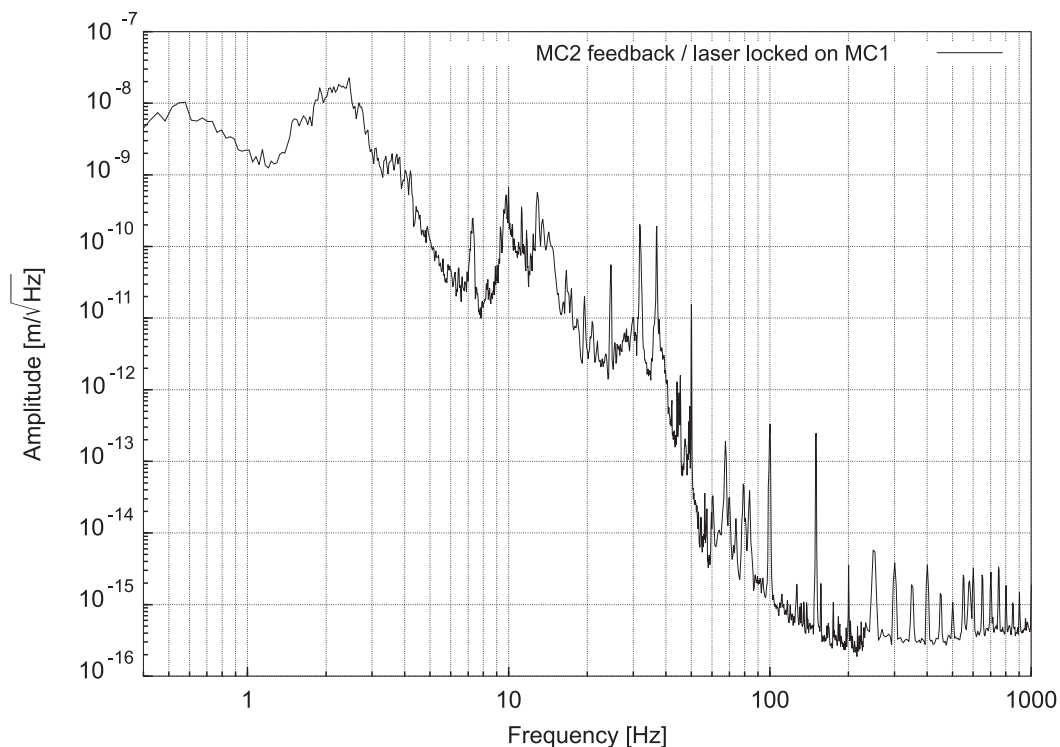


**Figure 3.6:** Differential length noise of the two modecleaners. To record this spectrum the laser was locked to the free hanging first modecleaner, thus keeping it transparent. Then the second modecleaner was locked to the first one as well. Displayed is a calibrated feedback spectrum of the second modecleaner.

are now damped at their centers with styrofoam blocks. The vertical resonance of the double pendulums (common mode at 11.8 Hz) as well as the roll mode at 15 Hz remain undamped. The very narrow peak at 23.5 Hz belongs to a vacuum pump which is now suspended by a coil spring. The two sharp peaks at 31 Hz and 36 Hz are caused by the undamped differential vertical mode of the two pendulum stages and another roll mode, also undamped.

The residual differential motion of the two cavities around 100 Hz is

$$\delta L = 10^{-15}\,\mathrm{m}/\sqrt{\mathrm{Hz}} \tag{3.2}$$

By the use of

$$\frac{\delta L}{L} = \frac{\delta \nu}{\nu} \tag{3.3}$$

where $\nu \simeq 2.82 \cdot 10^{14}\,\mathrm{Hz}$ is the laser frequency and $L \simeq 8\,\mathrm{m}$ is the optical path length, the corresponding frequency stability is obtained to be

$$\delta \nu \simeq 30\,\mathrm{mHz}/\sqrt{\mathrm{Hz}} \tag{3.4}$$

at 100 Hz. This reflects the stability of the modecleaner system without any further stabilization. In the operating modus of GEO 600, the length of the second modecleaner is locked to the 1200 m long power-recycling cavity. The resulting frequency stability is then $\delta \nu = 100\,\mu\mathrm{Hz}/\sqrt{\mathrm{Hz}}$ [Freise '02].

### 3.3.5 $Q$ of the pendulums

The reaction mass of the second modecleaner **RMMC2** was used to excite the violin modes of the lower stage of the corresponding mirror double pendulum **MMC2b** to measure the mechanical quality factor of this pendulum stage. Since the first modecleaner is slaved to follow the length of the second modecleaner, the introduced length oscillation

| | |
|---|---|
| [Gillespie '93] | $Q \simeq 3.0 \cdot 10^5$ |
| Caltech 40 m prototype [Gillespie '94] | $Q \simeq 4.3 \cdot 10^5$ |
| [Dawid '97] | $Q \simeq 1.8 \cdot 10^5$ |
| LIGO test-mass suspension | $Q \simeq 2 \cdot 10^5$ |
| TAMA300 test-mass suspension (Tungsten wires) | $Q \simeq 2.5 \cdot 10^5$ |
| GEO 600 modecleaner suspension | $Q \simeq 5 \cdot 10^5 - 10^6$ |

**Table 3.3:** Reported violin-mode $Q$'s of steel-wire suspensions. A description of the test-mass suspensions of LIGO and TAMA300 is provided in Section 3.12.
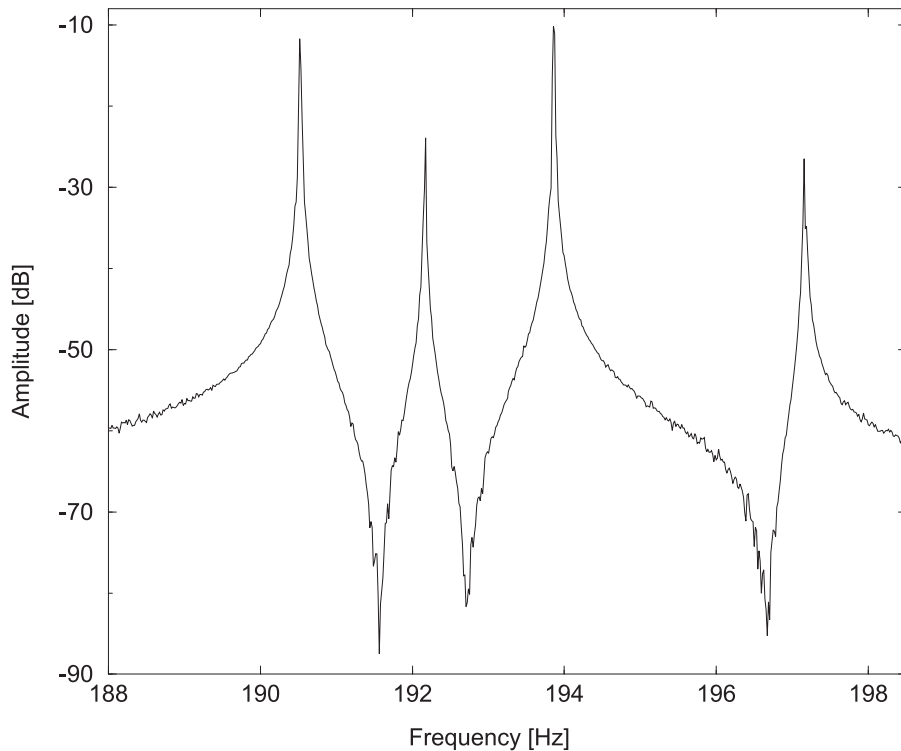
**Figure 3.7:**  A section of the feedback spectrum of the second modecleaner, showing the violin-mode resonances of the lower-stage wires of the **MMC2b** pendulum.

can be read out using the feedback signal of the first modecleaner cavity. The resonance frequencies of the violin modes of the lower wires are calculated to be 195 Hz and are measured to be between 190.6 Hz and 197.1 Hz (see Figure 3.7). The mechanical quality factors of the violin modes of the lower suspension stage of **MMC2b** have been measured to be $Q \simeq 5 \cdot 10^5 - 10^6$ [Goßler '02], which is the maximum value that has been reported for steel wires. Reported values for violin-mode $Q$'s are given in Table 3.3 . Violin-mode measurements of the GEO 600 test-mass suspensions are discussed in Section 5.5 and Section 5.6 .

## 3.4  BDOMC2 and BDIPR

The two required beam-steering mirrors between the second modecleaner and the power-recycling mirror **BDOMC2** (**B**eam **D**irector **O**utput **M**ode**C**leaner **2**) and **BDIPR** (**B**eam **D**irector **I**nput **P**ower **R**ecycling) are suspended as double pendulums as the modecleaner mirrors. The beam-steering mirrors are slightly bigger than the modecleaner mirrors (120 mm diameter, 50 mm thick, 1.244 kg, made from BK7). Steel wires with a diameter of 152 µm were used for the upper suspension stages and steel-wire loops of 128 µm diameter were used for the lower stages. The two beam-steering mirrors have in addition to the local-control coils at the upper mass a fast feedback actuation at the

mirror itself. The feedback actuator is a magnet coil-drive with three magnet-coil pairs. The magnets are attached to the rear surface of the mirror, using Ceramabond 571 VFG. Since the requirements for the seismic isolation of the coil holders are relaxed for feeding back to non-cavity mirrors, the coils are supported by a rigid structure, clamped to the bottom plate of the vacuum tank. The coils are arranged such that the fraction of the beam transmitted through the mirror is not disturbed, since it contains information required for the auto alignment and spot position control. A photograph of **BDIPR** and the coil holding structure is displayed in Figure 3.9.

## 3.5 The power-recycling suspension

A very compact design had to be chosen for the power-recycling suspension, since its tank has a diameter of only 80 cm and also houses the **BDIPR** suspension. In the initial design of GEO 600 the power-recycling mirror was foreseen to be suspended in the beamsplitter tank. As simulations of the rather complex optical configuration of GEO 600, performed since then, favored an almost equal length of the power-recycling cavity and the signal-recycling cavity, the power-recycling mirror had to be installed in the smaller tank **TCIb**. As the space for the coil holder and its attachment to the top plate was strongly limited, the upper pendulum masses had to be down-sized in the lateral dimension, consequently decreasing the coupling of the roll and yaw modes to the suspended optics.

The power-recycling suspension is supported by three active stacks, as described in Section 3.6. The suspension system consists of two double pendulums, each of them incorporating an additional vertical cantilever spring stage. One pendulum contains the mirror, while the other pendulum serves as a reaction chain from which to apply the length control feedback. The power-recycling mirror is made from Suprasil® 2. It has a diameter of 150 mm, is 75 mm thick, and weighs 2.92 kg. The transmissivity of the power-recycling mirror was measured to be 1.45%. The resulting power-recycling factor is about 300. This currently installed mirror is a preliminary solution for the commisioning phase of the dual-recycled Michelson interferometer. In the final configuration a power-recycling mirror with 0.1% transmissivity will be used. The use of the final power-recycling mirror will eventually lead to a power-recycling factor of about 2000.

High tensile C 70 steel (breaking stress ∼ 2.9 GPa) was used for the power-recycling suspension. The upper suspension wires of 300 μm diameter (14 % breaking load) are clamped to the intermediate mass and to a set of cantilever springs that are attached to a revolvable plate. The plate itself is bolted to the top plate. For details regarding the cantilever springs see Section 3.6.4. The intermediate mass is an aluminum block of 150 mm length, 85 mm witdh, and 85 mm height. as the mirror it weighs 2.92 kg. Two steel wire loops (wire separation 53 mm, wire diameter 162 μm, 12 % breaking load) are clamped to the intermediate mass to suspend the mirror.

As in the case of the two modecleaner mirrors **MMC1b** and **MMC2b**, a reaction pendulum is suspended behind the mirror pendulum. The reaction pendulum has the same properties as the mirror pendulum, but contains a reaction mass to support three coils. The power-recycling mirror has three magnets bonded onto the optical surface facing the coils. In order to realize the desired distance of 1.145 m from the beamsplitter,
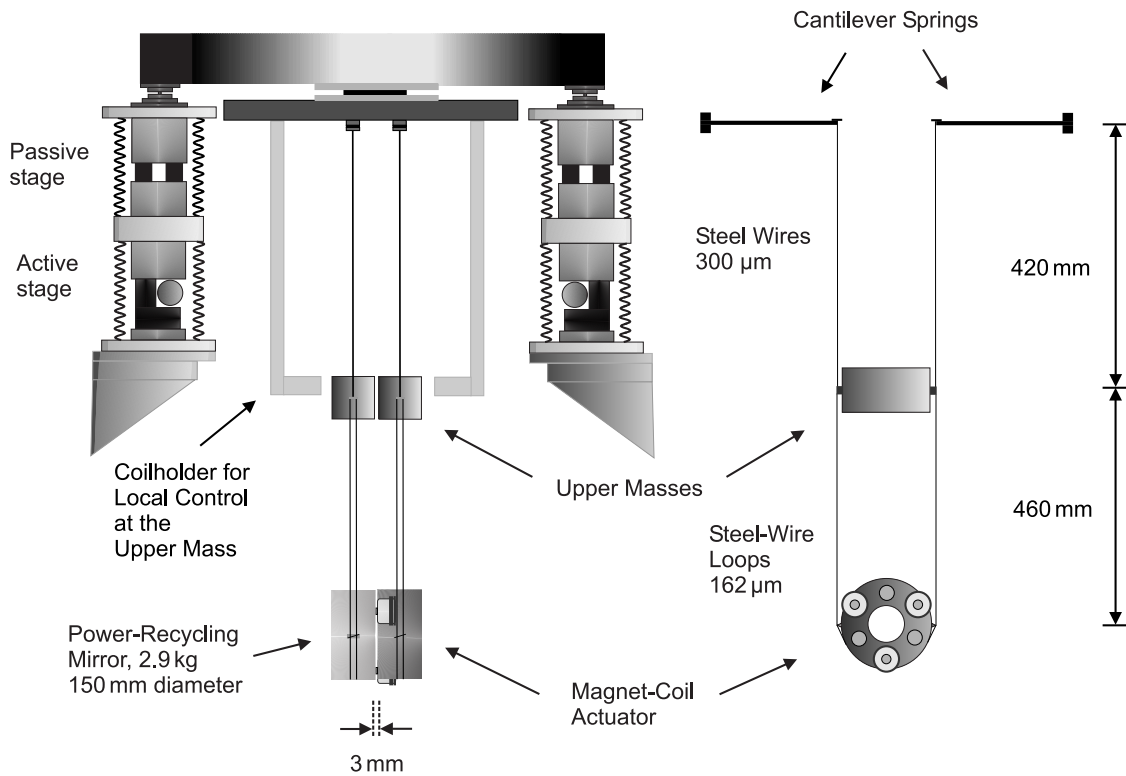
**Figure 3.8:** The power-recycling suspension. **Left:** Three passive double-layer stacks support the top plate. The power-recycling suspension includes a reaction-mass suspension, which is installed 3 mm behind the mirror pendulum.
**Right:** Front view of the reaction pendulum. The upper mass of both pendulums had to be shrunk in the lateral dimensions to fit the space restrictions. Each double pendulum suspension incorporates a single additional vertical cantilever-spring stage. The reaction mass that forms the lower stage of the reaction pendulum supports three coils that match three magnets at the mirror.

the reaction pendulum had to be suspended inside the power-recycling cavity. Since the fundamental mode inside the power-recycling cavity has its waist with radius $w_0 = 9$ mm at the planar power-recycling mirror, a clear aperture of 37.5 mm radius, cut in the center of the reaction mass, is sufficient to ensures a clean transmittance of the laser light without cutting the edges of the beam. Figure 3.8 displays a schematic overview of the power-recycling suspension. A picture of the suspended power-recycling optics is shown in Figure 3.9. Table 3.4 provides the calculated resonance frequencies of the power-recycling suspension.

### 3.5.1 Pre-alignment of the power-recycling mirror

The mechanical alignment (in the following referred to as "pre-alignment") of the power-recycling mirror is done with the help of an autocollimator. The design principle of an autocollimator is shown in Figure 3.10. The autocollimator is a device that compares
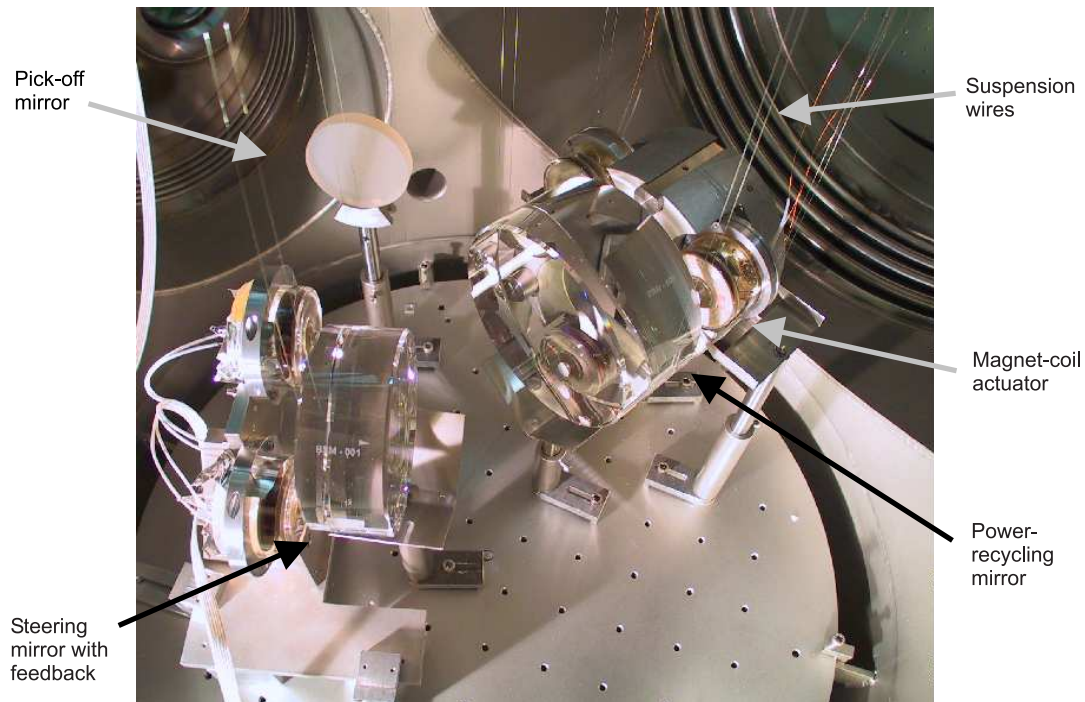
**Figure 3.9:** Suspended power-recycling mirror (MPR) with reaction mass and the beam-steering mirror (BDIPR) with feedback from a rigid coil holder. The V-shaped metal plates below the optics act as simple catchers. The reaction mass to the right is surrounded by additional limiters to prevent a collision with the mirror.

| Mode | Resonance frequency [Hz] |
|---|---|
| Longitudinal, pitch | 0.57, 0.6, 1.5, 4.3 |
| Sideways, roll | 0.6, 1.5, 3.1, 35.7 |
| Yaw | 0.76, 1.76 |
| Vertical | 1.4, 30.8 |

**Table 3.4:** The calculated resonance frequencies of the power-recycling suspension.

the direction of a reference beam reflected at an optical surface with the direction the autocollimator is adjusted to. It consists of a telescope with internal light source, two cross hairs, and a beamsplitter. One cross hair is realized as transmissive lines in an etched glass plate in front of the light source. The beamsplitter is adjusted such that the transmitted light is emitted by the telescope. When the autocollimator is pointed toward a reflecting surface, the light reflected from the optical surface yields a bright reflection of the transmissive cross hair. By looking through the telescope one sees the second, real, cross hair as a black structure in the reflected diffuse light. Thus, the reference cross
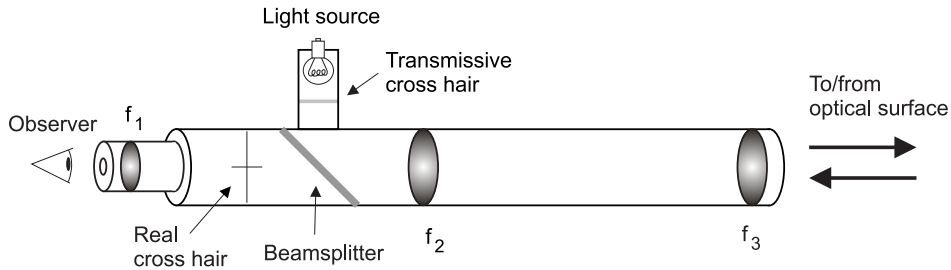
**Figure 3.10:**  Principle of an autocollimator: A system of lenses form a telescope with a reflecting cross hair inside. The cross hair is illuminated from the side such that its reflection is emitted by the autocollimator toward the optical surface in question. The reflection of this light at the optical surface can be superimposed with the cross hair position in the initial light path. Thus, the angle between the autocollimator and the surface can be measured with a high precision.

hair is dark, while the cross hair reflected from the optics is bright. The output of the autocollimator is visualized with a CCD-camera and a monitor. The relative alignment of the optical surface to the autocollimator is done by superimposing the reflected cross hair with the real cross hair.

Obviously the adjustment of the autocollimator itself plays a critical role for the pre-alignment precision. In the case of the power-recycling mirror it is adjusted to a bright light source behind the far east mirror **MFe**. The autocollimator is set up on a sturdy post inside the small tank **TCIb**, pointing toward the light source via the beam steering mirror **BDIPR**, through the power-recycling mirror. Eventually the autocollimator is clamped to the position obtained.

The adjustment of the yaw alignment of the suspended mirror is done via the revolvable plate, from which the pendulum is suspended. Eventually the plate is clamped at the final rotational position. A small balancing weight on top of the upper mass is shifted to obtain the pitch alignment. The weight is finally bonded to the upper mass with Ceramabond 571 VFG. The residual misalignment has to be corrected via bias currents through the local-control coils. These currents can be set from a LabVIEW$^{®}$ VI in both pitch and yaw each by $\pm 2048$ increments. By measuring the resulting spot-position change at the 600 m distant mirror, these increments are calibrated for each individual suspension. The calibration obtained depends not only on the geometry and dimensions of the suspension system but also on the actual gain settings of the relevant local-control module. From the obtained calibration factor, the dynamical range of the power-recycling mirror allows for a pitch adjustment of $\pm 12.90$ mrad and for a yaw adjustment of 5.32 mrad. The achieved pre-alignment accuracy for the power-recycling mirror is 3.49 mrad in pitch and 0.56 mrad in yaw.

The relative alignment between the mirror and the reaction mass is adjusted as the last pre-alignment step before the local-control coils can be set to the final positions. The relative alignment is judged with a caliper and corrected by adapting the position of the reaction mass to the mirror position. This is done by shifting the cantilever springs for the yaw alignment. Three balancing rods in the reaction mass are used for the adjustment of the pitch alignment.

## 3.6 The main suspension

In order to achieve the required isolation performance, allowing for a remaining displacement noise of the mirrors of $\delta \mathrm{x} \simeq 2.4 \cdot 10^{-20}\,\mathrm{m}/\sqrt{\mathrm{Hz}}$ at 50 Hz, the suspension of the GEO 600 interferometer mirrors (referred to as main suspension) is realized as a triple-pendulum suspension, including two vertical cantilever-spring stages. The quoted requirement corresponds to a seismically induced noise level, that is approximately a factor of three lower than the expected noise level due to thermal noise associated with the internal modes [Plissi '98]. The suspension system is pre-isolated by means of three stack isolators, similar to the ones described in Section 3.2. The stacks for the pre-isolation of the main suspension have one passive isolation layer and one active layer that is used for feed-forward control. The active stage consists of geophones[6] that are sensitive in the $x$, $y$, and $z$ direction, and three large piezo actuators[7]. The piezo drives are fed with a DC-voltage from 0 to 50 V, leading to a dynamic range of up to 25 μm in each degree of freedom. However, it turned out that the sensitivity of the geophones is not sufficient at the frequencies where an additional attenuation of the seismic would be required. Streckeisen STS2 seismometers are now placed in the central station and in the end stations of GEO 600 in order to obtain the ground-motion information required for a feed-forward control of the piezo actuators. See Section 4.4 for a description of the feed-forward systems employed for the main suspensions and the beamsplitter.

Placed above the active layer is a steel mass of 9 kg, followed by the passive RTV layer and a 7 kg steel mass. On top of each stack is a flex pivot mounted to decouple rotational motion of the stacks from the suspension system. The three stacks are connected to each other by the so-called stack stabilizer, which is clamped to the flex pivots. The stack stabilizer is a hollow hexagonal steel structure, internally damped with graphite-loaded silicone rubber. At three sections of the hexagon a ball bearing is attached to guide the so-called rotational stage, which is another hexagon mounted on top of the first one. The stack stabilizer has three rectangular recesses machined into its upper surface, into which polished ceramic plates are inserted. The rotational stage has circular recesses at the sections opposing the three ceramic plates. In these recesses, polished 10 mm high sapphire cylinders, that were cut from a rod with 10 mm diameter, are inserted to match the plates. These two components form a bearing on which the rotational stage slides when being rotated for pre-alignment purposes. The rotational stage can be rotated via two fine-threaded bolts that press against a block attached to the stack stabilizer. This technique allows the application of a differential rotational force between the stack stabilizer and the rotational stage without stressing the stacks themselves. Once the rotational position is set, the rotational stage is blocked from further rotation by tightening both adjustment bolts to the block. Figure 3.12 displays a view inside an inboard tank, showing the stack stabilizer and the rotational stage.

The rotational stage has two cross bars providing attachment points for the coil holder. The coil holder is clamped to the crossbars via base plates and bars. Two arms extend downward from these base plates to hold a U-shaped steel structure. This structure

---

[6]MARK Products Inc., 10502 Fallstone Rd., Houston, Texas 77099

[7]marco Systemanalyse und Entwicklung GmbH, http://www.marco.de/
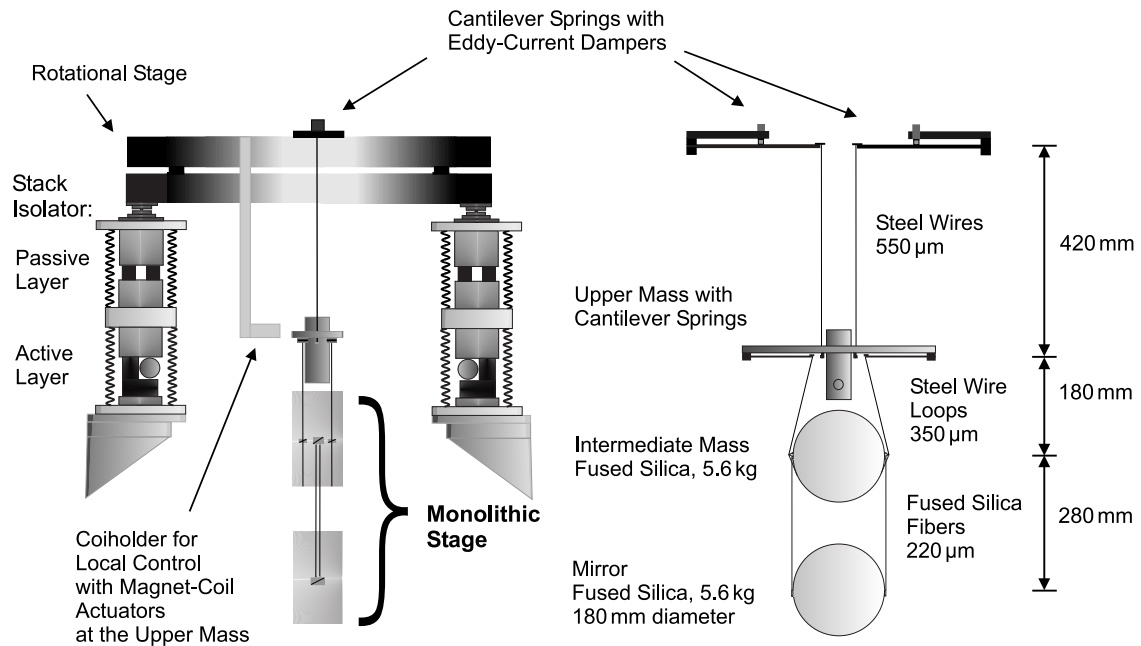
**Figure 3.11:** Drawing of the triple-pendulum suspension for the GEO 600 test masses: **Left:** The fused-silica mirror is suspended with four fused-silica fibers from the fused-silica intermediate mass. This monolithic stage is suspended as the third stage of the triple pendulum. Test mirrors were first suspended in steel-wire loops for the commissioning phase of the power-recycled Michelson interferometer. Both the upper mass and the intermediate mass are suspended by steel wires. The relevant eigenmodes of the triple pendulum are damped at the upper mass with magnet-coil actuators in all six degrees of freedom.
**Right:** Front view of the triple pendulum, comprising two cantilever-spring stages.

supports six clamps in which the coils are inserted. As in the modecleaner case, the relevant eigenmodes of the suspension are damped by sensing the motion of the upper mass with shadow sensors and feeding a current back to magnet-coil actuators, located at the upper mass. In contrast to the modecleaner suspension, the main suspension is damped in all six degrees of freedom. Excessive movements of the upper mass are prevented by the use of adjustable end stops that are also attached to the coil holder. These stops are set to allow a movement of the pendulum of about 3 mm in all degrees of freedom.

Big cantilever springs are bolted to the base plate near the upper attachment point of the two coil-holder arms. The performance of these cantilever springs is discussed in detail in Section 3.6.4 . The two upper suspension wires of a pendulum are attached to the tips of two springs, using small titanium clamps (2.5 g each). The wire separation at the tips is with 6 cm smaller than at the upper mass, providing a lower yaw frequency. The suspension wires are made from high tensile C 70 steel of 550 μm diameter. Thus, the wires are loaded to 12 % of the breaking load. The lower ends of the wires are clamped with steel clamps to the T-shaped upper mass (made from stainless steel, 5.6 kg) such that
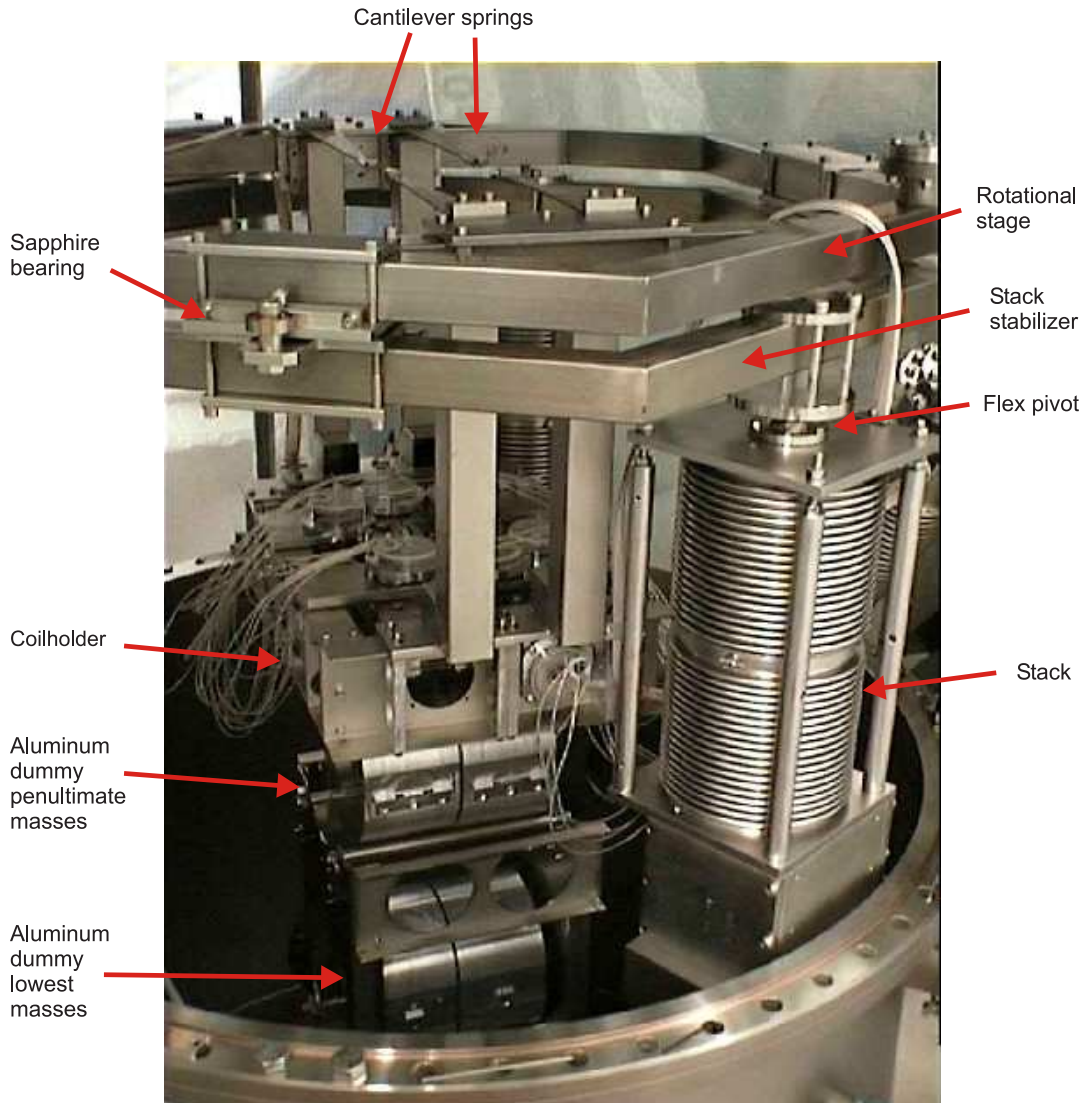
**Figure 3.12:**  View inside a tank with two triple pendulums installed, supporting aluminum dummy masses.

they break off 1 mm above the center of mass (COM). The horizontal plate of the upper mass is 370 mm long, 100 mm wide, and 12 mm thick. The vertical bar has a rectangular cross section of 49 mm$^2$ and is 137 mm long. The length of the upper stage, measured from the tips of the big cantilever springs to the COM of the upper mass, is 420 mm.

A jig that allows to attach the clamps to the wire when it is loaded with the nominal weight is used to set the wire length. By applying a well-defined tension to the wire, the reproducibility of the wire lengths is improved when producing several upper suspension wires. Figure 3.13 displays a schematic drawing of such a jig.

Four smaller cantilever springs are attached to the lower side of the upper mass. Smaller titanium clamps (2 g each) at the tips of these springs hold the intermediate

suspension wires. The intermediate stage is realized by two steel wire loops with a separation of 6 cm. The wires break off the upper mass 1 mm below the COM. The wire diameter is 350 μm (10 % breaking load), while the length of the intermediate stage is 180 mm measured from COM to COM. The wire length is set with a jig similar to the one described above. The cylindrical intermediate mass that has break-off-position defining prisms attached to its sides 1 mm above COM, lies in these wire loops. The dimensions of the intermediate mass are 180 mm diameter, 100 mm thick, weighing 5.6 kg as the upper mass. For the first commissioning phase of the power-recycled Michelson interferometer the intermediate masses were made from aluminum. The aluminum intermediate masses have the nominal outer dimensions but a hole machined into the center to compensate for the different mass densities of aluminum ($\rho = 2.7 \, \mathrm{g/cm^2}$) and fused silica ($\rho = 2.2 \, \mathrm{g/cm^2}$), which is the material the final intermediate mass is made from. Since the masses are suspended from two cantilever-spring stages, the overall mass of all three stages as well as the total mass of the lower two stages has to be kept constant in order to match the feedback actuator coils at the upper mass as well as at the intermediate mass. The full description of the two actuator arrangements is given in the sections 3.6.3 and 3.9). Table 3.5 provides the calculated resonance frequencies of the main suspension.
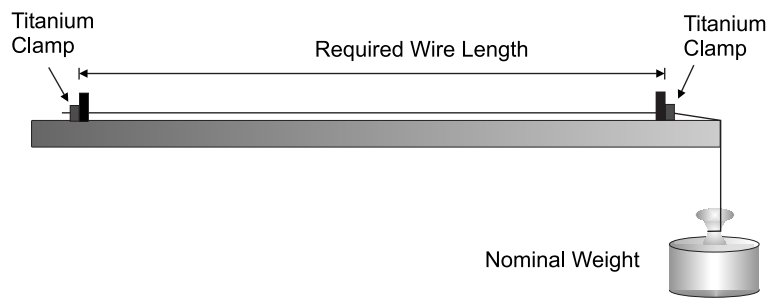


**Figure 3.13:** Jig to set the wire length. Jigs of this kind are used for the upper and intermediate wires. Two stoppers are mounted on an aluminum bar, giving the wire length. The titanium clamps are fixed to the wire while it is loaded with the nominal weight.

For experiments that were performed before the first commissioning phase of the power-recycled Michelson interferometer, one arm of GEO 600 and the power-recycling mirror was used as a 1200 m long cavity [Freise '02]. For these experiments test optics were suspended in steel-wire loops in the far east tank (**MFe** in **TFe**) and in the east inboard tank (**MCe** in **TCe**). These test optics have the same dimensions and weight as the final optics: 180 mm diameter, 100 mm thick, and 5.6 kg. However, these mirrors are made from BQ4H (by SICO, Jena) a comparatively cheap material that does not meet the high demands of GEO 600 in its final configuration. This refers to both the mechanical and the optical quality of the test mirrors.

Before the installation, these mirrors were cleaned with a so called $CO_2$-snow jet. The cleaning process is based upon the expansion of either liquid or gaseous carbon dioxide through an orifice. The clean $CO_2$ is provided by a tank under a constant pressure of $58.5 \cdot 10^5 \, \mathrm{Pa}$ (vapor pressure of liquid carbon dioxide at room temperature). The expansion

leads to the nucleation of small dry-ice particles and a high-velocity gas carrier stream. The orifice is held such that the flow hits the mirror surface under an angle of about $30\,°$. Upon impact with the surface, the dry-ice media removes particles down to sub-micron size by momentum transfer. Hydrocarbons are removed via a transient solvent or a freeze fracture mechanism. The final mirrors were, however, cleaned by wiping with a mixture of methanol and deionized water.

Subsequent to the cleaning process the mirror has to be discharged to counteract the effect from the friction with the $CO_2$ beam. A deionization gun supplies a gentle stream of clean nitrogen that has been ionized in a corona discharge. This stream is also used to blow potential adherent dust particles off the mirror as the final step prior to closing a vacuum tank.

The lowest pendulum stage has a length of $280\,mm$, measured from COM to COM. The wire separation is $10\,mm$, the wire diameter is $300\,\mu m$ ($7\,\%$ breaking load). The break-off position is defined by a prism at the mirrors side, $1\,mm$ above its COM. The two wire loops are produced by clamping the four ends of two wires onto one small aluminum base plate with two small aluminum blocks. The wire lengths are set by the use of a plate with two recesses for two aluminum mirror-sized dummy masses, with the precise separation. The wires are adjusted around the positioned dummy masses and loaded with the nominal weight when the clamps are fastened.

| Mode | Resonance frequency [Hz] |
| --- | --- |
| Longitudinal, pitch | 0.5, 0.6, 1.4, 2.1, 2.7, 3.6 |
| Sideways, roll | 0.6, 1.1, 1.4, 2.6, 4.0, 38 |
| Yaw | 0.4, 1.6, 3.2 |
| Vertical | 1.4, 4.7, 26 |

**Table 3.5:** The calculated frequencies of the relevant eigenmodes of the main suspension.

### 3.6.1 Pre-assembly of the suspensions

For the assembly and debugging of the mechanical suspension setup, an assembly bench was prepared on the east half of the detection bench of GEO 600. Three sturdy posts of about $1.3\,m$ height were set up to allow the mounting of the stack stabilizer. Each suspension installed in the central station was put together on this assembly setup. All parts of the suspensions had been cleaned before to fulfill the UHV requirements. Aluminum parts are cleaned with an ultrasonic bath in demineralized water with the alkaline degreaser P3-Almeco $18^{®8}$ at $75\,°C$ for $30\,min$ and are then rinsed in a dishwasher that is run with demineralized water. Stainless steel parts are cleaned also in an ultra-sonic

---

[8]http://www.henkel.de/

bath with demineralized water, but with the alkaline agent Surtec [9] at $80\,°C$ for $30\,min$ before rinsing them in the dishwasher.

The suspensions are completely assembled on the assembly bench, except for the local control and the optics. Instead of the real optics, aluminum dummy masses are used to load the cantilever springs in order to obtain the nominal deflection. First tests of the suspensions include a height check of the suspended mass above ground, the pendulum lengths and cantilever springs' deflections. The pitch of the upper mass can be leveled by shifting the attachment points of the upper wires points along the longitudinal axis. The relative position of the upper mass to the local-control coils has to be adjusted in most of the cases. This is due to the slightly different deflection of the upper cantilever springs. In order to obtain the height alignment and the roll alignment of the upper mass relative to the coils, the lengths of the upper wires are individually adapted to the deflection of the relevant spring. The required length change of the upper wires is measured with a caliper. The upper mass is then clamped with the upper limiter bolts while the upper cantilever springs are held down by two cross bars, such that the wires are not under tension. The small clamps at the tips of the springs can now be opened and the wire length can be adjusted. The wires can only be shortened by this procedure, since the clamping damages the wires. As a next step, the yaw alignment of the upper mass with respect to the coil holder and the longitudinal distance has to be set. This is done by moving the upper cantilever springs. The relative yaw alignment of the masses to each other has to be scrutinized and in most of the cases corrected. This is due to the different deflection of the small cantilever springs. It has proved that the springs need to be matched exactly to the weight beforehand. The matching of the deflection can be done by fixing the base to a sturdy frame, loading the spring with the nominal load, and then measuring the deflection. By bending the springs carefully beyond the elastic limit, they can be matched such that the deflection variation in a set of four springs is smaller than $\pm1\,mm$. This procedure was employed for the signal-recycling suspension. The spring constants of the cantilever springs remain unmatched however. The influence of mismatched cantilever springs on the temperature dependent alignment stability is analyzed in detail in Section 3.11.3.

It has to be made sure that the pendulum is free to move by at least $3\,mm$ in all degrees of freedom. Then the limiters have to be set. In the case of a suspension with a feedback pendulum, the distance between the two pendulums has to be set to $3\,mm$ by shifting the tips of the upper cantilever spring. The reaction mass supporting the feedback coils has to be balanced and the differential pitch and yaw alignments of the two pendulums have to be adjusted. Finally the free movement of the rotational stage has to be checked. After all test are performed, the dummy masses are taken out and the upper masses are clamped in position. The rotational stage is clamped to the stack stabilizer and the whole thing can be moved with three people to transfer it into a vacuum tank.

The described procedure applies only to the suspensions housed in the central station. Due to the limited space in the end stations no assembly bench could be set up. Consequently, the far-mirror suspensions were assembled *in situ* inside the vacuum tanks.

---

[9]http://www.surtec.com/

### 3.6.2 Installation of the optics

The prepared suspension is positioned on top of the flex pivots on the stacks in the vacuum tank. After clamping it to this position, the local-control coils can be inserted and wired. Teflon® coated cable is used for the in-vacuum wiring. 72 cables are required for the 12 coils of a suspension with reaction pendulum. Now the upper masses can be released and the intermediate masses can be suspended. The coils of the intermediate-mass actuators are wired with bare copper wires of only about $50\,\mu$m diameter to avoid a mechanical shortcut via the cables. The same cables are used for the wiring of the electrostatic actuators (Section 3.9). Now the lower masses are inserted, but still a dummy mass is used instead of the optics. After adjusting residual relative misalignments of the pendulums, the upper masses are re-clamped. The magnets and flags are attached to the spacers at the upper masses at this stage of the installation. Then the optics are suspended in the lower wire loops, after removing the dummy mass. The final mechanical alignment of the optics and reaction mass, which is described in Section 3.6.5, ends with the adjustment of the local-control coils.

Once suspended in the tank, the mirror had to be surrounded by a catcher that prevents both the mirror and the intermediate mass from falling in case a wire breaks. For the test optics this catcher was a rather simple device consisting of two big steel front plates connected via four small side plates. The front plates have an aperture of 175 mm and four smaller holes with clamps. In these smaller holes steel bars of 10 mm diameter are inserted and then clamped. Each two of these bars are fixed to a position 3 mm below the intermediate mass and the mirror, respectively. The exact height of each bar can be set individually by shifting its clamps.

In order to adjust the mechanical properties and to debug the complex double-triple suspension, test optics were also installed in the north inboard tank. The far north suspension was, however, debugged and adjusted only with aluminum dummy masses before the installation of the final optics.

Before implementing the final optics, a test of the vacuum status with all suspension systems installed was required to ensure a non-contaminating environment. The pressure in the far east tank proved to be of the order of $1.3 \cdot 10^{-4}\,$Pa $(1.3 \cdot 10^{-8}\,$mbar$)$, in the central cluster it was $4.5 \cdot 10^{-6}\,$Pa $(4.5 \cdot 10^{-8}\,$mbar$)$, dominated by residual air leaks. The partial pressure of hydrocarbons is below $10^{-8}\,$Pa $(10^{-13}\,$mbar$)$. These vacuum conditions are sufficiently clean to install the final optics. The lowest pendulum stage of the final suspension is entirely made of fused silica. The properties, the production and implementation, and the obtained performance of the monolithic suspensions is described in detail in Chapter 4.

The inboard mirror suspensions are installed 12.5 cm higher than the far mirrors, measured from the COM of the mirror to the bottom plate of the tank. This difference in height and the fact that the far mirrors themselves are 12.5 cm higher than the beamsplitter, allows the folding of the interferometer arms: the beam reflected back from the far mirror toward the beamsplitter passes 25 cm below the center of mass of the inboard mirror. To raise the whole suspension system, U-shaped stainless steel spacers are mounted underneath the stacks. The second difference to the far suspensions is the application of longitudinal feedback signals to the two lower pendulum stages of the inboard suspensions
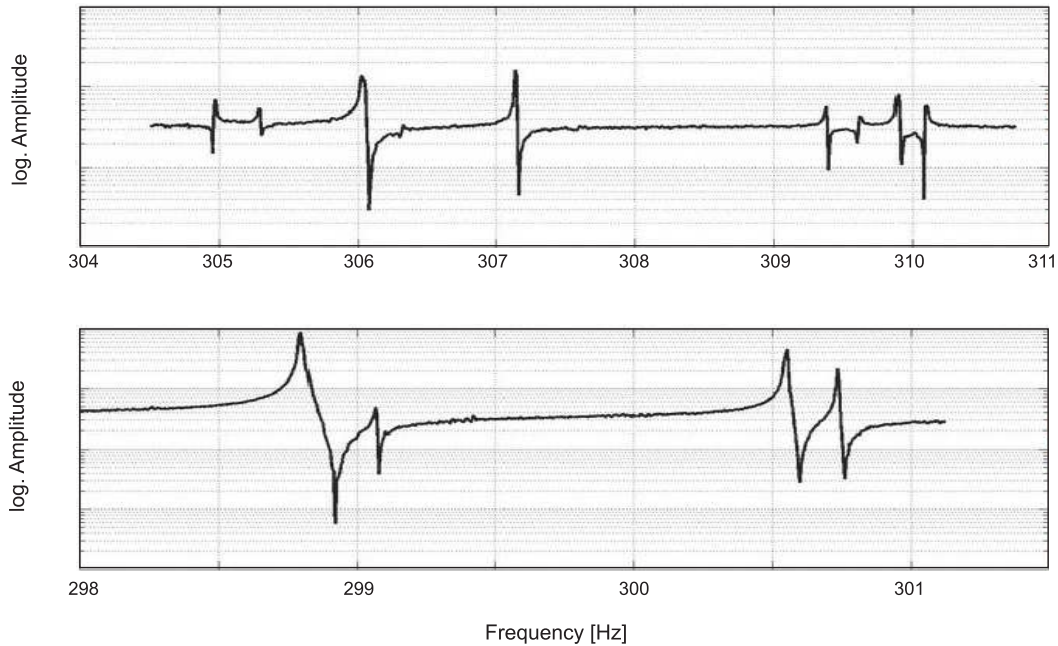
**Figure 3.14:** Two stretches of the error-point spectrum of the length control servo, featuring the violin modes of the steel wire inboard suspensions.

from a reaction pendulum.

Measurements of the violin modes of the steel-wire inboard mirror suspensions are shown in Figure 3.14. While the frequencies are very close to the calculated values around 300 Hz, the mechanical quality factors showed unexpectedly low values. Thus, it seems very likely that the electrostatic actuator strongly interacted with the suspension wires themselves. Measurements of the $Q$'s of the final silica suspensions are presented in Chapter 5.

### 3.6.3 Local control

The relevant mechanical eigenmodes of the main suspensions are damped with magnet-coil actuators as the modecleaner suspensions. Also the same kind of infrared shadow sensor is used for the local control of the main suspension. The position and orientation readout noise is of the order of $3 \cdot 10^{-10}\,\mathrm{m}/\sqrt{\mathrm{Hz}}$ at 10 Hz. Thus, the readout and damping has to be employed at the uppermost pendulum stage to benefit from the filtering of the lower stages at frequencies relevant for the gravitational-wave detection. Figure 3.16 displays a CAD drawing of a coil holder for an inboard test-mass suspension. Magnets of the same kind but 10 mm in length and diameter are bonded with Ceramabond 813 A onto aluminum spacers that are attached to the upper masses. Table 3.6 provides the properties of the single-component UHV compatible ceramic bonding agent. A clear advantage of the 813 A over the 571 VFG is the shorter setting time of only 4 h (at least 24 h are needed for 571 VFG). The paste-like viscosity helps with the attachment of vertically bonded parts. The CTE of Ceramabond 813 A is similar to the CTE of the

| No. of components | Main constituent | CTE | Viscosity | Air set | Bake |
|:---:|:---:|:---:|:---:|:---:|:---:|
| 1 | Alumina | $7.2 \cdot 10^{-6}\,\mathrm{K}^{-1}$ | Paste | 4 h | − |

**Table 3.6:** Properties of the single-component ceramic bonding agent Ceramabond 813 A.

aluminum alloys used to machine the spacers for the magnets from (CTE of the most common AlSiMg alloys is $7 - 8.5 \cdot 10^{-6}\,\mathrm{K}^{-1}$).

The main suspension is damped in all six degrees of freedom by the use of six magnet-coil pairs. The three coils (coils No. 4, No. 5, and No. 6) on top of the upper mass allow a damping of the pitch, vertical, and the roll modes of the suspension. The two coils at the long side of the upper mass (coil No. 1 and coil No. 2) provide the damping of the yaw and longitudinal modes. Coil No. 6 damps the lateral (or sideways) movement of the pendulum.

The glass encapsulated coils are adapted to the greater mass of the main suspension and the stronger magnets by the use of thicker wire, in order to allow for a higher driver current (1100 turns of $250\,\mu\mathrm{m}$ diameter wire, $37\,\Omega$ at room temperature, max. driver current $\sim 100\,\mathrm{mA}$) than for the modecleaner coils (1280 turns of $100\,\mu\mathrm{m}$ diameter wire, $270\,\Omega$, max. driver current $\sim 30\,\mathrm{mA}$). The peak force of the magnet-coil actuator is of the order of $F \leq 0.1\,\mathrm{N}$. As in the modecleaner case, the shadow sensors are co-located with the coils inside the encapsulation. The shadow sensor position has to be set to mid-range after the pre-alignment of the suspended optics, to provide enough range margin for the
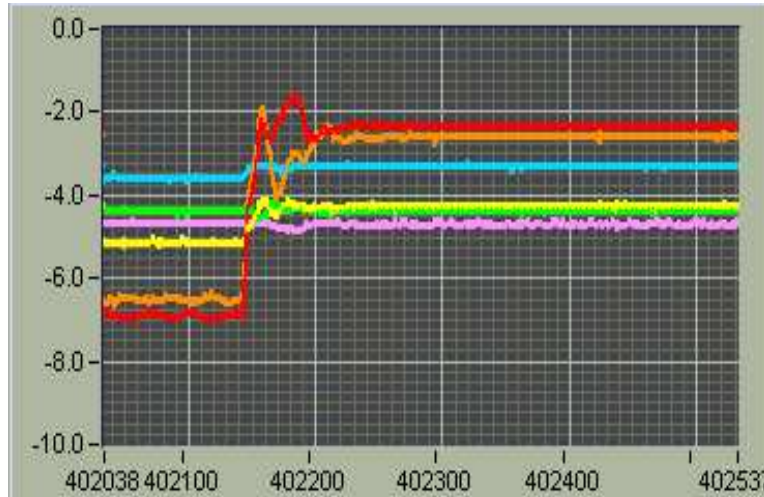


**Figure 3.15:** Screen shot of a LabVIEW® VI, showing the shadow-sensor signals of **MFe** after the application of a step function in the longitudinal direction. A mechanical quality factor in the range of $Q = 3 - 5$ can be derived from the decay time of the damped oscillation.
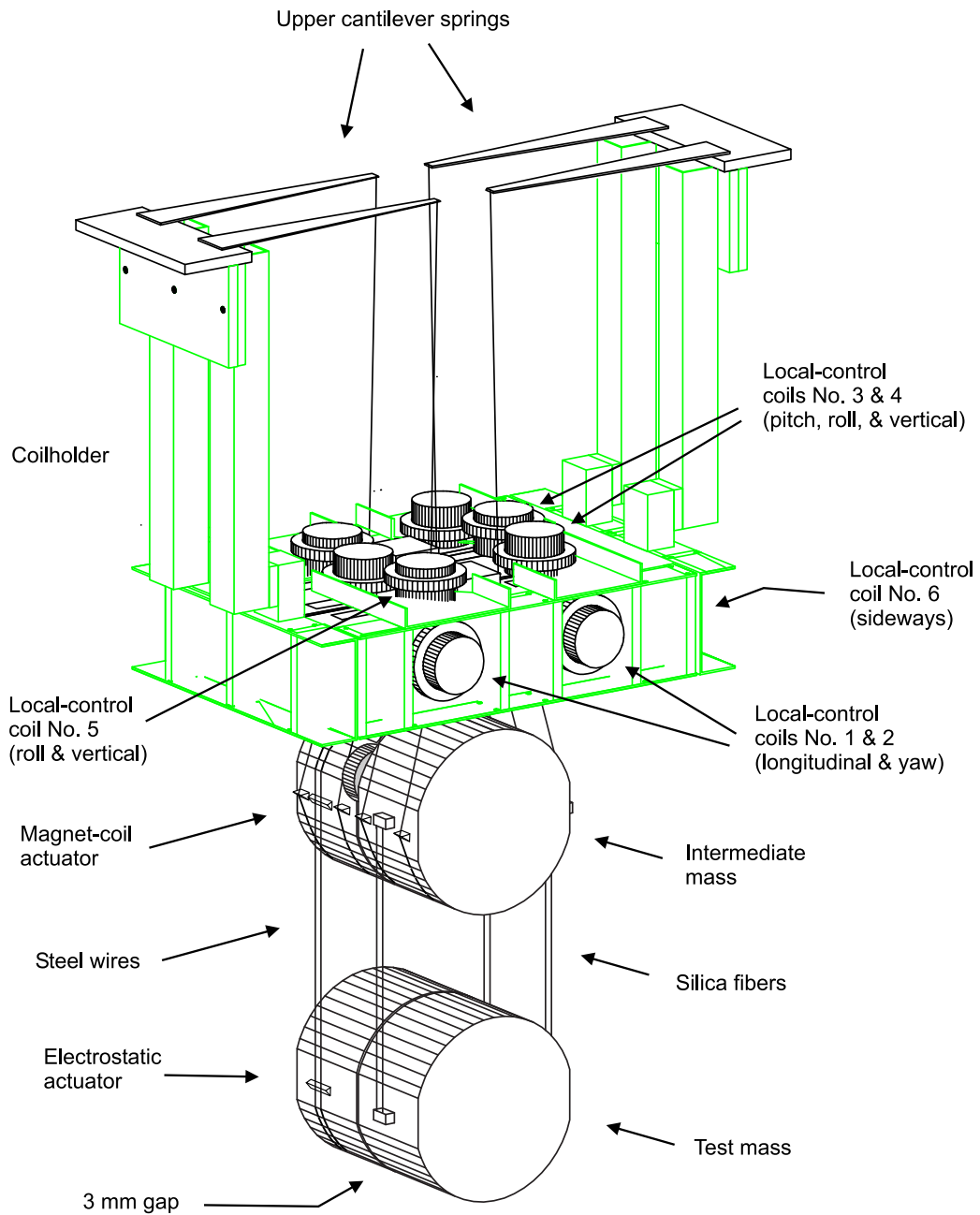
**Figure 3.16:** CAD drawing of the coil holder for an inboard mirror suspension. 12 local-control coils for the two pendulums are supported by one common sturdy structure. The coils relevant for the mirror pendulum are marked in the drawing, except for coil No. 6, which is hidden behind the coil holder. The eddy-current damping of the cantilever spring has been omitted for clarity. The plates to which the upper cantilever springs are attached are part of a clamping system that is used to fix the coil holder to the cross bars inside the rotational-stage hexagon.

final alignment. The sensor position is set by shifting the glass encapsulation back and forth inside its clamp. In order to clamp the fragile glass body firmly enough but avoid crushing it, the aluminum clamps have to be operated with great care. The former use of corrugated tantalum inlays inside a recess in the clamps was abandoned for practical reasons. The coils have to be set with a precision of the order of 0.1 mm, to set the shadow sensor to mid-range.

A spectrum of the residual pitch-alignment fluctuations of the far east mirror **MFe** is shown in Figure 3.17. The spectrum is derived from a measurement of the laser spot position at the east inboard mirror **MCe**. Hence, the vertical fluctuations of the beam before hitting **MFe** also contribute to the measurement. Also fluctuations in the other degrees of freedom of the pendulum couple with individual coefficients to the spot position. Thus, the given spectrum can be considered as an upper limit. The RMS deviation of the spot position was 0.6 mm. The spectrum is clearly dominated by the pendulum resonances. The broad peak at 0.59 Hz is caused by the longitudinal mode of the triple pendulum. The common-mode pitch motion is responsible for the small bump at 0.67 Hz. The big structure above 1 Hz is due to a combination of the 1.4 Hz differential longitudinal or pitch mode and the 1.1 Hz sideways or roll mode. The two peaks at 2.18 Hz and 2.70 Hz are due to different differential pitch or longitudinal modes. The peak at 3.03 Hz is very likely caused by the differential longitudinal or pitch mode of the beamsplitter that was calculated to be 2.9 Hz. The small structure at 4.3 Hz is caused by a differential pitch mode of the power-recycling suspension.

The actual eigenfrequencies of the pendulum modes can also be revealed by analyzing injected calibration frequency lines. This analysis is based on the inspection of a spectrogram with a frequency resolution of 1 mHz, generated out of a data set of 330 h
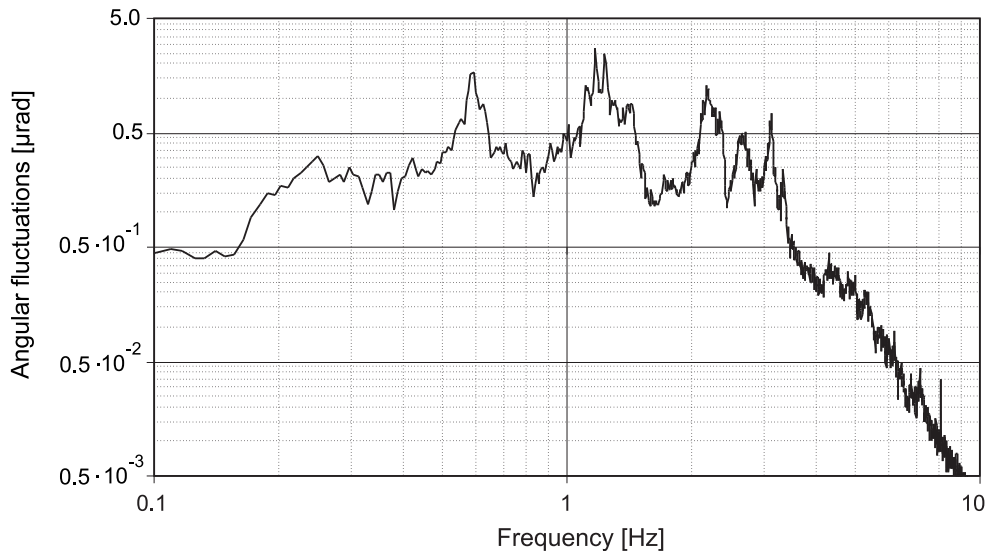


**Figure 3.17:** Angular alignment fluctuations of the far east mirror **MFe**, derived from a spot position measurement using a quadrant photo diode behind the 600 m distant east inboard mirror **MCe**.
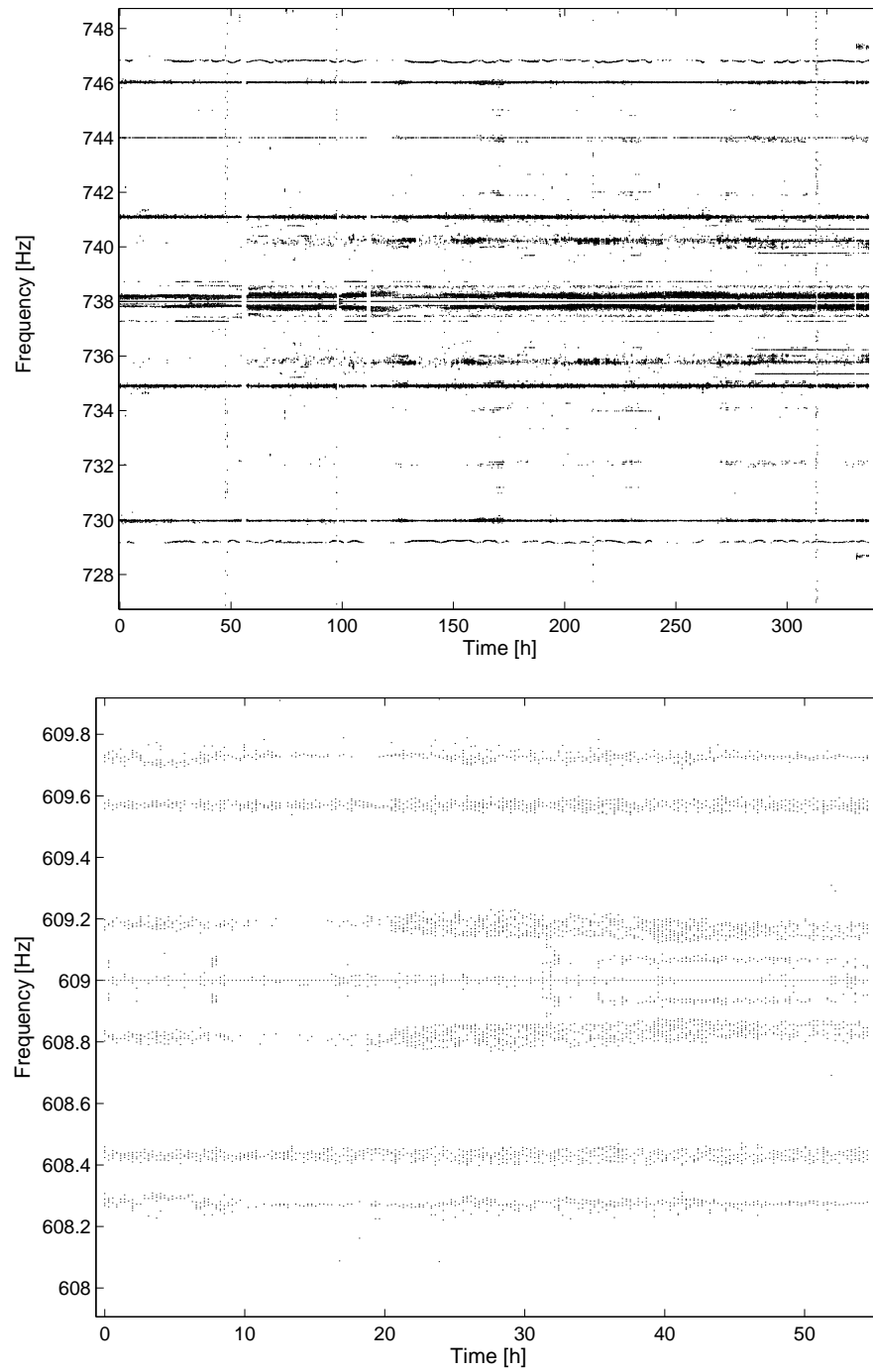
**Figure 3.18:** Two injected calibration lines at 738 Hz and at 609 Hz, with sidebands at the micro-seismic frequency (166 mHz) and at the most prominent pendulum mode frequencies. The lower graph is zoomed in further to reveal the lowest pendulum-mode frequencies.

| Modeled value [Hz] | Spot position [Hz] | Spectrogram [Hz] |
|---|---|---|
| 0.4 | — | — |
| 0.5 | — | — |
| 0.6 | 0.59 | 0.58 |
| 0.7  (Yaw **BS**) | 0.73 | 0.71 |
| 1.4 | — | 1.23 |
| 1.6 | — | — |
| 2.1 | 2.2 | 2.20 |
| 2.7 | — | — |
| 3.2 | 3.1 | 3.15 |
| 3.6 | — | — |
| — | 8.03 | 8.05 |
| — | 8.81 | 8.75 |

**Table 3.7:** The calculated frequencies of the main suspension and the beamsplitter versus the measured frequencies. The calculated frequencies are only given for the longitudinal, pitch, and yaw eigenmodes, since the other degrees of freedom couple less strongly into the direction relevant for the measurements. As most of the calculated frequencies for the main suspension and the beamsplitter suspension are of similar values, only the yaw mode of the beamsplitter suspension at 0.7 Hz has been accounted for.

from an error-point spectrum of the interferometer length control servo. The calibration line frequencies used for the analysis (609 Hz and 738 Hz, locked to a rubidium oscillator) are modulated by the pendulum motion and hence, show sidebands at the respective frequencies. Figure 3.18 shows a section of the spectrogram centered around the 738 Hz line and a section centered around the 609 Hz line. The latter one is zoomed in further, to accentuate the two lowest frequencies that appear at 0.58 Hz and 0.73 Hz, respectively. Due to the local-control damping, the $Q$ of the pendulum modes is of the order of only $Q \simeq 3 - 5$. Hence, the modes have a comparatively broad linewidth, causing the fuzzy sidebands of the calibration line. The noisy sidebands at 166 mHz are due to the so-called micro-seismic peak. The frequencies obtained by these two methods are compared with the calculated values in Table 3.7. The table provides the calculated frequencies of the modes that couple most strongly to the degree of freedom relevant for the measurements.

### 3.6.4 Vertical isolation

The vertical resonance frequencies are higher than for the other degrees of freedom (see Table 3.5). Due to the unavoidable cross coupling between the different degrees of freedom (a coefficient of 1/1000 is assumed for the coupling of vertical to longitudinal in the currently employed MatLab model), additional vertical isolation is required. As described

above, two stages of cantilever springs are used in the main suspension to improve the isolation.

The suspension wires are attached to the cantilever springs by small titanium clamps (2.5 g for the upper cantilever spring and 2 g for the lower springs), which are bolted to the tips of the springs. These small clamps have a recess to center the wire within the clamp. Titanium was chosen for the clamps material because it is relatively hard (Brinell hardness: $7.16 \cdot 10^8$ Pa) while being relatively light ($\rho = 4.5$ g/cm$^3$). Former measurements revealed titanium as a clamp material that allows for low dissipative wire clamping [Dawid '97].

The cantilever springs decouple the pendulum itself from the dynamic load of the stacks at frequencies above the eigenfrequency of the upper springs at 2.7 Hz. In order to load the stacks to the nominal load of about 14 kg per stack, three additional weights of 4.9 kg each are attached to the rotational stage of the far mirror suspensions. The near mirror suspensions have each three additional weights of 1.4 kg attached to their rotational stages. The increase of load leads to a decrease of the vertical resonance frequency of the stacks to the design value of 15 Hz (Section 3.2).

The cantilever springs are made from Marval 18 maraging steel, a precipitation hardened material that provides a low creep noise.[10] The spring constant $\kappa$ of a cantilever spring is given by [Plissi '00]

$$\kappa = \frac{E\,a\,h^3}{4\,l^3\alpha} \tag{3.5}$$

where $E$ is the Young's modulus of the spring material ($E \simeq 1.86 \cdot 10^{11}$ Pa for Marval 18 steel), $l$ is the length of the cantilever spring, $h$ is the thickness of the spring, and $a$ is the width of the base of the spring. $\alpha$ is the shape factor of the nearly trapezoidal shaped spring, which is related to the ratio of the width of the base and the width of the tip of the spring. $\alpha$ equals unity for the case of a rectangular spring and $\alpha = 1.5$ for a triangular cantilever spring.

$$\alpha = \frac{3}{2\,(1-\beta)}\left[3 - \frac{2}{1-\beta}\left(1 + \frac{\beta^2\log\beta}{1-\beta}\right)\right] \tag{3.6}$$

where $\beta$ denotes the ratio between the base width and the tip width of the cantilever spring. The cantilever springs used for the GEO 600 suspensions have $\alpha \simeq 1.42 - 1.45$. Please see Figure 3.19 for a schematic drawing of the cantilever springs. The bending (vertical) mode frequency of the springs is given by

$$\omega = \sqrt{\frac{\kappa}{m}} = \sqrt{\frac{E\,a\,h^3}{4\,m\,l^3\alpha}} \tag{3.7}$$

where $m$ is the mass suspended from the spring. The parameters of the upper cantilever springs are: $l = 240$ mm, $a = 40$ mm, and $h = 2$ mm. The uncoupled resonance frequency

---

[10]During its production process the steel is heated for four hours to 480 °C to allow for a relaxation of inherent mechanical strain.
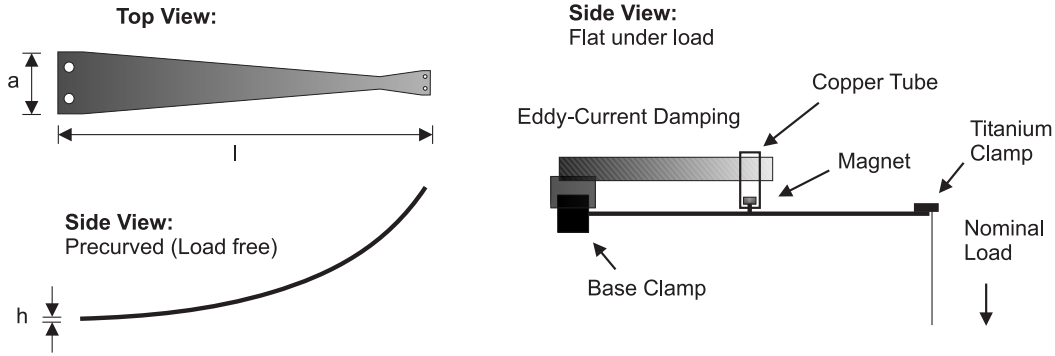
**Figure 3.19:** Schematic drawing of a cantilever spring. The springs are precurved such that they are flat under the nominal load. At the upper set of cantilever springs eddy-current damping of the fundamental internal eigenmode is applied.

of these springs is about 2.7 Hz. The set of smaller cantilever springs, located at the lower side of the upper mass has the following parameters: $l = 124$ mm, $a = 28$ mm, $h = 1$ mm, and an uncoupled vertical resonance frequency of about 3.0 Hz.

The fundamental internal eigenmode of the upper cantilever springs was measured with a diminutive accelerometer [11] to be about 100 Hz. In order to damp these modes, eddy-current damping is applied at half length of the springs. A magnet with 10 mm diameter and 5 mm height is bonded onto a small spacer that is bolted to the center of the spring. A corresponding copper tube is held by an aluminum arm that is clamped to the base clamp of the spring. The magnet fits in the copper tube, leaving a tight gap of 0.5 mm (see Figure 3.19). The frequency of the fundamental internal eigenmode of the smaller cantilever springs is 220 Hz. Due to the mechanical attenuation of the subsequent stages at these relatively high frequencies, no damping of the internal modes is required for the small springs.

The deflection $\lambda$ of a cantilever spring follows the equation

$$\lambda = \frac{mg}{\kappa} = \frac{4\,mg\,l^3\,\alpha}{E\,a\,h^3} \tag{3.8}$$

with $g \simeq 9.81\,\mathrm{m\,s^{-2}}$ being the acceleration due to gravity at the earth's surface. The deflection of the upper cantilever springs can be calculated with the parameters given above and the supported load of $3 \cdot 5.6/2$ kg per spring, to be 11.02 cm. The observed deflection is, however, about 1 cm less. Furthermore, the deflection varies from spring to spring by about $\delta\lambda \simeq \pm 1$ cm. The greatest error in the formula arises from the strong influence of the cantilever spring's thickness $h$. A deviation of $\delta h \simeq +65 \pm 65$ μm explains the observed effect. The lower cantilever springs are calculated to deflect 5.8 cm under the nominal load of $m = 2 \cdot 5.6/2$ kg. The observed deflection is, however, about 5 mm greater and varies by about $\pm 3$ mm. These effects can be explained by a deviation of $\delta h \simeq -32 \pm 16$ μm.

---

[11] Bruel and Kjaer, http://www.bksv.com/bksv/

In order to compensate for the different deflection of the upper cantilever springs and the thereby induced roll misalignment of the upper mass, the length of the upper wires were adapted. For the compensation of the pitch misalignment of the penultimate mass, due to the mismatch of the lower cantilever springs, the effective lengths of the intermediate wires were adapted. The introduced roll misalignment of the penultimate mass was not completely corrected for, since a small static roll misalignment does not affect the interferometer alignment.

### 3.6.4.1 Matching the cantilever springs

Depending on the homogeneity of the deflection of the lower cantilever springs a static pitch misalignment of the test mass is introduced. Initially a deflection mismatch of up to 3 mm was observed for the small springs. A mismatch in the deflection of the springs of 1 mm leads already to a pitch misalignment of the mirror of 33 mrad. This misalignment translates into a vertical shift of the beam position at the place of the 600 m distant mirror of about 40 m. Hence, sets of each four springs had to be preselected and matched. A possible way of matching the springs is to measure the actual deflection and then carefully bending it beyond the elastic limit. Thereby the radius of pre-curvature of the spring is changed and the obtained effective deflection can be adapted. This matching was, however, only done for the signal-recycling suspension. As mentioned in the above section, for the test-mass suspensions the effective wire lengths were adapted to correct for the pitch misalignment.

Advanced LIGO will, however, follow a different approach by using a clamp library. The substance of this library is an assortment of wedged base clamps with different wedge angles. After measuring the deflection of a spring, the clamp with the appropriate angle can be picked from the library to compensate for an excess or lack of deflection.

It should be noted that either of these approaches tackles the result rather than the cause. Both methods change the effective deflection instead of the effective spring constant. Changing the pre-curvature merely relocates the tip of the unloaded spring and thereby the end point of the deflection (apparent deflection), while the overall (real) deflection $\lambda$ of the cantilever spring remains unchanged. Exactly the same is done by the use of a wedged base clamp. From the measurements presented in Section 3.11.1, it is evident that the remaining mismatch in real deflection leads to temperature dependent pitch- and roll-alignment fluctuations. A possible solution to reduce these fluctuations (thus reducing the demands on the active alignment control) is a thorough temperature control. A more appropriate way is to reduce the coupling of temperature to the alignment by matching the spring constants instead of the apparent deflections. This can be done by adapting the deflection of the springs via a clamp library containing wire clamps of different lengths instead of base clamps with different wedge angles. The wire clamp is mounted at the tip of the spring, holding the wire. By an alteration of the length of this clamp, the effective length of the spring and thereby the spring constant is altered. Thus, by adapting the deflection via the length of the springs the spring constants can be matched, provided the springs have a similar precurvature. Similar precurvature is a criterion that can easily be judged beforehand and thereby allows for a straightforward pre-selection of cantilever spring sets.

### 3.6.5 Pre-alignment the interferometer mirrors

Once the optics are suspended, they need to be aligned with respect to each other. The crude alignment (pre-alignment) is done mechanically before the vacuum tank is closed. The remaining misalignment has to be compensated by bias currents through the local-control coils. The energy dissipated in the coils can lead, due to the poor thermal transportation rates under vacuum conditions, to a significant heating of the glass-encapsulated coils. It is very likely that the observed decrease of the output range of some of the shadow sensors, located within the same encapsulation, was caused by this heating (shadow sensors of the same kind were used in a different experiment, where they have only temporarily been powered, without any noticeable degradation over years). Hence, the pre-alignment needs to be done as precisely as possible. An autocollimator is used to read out the mirror's relative alignment with respect to pitch and yaw (rotation around the horizontal and vertical axis, respectively). The principle idea behind an autocollimator is described in Section 3.5.1. The autocollimator output is sensed with a CCD and displayed on a monitor.

Due to the limited space behind the suspended masses, the pre-alignment of the inboard mirrors has to be done via a pick-off mirror through the electrostatic reaction mass and through the mirror itself. These additional optical surfaces in the light path make the reflected cross hair less clearly visible. Consequently, a very bright light source for the autocollimator and a dark environment are required for the pre-alignment of the main suspension. The autocollimator is adjusted to a light source located outside a view port behind the corresponding far mirror for the pre-alignment of the inboard suspensions. For the far mirror pre-alignment the autocollimator is adjusted to a light source behind the beamsplitter.

In order to change the alignment of the suspended optics in yaw, the rotational stage is rotated. For the pitch alignment a balancing rod in the lower part of the vertical bar of the upper T-shaped mass can be moved to shift the COM of the upper mass. After closing the tanks, the fine alignment is done electronically via the local-control coils. The analog local-control servos are digitally supervised, as described in Section 3.6.3. In a LabVIEW$^{®}$ VI the offset currents through the coils can be set stepwise by $\pm 2048$ increments. The calibration factor for an increment depends on the individual gain settings of the actual local-control module, as well as on the dimensions and geometry of the relevant suspension. A typical calibration for a main suspension is $2.2\,\mu$rad per increment for pitch and $17.0\,\mu$rad per increment for yaw, respectively. A typical dynamical range of the local control actuators for a main suspension is of the order of $\pm 5\,$mrad in pitch and $\pm 35\,$mrad in yaw. The typical angular pre-alignment precision is of the order of $\pm 1\,$mrad. This translates into a lateral shift of the beam position of about $\pm 120\,$cm at $600\,$m distance.

CCD cameras behind the mirrors are used for the crude electronic alignment. Then the visibility of the flashing or even locked cavity can be used for further alignment corrections. Finally even the shape of the output mode, recorded by a CCD camera and visualized on a monitor, can be used for a further improvement of the alignment. In the operating modus of GEO 600, these fine-alignment settings are eventually controlled by the automatic alignment system [Grote '04].

The local-control shadow-sensor positions can be used to obtain an even better pre-alignment: Once the optics are electronically fine-aligned, the sensor positions can be used to adjust the mechanical alignment the next time the vacuum tank is opened. By doing this for the pitch alignment of the east inboard suspension a pre-alignment precision of 51 µrad was achieved. Table 3.8 gives the residual misalignments for some mirrors, demonstrating the accuracy of the pre-alignment procedure.

|  | MCe | BS | MSR |
|---|---|---|---|
| Pitch | 51 µrad | 497 µrad | 196 µrad |
| Yaw | 731 µrad | 1.775 mrad | 1.632 mrad |
| Range: |  |  |  |
| Pitch | ± 4.510 mrad | ± 9.010 mrad | ± 57.340 mrad |
| Yaw | ± 34.820 mrad | ± 13.720 mrad | ± 34.820 mrad |

**Table 3.8:** The pre-alignment precision achieved for **MCe, BS**, and **MSR**. Provided are the individual residual pitch and yaw misalignments. The maximum dynamic range of the local control actuators is ± 2048 increments in both relevant degrees of freedom. The calibrated dynamic range of the suspended optics is given in the two lower rows.

## 3.7 The signal-recycling suspension

The design of the main suspension was adapted for the smaller signal-recycling suspension. It consists also of a triple pendulum suspension with two vertical cantilever-spring stages. However, the signal-recycling mirror has the same dimensions as the power-recycling mirror: 150 mm diameter and 75 mm thick, weighing 2.92 kg. Again a reaction pendulum for the longitudinal feedback actuation is suspended 3 mm behind the mirror pendulum. But unlike the reaction pendulums for the main suspension, only one actuation stage is employed here. As for the power-recycling mirror the actuation is done at the lowest stage of the pendulum via three magnet-coil actuators.

The signal-recycling suspension is supported by three active/passive stacks, like the main suspension. In order to compensate for the reduced load on the stacks, three steel weights of 2.7 kg each are mounted on top of the rotational stage. The stack stabilizer and rotational stage arrangement for the signal-recycling suspension is identical to the main suspension. The lower part of the coil holder is, in contrast to the main suspension coil holder (20 pieces, 80 bolts), made of one piece of stainless steel. This design is much simpler but leaves less freedom for later adjustments. This lower part supports six coils each for the mirror pendulum and for the reaction pendulum. End stops and catchers for the two T-shaped upper masses are provided at the coil holder as well.
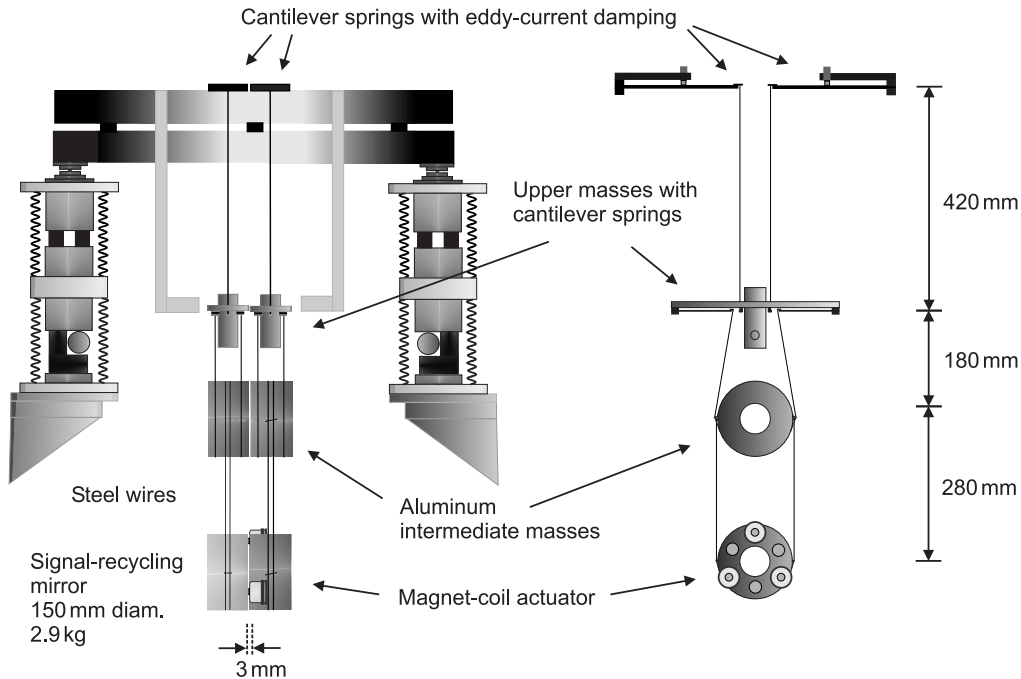
**Figure 3.20:** Schematic drawing of the signal-recycling suspension. Two triple pendulums are suspended with steel wires. The feedback signals are applied via three magnet-coil actuators at the mirror itself.

The cantilever springs for the upper suspension stage are attached to the cross bars of the rotational stage, as for the main suspension. The springs are 250 mm long and have a thickness of 1.5 mm. Eddy-current damping is applied at half length of the springs to damp the fundamental internal eigenmode. The eddy-current dampers are copied from the main suspension, but adapted to the shorter springs. The upper two steel wires, having a diameter of 360 μm (15 % breaking load), are attached via titanium clamps (2.5 g) to the tips of the springs. The intermediate mass is suspended from smaller cantilever springs (120 mm length, 1 mm thickness), as in the main suspension case, but with a wire separation of 53 mm. The intermediate mass is made from aluminum, as the intermediate masses for the test optics suspension, described in Section 3.6 . But since the signal-recycling suspension was installed right away with the final optics [12], the aluminum mass is the permanent solution. The steel wires used for the intermediate stage loops have a diameter of 200 μm (15 % breaking load). A wire diameter of 162 μm (12 % breaking load) was chosen to form the lower loops. The three stages have the same lengths as the main suspension stages, 420 mm, 180 mm, and 280 mm. Figure 3.20 shows a schematic drawing of the signal-recycling suspension.

---

[12]In the case of the signal-recycling mirror it is not exactly right to talk about final optics. Since the bandwidth of the signal-recycling cavity, and thus the bandwidth of the frequency response of GEO 600, depends on the reflectivity of the signal-recycling mirror, it is most likely that it has to be changed more than one time to adapt GEO 600 to the astro-physical sources of interest. New technologies may allow for a thermal alteration of the reflectivity of the signal-recycling mirror *in vivo*, without opening the vacuum system or even without losing lock of the dual-recycled Michelson interferometer.

The signal-recycling suspension is the first suspension in GEO 600 that has no on-bonded magnets at the upper mass. It turned out that the different bonds used for the different suspension systems are weakened under vacuum conditions. After maintenance work on a suspension, it is a recurring task to re-bond the flags and magnets that were chopped off during the work. As the bond takes several hours up to a day to set and a complete readjustment of the local-control coils is necessary, this a time consuming task. The magnets required for the local control of the signal-recycling suspension are attached to thin plates, made from magnetizable stainless steel, which are bolted onto spacers at the upper mass. Onto these plates the magnets are attached by their own magnetic force. The "soft attachment" of the magnets prevents them from being accidentally chopped off. They just shift off their position and can be slid back in virtually no time. This is a noticeable step forward for the installation and maintenance work at the suspensions.

The longitudinal feedback for the signal-recycling cavity, applied from a suspended reaction mass, requires the bonding of magnets onto the mirror's rear surface. This was accomplished by using Vacseal$^{®}$. Small Nd:Fe:B magnets of only 3 mm diameter and 3 mm height were used, to minimize the influence on the mechanical quality factor of the mirror and thus on the thermal noise performance, and to limit the influence of stray magnetic fields onto the position of the signal-recycling mirror. The three feedback coils facing the magnets are supported by the aluminum reaction mass. Three copper balancing rods are inserted into the reaction mass to balance it and to level its overall weight to 2.9 kg. Copper was chosen because of its relatively high density ($\rho = 8.96 \, \text{g/cm}^3$), while being UHV compatible and well machinable.

### 3.7.1 Pre-alignment of the signal-recycling mirror

As for the main suspensions, an autocollimator with CCD-camera is used for the pre-alignment of the signal-recycling mirror. Due to the limited space, it has to be set up on the detection bench, pointing toward the signal-recycling mirror via the preliminary output beam director in **TCOb**. The autocollimator was adjusted to a bright light source behind the far north mirror **MFn**. Because of the long distance of more than 2 m between the autocollimator and the mirror and because of the limited reflectivity of the beam director for visible light, the reflection of the cross hair is rather dim. In order to increase the contrast on the CCD-camera, the pre-alignment of the signal-recycling mirror has to be performed in a completely dark environment.

The mechanical part of the pre-alignment is done as for the main suspension. The yaw alignment is set by rotating the rotational stage with the fine-threaded drive. The pitch alignment is done via a balancing rod in the lower part of the vertical bar of the T-shaped mass. The relative yaw alignment between the mirror pendulum and the reaction pendulum is adjusted by shifting the the upper cantilever springs of the reaction pendulum. The relative pitch alignment is accomplished by operating the balancing rods inside of the reaction mass. Measurements with a caliper ensure the parallelism of the mirror and the reaction mass.

## 3.8 The beamsplitter suspension

The beamsplitter suspension is a copy of the main suspension, except for the bigger masses. The diameter of the beamsplitter is 260 mm, it is 80 mm thick and weighs 9.3 kg. The upper mass of the beamsplitter pendulum is suspended with two steel wires of 420 mm length and a diameter of 600 µm. The upper cantilever springs have a length of 240 mm and are 2 mm thick. In order to obtain a small enough footprint to allow for a second suspension (the compensation-plate suspension, see Section 3.8.3) inside the beamsplitter tank, the springs had to be crossed. Eddy-current damping is applied at half length of the springs, as in the main suspension case. The intermediate stage, formed by two steel wire loops attached to small cantilever springs (175 mm length, 1 mm thickness) below the intermediate mass, has a length of 180 mm. The wire diameter is 400 µm. For the first commissioning phase of the interferometer a test beamsplitter was suspended in steel wire loops from an aluminum intermediate mass. The test beamsplitter made from Suprasil® SV 312, has a diameter of only 235 mm and hence weighs only 7.6 kg. In order to obtain the nominal cantilever spring deflection, the missing weight was compensated by a heavier intermediate mass. The 280 mm long steel wire loops used to suspend the test beamsplitter had a diameter of 250 µm. To complete the final configuration of the GEO 600 interferometer the beamsplitter was eventually monolithically suspended. A detailed description of the monolithic beamsplitter suspension is given in Section 4.6 . Figure 3.21 provides a schematic drawing of the beamsplitter suspension. Table 3.9 gives the calculated resonance frequencies.

The anti-reflection (AR) coating on the rear surface of the test beamsplitter turned out to have too high a reflectivity and hence did not fulfill the requirements (i.e., 50 ppm residual reflectivity). In order to minimize the optical loss inside the power-recycling cavity, introduced by the excessive residual reflection of the AR-coating, the test beamsplitter was replaced by the final one earlier than originally scheduled. As a preliminary solution the final Suprasil® SV 311 beamsplitter was temporarily suspended in steel wire loops. The ears for the silica fiber attachment, which were already bonded onto the flat sides of the substrate, were covered by a pair of aluminum bridges to avoid any damage. The steel wires pass over these bridges that provide break-off-position defining grooves. Due to the greater diameter of the final beamsplitter, the intermediate mass had to be replaced as well to keep the total pendulum weight constant.

| Mode | Resonance frequency [Hz] |
|---|---|
| Longitudinal, pitch | 0.4, 0.6, 1.3, 1.35, 2.3, 2.9 |
| Sideways, roll | 0.6, 1.35, 1.6, 2.8, 4.3, 28.3 |
| Yaw | 0.7, 2.1, 3.6 |
| Vertical | 1.2, 4.4, 21.2 |

**Table 3.9:** The calculated frequencies of the relevant eigenmodes of the beamsplitter suspension.
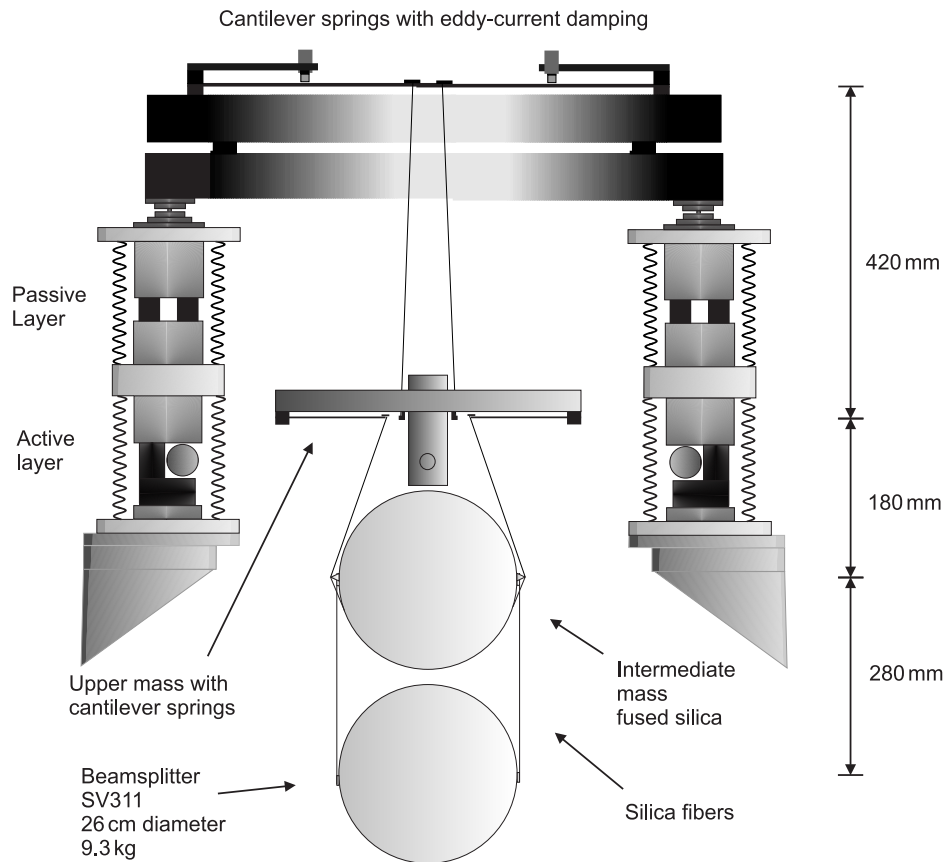
**Figure 3.21:** Schematic drawing of the beamsplitter suspension. The beamsplitter is the biggest suspended optics in GEO 600. It has a diameter of 26 cm, is 8 cm thick, and weighs 9.3 kg.

The test beamsplitter as well as the final beamsplitter and their intermediate mass had to be protected by a catcher that prevents a damage of the optics in case a wire breaks. Before installing the monolithic beamsplitter stage, a comparatively simple catcher was used. It consists of a square base plate with four threaded holes at the corners. Via bolts and counter nuts the base plate can be adjusted in height and leveled before it is clamped to the bottom plate of the vacuum tank. Four posts protrude from the base plate, holding two rods 3 mm below the beamsplitter. An F-shaped aluminum part is horizontally bolted to a long hole in a sturdy post that extends from the base plate. The gap in the horizontal F reaches over the upper rim of the beamsplitter to prevent it from overbalancing. Another bar is attached to the top of the same post at a second long hole. This bar penetrates through the aperture in the intermediate mass, preventing it from falling. The catcher is set such that the beamsplitter and the intermediate mass have 3 mm freedom in all degrees of freedom. This preliminary catcher was replaced by the final one when installing the final monolithic suspension. Figure 3.22 shows the lower part of this arrangement and the light path from a top view.
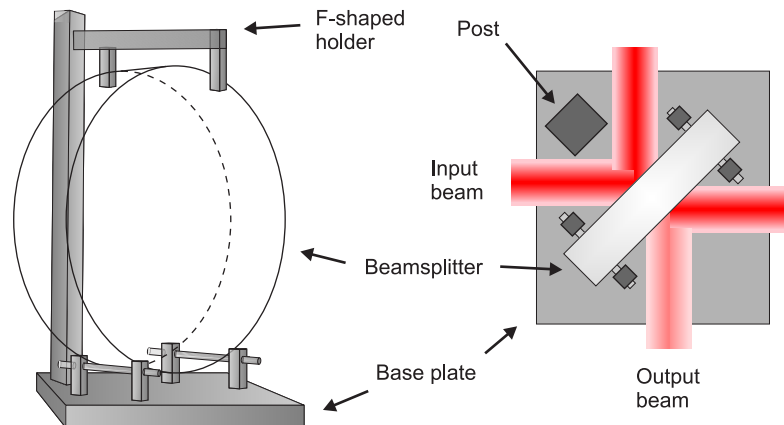
**Figure 3.22:** Schematic drawing of the lower part of the preliminary beamsplitter catcher. The top view on the right hand side shows the respective light path (the F-shaped holder has been omitted for clarity).

### 3.8.1 Pre-alignment of the beamsplitter

Two bright light sources (i.e., halogen lamps) are placed outside the view ports behind the far mirrors to pre-align the beamsplitter. A CCD camera on an adjustable post is positioned inside the beamsplitter tank in the south port. The camera is then adjusted and focused through the beamsplitter onto the 600 m distant light source behind the far north mirror **MFn**. Now the rotational stage of the beamsplitter suspension is rotated in the same way as in the main suspension case, by operating two big bolts that press against a block attached to the stack stabilizer. The rotational stage is rotated until the spot from the light source behind the far east mirror **MFe**, reflected at the beamsplitter, matches the spot from the north in yaw. By applying a differential bias current to coils No. 1 and No. 2, a defined small offset in the yaw alignment is introduced. This improves the contrast on the screen helping with the judgment for the pitch alignment and can easily be reversed. The pitch adjustment is then done via a balancing rod in the T-shaped upper mass. Finally the bias is set to zero to obtain the final pre-aligned position of the beamsplitter. By this procedure an alignment precision of 497 µrad could be achieved in pitch and 1775 µrad in yaw.

### 3.8.2 Pick-off mirrors and parasitic beams

Four beam blocks are placed in the beamsplitter tank to dump the laser beams originating from parasitic reflections at the beamsplitter (see Figure 3.23). These parasitic beams are well separated from the main beam by more than three 1/e beam radii. Figure 3.23 gives an overview of the beams that need to be blocked and of the beams that need to be directed out of the vacuum system to make them accessible for control purposes.

The beam-steering mirrors (diameter of 80 mm) are mounted on adjustable posts on the bottom plate of the vacuum tank. The beam blocks are made from Schott neutral-
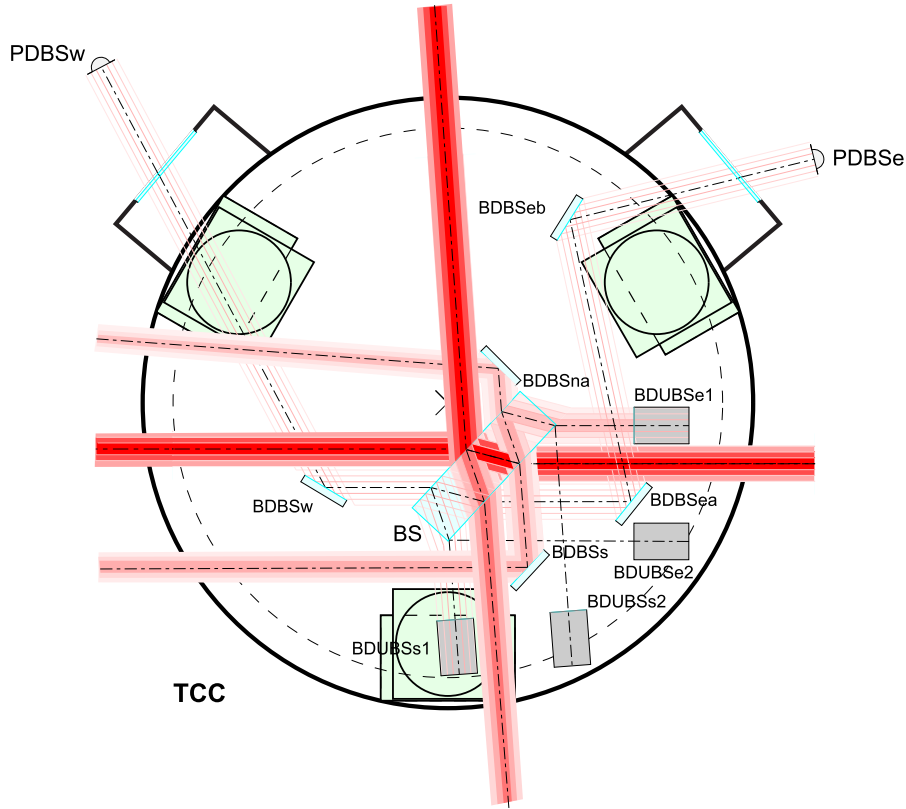
**Figure 3.23:** Optical layout of the beamsplitter tank. Several beams required for control reasons are created by internal reflections inside the beamsplitter (**BS**) substrate. These beams are picked up with the small mirrors **BDBSs, BDBSea, BDBSeb, BDBSna** and **BDBSw** and directed onto photo diodes outside the vacuum system. The blocks marked with **BDUBSx** are beam blocks that dump some beams originating from parasitic reflections inside the beamsplitter.

density optical glass filters, type NG 1 [13]. The filters are 3 mm thick, 120 mm long, and 65 mm wide. The filters are clamped onto sand blasted steel plates, that are mounted on the bottom plate. The extinction of the neutral-density filter is $10^4$ for light of a wave length of 1064 nm. Light that is scattered back from the steel plate has to pass the filter twice, leading to an extinction of $10^8$. The filters are mounted under Brewster angle with an angular precision better than $\pm 3°$. The residual light power reflection $P_{\text{refl}}$ scales with the deviation from the Brewster angle $\Phi_{\text{Br}}$ with

$$P_{\text{refl}} = \frac{1}{3} \left( \Phi - \Phi_{\text{Br}} \right)^2 \tag{3.9}$$

Thus, for a well polarized beam incident with a deviation of less than $\pm 55$ mrad ($\pm 3°$) from the Brewster angle, the residual reflectivity is less than $10^{-3}$.

---

[13]http://www.optical-filters.com/schott-ng-glass.html

Even though the beamsplitter has an extremely high-quality anti-reflective (AR) coating of about 50 ppm residual reflection at the rear surface, the light reflected from the AR coating still has, due to the high power inside the power-recycling cavity of up to 5 kW in each arm, a considerable power. The beam sent out by the pick-off mirror **BDBSs** has a power of up to 250 mW. It is used to measure the intra-cavity power, required for the automatic gain control of the power-recycling stabilization. The beam steered by **BDBSna** contains 125 mW of light power. This beam is not used at the moment but blocked outside the vacuum system. A light power of about 65 mW each is blocked at **BDUBSe1** and at **BDUBSs2**. The beam directed by the mirror pair **BDBSea** and **BDBSeb** carries the information required for the signal-recycling lock.

The beam blocks were positioned using a collimated HeNe laser beam, sent along the east tube from the east end station. The position of the beam block **BDUBSe1** and the pick-off mirror **BDBSea** were adjusted such that their shadows in the HeNe light match the 65 mm free aperture of the power-recycling reaction mass. The beam block **BDUBSs1** and the pick-off mirror **BDBSs** in the south port were adjusted such that their shadows in the HeNe light reflected from the beamsplitter match the free aperture of the gate valve between the central cluster and the signal-recycling cluster. The other pick-off mirrors were adjusted with a leveled laser pointer temporarily mounted inside the beamsplitter tank.

### 3.8.3 The compensation plate

Initially it was planned to suspend a second substrate of the same dimensions as the beamsplitter, the so-called compensation plate, in the north arm in order to compensate for the thermal lens introduced in the beamsplitter substrate. However, latest calculations indicate that a mismatch of the beam radii (and the radii of curvature of the phase fronts) caused by the thermal lens in only one arm, would harm the sensitivity of GEO 600 less than the thermo-refractive noise introduced by the compensation plate. This mismatch of the arms leads to excess light in higher-order modes at the output port of the interferometer. Due to the different beam radii at the beamsplitter, mainly $TEM_{02}$ modes contribute to this excess light. A considerable light power will leave the dark port in the final configuration, most of it being in the $TEM_{02}$ mode. However, light in higher-order modes can be rejected by the use of an output modecleaner. Appendix A gives a description of the output suspension and the output modecleaner.

## 3.9 Reaction-mass suspensions

The control scheme of GEO 600 (described in Section 1.5) necessitates a longitudinal feedback actuation at two of the four mirror suspensions. These mirrors (the inboard mirrors **MCe** and **MCn**) are locked to the free differential motion of the far mirrors to obtain the Michelson interferometer lock. As already described, a second triple pendulum is suspended 3 mm behind each inboard-mirror pendulum (see Figure 3.24), in order to apply the required feedback from a seismically isolated platform. This reaction pendulum is an exact copy of the mirror pendulum, except for the two lower masses and for the fact that the last suspension stage is realized by steel wires. The intermediate mass is
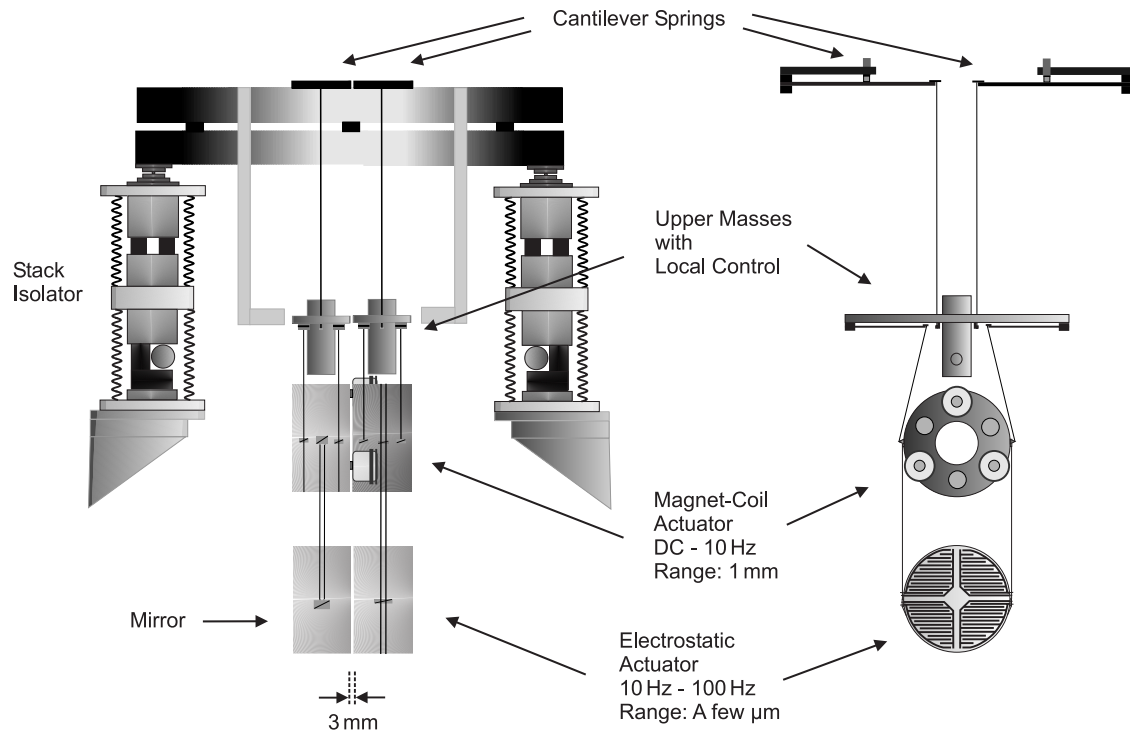
**Figure 3.24:** Schematic drawing of the GEO 600 inboard suspensions:
**Left:** The mirror triple pendulum is similar to the far mirror suspension but 3 mm behind the mirror pendulum a second triple pendulum is suspended to allow for the actuation on the mirror pendulum from a seismically isolated platform. For the low-frequency feedback a magnet-coil actuator is used at the intermediate mass while an electrostatic actuator is employed for fast feedback at the mirror itself.
**Right:** The reaction pendulum used for the inboard suspensions. The intermediate reaction mass supports the three coils for the magnet-coil actuators. The lowest mass carries the electrostatic actuator. It is made from fused silica with an on-coated comb-like gold pattern, forming four independent capacitors.

made from aluminum and supports three coils. To compensate for the mismatch in the mass distribution, three stainless-steel balancing rods are incorporated in the intermediate mass. The mass is suspended by four steel wires of 274 µm diameter that are clamped to the intermediate mass. The three coils match three magnets, 3 mm in diameter and 3 mm thick, bonded with Vacseal® onto the intermediate mass of the mirror pendulum. This intermediate-mass magnet-coil actuator is used for the slow longitudinal feedback from DC to about 10 Hz with a dynamic range of a few hundred µm.

## 3.9.1 The electrostatic actuator

The lower mass is suspended by two steel-wire loops of 174 µm diameter from the intermediate mass. This lower mass has a gold pattern coated onto the side that faces the mirror. The pattern is separated into four quadrants, each consisting of two comb like, interleaving patterns. Thus, four independent capacitors are formed. The two plates of

each capacitor lie in one common plane. Since the electric field has only a normal component at the surface of the capacitor plates, the electric field of the capacitor has a strong gradient along the normal of the reaction mass. If the mirror is brought into the capacitor's field, it consequently always experiences an attractive force. To enable control of the mirror in push and pull, a bias voltage of 500 V is applied to the electrostatic actuator. The electrostatic actuator is used for the fast feedback from 10 Hz to 100 Hz. A further increase of the unity gain frequency of the longitudinal servo might be implemented on the long term. The actuation range of a few μm proved to be sufficient to acquire a lock of the Michelson interferometer using only the two electrostatic actuators. After the lock lasted for 200 ms the intermediate mass actuator is switched on, extending the lock over longer periods of time.

Both the intermediate reaction mass and the electrostatic actuator are protected from falling, in case a wire breaks, by rods that extend from the mirror catcher, which is described in detail in Section 4.3 .
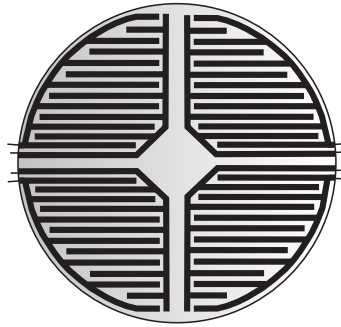


**Figure 3.25:** The electrostatic actuator used for the fast feedback at the mirror itself. The electrostatic actuator has eight comb-like interleaving patterns coated onto its front side. These patterns form four capacitors which can independently be charged with high voltage.

### 3.9.2 Alignment of the reaction masses

The force of the electrostatic actuator on the mirror falls off with the cube of the distance between the two masses. Hence, the masses should not only be suspended as close together as alignment considerations allow, but also need a precise alignment to the mirror. Any misalignment weakens the actuator due to the required orthogonalization of the quadrants. The relative alignment of the electrostatic actuators to the mirrors is also done with the autocollimator. The cross hair reflected by the mirror can clearly be distinguished from the one reflected by the reaction mass by manually moving the one or the other pendulum. A balancing rod at the upper mass of the reaction pendulum is used to overlay the two cross hairs for the pitch alignment. For the yaw alignment of the electrostatic actuator relative to the mirror, the upper cantilever springs have to be moved *in situ* with the pendulum suspended. The relative pitch alignment is achieved using the balancing rods in the intermediate reaction mass and the balancing rod in the

vertical bar of the T-shaped upper mass. The use of both balancing systems allows a better simultaneous match of all actuator stages. This can be accomplished by the introduction of a differential pitch between the upper mass and the penultimate mass, if needed.

Another important aspect is the separation between the reaction masses and the mirrors. In order to obtain a similar calibration for the two electrostatic actuators, the gaps between the actuators and the relevant mirrors have to have a similar width. Since the force of the electrostatic actuator scales with the cube of the distance to the mirror, the separation accuracy requirement is demanding. The electrostatic actuators are calibrated by applying a test signal at 281 Hz to only one actuator. The resulting length change of the relevant interferometer arm leads to a shift of the resonance frequency of the power-recycling cavity. Since the second modecleaner is slaved to follow the laser frequency, the resulting frequency change can be read out in the previously calibrated feedback spectrum of **MMC2b**. Since the electrostatic actuator for the east inboard mirror **MCe** was found to be weaker than the one for **MCn**, a small longitudinal offset was applied via the local-control actuators to the east reaction pendulum. The new calibration yields a difference in force of the two electrostatic actuator by less than 5%. This translates into a separation difference of less than 50 μm.

## 3.10  Preliminary output optics

The laser light leaving the interferometer through the dark port is picked up on the detection bench by a photo diode for the control of the differential stabilization (interferometer lock) and by a CCD-camera for the visualization of the output mode shape. Directing the light toward the detection bench requires a beam steering mirror in the output tank **TCOb**. Since the mirror is hit under 45 ° and the beam radius is $w_z \geq 9$ mm at this place, the beam steerer has to have a diameter of at least 80 mm to allow for a reflection of $3 \cdot w_z$. Hence, the 90° beam-steering mirror **BDO3** that is foreseen to be used in the final output telescope is already employed to accomplish this task. The mirror has the same dimension as the modecleaner mirrors: 100 mm diameter, 50 mm thick, weighing 864 g. It is mounted on a sturdy post, clamped to the bottom plate of the vacuum tank. The mirror is adjusted such that the laser beam leaves the vacuum system under an angle of about 4°. This small angle leads to a separation of the beam reflected back from the AR-coated view port and the original beam of 15 cm at the beam steerer. Thus, the reflected beam can be blocked behind the mirror by a Schott NG 1 neutral density filter, mounted under Brewster angle. A well defined blocking of the reflected laser power is essential to avoid any stray light that could possibly scatter back into the interferometer. Figure 3.26 shows the described optical paths. For further reading on the blocking of parasitic beams inside the UHV system see Section 3.8.2 .

The full description of the final output optics and the required suspension systems is given in Appendix A.
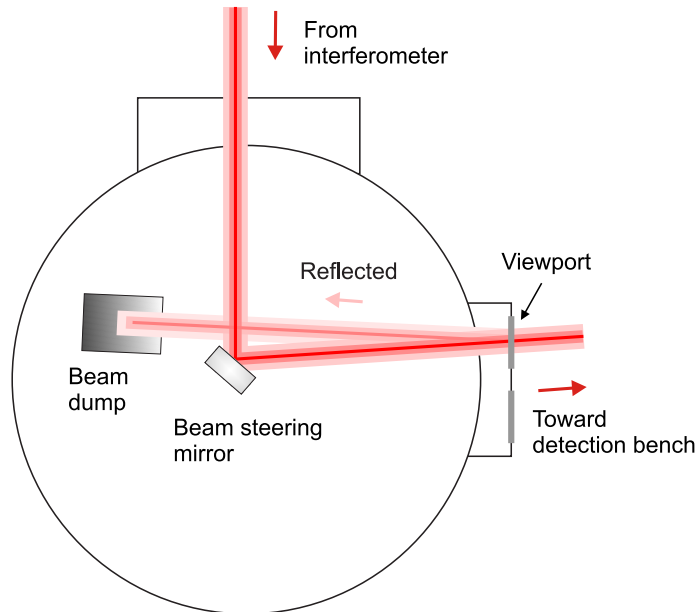
**Figure 3.26:** Currently installed output optics. The light reflected by the AR-coated view port is blocked by a NG 1 neutral density optical filter, which is installed under Brewster angle to avoid any stray light.

## 3.11 Long-term analysis of the test-mass suspensions

The position and orientation of the suspended test masses are, due to various reasons, subject to certain drifts. The fluctuations on times scales shorter than a few seconds are dominated by either seismic, electronic, or thermal noise. On longer time scales, however, environmental influences like the temperature dominate the drift of the test masses.

While the pitch, yaw, and longitudinal [14] degrees of freedom are automatically controlled to maintain the interferometer alignment, others are left to drift. Understanding and consequently reducing the drifts in all degrees of freedom decreases the demands on the alignment control. As will be explained even a direct influence on the detector sensitivity can arise from the drift of the roll alignment.

The data used for this analysis were acquired during the 14 days long second participation phase of GEO 600 in the scientific data run S3 (in the following referred to as S3 II). The remarkable duty cycle of about 97% previously achieved during the S1 run, was further improved to 98.8%. Losses of lock triggered by seismic events were, e.g., due to an earthquake of magnitude 6.4 in New Caledonia or a truck passing nearby one of the end stations of GEO 600. In addition, as the detector sensitivity was substantially improved during the last months of 2003, measurements of some aspects of the suspension systems that were previously not possible, could be performed during the S3 II run. The

---

[14]The inboard mirrors are controlled to follow the longitudinal motion of the far mirrors at frequencies up to 100 Hz. The lower frequency feedback up to 10 Hz is provided by the magnet-coil actuators at the intermediate masses. In order to reduce the DC load of this actuator, the local control actuators of the far suspensions are used to compensate for long-term drifts.

permanent monitoring of the drift of the violin-mode frequencies, presented in Section 5.8 was, for example, used to obtain the roll alignment drift, which in turn allowed for an estimation of the vertical drift.

### 3.11.1 Vertical alignment drift

Temperature changes cause not only thermal expansion but moreover a change of the Young's moduli of the materials used for the suspension systems. The latter fact generates a coupling of the temperature to the test-mass position and orientation via all materials under tension. More precisely speaking, the coupling arises by the temperature dependent relative change of any elongation, deflection, or compression that is caused by an external force. The deflection of the loaded upper cantilever springs is, e.g., 11 cm, while the elongation of the loaded suspension fibers is only of the order of 1 mm. Since the temperature dependence of the Young's moduli for both materials differs by only about 25%, the effect from the coupling of the cantilever springs to temperature changes is much stronger.

As a consequence, the vertical alignment drift is expected to be dominated by the thermal dependence of the deflection of the cantilever springs. Due to the better air conditioning of the central station, the far suspensions are subject to much greater temperature changes than the inboard suspensions. Hence, the far suspensions are more likely to reveal temperature dependent drifts while the inboard suspension fibers may be dominated by effects that less strongly depend on the temperature. In the following the drift of the vertical alignment is discussed at the example of the far north suspension.

The deflection $\lambda$ of the upper cantilever springs was calculated in Section 3.6.4 using

$$\lambda = \frac{4\,mg\,l^3\,\alpha}{E\,a\,h^3} \tag{3.10}$$

From the parameters of the upper cantilever springs given in that section, the deflection was calculated to be about 11 cm. This formula is now used to derive the temperature dependence of the cantilever spring deflection, based on the value for the temperature dependence of the Young's modulus for Marval 18, previously measured by [Braccini '00]. The reported value was obtained by measuring two vibrational-mode frequencies and a torsional-mode frequency versus temperature.

The temperature dependence was measured to be

$$\frac{dE/dT}{E} = -2.54 \cdot 10^{-4}\,\mathrm{K}^{-1} \tag{3.11}$$

Inserting this value along with the parameters of the upper cantilever springs into Equation (3.10) yields a deflection change of

$$\delta\lambda = 28 \pm 3\,\mathrm{\mu m\,K}^{-1} \tag{3.12}$$

The error arises from the actual static deflection of the cantilever springs, which is not known to high precision.
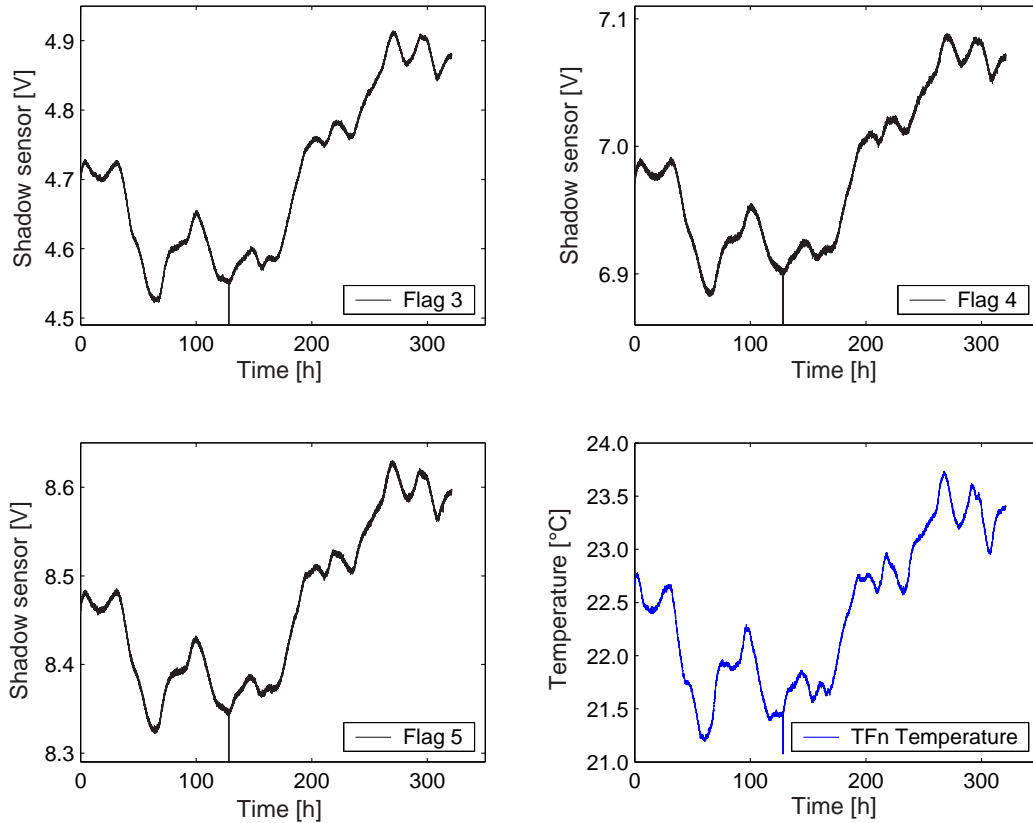
**Figure 3.27:** Vertical drift of the far north suspension over S3II due to temperature. Displayed are the signals from the three shadow sensors above the upper pendulum mass and the respective temperature characteristic measured at the far north tank (lower right graph). It is evident that the whole suspension is raised and lowered with temperature. A higher sensors output correspondes to a lowering of the respective flag position.

The differential motion between the coil holder supporting the shadow sensor, and the upper pendulum mass due to thermal expansion is given by the CTE of the materials used. Since the CTE of these materials is only of the order of $10^{-5}\,\mathrm{K}^{-1}$ and furthermore the material of the upper suspension wires has a similar CTE as the coil holder material, no considerable differential effect occurs.

The signals of the three upper shadow sensors (No. 3, No. 4, and No. 5, referring to Figure 3.6.3) of the far north suspension were used to obtain the deflection change of the upper cantilever springs with temperature. These sensors sense the position of the flags mounted on top of the upper mass. Consequently, pitch, roll, and vertical fluctuations show up in these three sensor channels. Since no alignment control is implemented for the roll or vertical degree of freedom and the calibration of the sensors is know to change with time [15], no calibration of the sensor No. 5, can be obtained. Thus, the absolute value

---

[15]The observed calibration changes are due to individual degradations of the output of the shadow sensors, as is described in Section 3.6.3.

of vertical motion of the pendulum can, based on the known facts, only be estimated.

Figure 3.27 shows the signals of the three shadow sensors on top of the upper mass along with the temperature measured at the respective vacuum tank **TFn**. The coherence of the signals is evidently due to a rising and sinking of the whole pendulum with temperature. The different scalings of the sensor outputs are due to the different calibrations of the sensor and to the superimposed roll and pitch motion. The roll alignment is is not directly revealed due to the aforementioned lack of calibration of sensor No. 5. The measurements discussed in Section 3.11.3 and Section 5.8 allow, however, to set an upper limit to the actual roll alignment drift. This limit corresponds to a height change of $\pm 12\,\mu$m (for $\delta T = 2.45\,$K) for either of the respective flag positions. Based on this limit, the known calibration of the sensors No. 3 and No. 4, and the actual pitch alignment drift (derived from the calibrated spot position measurement, shown in Figure 3.17, to be $\pm 1\,\mu$rad), the vertical motion can be estimated to be $22 \pm 8\,\mu$m K$^{-1}$. The result is, if somewhat low, in agreement with the calculations.

### 3.11.2 Pitch alignment drift

A mismatch of the spring constants $\kappa$ between the cantilever springs attached to the front and rear side of the upper mass translates to a temperature depended pitch alignment of the mirrors via the temperature dependence of $\kappa$ (itself depending on the Young's modulus). Due to the observed mismatch of the lower cantilever springs of $\pm 3\,$mm, a differential deflection of up to $1.6\,\mu$m K$^{-1}$ may arise. With the geometry of the upper mass (separation of the small cantilever springs of $6\,$cm) this translates into a pitch misalignment of up to $26\,\mu$rad K$^{-1}$.

Figure 3.28 shows the calibrated pitch feedback applied to the far north suspension during S3 II along with the temperature as recorded in the respective end station. A correction equivalent to $68\,\mu$rad$_{\mathrm{pp}}$ was required to maintain the pitch alignment within $\pm 1\,\mu$rad during the $330\,$h measurement period. This translates into a drift of $28\,\mu$rad K$^{-1}$, slightly higher than the assumed maximum value.

The superimposed oscillation with a period of about $12\,$h $25\,$min is due to the earth tides as discussed in Section 3.11.4 .

### 3.11.3 Roll alignment drift

While the differential deflection of the upper cantilever springs dominates the roll alignment of the upper mass, the lower cantilever springs can cause a differential roll drift between the upper mass and the two lower masses. Although there is no direct measure for this kind of alignment drift in GEO 600, strong evidence was found in the violin-mode frequency drift of the far north suspension fibers (please see Section 5.8). These violin-mode frequencies were found to drift with the temperature characteristic of the respective end station but in different directions and with different drift rates. As is described in Section 5.8, this effect can be explained by a drift of either the pitch or the yaw alignment.

The pitch alignment of the mirror is maintained by the automatic drift control. Since the required actuation is applied at the upper mass, no pitch drift of the penultimate mass is possible.
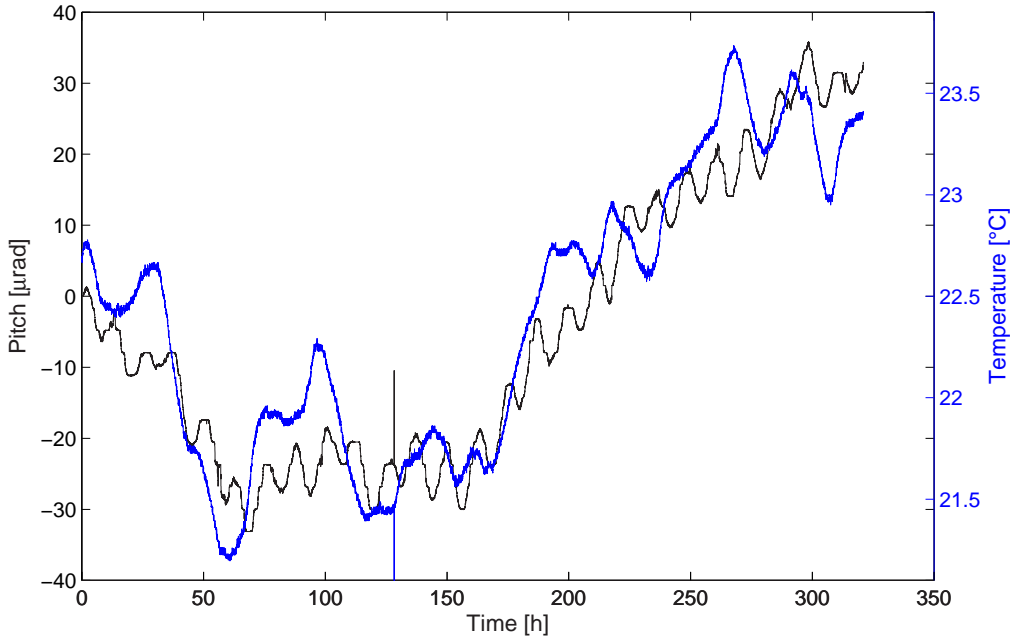
**Figure 3.28:** Pitch alignment feedback signals applied to **MFn** during S3 II.

The roll alignment in contrast is not controlled, and thus free to drift. The actual drift of the upper mass can, due to the aforementioned lack of calibration of the shadow sensor No. 5 and the superimposed signals for vertical and pitch, not be worked out directly. The differential roll alignment between the upper mass and the two lower masses is also not directly accessible.

The maximum differential deflection between the upper cantilever springs as calculated from the observed mismatch of $\pm 5\,\mathrm{mm}$ can be taken from Equation (3.12) to be $6\,\mu\mathrm{m\,K^{-1}}$. This translates into a roll drift of up to $100\,\mu\mathrm{rad\,K^{-1}}$. The maximum differential deflection of the small cantilever springs was given in the above section to be $1.6\,\mu\mathrm{m\,K^{-1}}$, corresponding to a roll drift of $20\,\mu\mathrm{rad\,K^{-1}}$.

From the mirror's geometry, formula 5.44, and formula 5.8 it can be calculated that the observed drift of the violin-mode frequencies requires a roll drift of $190\,\mu\mathrm{rad_{pp}}$, or $75\,\mu\mathrm{rad\,K^{-1}}$. This effect can readily be explained by the interplay of mismatches of the upper and lower cantilever springs.

A further explanation for roll drift lies, however, in the installation of the monolithic stages. Besides the spring constant also the static deflection is of relevance for the temperature dependence of the deflection (Equation (3.10)). The mismatch in deflection between the lateral spring pairs does not solely originate from an initial mismatch of the cantilever springs but was partially introduced by the installation of the last suspension stage. Such a deflection mismatch can be introduced by an initial static differential roll misalignment between the lower two masses and the upper mass. Since the handling of the monolithic suspension stages is rather delicate, every action has to be evaluated

in terms of risk versus gain. The *in situ* correction of the residual roll misalignment of the monolithic stage is in particular regarded a high risk operation. Thus, the roll misalignment was only roughly corrected for.

### 3.11.4 Longitudinal drift

The drift of the suspended masses along the optical axis is caused by different influences. In order to obtain information about the longitudinal alignment drift, the calibrated shadow sensors No. 1 and No. 2 were used. The longitudinal long-term drift of the north arm of the interferometer is controlled via the two magnet-coil actuators according to these shadow sensors. The control is done such that the offset current through the intermediate mass actuators at the inboard suspensions, required to maintain the interferometer locked to its operating point, is kept close to zero. As a consequence, the far north mirror is forced to follow the longitudinal long-term drift of the north inboard mirror.

A longitudinal drift may arise, e.g., from changes of the air pressure, coupling to the position of the vacuum tanks. The tanks are anchored to the ground and attached to the vacuum tube via flexible bellows such that, for an ideally symmetrical configuration, the air pressure would not exert a static force on the tanks themselves. Any deviation from a symmetrical configuration leads, however, to a net force on the respective tank.
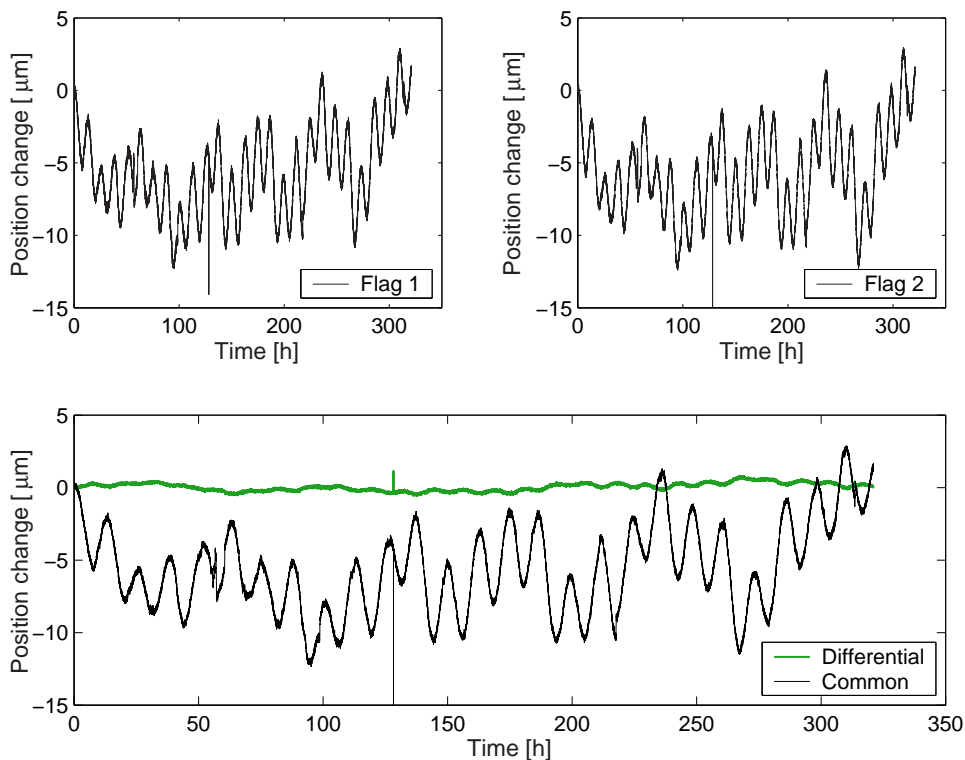


**Figure 3.29:** Calibrated signals of the shadow sensors No. 1 and No. 2 (upper graphs) along with the derived contributions for longitudinal and yaw alignment (lower graph).

Since the static force on the anchors is about 2800 kg even small asymmetries can lead to considerable forces on the tanks. Thus, changes of the air pressure can couple to the longitudinal position and the yaw orientation of the test masses.

A second influence arises from the earth tides, which cause a periodic longitudinal and rotational drift of the test masses, modulated by the relative position of the sun (or the moon phase). Tidal forces cause a common-mode effect of the inboard and the far mirror. While the motion inboard mirror follows the tidal force, the motion of the far mirror follows the inboard mirror at very low frequencies. Hence, the flag positions of the **MFn** suspension reveal the longitudinal effects from the north inboard mirror and the effect of air pressure changes on both respective tanks.

Figure 3.29 shows the signals of the flag-position sensors No. 1 and No. 2. By taking the sum or the difference of the signals, the common-mode signal (longitudinal) or the differential-mode signal (yaw) of the two sensors were derived. These signals are displayed in the lower graph.
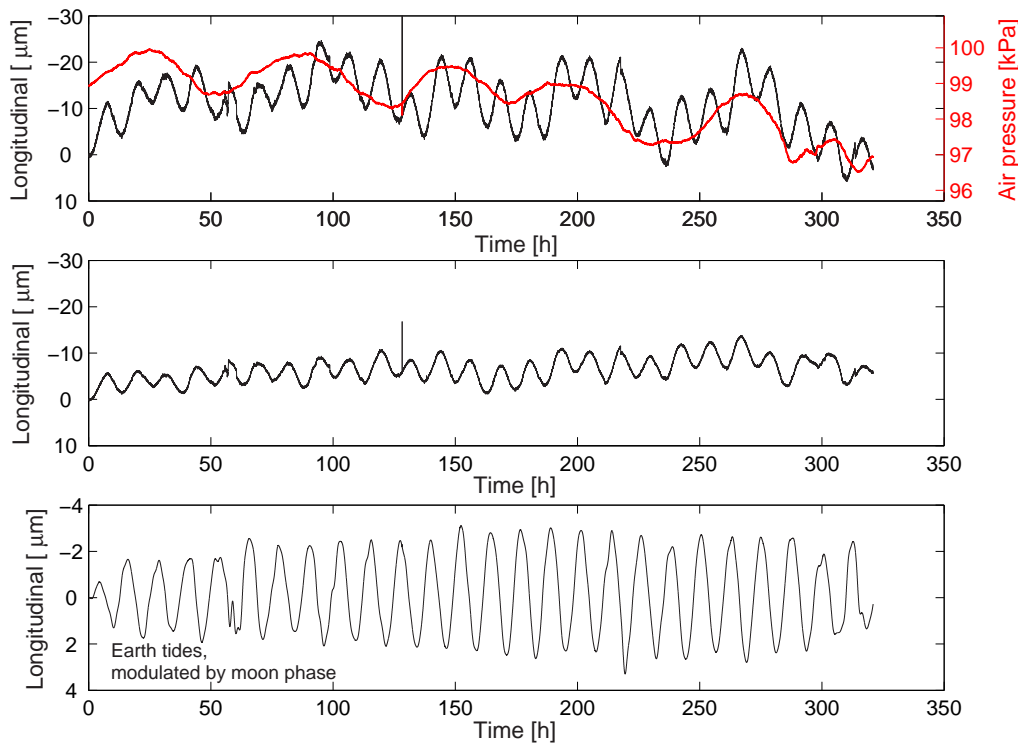


**Figure 3.30:** Longitudinal alignment drift of **MFn** as derived from the flag signals. The upper graph shows the alignment drift along with the air pressure change (in order to facilitate the comparison, the left y-axis was inverted). The middle graph shows the alignment drift after subtracting the effect due to the air pressure. The lower graph eventually displays a (numerically) band-pass filtered version of the middle graph. The strong modulation is caused by the earth tides, amplitude modulated by the moon phase. Due to the spring tide at January 7th the amplitude modulation passed its maximum at hour 192.

The upper graph in Figure 3.30 shows the derived longitudinal signals along with the measured air pressure. As expected, the pressure is of noticeable influence on the alignment. The middle graph of Figure 3.30 displays the longitudinal motion after subtracting the air pressure effects. In order to accentuate the strong remaining modulation, the signal was numerically band-pass filtered (lower graph). The modulation is caused by the earth tides, itself amplitude modulated by the relative position of sun and moon (or the moon phase). This amplitude modulation of the earth tides passed through its maximum due to the spring tide (full moon at the 7th of January at 15:31 MEZ) at hour 192.

### 3.11.5 Yaw alignment drift

The long-term yaw alignment drift is controlled via the local-control coils No. 1 and No. 2. The measure for the actual deviation from the setpoint is the position of the laser beam, measured behind **MCn**. This measurement employs a position-sensitive quadrant photo diode. The same kind of measurement is performed behind the far mirrors to obtain control signals for an actuation on the beamsplitter and the inboard mirrors, keeping the laser beam centered on the far mirrors. As a result, the far mirrors are not forced to follow any other pendulum's drift. The feedback signals hence reveal the drift of the pendulum with respect to the interferometer, while the flag signals include only the common drift of the suspension together with its support structure.
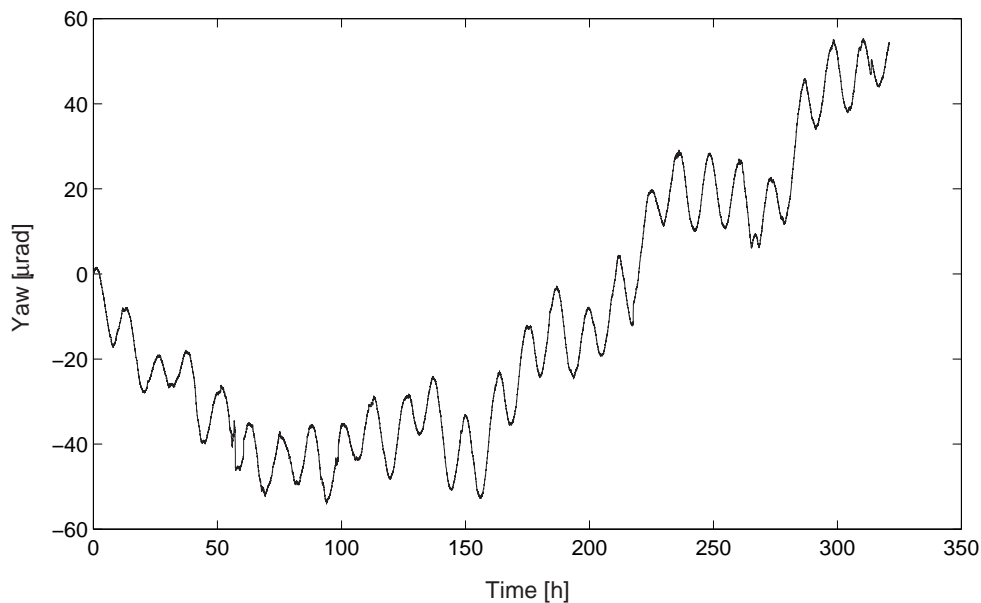


**Figure 3.31:** Yaw alignment feedback of **MFn** in µrad. The strongest contribution on time scales of a days is due to the earth tides. On longer time scales clearly the temperature change dominates the drift. A contribution from the air pressure changes can also clearly be seen.

The consideration of influences on the yaw alignment follows an argument similar to that used for the longitudinal drift. Figure 3.31 shows a times series of the yaw feedback applied to far north suspension. As the longitudinal feedback it is dominated by the earth tides on short time scales of the order of a day. On longer time scales the yaw feedback follows, however, the temperature characteristics, modulated by the air pressure changes (please see Figure 3.30 for the the air pressure changes).

### 3.11.6 Sideways drift

Eventually a brief description of the sideways drift observed during the S3 II run shall be given. Besides the local-control damping at the upper pendulum mass, there is no active control of the sideways motion of the suspended test masses. As a consequence, the motion of the pendulum with respect to the tank is directly visible in the signal of the respective shadow sensor. On the other hand, no calibration of the sideways shadow sensor, sensor No. 6, can be obtained due to the lack of feedback (and measure). Figure 3.32 displays the signals of the shadow sensor No. 6 for the two far suspensions along with the temperature as recorded in the respective end stations. A possible reason for the observed correlation of the sideways drift with the temperature lies in a potential mismatch of the stacks' vertical spring constants. The spring constant was given in Section 3.2 to be $\kappa = 1.25 \cdot 10^5 \, \mathrm{N \, m^{-1}}$. Via the thermal dependence of the resulting compression of the stacks, the support structure can be subject to a temperature dependent tilt, leading to, e.g., sideways motion of the suspended mass.

### 3.11.7 Lessons learned from the drift analysis

Although the automatic alignment and drift control of GEO 600 can correct for the described alignment deviations in the controlled degrees of freedom, a reduction of the drifts could help in lowering the demands on the alignment system. Furthermore, the drift of the roll alignment is of direct influence on the detector sensitivity. Any alignment drift
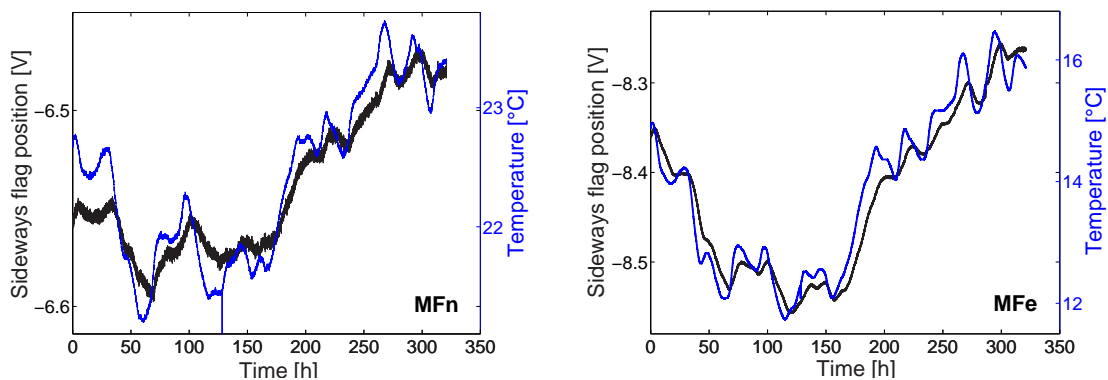


**Figure 3.32:** The shadow sensor signals for the sideways motion of both far suspensions as recorded during S3 II. The graph to the left shows the motion of the far north suspension with the respective temperature, while the graph to the right shows the motion and temperature for **MFe**.

in this degree of freedom causes an alteration of the violin-mode frequencies. The peaks in the error-point spectrum caused by the violin modes have a natural linewidth of the order of 1 mHz due to the high mechanical $Q$ of the violin modes [16]. The detector sensitivity can, however, be spoiled over a much greater frequency band by the drift of the violin-mode frequencies.

The coupling of the position and orientation of the suspended masses to temperature fluctuations can be reduced by a better initial matching of the cantilever springs. This can be done by a thorough pre-selection and the adaption of the spring constants, where required. The use of a clamp library containing an assortment of wedged base clamps as planned for Advanced LIGO (Section 3.6.4.1) reduces, however, only thermostatic effects but does not decrease the temperature coupling. A better solution would be the use of a library of wire clamps of different lengths to adapt the length of the cantilever springs instead of the mounting angle. Changing the length of the spring, leads to a change of the effective spring constant $\kappa$, which is the relevant parameter for the thermal coupling.

Since no work on the already installed cantilever springs is possible, a better temperature stabilization of the end stations would be desirable for GEO 600 in order to facilitate the active alignment control. A better temperature control would also decrease the thermal drift of the violin-mode frequencies due to the temperature dependence of the fiber material's Young's modulus (see Section 5.8). Both the reduction of roll alignment drift and thermal drift of the violin-mode frequencies themselves lead to a direct improvement of the sensitivity of GEO 600, when integrated over long periods of time.

## 3.12 The test-mass suspensions of the operating interferometric gravitational-wave detectors

A short introduction to the test-mass suspensions of LIGO and TAMA300 is provided in this section, to allow for a comparison with the relevant GEO 600 suspensions. Since only LIGO, TAMA300, and GEO 600 acquired scientifically relevant astronomical data so far, only the suspensions of these three detectors can be found in this section. For this reason the Virgo suspensions are described under "Future perspectives" (Section 3.13.1), although the installation of test mirrors has recently been finished. Table 3.10 gives a short overview of the relevant suspension properties for GEO 600  LIGO, and TAMA300.

### 3.12.1 LIGO

As the GEO 600 mirrors, the test masses of the three LIGO detectors in the USA are made of fused silica. Having a diameter of 25 cm and being 10 cm thick, they weigh 10 kg each. The test-mass suspensions are mounted on top of isolating tables that contain three spring stages and thus provide a $f^{-6}$ isolation above the resonance frequencies $(1 - 14\,\text{Hz})$. The test masses are suspended as single pendulums in one steel-wire loop. Break-off-position defining glass rods are attached a few millimeters above the COM to ensure the stability of the suspended mess. Steel music wire with a diameter of 300 μm (40% yield load) was used for the suspension. The length of the pendulum is 450 mm

---

[16] Although damped, as described in Chapter 5, the violin-mode $Q$'s are still of the order of $10^6$.

|  | GEO 600 | LIGO | TAMA300 |
|---|---|---|---|
| Suspension type | Triple pendulum | Single pendulum | Double pendulum |
| Length | 880 mm | 450 mm | 435 mm |
| Last stage | 4 Silica fibers | 1 steel wire loop | 2 tungsten wire loops |
| Test mass | 180 mm diameter 5.6 kg | 250 mm diameter 10 kg | 100 mm diameter 1 kg |
| Actuation | MCD at the upper and penultimate mass. ESD at the test mass | MCD at the test mass | Eddy-current damping at the upper mass. MCD at the test mass |
| $Q$ | $> 10^8$ | $4 \cdot 10^5$ | $5 \cdot 10^5$ |

**Table 3.10:** The relevant properties of the test-mass suspensions of GEO 600, LIGO, and TAMA300. ESD stands for electrostatic drive, MCD for magnet-coil drive. The use of a MCD at the test mass requires bonding of magnets onto the mirror, thus degrading the internal mechanical quality factor (not given here).

from the suspension point to COM of the test mass. The resonance frequencies of the single pendulum are 0.74 Hz for the pendulum mode, 0.5 Hz for the yaw mode, 0.6 Hz for the pitch mode, 12.8 Hz for the bounce mode, 18 Hz for the roll mode, and 336 Hz for the fundamental violin mode. The mechanical quality factors of these modes have been measured to be of the order of $Q \simeq 2 - 4 \cdot 10^5$. [Romie, Shoemaker '04]

The local control, required to damp the eigenmodes of the pendulums, is performed at the test masses themselves. Hence, four magnets for the magnet-coil actuators had to be attached to the rear surface and to the sides of the test masses via metal standoff plates. The application of the longitudinal feedback signals is also done via these magnet-coil actuators.

An advantage of this straightforward suspension and control conception is the possibility to suspend a mirror in only one wire loop. Thus, both the pitch mode frequency and the coupling of seismic noise to the pitch motion are reduced. However, a reduction of the influence of the local-control sensor and actuator noise can be achieved by suspending the mirror in a multiple pendulum system and sensing and actuating at one or more stages away from the mirror. This low-noise control scheme necessitates more than a single wire loop for the suspension of each of the masses below the one at which the actuation is applied, since a finite wire separation along the longitudinal direction is required to force the mirror to follow the pitch orientation of the mass(es) above. Controlling the uppermost mass of a quadruple pendulum is planned for Advanced LIGO as is described in Section 3.13.2. For a further noise reduction it is foreseen for Advanced LIGO to (at least partially) reduce the local control gains, once the cavities are stabilized.

### 3.12.2 TAMA300

The test masses of TAMA300 are suspended as double pendulums using tungsten wires. The first isolation stage is realized by a three-stage passive stack isolator system that supports the actual suspension. Eddy-current damping of the pendulum modes is employed at the upper suspension stage. The required magnets are supported by flexible stainless steel rods in order not to excite the upper mass at the observation band. This stage consists of an aluminum block of 1.29 kg (80 mm by 100 mm by 60 mm), suspended by four tungsten wires. Tungsten was chosen to avoid interaction of the wires with the damping magnets. The wire diameter is 100 μm, which results in 33% breaking load. The length of the stage is 185 mm. The upper stage is suspended from steel bellows with a spring constant of $500\,\mathrm{N\,m^{-1}}$, providing additional vertical isolation. Unlike done for the GEO 600 suspensions, in TAMA300 all masses are suspended in the COM (referring to the vertical direction). The mirrors have 100 mm diameter, are 60 mm thick, and weigh 1.034 kg. Each mirror is suspended from its upper mass by two loops of tungsten wire with a diameter of 50 μm (50% breaking load). The fundamental violin-mode $Q$ of the wires was measured to be $2.5 \cdot 10^5$ [Arai]. With a length of 250 mm for the lower stage, the overall suspension length is 435 mm.

Due to the previously experienced large pitch fluctuations of the suspended masses, the suspension system had to be modified by reducing the upper wires' separation from 9 cm to 2 cm. This alteration led to a decrease of the pitch frequency from 5 Hz to 1.8 Hz [Takahashi '02]. Furthermore each suspension system, including the stack system (overall about 1500 kg), is now mounted on top of four pneumatic actuators each, providing active seismic isolation.

Picomotors, incorporated at the upper suspension point, control the pre-alignment of the optics in five degrees of freedom. The longitudinal control and the fast alignment control of the mass is done by using magnet-coil actuators at the mirror itself. Hence, four magnets had to be glued to its rear surface.

The implementation of an X-pendulum above the existing double-pendulum suspension was initially planned for TAMA300 but has been abandoned. Instead an upgrade to the so-called TAMA SAS (Seismic Attenuation System) is planned to be started in 2005. The SAS consists of an three-leg inverted pendulum that supports a top mass. This mass has a series of monolithic geometrical anti-spring filters (MGASF [Bertolini '99]) incorporated in order to provide vertical isolation for the subsequent triple pendulum. The lower two stages remain basically as before but will be suspended from a third bigger mass. [Màrka '02]

Upgrading the isolation system by using monolithic suspensions is, however, not foreseen for TAMA300. Instead it is planned to utilize monolithic suspension at cryogenic temperatures for the follow-up project LCGT (see Section 4.7.3).

## 3.13 Future perspectives

Among the two major challenges for the next generation of earth-bound interferometric gravitational-wave detector are:

1. Increase the sensitivity in the frequency band of the already existing detectors

2. Enlarge the bandwidth to the low frequency side

Both objectives set very demanding requirements on the suspension system of future detectors. In order to accomplish these high requirements a suspension design based on the existing main suspensions of GEO 600 will be used for the next generation detector Advanced LIGO in the USA.

The suspension system employed for the French–Italian detector Virgo allows for a strong attenuation of the seismic at very low frequencies by using an inverted pendulum and a multiply cascaded pendulum suspension.

### 3.13.1 Virgo

The seismic isolation system of the 3 km Virgo interferometer is based on the so far most complex suspension system, the so-called super attenuator [Braccini '02]. The objective is to achieve a thermal-noise-limited displacement sensitivity of the interferometer above 4 Hz up to a few tens of Hz.

The first horizontal isolation stage is realized by a 6 m tall inverted pendulum. The inverted pendulum is damped with three magnet-coil actuators at the resonance frequency of 30–40 mHz. From the top of this isolator a chain of six filter stages is suspended. Each of the upper five filter stages consists of a drum-shaped mass (100 kg) made from stainless steel, suspended from a single high tensile C 85 steel wire. A set of cantilever springs, made from Marval 18 maraging steel, is clamped to the outer circumference of the lower side of the steel mass. These springs provide vertical elasticity of the suspension showing, however, intolerable resonance frequencies around 7 Hz. As a consequence, a magnetical anti-spring system had to be employed at each filter stage to lower the resonance frequencies below 2 Hz.

The lowest filter stage, supporting the test mass, is realized by the so called marionetta. The marionetta can be steered in all degrees of freedom via magnet-coil actuators. The coils are attached to a rigid frame, extending from the last filter stage. The test mass itself is suspended by two C 85 steel wire loops from the marionetta. The loops are separated by 5 cm, forming a pendulum length of 70 cm. The mass has a diameter of 35 cm, is 10 cm thick, and weighs 21 kg. The wires have a diameter of only 200 μm, corresponding to a breaking load of about 60%. Four magnets are glued to the rear surface of the mirror to allow for longitudinal feedback via magnet-coil actuators. The coils facing the magnets are supported by a reaction mass that is as well suspended from the marionetta. Figure 3.33 shows a schematic drawing of the super attenuator.

The use of monolithic test-mass suspensions is foreseen for Virgo [Amico '02]. The 21 kg test masses shall be suspended by four silica fibers of 300 μm diameter. This corresponds to a breaking load of 15%. However, as a consession to the technical difficulties in
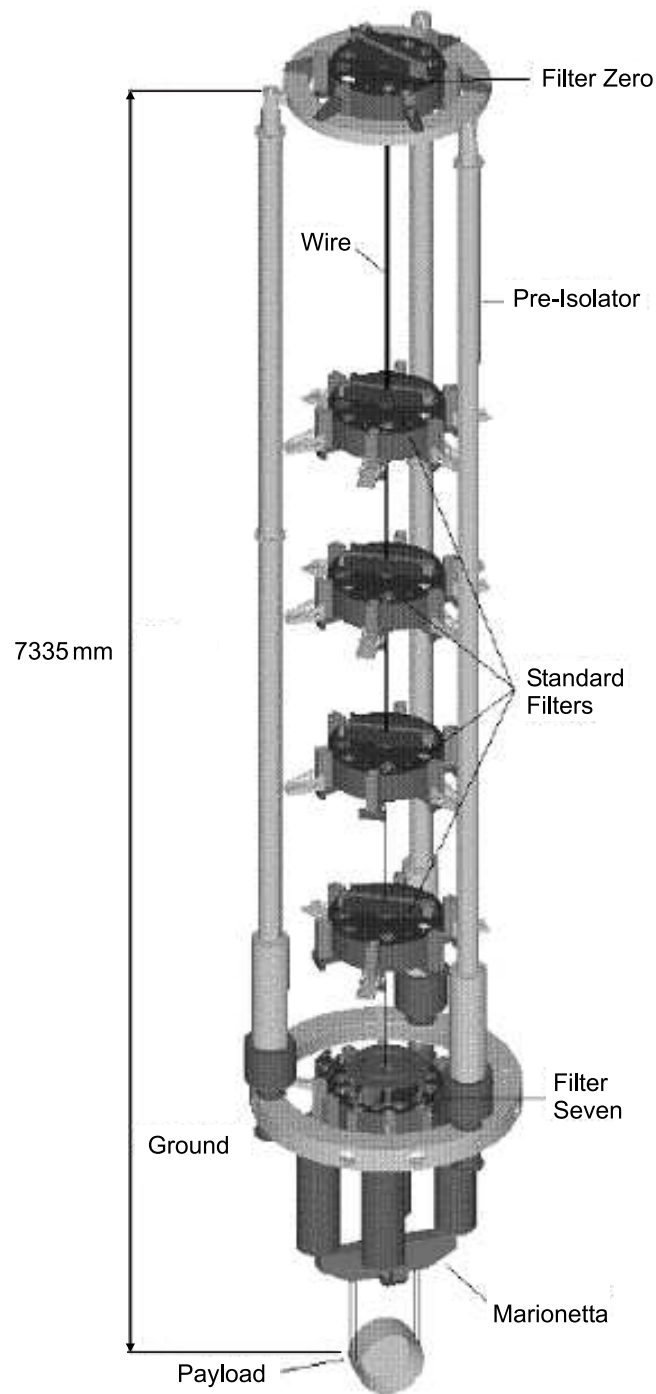
**Figure 3.33:** The Virgo super attenuator. A 6 m tall inverted pendulum supports the suspension point for a six-stage pendulum. Each stage (100 kg), suspended by a central steel wire, incorporates a cantilever-spring stage to improve the vertical isolation performance.

the realization of these fragile systems, the utilization of monolithic suspensions for Virgo has been postponed. Thus, the monolithic suspensions installed in GEO 600 will remain the only ones incorporated in an interferometric gravitational-wave detector for the next few years, possibly until the suspension systems for Advanced LIGO will be installed (the installation is scheduled to start in 2007).

### 3.13.2 Advanced LIGO

The proposed advanced gravitational-wave detectors in the USA will achieve a sensitivity not only ten times better than the initial LIGO detectors but will as well open a lower frequency regime for the observation. The modecleaner suspensions for Advanced LIGO will be exact copies of the GEO 600 main suspension. The experience gained from the installation of the GEO 600 suspension systems was used to adjust some details that will help during the installation and alignment of the optics. However, to achieve the more ambitious target suspension-noise level of $10^{-19}\,\mathrm{m}/\sqrt{\mathrm{Hz}}$ at 10 Hz, the requirements on the test-mass suspension systems are more stringent than for the GEO 600 suspensions.

An active isolation system will be employed to decouple the suspension point from the seismic noise [Abbott '02]. The suspension of the core optics will be accomplished from this isolated platform by a quadruple pendulum. The design of this system is also based
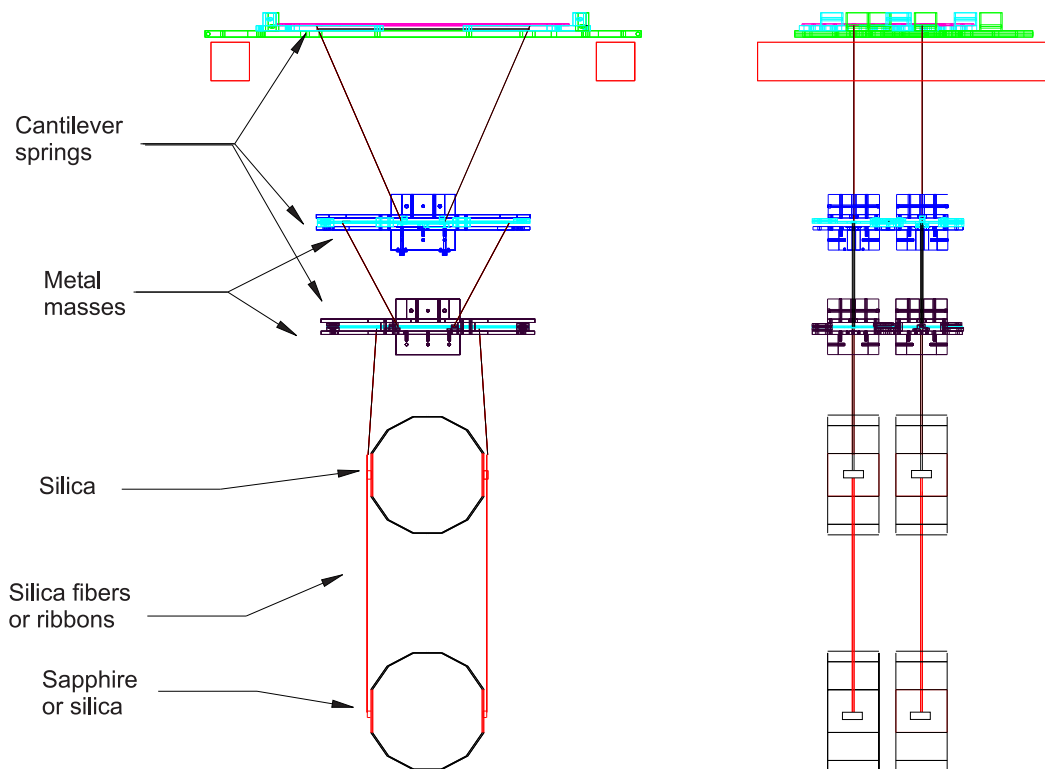


**Figure 3.34:** The Advanced LIGO quadruple suspension is derived from the GEO 600 main suspension. It consists of a monolithic lowest stage and three steel-wire stages. Additional vertical isolation is provided from three cascaded cantilever-spring stages.

on the GEO 600 main suspension but is scaled up in all dimensions and has an additional stage above it. This additional stage is realized by another T-shaped mass. Each of the three upper stages is suspended by steel wires from an individual cantilever-spring stage. Figure 3.34 shows the baseline design of the Advanced LIGO quadruple suspension.

The lowest mass will be monolithically suspended from the penultimate mass as in GEO 600. The down-selection of either using silica fibers or ribbons for this last stage is still to be made. The main differences of these two approaches are discussed in Section 4.7.1. The mirrors will weigh 40 kg and have a diameter of either 34 cm or 31.4 cm. The diameter depends on the material choice, which still needs to be made. The two options are sapphire or silica, both discussed in Section 4.7.2. Table 3.11 provides the most relevant parameters of the Advanced LIGO suspensions. In order to benefit from the experience made during the installation of the monolithic suspensions in GEO 600, the design of the catcher was transferred to Advanced LIGO and adapted to the different requirements.

| | | |
|---|---|---|
| Test mass | 40 kg | |
| | For sapphire: | 31.4 cm diameter, 13 cm thickness |
| | For silica: | 34.0 cm diameter, 13 cm thickness |
| Penultimate mass | 40 kg, silica | |
| T-shaped masses | 36 kg, steel | |
| Suspension length | 170 cm | |

**Table 3.11:** The relevant parameters of the quadruple suspensions for Advanced LIGO.

# Chapter 4

# The monolithic suspensions

## 4.1 Introduction

The low Q of the steel music wires used for the suspension of the 40 m prototype at Caltech was reported already by [Gillespie '93] to limit the suspension thermal noise. Still thermal noise of the test masses and their suspensions is among the most important limitations to the sensitivity of the interferometric gravitational-wave detectors (see Figure 5.19 for the individual contributions to the GEO 600 overall noise budget). While for GEO 600 the internal thermal noise of the test masses constitutes the main limitation, the low-frequency part of the Virgo sensitivity curve is expected to be directly shaped by thermal noise of the suspensions themselves. Since the thermal noise is closely related to the dissipation, as is described in Section 2.3 ff, one of the the main objectives for the suspension systems is to accomplish a low-dissipation environment for the test masses. As a consequence, the materials used for the optics and suspensions must have a low intrinsic loss. The inter-material connections between the optics and the suspension fibers must give low loss while providing a sufficient strength to support the optics.

Even moderately high quality factors can only be achieved for steel suspension wires if the wire clamps are well designed and the wires are loaded to a considerable fraction of the breaking load. Early results on the loss of steel wire suspensions are given by [Gillespie '94]. Various noise sources of steel wire suspensions are discussed in [Cagnoli '96, Cagnoli '97, Huang '98, Ageev '98]. [Cagnoli '99, Dawid '97] report on the results achieved for steel wire suspensions made from different materials. The highest violin-mode $Q$'s of steel wire suspensions reported so far, are of the order of $Q \simeq 5 \cdot 10^5 - 10^6$, obtained for the GEO 600 modecleaner suspensions [Goßler '02] (for a detailed description of the modecleaner suspensions and the violin-mode measurements see Section 3.3).

Regarding these results it is imperative for the next generation of interferometric gravitational-wave detectors to employ monolithic test-mass suspensions. Early results on a monolithic mirror suspension are given by [Träger '97] for a one-inch mirror substrate, and by [Braginsky '96] for a 2 kg mass. The latter reference reports on a quality factor for the pendulum mode of $Q \simeq 10^8$, corresponding to a 1/e amplitude ringdown time of three years. Since then quite a few experiments have been performed to get a better understanding of the potential loss mechanisms in silica suspensions (e.g., [Gretarsson '99, Penn '01, Barr '02]. Latest measurements demonstrated $Q$'s in excess of $5 \cdot 10^8$ [Willems '02] for loaded silica fibers, $Q$'s of up to $2 \cdot 10^8$ for silica masses, and $Q$'s of up to $3 \cdot 10^8$ for sapphire masses.

While being planned for Advanced LIGO, VIRGO, and LCGT these novel suspension types are already installed in GEO 600. Based on the research performed in Glasgow, the material for the mirrors and suspensions of GEO 600 was chosen to be fused silica. The same material is being considered for Advanced LIGO, as is described in Section 3.13.2 . The inter-material connections are accomplished by a hydroxy-catalysed bonding procedure, referred to as silicate bonding [Gwo '98, Sneddon '03, Smith '03], and by welding with a hydrogen-oxygen flame. In this way a monolithic structure is created that forms the last suspension stage of the GEO 600 main suspension. Such a monolithic stage consists of the mirror, the intermediate mass, standoff plates at the sides of each mass, and the suspension fibers. The standoff plates, the so called ears, are bonded onto the flat sides of the mirror and the intermediate mass substrate. Two fibers are welded to each ear, with a total of four fibers per suspension. Thus, the two masses are connected to form the monolithic stage. The implementation of a monolithic suspension stage completes the most complex suspension system of the so far working detectors. All other detectors will operate suspension systems based on steel wires, most likely until the construction of Advanced LIGO will start in 2007.

This chapter describes the production of the monolithic suspensions and the installation inside the vacuum system. It is also dedicated to the fabrication of the suspension fibers and the required tools. Measurements of the mechanical quality factors of the monolithically suspended test masses are provided in this chapter, while the $Q$ measurements of the suspension fibers are given in Section 5.6 .

## 4.2 The suspension fibers

The fibers are flame-drawn from a silica rod by a pulling machine that is controlled by LabVIEW$^{\circledR}$ software on a personal computer. A hydrogen-oxygen flame is employed to heat the fiber material before the actual pulling extension. The pulling machine was developed and built in Glasgow and then shipped to Hannover.

### 4.2.1 The fiber pulling machine

A schematic drawing of fiber pulling machine is shown in Figure 4.2 . The heart of the fiber pulling machine consists of five hydrogen-oxygen burners arranged in a star pattern. This burner arrangement allows to heat the glass rod uniformly along its circumference. Each burner has a valve of its own to allow for an individual adjustment of the gas flow. The five burners are mounted together with two fans on a small horizontally moving slider that has a computer controlled electro-magnetic lock. The two fans are arranged together with a set of air baffles such that both ends of the glass rod are cooled. By setting the air baffles, the size and geometry of the melted section can be defined. Two sturdy hard-chromium plated slider posts build together with a top plate and a base plate the frame of the fiber pulling machine. The two sturdy posts guide two big chain driven sliders. Clamps to hold the glass rod are attached to each of the big sliders. In order to produce a fiber, an 8 cm long silica rod is clamped at each end to one of the two big sliders. Then the burners are ignited and the small slider is set into position. Once the small slider is in position it is held by the electro-magnetic lock. Simultaneously the

|                 | Heating time | Pulling duration | Pulling voltage |
|-----------------|--------------|------------------|-----------------|
| Neck extension  | 12 s         | 0.13 s           | 8 V             |
| Fiber extension | 2 s          | —                | 8 V             |

**Table 4.1:** Typical parameters used for the fiber pulling machine. The heating time has to be set as well as the pulling duration and the pulling speed (set by the motor-drive voltage).

computer takes the control. The program releases the electro-magnetic lock after the set burn time has elapsed. The small slider snaps aside under the force of a return spring and the big sliders pull by the amount that had been set before. As described below in Section 4.2.2, the fibers are pulled in a two-step procedure. The first extension is set by the voltage applied to the motor drive of the big sliders and by the length of time that the voltage is applied. The second extension, determining the actual length of the fiber, is set by a switch mounted to one of the sturdy posts of the fiber-pulling machine. The upper slider activates the switch, which in turn stops the pulling motor. In order to set the fiber length the switch is shifted to the appropriate position.

Concluding, the resulting fiber parameters (i.e., length, diameter, homogeinity, shape of the neck, etc.) are influenced by the individual burner settings, the air baffle settings, the heating time, the pulling voltage, and the pulling duration. Typical values that are used to operate the fiber pulling machine to produce fibers as those used for the inboard suspensions, are given in Table 4.1.

### 4.2.2 The fibers

As a first step a rod of Suprasil 2 with 5 mm diameter is heated and pulled by about 52 mm to produce a thinner region of about 3 mm diameter. Figure 4.1 shows the product of the first pull extension, the so called neck. The neck defines the shape of the tapered fiber ends. This shape determines the length of the bending region of the fiber when the suspended mass is pitched. It would be preferable to minimize the length of this region to decouple the longitudinal and pitch motion of the suspension, but on the other hand it is very difficult to weld a piece of silica as thin as a bare suspension fiber. When welding very thin parts, the heat flow has to be controlled very accurately. With insufficient heat the weld will be not strong enough while excessive heat simply melts the fiber away. Also the repeatability of obtaining strong welds proved to be greater when the two counterparts have approximately the same heat capacity. A third reason is the greater strength of the welds due to the increased cross section at the welding point, caused by the tapered ends. Thus, the fibers need to have a dumbbell shape to allow for reliable welding.



**Figure 4.1:** In a first pull extension the so-called neck is produced. The neck defines the shape of the tapered fiber ends, which is of relevance for the welding.

Top plate

Left slider post

Right slider post

Burners and
fans on a small
horizontal slider

**Pull**

Upper cross bar
slider

Switch for
heating-time
control
and
electro-magnetic
lock

Return spring
for burners
and fans

Small horizontal
slider

Lower cross bar
slider

Product of first
pull extend

**Pull**

Clamp for
glass rod

Chain drive for
cross bar sliders

Computer controlled
motor for chain drive

Base plate

**Figure 4.2:** The fiber pulling machine. A glass rod is clamped with both ends to two cross-bar
sliders. These sliders move under the force of a chain drive along two hard-chromium
plated posts. The burners are mounted together with two fans on a smaller horizontal
slider that engages an electro-magnetic lock. The heating time, the drive speed, and
the extension length are computer controlled.
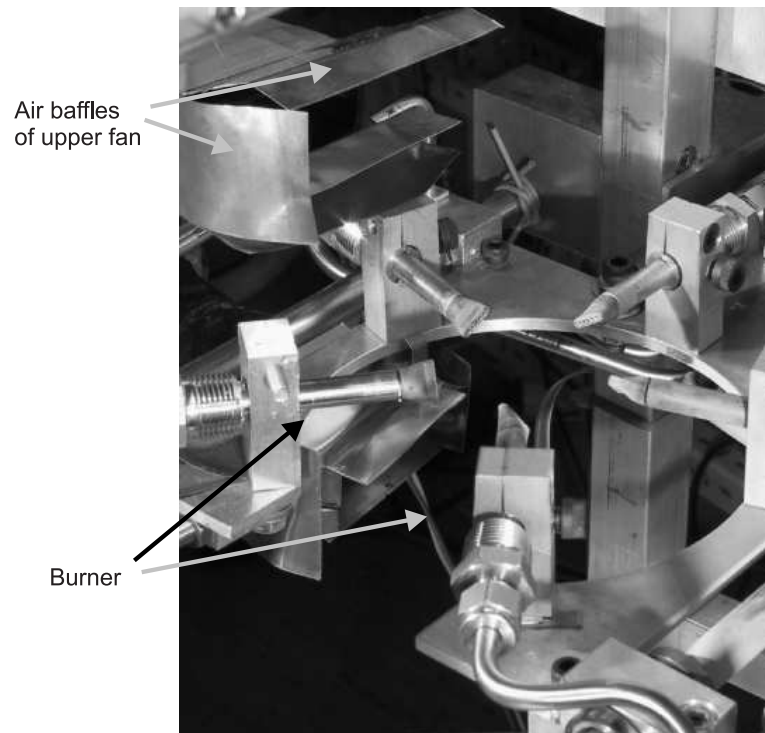
**Figure 4.3:** The five hydrogen-oxygen burners in a star pattern arrangement, used for the fiber pulling machine. Parts of the air baffles of the upper fan can be seen in the upper left corner of the photograph.

As a second step the neck is heated again and pulled by approx. 280 mm to produce the actual fiber. The quality of the fiber is then judged by its length, strength, vertical resonance frequency and the first two violin-mode frequencies. First the length is judged with a ruler then the fiber's strength is confirmed by loading it with 1.4 kg, the load it will have to support in the monolithic stage. Under these conditions the vertical-mode frequency is measured.

### 4.2.2.1 Vertical resonance frequency

For the measurement of the vertical resonance frequency one side of the fiber is clamped into a sturdy frame. The fiber is loaded with the nominal weight of 1.4 kg using a clamp at the lower end. A permanent magnet is attached to the lower side of the clamp, facing a coil. The coil is driven with a sinusoidal current, supplied by a waveform generator and a power supply. A split photo diode and a flag, mounted to the lower clamp, allows the readout of the fiber's vertical oscillation amplitude. The differential signal of the two photo-diode sections are monitored with a software spectrum analyzer. Tuning of the modulation frequency reveals the frequency of maximum fiber oscillation amplitude and thus the natural frequency of the vertical eigenmode.

The vertical resonance frequency has to be as low as possible to keep the thermal noise of the vertical mode outside of the most sensitive frequency range of GEO 600. The

second aspect to be considered is the damping of the vertical mode by means of local control. The local-control gain follows a steep roll off to reduce the coupling of sensor noise to the suspension at sensitive frequencies. Following this objective it is obvious to aim for a low vertical-mode frequency. Hence, the production of the fibers is a trade-off between the tolerable breaking stress of the fibers and the vertical-mode frequency. While the first argument leads to thick fibers, the latter one requires thin fibers. An uncoupled vertical resonance frequency of about 15 Hz is acceptable for the main suspensions, while the fiber diameter should not be below 200 µm to limit the stress to less than 20% of the breaking stress.

### 4.2.2.2 Breaking stress

During the production of a monolithic suspension the strength of the fibers is confirmed repeatedly. The breaking-stress limit of the fibers has been measured to be of the order of $\sigma_B = 2.0 - 4.0 \cdot 10^9$ Pa, which is comparable to that of steel wires ($\sigma_B = 2.9 \cdot 10^9$ Pa for C85 steel). However, this holds only if the fiber surface is untouched. During the pulling procedure all of the fiber material was melted. Thus, initially the surface is almost perfectly unscathed. Touching the fiber causes micro cracks in the surface to open, dramatically decreasing the breaking-stress limit. Humidity or even direct contact with water has to be avoided for the same reason. The first strength test is performed during the vertical-mode frequency test. The fiber is loaded with 1.4 kg and strongly driven at its resonance such that the resulting oscillation amplitude is of the order of $1 \, \text{mm}_{pp}$. Experience proved that a fiber is either intact and thus strong or it breaks right away when being loaded. Hence, all fibers that survived the vertical mode test are regarded as strong. Since the fibers are treated and repeatedly measured, as will be explained in Section 5, it is essential to reconfirm the strength of the fibers before welding. This is done manually by suspending about double the nominal weight (2.9 kg) from the fiber and letting the weight bounce. The great importance of the strength confirmation is founded on the experience that the failure of a single fiber in a monolithic suspension is very likely to cause at least one, if not all, other fibers to break. Section 4.3.3 gives a description of the final strength test of the new monolithic stage.

### 4.2.2.3 Violin-mode frequencies

The violin-mode frequencies need to be as high as possible as discussed in Section 5.2. This again requires thin fibers. The violin-mode frequencies are measured in the same apparatus as the vertical-mode frequencies. But this time the actuation is performed manually by softly tapping the upper end of the silica rod, which is not yet cut off, with another piece of silica rod. The sensing of the resulting oscillation is done with a HeNe laser and a split photo diode. The differential output of the photo diode is read with an oscilloscope and a spectrum analyzer. This method allows very fast location of the violin-mode frequencies up to about the seventh order. Above this mode number the decay time in air is too fast for this simple setup and a permanent drive would be required to resolve higher frequency modes. However, the issue of these measurements were only the first two violin modes, as explained in detail in Section 5.2.
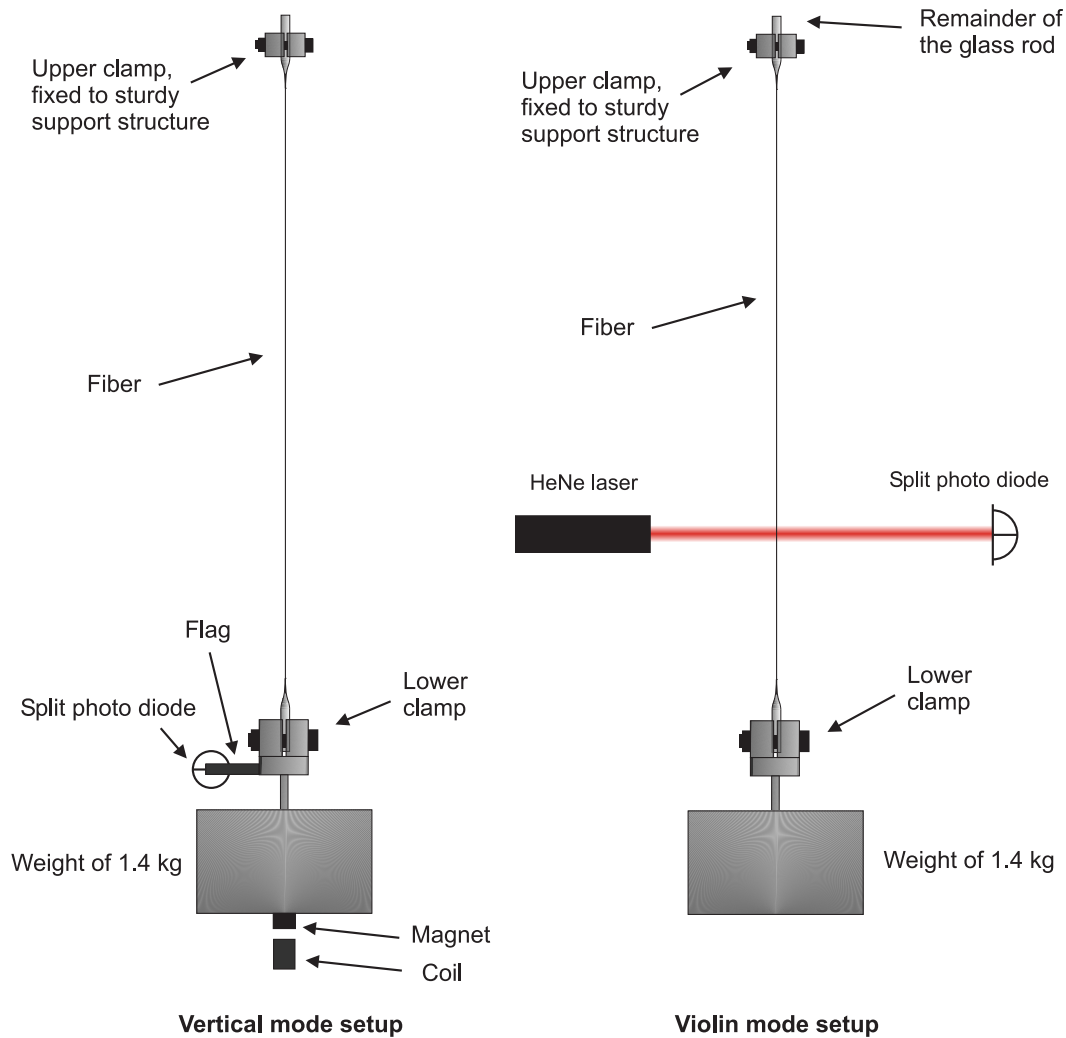
**Figure 4.4:** **Left:** The vertical-mode frequency measurement setup. The fiber is clamped to a sturdy support structure with the upper clamp. The fiber is loaded with 1.4 kg using a second clamp at the lower end. A magnet-coil actuator below the weight excites the vertical resonance. The modulation frequency for the magnet-coil drive, provided by a waveform generator, is set manually to the fiber resonance. The oscillation is then read out with a split photo diode, illuminated by an LED (omitted in the drawing). The signals are analyzed with a software spectrum analyzer. The strength of the fibers is confirmed by driving the vertical resonance of the loaded fiber at a high amplitude. **Right:** A similar setup is used for the violin-mode frequency measurements. In order to excite the violin modes, the remainder of the glass rod at the upper fiber end is tapped with a small glass rod. The resulting oscillation is then read out at one third of the fiber's length with a HeNe laser and a split photo diode. The read out position at one third of the fiber's length was chosen to obtain a sufficient sensitive for both the fundamental and the first higher-order mode. The signal from the photo diode is then analyzed with a spectrum analyzer.

The fibers are produced in Hannover and then transported to the 25 km distant GEO 600 site. The transportation is done with a box that carries up to 32 fibers. The box contains four frames that can be inserted or removed, sliding inside a guard rail. Each frame carries eight fibers, clamped at both ends with a quick-release clamp. It is of some importance to keep theses kind of mechanisms simple and easy to operate, even with gloves on while holding a fiber in one hand.

## 4.3 The catcher

Prior to the production of the monolithic stage, a sturdy mechanical device was developed to fulfill a number of different tasks:

1. Positioning of the two masses with respect to each other
2. Firm holding of the positioned masses
3. Allow free access to the ears to weld the fibers
4. Protection of the optical surfaces during the welding and installation
5. Allow strength tests of the new monolithic suspension
6. Allow to move and rotate the monolithic stage for the installation inside the vacuum tank
7. Provide a UHV compatible catching device that remains inside the vacuum tank to protect the lower two masses from falling in case a fiber or wire breaks

A schematic sketch of this device, the so called catcher, is displayed in Figure 4.5 from three different angles. The catcher provides the precise vertical distance between the two masses, as well as alignment marks that help adjusting the masses longitudinally along the normal of the optical surface. The alignment with respect to roll around the normal is done with a ruler, taking the distances between the ears of the mirror and the intermediate mass on both sides. The masses are then clamped in position by two clamps that have each an excentric drive. These clamps are inserted into the frame of the catcher like drawers and then fixed to position by knurled nuts. Each mass is clamped by revolving the relevant excentric drive with a handle. The drives now press onto two brass cantilever springs. These springs press two aluminum prisms onto the mass and thereby determine the force that is applied to hold the mass in position. Layers of Teflon$^{®}$ are placed between the masses and the catcher to avoid any contact of the fused silica with metal parts. Protective caps are used at the optical surfaces to avoid any contamination during the welding, during the required tests, and during the installation inside the vacuum tank. These caps are bolted to the catcher with cross bars and can be evacuated by a hand pump. The sides of the clamped masses are still accessible in order to weld the fibers to the ears. Once the masses are clamped into position the catcher allows to safely rotate the clamped suspension around all axis and to move it over long distances (e.g., from one end station of GEO 600 to the other). Four handles can be attached to the corners of the catcher to allow the handling of the up to 35 kg weighing device. This weight is obtained for the monolithic beamsplitter suspension, including the catcher and the suspension. Figure 4.6 shows a photograph of the catcher with a monolithic suspension clamped into
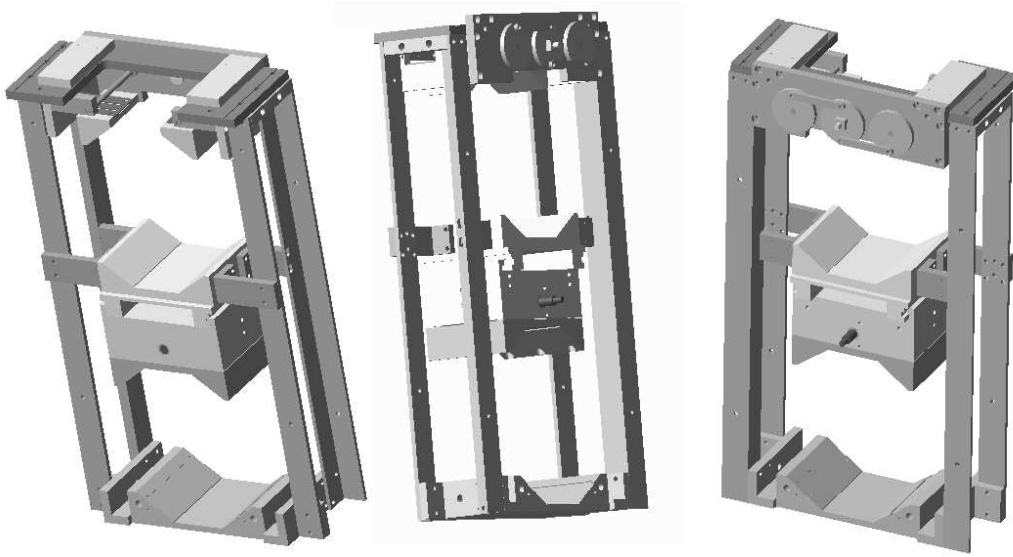
**Figure 4.5:** CAD drawing of the catcher [R. Jones]. The catcher provides a sturdy cage to keep the masses positioned with respect to each other during and after the welding. It serves as a transport cage for the monolithic stage and remains in the vacuum tank to prevent the masses from falling, in case a fiber or wire breaks.

it. The rear surfaces of the masses are covered by the protective caps. After positioning and arresting the intermediate mass and the mirror inside the catcher, the welding of the fibers is the next step toward the monolithic suspension. Before welding it is assured by a spirit level that the catcher is leveled.

### 4.3.1 Cutting the fibers

Prior to the welding the fibers need to be cut to the precise length. Even more important is to obtain an equal length for all the fibers. This is accomplished by the use of a so called cutting jig. The fiber is clamped into this jig by two quick-release clamps. The jig provides a mask that can be set to the required length and gives the cutting position. First the fiber is only scratched at this position with a glass saw or diamond file. Figure 4.7 shows this part of the cutting process. After removing the fiber from the jig, the ends can be broken off. Therefore it is necessary to hold the tapered end of the fiber with a pair of thin pliers directly below the scratch (i.e., at the about 2 mm long section between the scratch and the actual fiber). The remainder of the silica rod can now be broken off at the scratch. The surface damage at the fiber end will be cured during the welding procedure.

The fiber length for GEO 600 is 285 mm, measured from a point where the fiber already starts to increase in diameter. The remaining fiber section of bigger diameter is used for the welding of the fiber to the tip of the ear.

Upper clamp with
double excentric drive

Handle bar

Intermediate mass,
fused silica

Rigid frame

Lower clamp
with excentric drive

Mirror,
fused silica
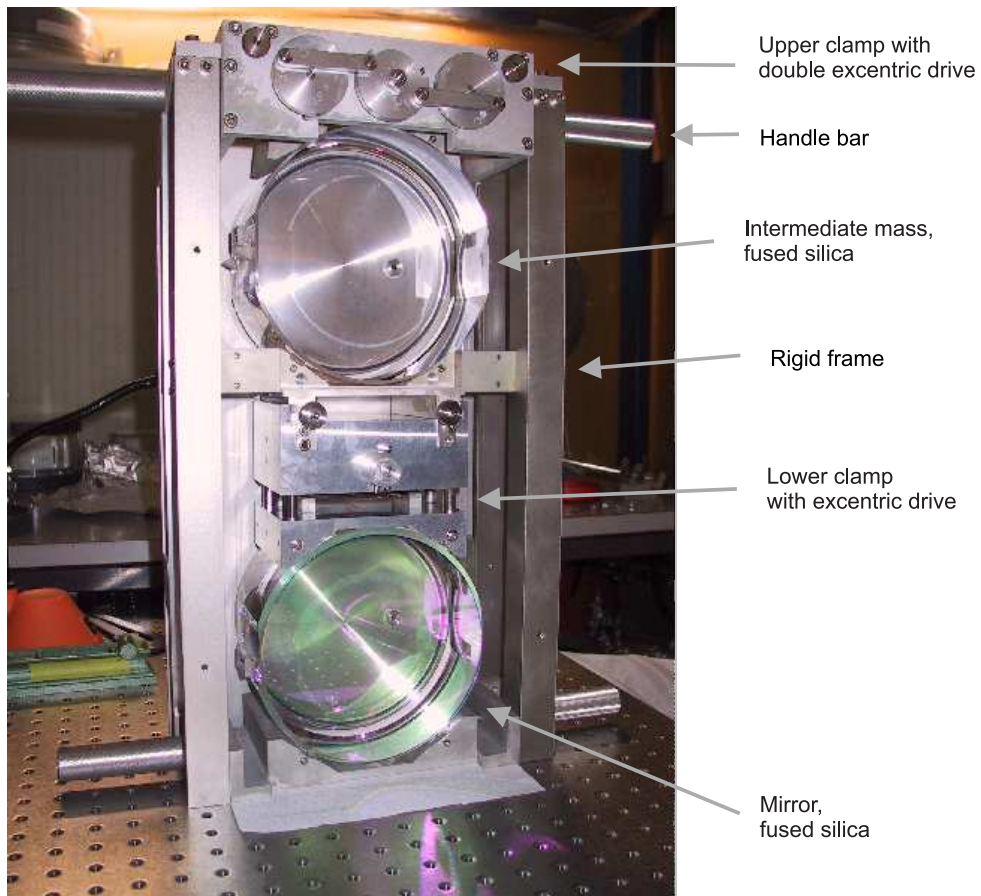
**Figure 4.6:** The catcher with a new monolithic stage. The rear surfaces of the two masses are covered by protective caps. Four handles are attached and both excentric drives are locked in preparation of transportation of the monolithic stage. The overall height is about 0.5 m.



Length mask

Quick-release
clamp

Fiber

Base plate
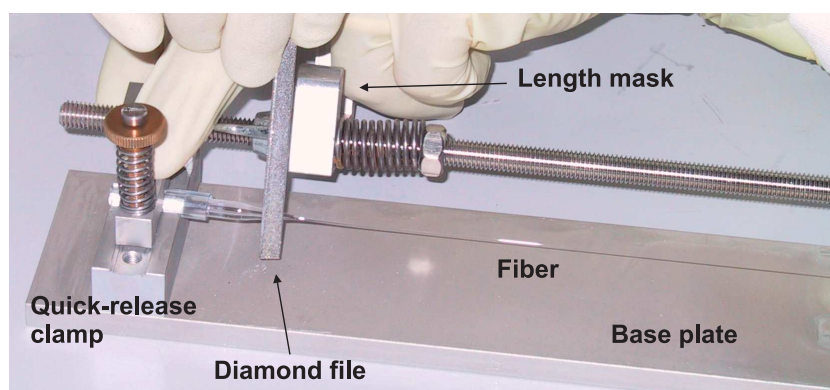
Diamond file

**Figure 4.7:** The fiber cutting jig. A fiber is clamped into position to be cut with a diamond file.

### 4.3.2 Welding the fibers

In order to hold the fiber in position for the welding, either a clamping system at the catcher can be used or the fiber can be held manually. A small handle, consisting of a broken-off end of a fiber, is temporarily welded to one end of the fiber to hold the fiber manually. This welding is done with a small hydrogen torch using a thin medicine needle as a nozzle. A thicker nozzle is required for the welding of the fiber to the ear, to ensure enough heat flow. It is of great importance for the strength of the weld that the whole cross section of the tips of both the fiber and the ear is melted when they are brought into contact. On the other hand not too much heat must be deposited in the tip of the ear or the ear itself. The thereby induced thermal stress can cause the material to crack even after a long period of time (i.e., more than one month after the welding). Hence, the ear needs to be cooled by periodic application of small amounts of deionized water during the welding. After the fiber and the tip of the ear are welded together, the weld area is annealed with the hydrogen torch using a smaller flame. By this procedure potential damages of the fiber surface close to the welded region are cured.

During the welding some silica evaporates and deposits on the area close to the weld. The deposition of silica leaves an opaque layer and is likely to increase the surface loss. However, by curing the surface damages the depositions are necessarily melted as well, restoring the high surface quality.
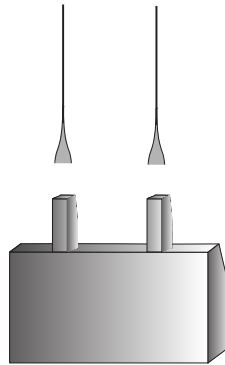


**Figure 4.8:** Ear with fiber ends.

Once all the four fibers are welded on and the welds are cured, the tension of the fibers needs to be adjusted. Evidently it is not possible to cut the fibers exactly to the same length and weld them in under exactly the same tension. Hence, a correction has to be performed. The fibers are straightened by pressing on the lower mass with the excentric drive while the intermediate mass is unclamped. The tension of the individual fibers can be judged by inspection of the resulting fiber oscillation when tapping the catcher. Fibers can be released by carefully heating the welded area under a slight tension. Tightening of a fiber is a more complex task that requires pulling with pliers at the tapered end of the fiber and thorough curing of that area. Obviously, this is the by far more risky alternative.

### 4.3.3 Strength test

Once the tension of the four fibers is matched, the clamps can be removed from the catcher. Now a small lab jack on an H-shaped base plate is clamped on top of the catcher. Two steel wire loops, attached to this lab jack, are used to lift the intermediate mass. The catcher provides end stops to accurately position the wire loops around the lower side of the intermediate mass. Four silica prisms at the intermediate mass define the break-off positions of the wires. First only some tension is applied to straighten the fibers to judge again the homogeneity of the four fiber lengths. By reheating some of the welded sections with a medium size flame, the fiber tensions can nearly be equalized. In the next step the intermediate mass is lifted up by some millimeters to suspend the monolithic stage inside the catcher. The initial aim of suspending the monolithic stage inside of the catcher is to confirm the strength of the eight welds and to reconfirm the strength of the fibers. A secondary aim is to perform violin-mode frequency measurements to reconfirm the effect of the treatment previously applied to the fibers. After taking the required data, the lab jack is released and the masses are reclamped. Further treatment of the fibers can now be applied. However, since the violin mode measurements and the fiber treatment are described in a chapter of their own, only the reference (Chapter 5) shall be given here. Eventually the strength of the monolithic stage is confirmed over night by leaving it suspended inside the catcher, which is kept under a PVC box to prevent a potential contact of the fibers with anything from the environment.

### 4.3.4 Suspending the monolithic stage

After its strength is confirmed, the new monolithic stage can be incorporated into the already existing triple-pendulum suspension in the tank. That means replacing the suspended test mirror and the aluminum penultimate mass by the monolithic stage. To avoid contamination and damage of the final optics, only test mirrors were suspended in the inboard tanks for the first commissioning phase of the power-recycled Michelson interferometer. These test optics had the same size and weight as the final optics. The suspension was realized by steel-wire loops from an aluminum intermediate mass. The wires had the same length and separation as the final silica fibers. The test mirrors and intermediate masses had to be removed before the remaining part of the suspension system could be prepared for the installation of the final optics. It is inevitable to clamp the uppermost pendulum mass down when removing a mirror, since the suspension is supported by cantilever springs. The clamping is done by setting the upper limiters of the upper mass to their lower extreme position, thereby pressing the mass onto its lower limiters and thus clamping it. Now the wire loops can be removed and eventually the mirror itself. The removal of the intermediate mass is now straightforward and much less delicate.

The excentric drives and protective caps are used again, to safely transport the monolithic stage into the tank. As a first step the catcher is clamped onto a steel pedestal inside of the tank. This pedestal serves as a spacer to set the catcher to the right height. After positioning the pedestal with the catcher inside the tank, the excentric drives as well as the caps at the intermediate mass are removed. The pedestal can now be lifted
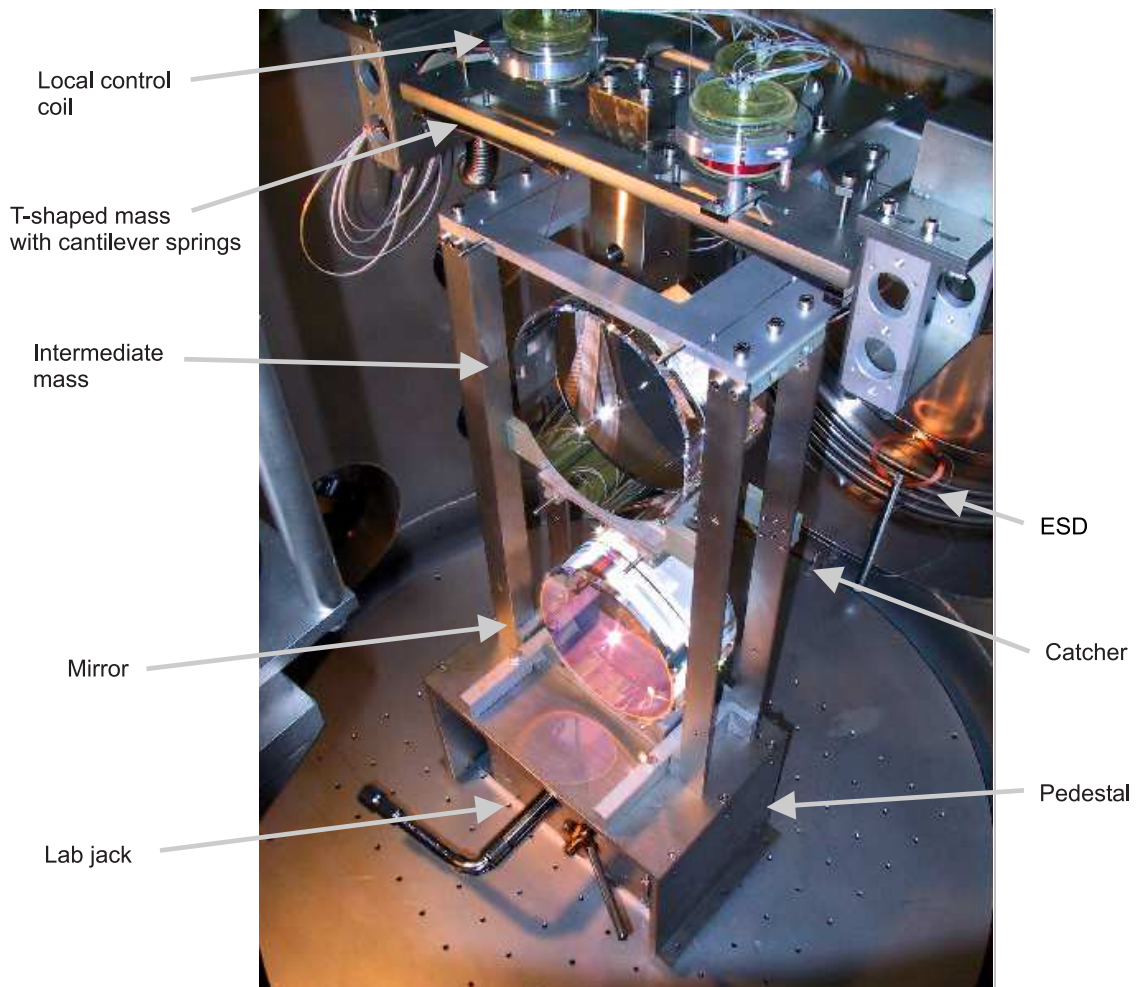
**Figure 4.9:** The far north mirror (**MFn**) suspension: The first-ever monolithic mirror suspension implemented in a gravitational-wave detector. The T-shaped upper mass can be seen at the upper side of the photograph. The fused-silica intermediate mass is suspended in steel-wire loops from cantilever springs below the upper mass. The 5.6 kg fused-silica mirror is suspended by four silica fibers of 250 μm diameter from the intermediate mass. The catcher surrounding the monolithic stage is clamped to a hollow pedestal that can be lifted by a big lab jack for installation purposes. The jack is still positioned inside the pedestal but has to be removed before closing the tank. In the background lies the small electrostatic actuator "on a stick" (ESD), which is used for the violin mode and internal mode measurements.

up by a big lab jack in order to raise it high enough to place the steel wire loops around the intermediate mass. The wire loops are attached to four small cantilever springs (see Section 3.6 for a detailed description of the main suspension). These springs are free of any load in this moment and hence, need to be held partly down until the monolithic stage is suspended. The upper cantilever springs are held down by the adjustable upper end stops of the upper mass.

Once the wire loops are in their precise positions provided by the catcher, the protective caps of the mirror are loosened and the big lab jack can slowly be released. The monolithic stage is thereby suspended as the lowest stage of the triple-pendulum suspension. The catcher remains in the vacuum system to prevent the masses from falling, in case a fiber or wire breaks. The distance of the catcher to the suspended masses is set by inserting shims under the pedestal before clamping it onto the bottom plate of the tank. The nominal distance is set to be 3 mm. Now the protective cap of the mirror can be removed completely to allow the prealignment of the optics (see Section 3).

### 4.3.4.1 Suspending the far mirrors

The first-ever monolithic mirror suspension implemented in a gravitational-wave detector was installed in the far north tank **TFn** in April 2001. Figure 4.9 shows a photograph of this particular suspension. The four fibers used to suspend the 5.6 kg mirror have a diameter of about 250 µm. This translates into a stress of $\sigma = 2.8 \cdot 10^8$ Pa, 13.5 % of the breaking stress.

The monolithic stage for the far east suspension was made in the north end station as well. It seemed more practical to rather use the already prepared environment in the north end station than to move all the required equipment to the east end station. After welding and strength testing the new monolithic stage for the far east suspension, it was reclamped into its catcher, wrapped with tinfoil, and laid into an aluminum transportation box. The box was then transported to the east end station by car and suspended after a new strength test.

As mentioned above, the violin modes of silica suspension fibers can have very high $Q$'s. In order to avoid an enhancement of the violin modes to high levels, a damping method was utilized the first time for these two suspensions. It is based on the application of a highly dissipative material onto certain sections of the fibers. Since there is no feedback to the far mirrors the only excitation of the violin modes could arise from the seismic. Thus, only slight damping was required. The full description of the damping method and the results achieved are given in Chapter 5.

### 4.3.4.2 Suspending the inboard mirrors

What makes the installation work for the inboard mirrors more precarious than for the far mirrors, is the fact that there is the reaction pendulum already installed 3 mm from the mirror position. The reaction mass must be guarded by a preliminary catcher to avoid any damage in case a wire breaks or is cut during the installation work.

Two of the small cantilever springs underneath the upper mass must be held down to free both intermediate wire loops. The local-control coil No. 1 or No. 2 has to be removed to clear the access to the springs (see Figure 3.16 for the numbering of the local-control coils). Through the remaining coil clamp a steel rod can be inserted between the upper mass and the springs, which have to be pressed down through a gap in the upper mass during this procedure. The wire loops, now free, are temporarily fixed to the coilholder to clear the space to position the fragile monolithic stage. The suspension of the monolithic stage is done as already described in Section 4.3.4. Great caution is required during
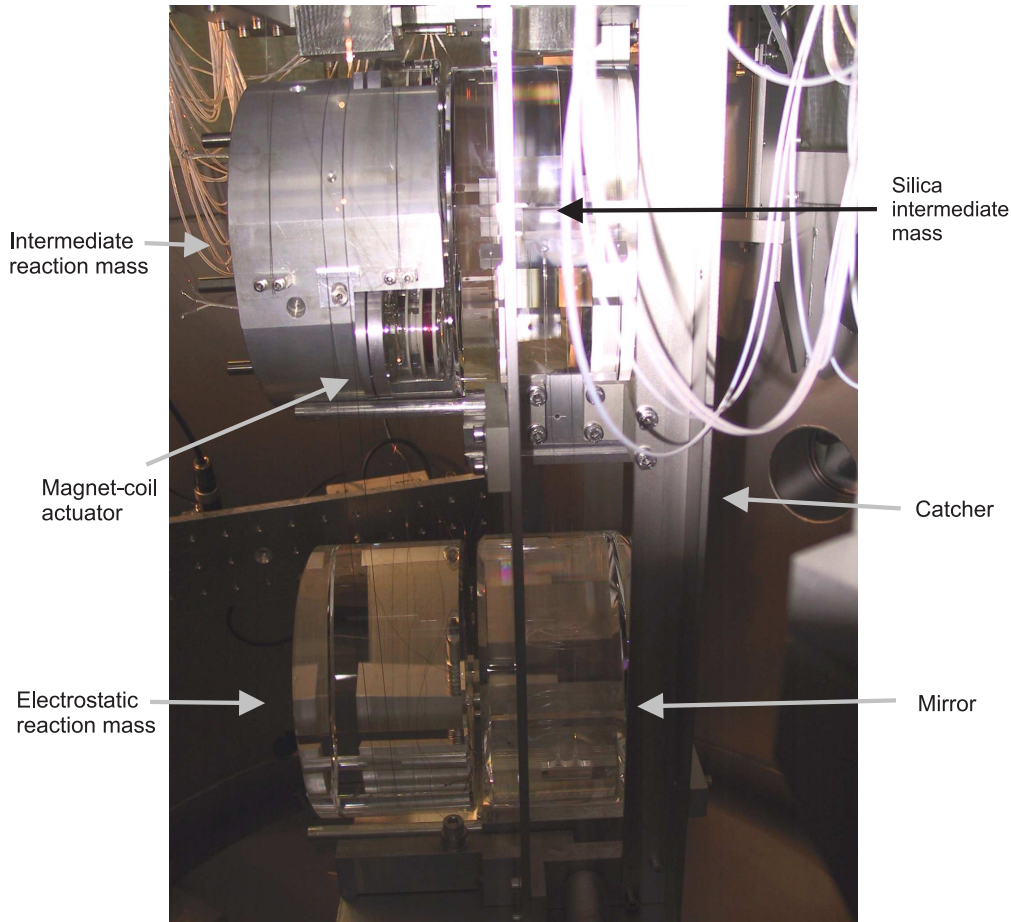
**Figure 4.10:** The north inboard mirror (**MCn**) suspension. The mirror has a diameter of 180 mm and weighs 5.6 kg. It is suspended with four silica fibers of 210 µm diameter. The reaction mass is suspended 3 mm behind the mirror via steel wires. The two pendulums are crude aligned with respect to each other such that the magnets at the intermediate mass match the coils. The fine relative alignment of the electrostatic actuator to the mirror is done with an autocollimator after the alignment of the mirror to the relevant interferometer arm.

the installation and prealignment phase of the inboard mirrors because a considerable amount of work and very expensive optics can be destroyed by virtually a hand wave. The preliminary catching device for the reaction mass suspension was eventually replaced by four aluminum rods that extend from the rear side of the final mirror catcher.

A special situation for the violin modes of the inboard mirror suspension fibers arises from the fact that fast feedback signals are applied to the mirror itself. As described in detail in Section 5.2, the excitation of the violin modes by the feedback actuators can interfere with the interferometer length control servo. To avoid servo instabilities, the violin modes were damped by the application of amorphous Teflon to certain sections of the fibers. In contrast to the far mirror suspensions, the damping of the inboard suspensions violin modes had to be more strongly and the violin-mode frequencies had

to be precisely matched. Please see Chapter 5 for the full description of the damping procedure and Section 5.6 for the results achieved for the inboard suspensions. Due to the added application of the damping material, the corresponding violin-mode frequencies are lowered. In order to compensate for this frequency shift, thinner fibers were used for the inboard suspensions. The fiber diameter is $210\,\mu m$ at the thinnest sections. The resulting stress is $\sigma = 3.6 \cdot 10^8\,Pa$, about $17.5\,\%$ of the breaking stress.

## 4.4 Longitudinal to pitch coupling

After the installation of the inboard monolithic suspensions it turned out that the cross coupling between different degrees of freedom had changed from the values obtained for the previously installed steel-wire suspensions. The strongest change of the coupling coefficient was observed for the longitudinal to pitch degrees of freedom. The origin of this strong crosstalk was found to lie in the bending point of the fibers not being well enough defined. The tapered fiber ends were found to bend over a region about $7\,mm$ long. The steel wires that were used before had a bending length of about $\sqrt{(EI/P)} \simeq 2.4\,mm$. Thus, the effective break-off position is no longer $1\,mm$ above/below COM for the mirror or the penultimate mass. Any force in the longitudinal direction thus couples more strongly into pitch of the relevant mass than before installing the monolithic stages.

Since the suspension of the upper mass is realized by only two wires, in first order approximation no pitch noise couples into the suspended optics. With the stronger longitudinal to pitch coupling, an enhancement of the seismical-driven pitch noise of the optics of about one order of magnitude was observed. In order to pre-isolate the suspension from the longitudinal component of the seismic noise, the active stack layers are employed. Since the built in geophones in the stacks proved to have no sufficient sensitivity at very low frequencies, commercial Streckeisen STS2 seismometers had to be set up to feed the piezo drives in the stacks with the appropriate signals. One Streckeisen STS2 seismometer each is set up in the central station and in both end stations for this purpose. A reduction of the seismical-driven pitch motion of about one order of magnitude could be achieved in the frequency range of $0.3\,Hz$ to $3.5\,Hz$. This reduction proved to be sufficient to allow for lock acquisition times of the order of one minute.

A further drawback of the more strongly longitudinal to pitch coupling showed up in the locked state. The applied longitudinal feedback produced a pitch motion of the relevant mirror of about $2\,\mu rad/\sqrt{Hz}$ at $1\,Hz$, for each inboard suspension. Although the automatic alignment system is capable to correct for such big fluctuations, the remaining control deviations can be minimized by reducing the fluctuations themselves. By the previously employed orthogonalization of the actuation signals the coupling between the different degrees of freedom were already minimized. However, since the dynamic response of the suspended masses in the region around the different resonance frequencies shows a strong frequency dependence, the analog control scheme could only be optimized for one frequency. Hence, a digital feedforward system was implemented to counteract for the mirror pitch introduced by the longitudinal feedback signals to the intermediate mass. By applying the corrective signals to the intermediate mass, the feedforward correction supplements the orthogonalization of the control signals.

## 4.5 Q measurements of the suspended test masses

The electrostatic actuators, suspended 3 mm behind the inboard mirrors **MCe** and **MCn**, were used to measure the $Q$'s of the monolithically suspended test masses. The small electrostatic actuator (also referred to as electrostatic actuator "on a stick") behind the far north mirror **MFn** was employed to measure the $Q$'s of this test mass. A description of the suspended electrostatic actuators can be found in Section 3.9. The electrostatic actuator on a stick behind **MFn** consists of a copper ring with 12 cm inner diameter that is mounted on an electrically isolated post. This ring can be charged with high voltage (a few hundred Volts), modulated at the desired frequencies. The modulation frequencies were supplied by a network analyzer, the high voltage by a transformer. The small electrostatic actuator on a stick is also set up 3 mm behind the mirror. The measurements were performed with the power-recycled Michelson interferometer in the locked state. Thus, the resonances of the test masses show up in the error-point spectrum of the interferometer length-control servo, which is routinely recorded by the GEO 600 data-acquisition system.

Because of the sharp resonance peaks it is essential to know the approximate frequencies to look for, prior to the measurements. The internal resonance frequencies and mode shapes of the test masses were modeled using the finite elements analysis (FEA) package Algor [J. R. Smith]. The set of calculated frequencies was then used to search for the resonances. The search was performed by the application of band limited (50 Hz to 100 Hz bandwidth) quasi-white noise and frequency chirps. After detecting a mode it was further exited solely at its natural frequency to a signal to noise ratio greater than 100. The free decay of the oscillation can be observed in the error-point spectrum of the interferometer length-control servo. The $Q$'s given below are taken from several ring-down time measurements.

The tables incorporated in Figure 4.12 and Figure 4.13 provide the measured resonance frequencies and $Q$'s of some of the eigenmodes of the test masses. The respective figures illustrate the measured $Q$'s graphically. Figure 4.11 shows the mode shapes of some of the measured modes.
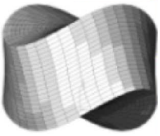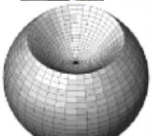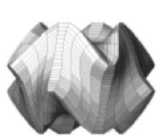


| Shape | | | | |
|---|---|---|---|---|
| Mode | Butterfly | Drum | Barrel | Double butterfly |
| Calculated frequency [Hz] | 10.97 | 15.08 | 25.56 | 26.20 |
| Measured frequency [Hz] | 11.062 | 15.193 | 25.717 | 26.479 |

**Figure 4.11:** The FEA-predicted mode shapes of some of the measured internal modes of the test masses. The calculated and the measured frequencies are given below the corresponding mode.

In order to obtain theoretical predictions of the quality factors, estimations of the relevant loss mechanisms have to be made. A first estimation of $\phi_{\text{overall}}$ accounts for [Smith '04]

$$\phi_{\text{overall}} \simeq \phi_{\text{bulk}} + \phi_{\text{bond}} + \phi_{\text{coating}} \tag{4.1}$$

The bulk loss of the test masses can be assumed to be $\phi_{\text{bulk}} \simeq 1.8 \cdot 10^{-8}$. The relative energy loss in the bonded area can be estimated to be in the range of $\phi_{\text{bond}} = 4.2 \cdot 10^{-9} - 1.3 \cdot 10^{-8}$. The relative coating loss for a GEO 600 test mass has been modeled to be of the order of $\phi_{\text{coating}} \simeq 5 \cdot 10^{-8}$. Thus, the overall loss is expected to be about

$$\phi_{\text{overall}} \simeq 8 \cdot 10^{-8} \tag{4.2}$$

This loss would be consistent with quality factors of $Q \simeq 10^7$. Since all measured $Q$'s are lower than this prediction, a more exact analysis has to be performed to explain
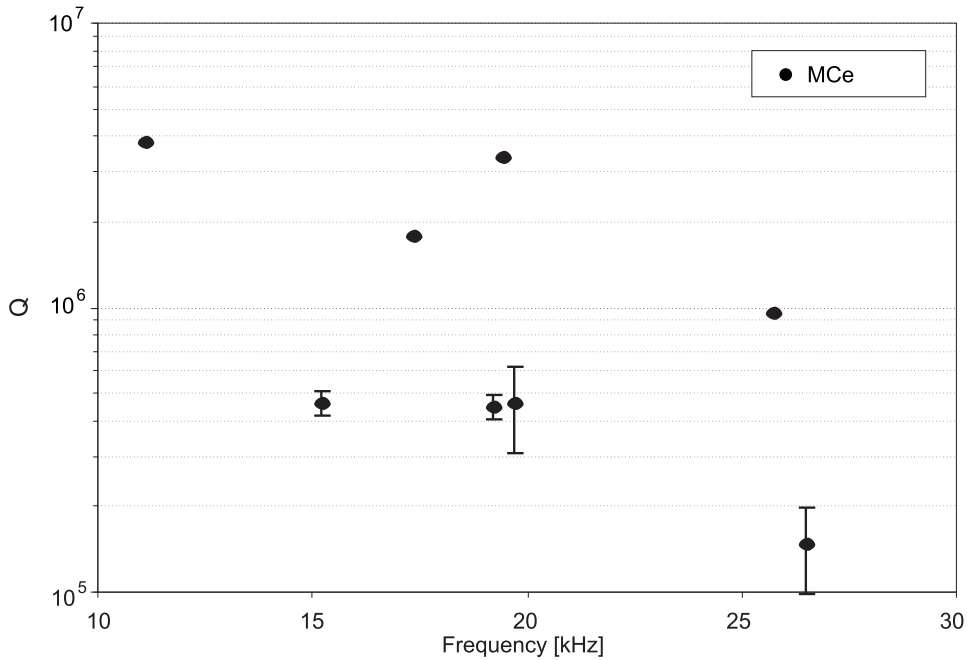


| $f$ [kHz] | 11.062 | 15.193 | 17.350 | 19.199 | 19.424 | 19.665 | 25.717 | 26.479 |
|-----------|--------|--------|--------|--------|--------|--------|--------|--------|
| $Q$ [$10^6$] | 3.84 | 0.46 | 1.18 | 0.45 | 3.42 | 0.46 | 0.96 | 0.15 |

**Figure 4.12:** $Q$ measurements of some of the internal modes of the east inboard mirror **MCe**. The modes were excited with the suspended electrostatic actuator. The $Q$'s are derived from ring-down time measurements. The error bars represent the standard deviations of the measurements.

the measured values. The most important alteration would be to take the nonuniform energy distribution of the different modes into account. Secondly the used bulk-loss factor was measured for Suprasil 2 instead of Suprasil 1, which is the actual material the test masses are made from. Neither surface loss from the barrel jacket nor recoil loss of the penultimate mass were taken into account.

It has been reported before that in high-$Q$ suspensions an energy dissipation via the suspension fiber's resonances was observed [Logan '92]. However, the fundamental thermal noise level should not be affected by this kind of energy dissipation via the fibers.
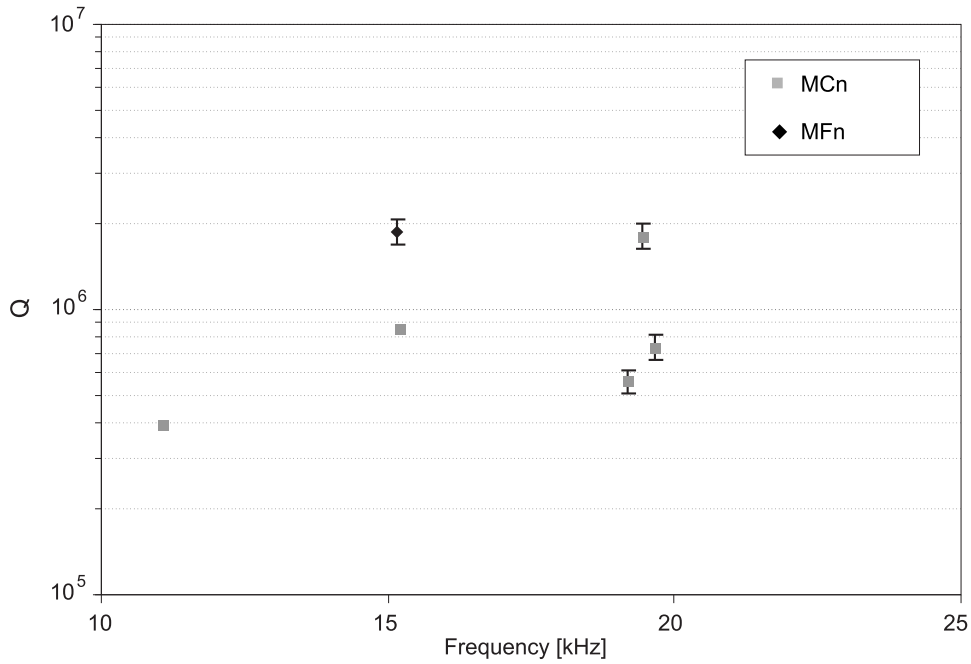


| $f$ [kHz] | 11.057 | 15183 (**MFn**) | 15.194 | 19.188 | 19.421 | 19.671 |
|---|---|---|---|---|---|---|
| $Q$ [$10^6$] | 0.40 | 0.86 | 0.56 | 1.81 | 0.74 | 1.87 |

**Figure 4.13:** $Q$ measurements of some of the internal modes of the north inboard mirror **MCn** and the far north mirror **MFn**. The modes of **MCn** were excited with the suspended electrostatic actuator, while the small electrostatic actuator on a stick was used for **MFn**. The $Q$'s are derived from ring-down time measurements. The error bars represent the standard deviations of the measurements.

## 4.6 The monolithic beamsplitter suspension

Each fiber of the beamsplitter suspension is loaded with 2.3 kg. To assure a reasonable safety margin in terms of breaking stress, fibers of about 300 μm diameter were used for the beamsplitter suspension. Fibers of this diameter have been proved to have a breaking load in excess of 15 kg ($\sigma_B \simeq 2.1 \cdot 10^9$ Pa). Thus, the fibers of the beamsplitter suspension are loaded to about 15 % of the breaking stress. The target frequency for the uncoupled vertical mode is 15 Hz, as for the main suspension. Since there is no feedback to the beamsplitter itself nor to the penultimate mass, only little damping of the violin-mode $Q$'s is required. Hence, the fibers were treated with the damping material in a similar way as the fibers for the far mirror suspensions to obtain a quality factor of $Q \leq 10^8$ for the fundamental violin mode.

For the commissioning phase of the power-recycled Michelson interferometer the beamsplitter was suspended in steel-wire loops (see Section 3.8). Before installing the monolithic beamsplitter stage, the beamsplitter, the intermediate mass, and the preliminary catcher had to be removed. Before removing the masses the upper mass has to be clamped by fastening the big central bolt that acts as a limiter in both vertical directions and for the translational degrees of freedom. After removing the lower two masses, the coil No. 2 has to be removed to allow to hold the two small cantilever springs on this side down. Since there are only 6.5 cm of free space between the beamsplitter and the bottom plate of the tank, the design of the big lab jack had to be altered to allow the lifting of the monolithic stage. A plate was attached to the front side of the jack to realize a fork lift. This plate can be inserted between the catcher and the bottom plate while the main part of the jack is clamped to the bottom plate. The monolithic beamsplitter suspension can now be lifted up to position the steel wire loops around the fused-silica intermediate mass. The design of the catcher itself was basically scaled up to fit the demands of the bigger beamsplitter and intermediate mass substrates. Since the diameter of the substrates is bigger but the separation of the COMs stays the same as for the main suspension, the spacing between the two substrates is reduced to 2 cm. This small gap makes an alteration of the lower clamp inevitable. The new clamp design has the springs attached to the outer sides and translates the forces via two levers onto the beamsplitter. This alteration allows to shift the clamp in and out with the required clearance.

Figure 4.14 shows a photograph of the monolithic beamsplitter suspension. The monolithic stage is surrounded by the catcher, which is clamped to the bottom plate of the vacuum tank. The catcher itself stands on shims that set the precise height of the catcher and thus the distance between the catcher and the suspended masses. The catcher is nominally set such that the suspension is free to move by 3 mm in all degrees of freedom. Four clamps attach the catcher to the bottom plate.

## 4.7 Future perspectives

Thermal noise of the test masses and of the suspensions themselves becomes more important with increasing sensitivity of the detectors. Thus, monolithic test-mass suspensions have to be used in the next generations of interferometric gravitational-wave detectors.
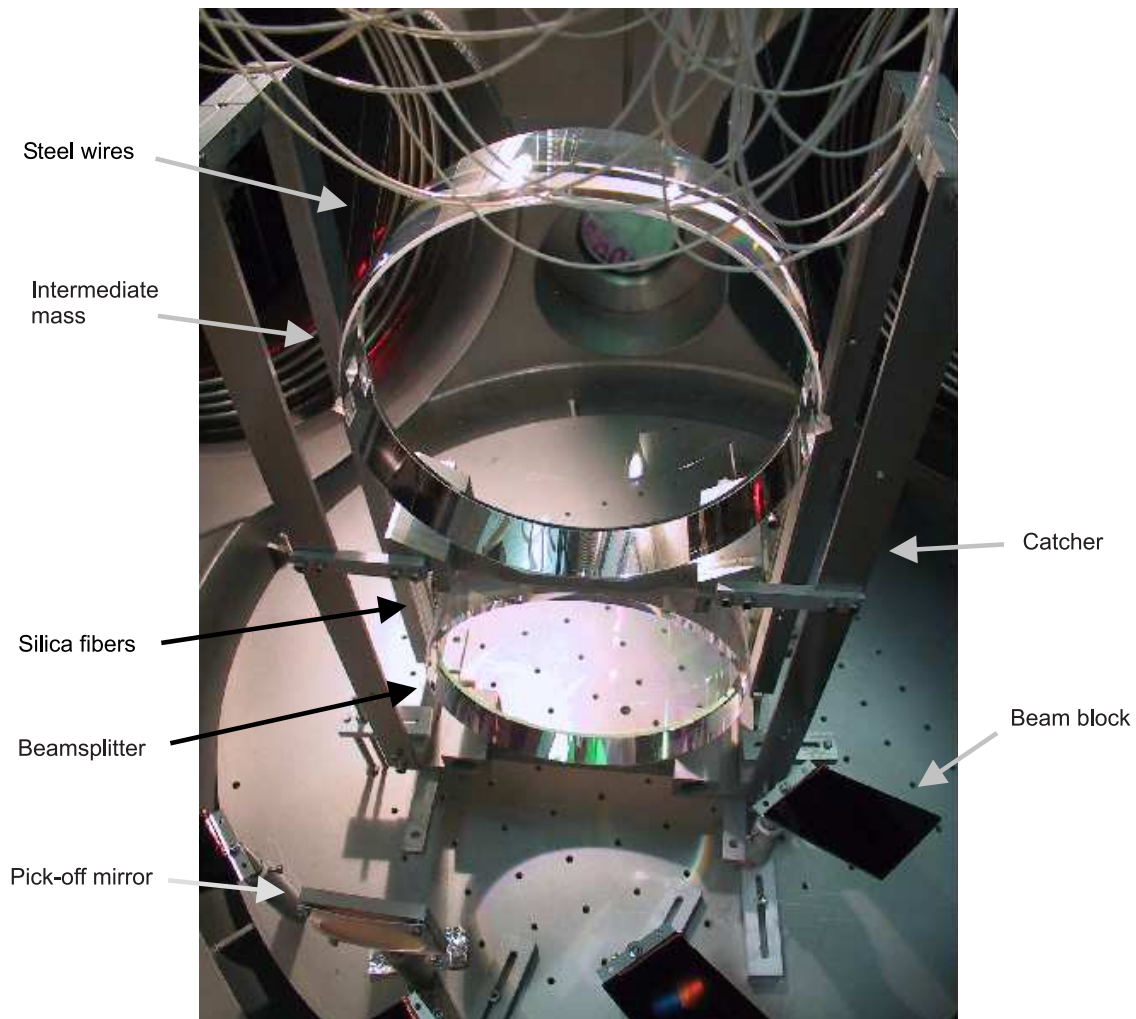
**Figure 4.14:** The monolithic beamsplitter suspension. The beamsplitter has a diameter of 26 cm and weighs 9.3 kg. It is suspended by four silica fibers of 300 μm diameter. Both silica masses are protected from falling by the catcher. The intermediate mass is suspended by two steel-wire loops (barely visible in the picture) from the upper mass (not on the photograph). UHV compatible beam blocks and pick-off mirrors are mounted around the beamsplitter.

As already described in Section 3.13.2, the Advanced LIGO detectors will use a last suspension stage as the one used in GEO 600. The Virgo detector will use steel wire suspensions in the first phase, but in the long term monolithic suspensions are foreseen to be implemented. The large cryogenic detector LCGT, proposed to be built in the Kamioka mine near Toyama, in Japan, will use monolithic suspensions as well. One remaining question to be solved in the nearer future is whether fibers or rather ribbons will be used for the future suspensions. The material for the test masses is another open issue. Eventually cooling of the mirrors has to be considered for further reduction of the thermal noise.

### 4.7.1 Ribbons or fibers?

Ribbons in contrast to fibers have a rectangular cross section. This difference in geometry causes a change of the pendulum thermal noise. Following [Gretarsson '00] the difference is illustrated by

$$
x^2(\omega) \;=\; \begin{cases} A(\omega) \cdot \frac{3}{4}\,[d_{\mathrm{f}}(\phi_{\mathrm{bulk}} \,+\, \phi_{\mathrm{therm}}) + 8\,d_{\mathrm{s}}\phi_{\mathrm{bulk}}] & \text{for fibers} \\[2mm] A(\omega) \cdot \quad [d_{\mathrm{r}}(\phi_{\mathrm{bulk}} \,+\, \phi_{\mathrm{therm}}) + (6 + 2\frac{d_{\mathrm{r}}}{4w_{\mathrm{r}}})\,d_{\mathrm{s}}\phi_{\mathrm{bulk}}] & \text{for ribbons} \end{cases}
$$

where $d_{\mathrm{f}}$ denotes the fiber diameter, $d_{\mathrm{r}}$ and $w_{\mathrm{r}}$ are the ribbon thickness and width, respectively. $A(\omega)$ is a frequency dependent coefficient that includes all factors common for ribbons and fibers. While the bulk loss $\phi_{\mathrm{bulk}}$ is a material parameter, the thermoelastic loss $\phi_{\mathrm{therm}}$ depends also on the geometry. However, the values of $\phi_{\mathrm{therm}}$ for ribbons and fibers are of comparable size. The dissipation depth $d_{\mathrm{s}} \simeq 100\,\mu\mathrm{m}$ is likely to be of the same length for both of the geometries.

The interpretation of the above formula reveals that dilution of the pendulum loss in dependence of the aspect ratio of the ribbons is the crucial parameter (please see Section 2.4.3 for the introduction of the dilution factor). For a given load the aspect ratio can be modified while keeping the filament stress constant. Thereby a higher dilution factor can be achieved: By reducing the thickness $d_{\mathrm{r}}$ (at the expense of an increase of the width $w_{\mathrm{r}}$) the length of the bending region $\lambda \simeq \sqrt{(E\,I/P)}$ of the ribbon due to the pendulum oscillation is reduced. An increase in the aspect ratio by a factor of ten leads to a factor of ten shorter bending length. At the same time the energy required to bend the ribbon is reduced with the thickness. Thus, by reducing the thickness in the direction relevant for the pendulum mode, the loss of the pendulum mode and thereby the thermal noise can be reduced with respect to fibers of similar strength. On the other hand a reduction of the thickness causes the surface loss to become more important. The increase of the thermal noise due to the greater relevance of surface loss moderates the gain in dilution and sets a limit to the possible reduction of the thermal noise.

The final decision about the use of fibers versus ribbons for the monolithic stages of the Advanced LIGO suspensions has not yet been made. Experimental work on the production and welding of ribbons as well as on quality factor measurements to gain a solid base for the down selection is currently performed in Glasgow. Previously obtained results can be found in, e.g., [Rowan '97].

### 4.7.2 Sapphire, silica or silicon?

The materials to choose from when talking about test masses for future monolithic suspensions are fused silica as used in GEO 600, sapphire as under investigation for Advanced LIGO, and silicon. The question gets more complex when thinking about arm cavities as used in LIGO. In this case there are two masses, the so called input test masses, through which the light has to be transmitted. Hence, not only high mechanical quality factors are required, but also the absorption has to be minimized. While fused silica of the SV311 type as used for the GEO 600 beamsplitter shows a very low absorption, the mechanical

quality factor may be not as high as for sapphire [1]. Sapphire now has a high intrinsic $Q$ [Rowan '00] while the optical quality seems to differ strongly with the samples under investigation [Willems]. However, an optical annealing can be performed to lower the absorption substantially [Reitze]. This can be done by heating the mass to about 1300 K and then cooling it down as rapidly as possible. The optical annealing stands in a clear contradiction to the mechanical annealing where the cool down of the masses takes about two weeks [Penn]. The influence of the optical annealing on the mechanical quality factor still needs to be investigated.

The third option is to use silicon test masses. This option might be considered when cooling of the mirrors is intended. The thermal-expansion coefficient of silicon equals zero at 120 K and at 20 K. Therefore the otherwise dominant source of thermal noise, the thermoelastic noise, can be circumvented. The structural losses of silicon are believed to be very low, close to the values for sapphire. This has to be experimentally verified for large masses in the near future. A further fact in favor of silicon substrates is the well developed technology for the production of very pure silicon.

### 4.7.3 Cold mirrors (LCGT)

Cooling of the test masses in order to further reduce the thermal noise will become more important in the next decade. In first experiments the $Q$ of a sapphire fiber could be increased by up to a factor of 10 when decreasing the temperature from 78 K to 6 K [Uchiyama '00] [2]. So far, however, the LCGT in Japan [Kuroda '02] is the only proposed large scale interferometric gravitational-wave detector using cooled mirrors. Cooling of the mirrors is a rather complex task, as the laser light power stored in the future interferometers will increase to the order of MW. Hence, very low absorption in the mirror coatings is imperative. Moreover, the use of Fabry-Perot cavities in the interferometer arms requires low absorption of the input test-mass substrate as well.

The heat contact of the mirror to a cold environment can be accomplished via the suspension fibers. In LCGT sapphire fibers are proposed to be used to transport the heat from the mirror to a penultimate mass [Uchiyama '04]. From here the thermal energy can be distracted via a thin aluminum wire. Sapphire and aluminum have similarly good thermal conductivity between $3 \cdot 10^2 \, \mathrm{Wm^{-1}K^{-1}}$ and $2 \cdot 10^4 \, \mathrm{Wm^{-1}K^{-1}}$ at the relevant temperatures between 100 K and 10 K, while silica has only a thermal conductivity of the order of $5 \cdot 10^{-1} \, \mathrm{Wm^{-1}K^{-1}}$ at these temperatures. The wire to the penultimate mass needs to have its own seismic isolation chain to avoid a mechanical short circuit. Eventually the heat link is connected to a heat bath (or "cold finger") at low temperature outside the cryostat. Figure 4.15 shows a cooling mechanism as the one proposed for LCGT.

---

[1] Latest measurements show that the quality factors of fused silica SV311 test masses can reach about the same mechanical quality factors as sapphire [Willems], but the $Q$ seems to depend greatly on the history of the individual specimen.

[2] For further reading on thermoelastic effects at low temperatures, see, e.g., [Cerdonio '01].
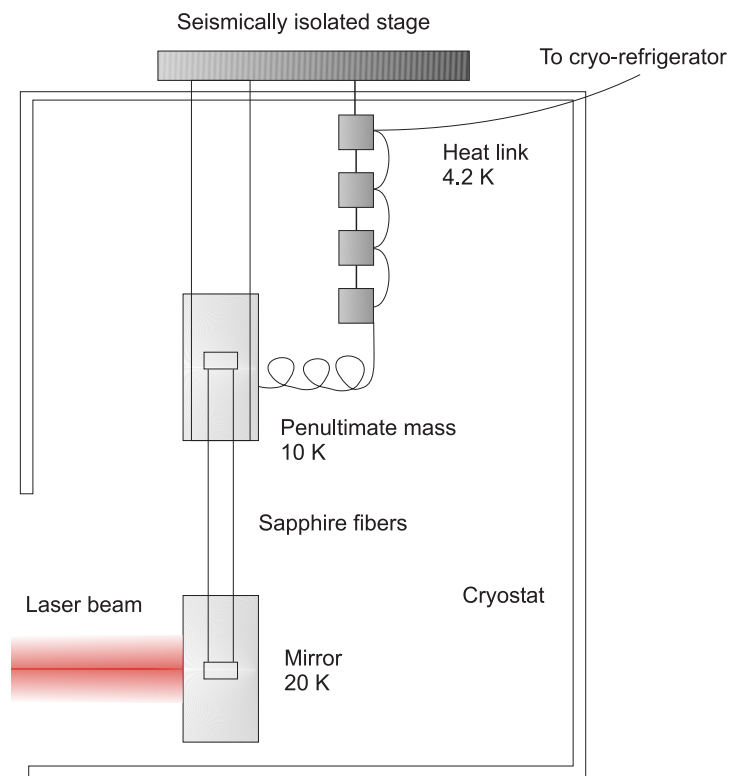
**Figure 4.15:** A mirror cooling scheme for a multiple-pendulum suspension as proposed for LCGT. Sapphire fibers are proposed for LCGT because the thermal conductivity of sapphire is four to five orders of magnitude greater than that of silica, at the relevant temperatures.

# Chapter 5

# Damping and tuning of the silica-fiber violin modes

## 5.1 Introduction

Besides the eigenmodes of the pendulum, the oscillations of the suspension fibers themselves are of importance for the performance of the suspension systems. The transversal mechanical eigenmodes of the suspension fibers, the so-called violin modes, are coupled to the longitudinal motion of the test masses and may thus cause instability of the interferometer length-control servo [Goßler '04]. These fiber modes can have very high mechanical $Q$'s in excess of $Q = 5 \cdot 10^8$ [Willems '02]. The ring-down time of such a high $Q$ oscillator at the typical violin-mode frequencies is of the order of a few days. Hence, the detector can experience long down-times caused by any accidental excitation of the violin modes. Possible sources for such an excitation are earthquakes or even the lock acquisition of the interferometer. Furthermore, the fibers may be subject to a permanent excitation by the length-control servo. As a consequence, the unity-gain frequency of the length-control servo is limited. To keep the servo stable and to allow for further increase of the unity-gain frequency in the future, the violin-mode $Q$'s had to be damped. Moreover, the violin-mode frequencies are required not to exceed a certain spread, to allow for high $Q$ notch filtering in the control electronics. Hence the violin-mode frequencies were tuned to obtain a spread within the requirements set by the servo demands. Based on thermal-noise considerations, the damping and frequency tuning was done in such a way that the $Q$ of the pendulum itself is degraded as little as possible.

The first sections of this chapter provide an introduction to the violin modes and give the requirements for the GEO 600 inboard mirror suspension fibers. The method to damp and tune the violin modes and the results achieved are presented in the subsequent sections. Long-term measurements of the violin-mode frequencies, obtained during the second participation phase of GEO 600 in the scientific data-taking run S3, allow for further analysis of the monolithic stages. Eventually the influence of the violin-mode damping on the vertical mode and on the suspension thermal noise is discussed.

### 5.1.1 Violin-mode frequencies

The natural frequencies of the fiber violin modes depend on the Young's modulus $E$ and the density $\rho$ of the fiber material, the tension $P$, and the fiber dimensions.

As the violin-mode frequencies and their variation, originating from different influences, are of major relevance for this chapter, the full deduction is provided here. The violin modes satisfy the dynamic beam equation [Willems '02] (also referred to as the time dependent Euler-Bernoulli equation), a fourth order partial differential equation.

$$E\,I\,\frac{\partial^4}{\partial z^4}x(z,t) \;-\; P\,\frac{\partial^2}{\partial z^2}x(z,t) \;=\; \rho_L\,\frac{dx^2(z,t)}{d^2\,x} \tag{5.1}$$

where $z$ is the axis parallel to the fiber, $\rho_L$ is the material linear mass density, and

$$I = \frac{\pi}{4}\cdot R^4 \tag{5.2}$$

is the bending moment of inertia (also referred to as the secondary moment of area) of the fiber, $R$ is the fiber radius. By separating the variables one finds (assuming that $x(z,t)$ is of the form $x(z)\,e^{i\omega t}$ )

$$E\,I\,\frac{\partial^4}{\partial z^4}x(z) \;-\; P\,\frac{\partial^2}{\partial z^2}x(z) + \rho_L\,\omega^2\,x(z) = 0 \tag{5.3}$$

where $\omega = 2\pi f$ is the angular frequency of the oscillation. The solution of this differential equation is the transcendental equation

$$X(z) = A\cos(k_-\,z) + B\sin(k_-\,z) + C\cosh(k_+\,z) \\ + D\sinh(k_+\,z) \tag{5.4}$$

with the coefficients $k_-$ and $k_+$ being

$$k_- = \left(\frac{\sqrt{P^2 + 4E\,I\rho_L\,\omega^2} - P}{2E\,I}\right)^{1/2}$$

$$\tag{5.5}$$

$$k_+ = \left(\frac{\sqrt{P^2 + 4E\,I\rho_L\,\omega^2} + P}{2E\,I}\right)^{1/2}$$

The fiber ends are attached to relatively heavy masses and hence, can be considered as fixed. Thus, the boundary conditions are given by

$$x(0) = \frac{\partial}{\partial z}x(0) = \frac{\partial}{\partial z}x(L) = x(L) = 0 \tag{5.6}$$



$f_1$  $f_2$

**Figure 5.1:** The first two violin modes of a fiber.

Using these boundary conditions leads to a system of coupled equations for the constants A, B, C, D in Equation (5.4). A nontrivial solution only exists if the characteristic equation of the system equals zero:

$$0 = 2k_+ \, k_- \, (1 - \cos(k_- \, L) \cosh(k_+ \, L)) \, + \, (k_+^2 - k_-^2) \sin(k_- \, L) \sinh(k_+ \, L) \qquad (5.7)$$

With the approximation that $1 \ll k_+ \, L$ follows an expression for the frequency of the $n$th violin mode

$$\omega_n = \frac{n\pi}{L} \sqrt{\frac{P}{\rho_L}} \left[ 1 + \frac{2}{L} \sqrt{\frac{E\,I}{P}} + \left( 4 + \frac{(n\pi)^2}{2} \right) \frac{2}{L^2} \frac{E\,I}{P} \right] \qquad (5.8)$$

The first term on the right hand side of Equation (5.8)

$$\omega_n = \frac{n\pi}{L} \sqrt{\frac{P}{\rho_L}} \qquad (5.9)$$

reflects the violin-mode frequency of an ideal string. However, the stiffness $EI$ of the fiber generates a recoil that leads to the additional terms in Equation (5.8). These two terms are also closely related to the dilution factor for the violin modes as will be shown in the next section.

### 5.1.2 Violin-mode $Q$'s

The $Q$ of the violin modes depends on various parameters: The bulk loss of the fiber material, the surface quality, the tension $P$, the density $\rho$ of the fiber material, the heat capacity, the thermal conductivity, the coefficient of thermal expansion, and the temperature dependence of the Young's modulus. Finally the fiber geometry in terms of the surface to volume ratio, the fiber length, and the shape of the fiber ends influence the $Q$.

The energy inherent in the violin-mode oscillation is only partly stored in elastic energy via the deformation of the suspension filament. Part of the energy is stored in the lossless gravitational field by lifting the suspended mass. As a consequence, the loss of the fiber $\phi_f$ itself is diluted by loading the fiber via a suspended mass. In the absence of velocity dependent damping such as residual gas damping, the effective loss for the $n$th violin-mode oscillation is described by

$$Q_n^{-1} = \phi_n = \phi_f / D_n \qquad (5.10)$$

where $D_n$ denotes the mode-number dependent dilution factor. The dilution factor is given by [Willems '02]

$$D_n^{-1} = \frac{2}{k_+ L} \left[ 1 + \left( 4 + \frac{(n\pi)^2}{2} \right) \frac{1}{(k_+ L)} \right] \qquad (5.11)$$

121

The loss of the fiber itself is composed of the bulk loss $\phi_{\text{bulk}}$, nonlinear thermoelastic loss $\phi_{\text{nonlin}}$ including linear thermoelastic loss, and loss due to dissipation associated with the surface. Please see Chapter 2 for a discussion of the origin of the different loss contributions.

$$\phi_{\text{f}} = D_n^{-1} \cdot \left[ \left( 1 + \frac{8\,d_s}{R} \right) \phi_{\text{bulk}} + \phi_{\text{nonlin}} \right] \tag{5.12}$$

where $d_s$ denotes the dissipation depth, a measure of the surface quality for a given material [1]. $d_s$ is related to the depth of micro cracks in the materials surface, which are believed to be responsible for the surface loss. Energy from the violin-mode oscillation is dissipated via friction inside these micro cracks. Thermal flow irreversibly distributes the energy in the fiber material. Thus, the material's bulk loss is degraded at the surface. This effect leads to the dependence of the violin-mode $Q$'s on the surface to volume ratio.

The thermoelastic loss is described by

$$\phi_{\text{thermoel}} = \frac{E\,\alpha^2\,T}{C_v} \frac{\omega\tau_R}{1 + (\omega\tau_R)^2} \tag{5.13}$$

with $\alpha$ being the coefficient of thermal expansion (CTE) of the fiber material. $C_v$ is the materials heat capacity per volume and

$$\tau_R = \frac{4R^2}{13.55\,D} \tag{5.14}$$

with $D$ denoting the thermal diffusion coefficient. The nonlinear part of the thermoelastic loss is accounted for by expanding Equation (5.13) to

$$\phi_{\text{nonlin}} = \frac{E\,(\alpha - u_0\beta\,)^2\,T}{C_v} \frac{\omega\tau_R}{1 + (\omega\tau_R)^2} \tag{5.15}$$

where $u_0$ is the static strain in the suspension fiber.

$$u_0 = \frac{P}{A\,E} \tag{5.16}$$

$\beta$ describes the temperature dependence of the Young's modulus of the fiber material

$$\beta = \frac{(dE/dT)}{E} \tag{5.17}$$

Eventually the recoil loss from the support structure may degrade the violin-mode $Q$. The loss $\phi_n^{\text{recoil}}$ of the $n$th violin mode due to recoil loss can be estimated from a coupled-oscillators analysis [Gillespie '94].

---

[1]The dissipation depth for flame drawn fused-silica fibers is $d_s \simeq 100\,\mu\text{m}$ [Gretarsson '00].

$$\phi_n^{\mathrm{recoil}} \simeq \frac{(m_n/m_{\mathrm{struct}})\,\omega_n^2\,\omega_{\mathrm{struct}}^2\,\phi_{\mathrm{struct}}}{(\omega_{\mathrm{struct}}^2 - \omega_n^2)^2 + \omega_{\mathrm{struct}}^4\phi_{\mathrm{struct}}^2} \tag{5.18}$$

where $m_n$ denotes the effective mass of the fiber for the $n$th violin mode, $m_{\mathrm{struct}}$ is the mass of the support structure, $\omega_{\mathrm{struct}}$ is the resonance frequency of the support structure, and $\phi_{\mathrm{struct}}$ is the loss of the support structure.

The shape of the fiber ends and the shape of the pin to which the fiber is welded to suspend the mass are also of relevance for the achievable $Q$. A steep step in radius from the fiber to the pin would be desirable, referring to the $Q$. A dumbbell shaped fiber as used for the GEO 600 suspensions, accomplishes a better matching of the mechanical impedance of the fiber and the pin. This is due to the gradual increase of the fiber radius until it meets the radius of the pin. However, as described in Section 4.2.2, the shape of the fiber ends follows the requirements set by the welding procedure.

The best achievable $Q$ of steel-wire violin modes lies of the order $Q \simeq 10^6$ (Section 3.3.5), whereas the $Q$'s of silica suspensions can easily exceed $10^8$. The GEO 600 far-mirror monolithic suspensions show, even though the violin modes are slightly damped, values up to $Q \simeq 2.5 \cdot 10^8$ (Section 5.5). Measurements from Caltech demonstrated violin-mode $Q$'s of up to $5 \cdot 10^8$ [Willems '02].

## 5.2 The requirements for the inboard suspensions

Once the violin modes are excited, they cause the suspended mirror to oscillate as well. Given the fact that the resonant enhancement of the fiber motion scales with the $Q$, the oscillation can reach a significant amplitude. Thus, the fiber motion can be driven by the interferometer length-control feedback actuators to amplitudes that lead, via the induced mirror motion, to instabilities of the length-control servo. A well designed servo could in principle have a unity gain frequency even beyond these resonances without experiencing instabilities. Unfortunately the situation is more complex for the violin modes. The complexity arises from the geometry of the fibers cross section. Due to the production process (Section 4.2), the cross section of the fibers is slightly elliptical. Due to this ellipticity the degeneracy of the two orthogonal eigenmodes of the fiber is broken. During either the fiber production or the welding, the fibers get slightly twisted. By this torque a pair of coupled oscillators is generated, which can cause a phase shift in excess of 180°, as was derived from the measurements of the violin modes of the far north suspension.

Even if the servo design allows for a stable operation due to a low unity gain frequency, other events could excite the violin modes to high amplitudes. Then, as the 1/e amplitude decay time $\tau$ of the fiber motion obeys the law

$$\tau = \frac{Q}{\pi\,f_n} \tag{5.19}$$

the disturbance may last for a long time, affecting the sensitive operation of the detector.

As described in Section 3.9, the interferometer length-control scheme requires the application of feedback signals to the inboard suspensions, using the two actuators of

the reaction pendulum. In order to avoid an excitation of the violin modes by these actuators and for the reasons discussed above, not only the length-control servo must be carefully designed, but also the violin modes must fulfill certain requirements, referring to their $Q$'s and frequencies. At least one high $Q$ notch filter must be included in the servo design to avoid instability at the violin-mode frequencies. The number and shape of the filters needed, depends significantly on the $Q$'s and on the frequency spread of the violin modes. From modeling possible transfer functions of the length-control servo, the following requirements for the violin modes were derived:

1. Fundamental violin mode $Q_1 \leq 3 \cdot 10^6$

2. First harmonic violin mode $Q_2 \leq 2 \cdot 10^6$

3. All frequencies within one mode $f_n$ (i.e., eight frequencies per mode for the two suspensions) within $\pm 5\%$, for the first two modes $f_1$, $f_2$

4. Violin-mode frequencies as high as possible ($f_1 \simeq 650\,\text{Hz}$)

5. Uncoupled vertical mode frequencies $f_\text{v} \simeq 15\,\text{Hz}$

Since the higher order violin modes couple less strongly to the length-control servo, they do not need any extra damping. However, most of the higher order modes will be well damped by the damping of the first two modes.

## 5.3 The Q-measurement facility

For the development and characterization of the damping and tuning method a facility, capable of measuring violin-mode $Q$'s in excess of $10^7$, was set up. Measuring high $Q$ violin modes requires a low dissipation environment. In order to realize this, the fiber under investigation (in the following referred to as the sample fiber) was suspended as the lower stage of an all-monolithic double pendulum (see Figure 5.2). In order to minimize the coupling of the sample fiber to the environment, an isolation bob was suspended monolithically from a fused-silica plate. A silica fiber was welded to a tip, machined into the silica plate. The cylindrical tip has a diameter of 3 mm and a length of 5 mm. Similar tips are machined (i.e., grinded) into both sides of the isolation bob and into the lower mass, both made from fused quartz. A fiber of different length and diameter was taken for the isolation stage, to reduce the coupling between the two pendulum stages. With a weight of 220 g, the isolation bob provides a good bob/sample mass ratio, since the mass $m$ of the fiber is only about

$$m \simeq \pi\, r^2\, L\, \rho \simeq 24.5\,\text{mg} \tag{5.20}$$

where $L$ denotes the fiber length and $\rho = 2.2\,\text{g}\,\text{cm}^{-3}$ the mass density of fused silica. In Equation (5.20) the fiber is assumed to be of an ideal cylindrical shape with a radius of $112.5\,\mu\text{m}$. A more thorough calculation, based on the measured fiber radii, accounts for

the variation of the fiber diameter along the fiber length. The radius of the fibers can approximately be described by

$$
r(z) \simeq \begin{cases} 105\,\mu\text{m} + 15\,\mu\text{m} \cdot \cos\left(\frac{2\pi}{L} \cdot z\right) & \text{for} \quad \frac{L}{4} \leq z \leq \frac{3L}{4} \\ 105\,\mu\text{m} & \text{else} \end{cases}
\tag{5.21}
$$

The mass of the fiber is thus given by

$$
m = \pi\,\rho \int_0^L r^2(z)\,dz \simeq 23.4\,\text{mg}
\tag{5.22}
$$

However, since the ends of the fiber are in very good approximation fixed, the central section of the fiber experiences a much greater amplitude than the ends. Hence, the mass of the fiber has to be weighted with the oscillation amplitude distribution over the fiber length to obtain the effective mass. The effective mass of the oscillating fiber can be derived from the velocity $\dot{x}(z,t)$ of the fiber. The displacement of the fiber can be described by

$$
x(z,t) = C \sin\left(\frac{\pi}{L} \cdot z\right) \cos(\omega t)
\tag{5.23}
$$

where $z$ is measured along the longitudinal axis of the fiber and $C$ denotes the amplitude of the oscillation.

$$
\dot{x}(z,t) = \frac{dx(z,t)}{dt} = C\,\omega \sin\left(\frac{\pi}{L} \cdot z\right) \sin(\omega t)
\tag{5.24}
$$

The absolute value of the velocity $|\dot{x}(z,t)|$ is maximal at times $\omega t = \pi\,n$, $n \in \mathbb{N}$, which are the zero crossings of the fiber.

$$
|\dot{x}(z,t)|_{max} = C\,\omega \sin\left(\frac{\pi}{L} \cdot z\right)
\tag{5.25}
$$

At this moments the energy E stored in the fiber is purely kinetic. With $A$ being the cross section of the fiber, the energy is given by

$$
\begin{aligned}
\text{E} &= \frac{1}{2}\,A\,\rho \int_0^L |\dot{x}(z,t)|_{max}^2\,dz \\
&= \frac{1}{2}\,A\,\rho\,C^2\,\omega^2 \int_0^L \sin^2\left(\frac{\pi}{\text{L}} \cdot z\right) dz \\
&= \frac{1}{2}\,A\,\rho\,C^2\,\omega^2 \cdot \left(\frac{L}{2} - \frac{L}{4\pi}\sin\left(\frac{2\pi}{L} \cdot L\right)\right) \\
&= \frac{1}{2}\,A\,\rho\,C^2\,\omega^2 \cdot \frac{L}{2} = \frac{1}{2}\,\frac{A\,\rho\,L}{2}\,C^2\,\omega^2 \\
&= \frac{1}{2}\,\frac{m}{2}\,\omega^2\,C^2
\end{aligned}
\tag{5.26}
$$

The factor $\omega^2 C^2$ is the square of the velocity of the central section of the fiber at the zero crossing. Hence Equation (5.26) gives the energy of an oscillator with the frequency $\omega$ with a point mass $m/2$ at half length of the fiber. This is the effective mass of the oscillating fiber for the fundamental violin mode. Hence, the effective mass ratio of the isolation bob to the sample fiber is of the order of $2 \cdot 10^4$.

For higher order violin modes the effective mass can be derived from a straightforward consideration of the symmetry.

$$
\begin{aligned}
\mathrm{E_n} &= \frac{n}{2}\, A\, \rho\, C_n^2\, \omega_n^2 \int_0^{L/n} \sin^2\left(\frac{\pi}{\mathrm{L/n}} \cdot z\right) dz \\
&= \frac{n}{2}\, A\, \rho\, C_n^2\, \omega_n^2 \cdot \left(\frac{L}{2n} - \frac{L}{4n\pi}\sin\left(\frac{2\pi}{L/n} \cdot L/n\right)\right) \\
&= \frac{1}{2}\,\frac{m}{2}\,\omega_n^2\, C_n^2 \qquad , n \in \mathbb{N}
\end{aligned}
\tag{5.27}
$$

where $n$ is the mode number starting from $n = 1$ for the fundamental mode $f_1$. Thus, the effective mass itself is independent of the mode number. For the case of the fibers used for the GEO 600 suspensions this does not hold completely due to the radius variation along the fibers length. A consequence of this variation is the fact that each mode has an individual effective radius. This effective radius becomes a rather complicated function for higher order modes. For the purposes of this chapter it is sufficient to assume an equal effective mass for the first two modes, bearing in mind that the mass of the $f_2$ mode is slightly lower than this estimate would suggest.

The isolation bob itself is suspended from a big fused-silica plate ($\sim 7\,\mathrm{kg}$) by the aforementioned isolation fiber. The fused-silica plate is clamped to the lower side of an aluminum top plate. By the use of clamps that exert the clamping force via a small steel ball on the silica plate and the use of small spacers between the silica plate and the top plate, friction loss of the clamping should be minimized. The aluminum top plate finally is supported by three sturdy aluminum posts. In order to decouple the suspension further from the support structure and thus reduce the recoil loss, the top plate is loaded with about 50 kg of extra weight. For a further decoupling of the whole setup from seismic noise, it was mounted on top of a granite plate of about 750 kg, supported by four rubber posts. The thereby formed mechanical low-pass filter, proved to provide a sufficient isolation performance to allow measurements at the comparatively high frequencies of several hundreds of Hz.

Another influence on the $Q$ is the velocity dependent gas damping. The $Q$ of a fiber violin mode under atmospheric pressure is only of the order of $\sim 10^3$. For the reduction of the dissipation due to gas damping, the pendulum and the support structure had to be enclosed into a vacuum system. When evacuating the vacuum system for the first time, the achievable pressure was of the order of $10^{-2}\,\mathrm{Pa}$ ($10^{-5}\,\mathrm{mbar}$), limited by the small turbo-molecular pump that was used. The achievable mechanical $Q$'s at this residual pressure were of the order of $Q \leq 10^6$. Thus, the pumping setup was changed to a double turbo-molecular pump, with a pump rate of about $200\,\mathrm{liter\,s^{-1}}$. By this change one order of magnitude in the residual pressure was gained, now allowing for $Q$'s of up to $3 \cdot 10^7$.
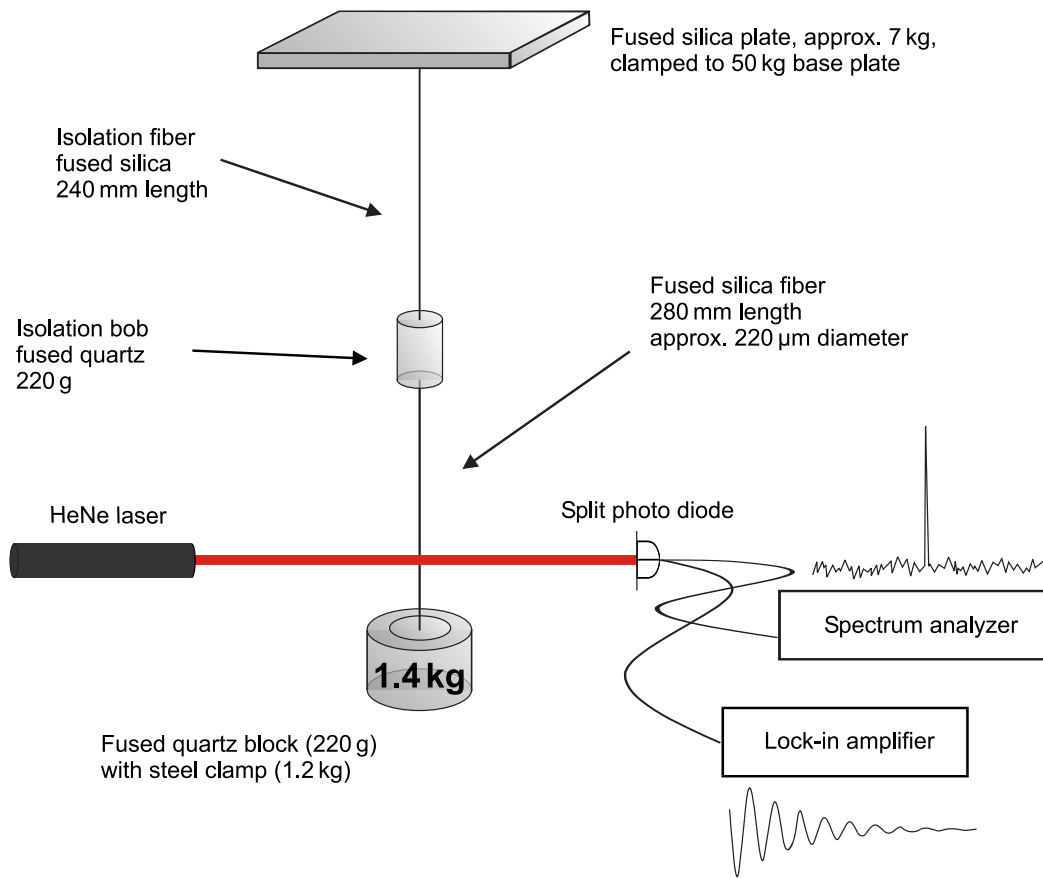
**Figure 5.2:** Setup for the *Q* measurements: A fused-silica plate is rigidly clamped to a top plate
that is mounted on three sturdy posts. A first monolithic suspension stage contains
an isolating bob of 220 g of fused quartz. A fiber having the parameters needed for
the GEO suspensions (i.e., length, diameter, bounce-mode frequency) is welded to the
bob. This fiber is loaded to the nominal load of 1.4 kg by welding it to a second bob,
which supports a stainless steel clamp. A HeNe Laser and a split photo diode are
used for the readout of the fiber motion, while an electrostatic actuator (not shown
here) is used to excite the fiber resonances.

The nearby roughing pump, required to pump the employed double turbo-molecular
pump, is suspended from a coil spring to minimize the vibrational coupling to the mea-
surement setup via the ground. Furthermore, the tube connecting the roughing pump
and the turbo pump is modified to form a double low pass filter. This is done by fixing
weights of about 10 kg to two sections of the tube.

In order to excite the violin modes for the measurements, a diminutive electrostatic
actuator is employed. This electrostatic actuator consists of a cylindrical Macor® block of
25 mm length and 8 mm diameter, with a bifilar thread machined around it. Two copper
wires are spooled around the cylinder in the two parallel grooves of the double thread.
One of the wires is grounded while the other wire is charged with amplitude-modulated
high voltage ($\sim 360\,\mathrm{V_{pp}}$). The modulation frequency is supplied by a spectrum analyzer

and adjusted manually without closing a feedback loop. This setup is capable to enhance the violin modes to about 80 dB above the noise level of the readout system.

A HeNe laser and a split-photo diode are used to read out the fiber oscillation. The enlarged laser beam is adjusted to illuminate the fiber through a view port in the vacuum tank and then sensed via the split-photo diode. This is done such that the shadow of the fiber covers a part of both independent sections of the split diode.

The differential signal of the split photo diode is heterodyned to a lower frequency by beating it against a local oscillator. This is achieved by the use of a lock-in amplifier, providing the signal that is eventually recorded with a computer based data-acquisition system.

The $Q$'s of the samples can be calculated from the ring-down times, using

$$Q_n = \pi \cdot f_n \cdot \tau \tag{5.28}$$

where $f_n$ is the resonance frequency of the $n$th eigenmode and $\tau$ is the time measured for the decay to 1/e amplitude.

## 5.4 Damping and tuning

The idea behind the damping method is to degrade the $Q$ of well defined sections of the fiber, while the $Q$ of the rest of the fiber should remain as it was. This is a useful approach since the loss of the violin modes is generated not solely at the fiber ends, where the strongest bending occurs, but also at certain sections along the fiber. Referring to Figure 5.1 the fiber bends along its entire length for the fundamental violin mode, whereas it has a bending node at the center for the first harmonic mode. As a result, part of the loss for these two modes is generated at different sections of the fiber. Except for the area close to the upper attachment point, an ideal fiber has an infinite radius of curvature over its entire length for the pendulum mode [Logan '93]. Hence, degrading the violin-mode $Q$ does not necessarily influence the $Q$ of the pendulum mode (see Section 5.4.7). The different dependence of the loss generation on the fiber sections for the different modes allows for the aimed mode-selective degradation of the $Q$'s.

The damping is done by the application of some "lossy" material to the relevant sections of the fiber. These sections are selected such that the fiber has a reasonable bending radius for the violin mode in question but not for the pendulum mode. As mentioned above, except for the area around the attachment points the smallest radius of curvature is in the fibers center for the fundamental eigenmode $f_1$, and at about one fourth of the fibers length for the first harmonic mode $f_2$, respectively. These section are used for the application of the damping material.

Due to the way the fibers are produced, their central section is slightly thicker than the outer sections. The breaking load and the dilution factor of the fiber are dominated by the thinner sections, while the violin-mode frequencies also depend on the thicker central section. To produce a strong fiber with high violin modes, it is desirable to produce a homogeneous fiber. However, the homogeneity of the fibers is sufficient when the above mentioned parameters are in the targeted region. Before coating the fiber, the

homogeneity of the fiber's diameter over its entire length is judged by visual inspection of the symmetry of the occurring bending radius over the fiber's length, when bending it such that it nearly forms an $\Omega$. The coating for the first higher order violin mode $f_2$ is then applied at the thinner side of the fiber, at one forth of the fibers length.

The lossy material was chosen to be amorphous Teflon® [2], because we have proven earlier that it is ultra-high vacuum compatible (Section 5.4.1) and does not degrade the fiber's strength [Barr '02]. The Teflon® is dissolved in Fluorinert™ [3] and its viscosity can be set by the amount of solvent added. To bring the Teflon® onto the fibers, a little stick of Teflon® is used to pick up a drop of the dissolved material. Only this drop is brought into contact with the fiber, because the fibers must not be touched with anything else. The drop is then guided back and forth until it is almost completely applied to the fiber. This is done several times, such that a coating is formed (see Figure 5.3). The solvent has a high vapor pressure and hence, it almost completely evaporates within half an hour, leaving the Teflon® coating on the fiber. By measuring fibers with different coating lengths and diameters, it was proved that the damping effect scales much more strongly with the coating diameter then with the coating length. This clearly indicates that the damping effect is not due to rubbing of the fiber with the damping material, but to the loss of the Teflon® itself (see Section 5.9). The downward shift of the violin-mode frequencies scales simply with the added mass, weighted with the coating position. Since the first harmonic violin mode has a node in the center of the fiber, the fundamental mode can be tuned with almost no influence on the first harmonic. Thus, by varying the position, length, and thickness of the coating the frequencies and $Q$'s of the first two violin modes can be separately tuned.
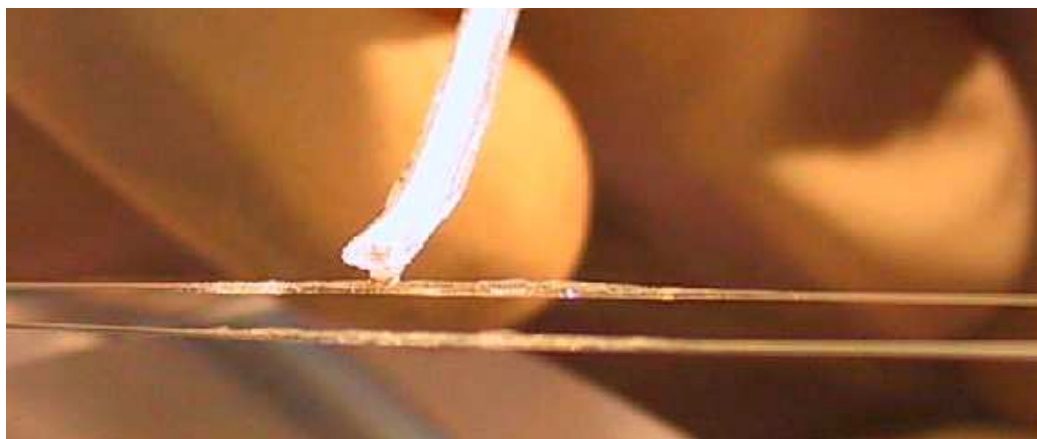


**Figure 5.3:** Close-up view of the coating process: A drop of the dissolved Teflon® is applied with a Teflon® stick, without touching the fiber.

---

[2] By DuPont™, http://www.dupont.com/teflon/
[3] By 3M™, http://www.3m.com/

### 5.4.1 Vacuum compatibility of the damping material

Before utilizing Teflon® as the damping material the vacuum compatibility had to be scrutinized. This was done by coating a comparatively large area (about $30\,\mathrm{cm}^2$) and testing it in a small vacuum chamber (about $10^3\,\mathrm{cm}^3$). The vacuum compatibility of the coating material was verified with a quadrupole mass spectrometer.

### 5.4.2 Compatibility with the mirror coatings

A thorough fluoride analysis of the Teflon® among with its solvent Fluorinert™ FC-75 was performed on behalf of Advanced LIGO in the JPL analytical chemistry labs. The analysis was done by Ion Chromatography (IC). IC separates ions in a sample solution by injecting it into an eluant buffer stream (a dilute aqueous carbonate bicarbonate solution) that is pumped through an anion exchange column. The separated ions are measured by a conductivity detector system. Prior to the detection the eluent is neutralized while the analytes are left in the charged form, thereby allowing for analyses at very low analyte concentrations.

The analysis revealed that the Teflon® solution has 0.67 ppm extractable fluoride, while the Fluorinert™ solvent has 0.025 ppm extractable fluoride. These very low levels indicate that the material is fully fluorinated with stable end groups and hence safe to use. [Armandula]

### 5.4.3 Measurements in the $Q$ lab

Using the $Q$-measurement setup and the damping method described above, a fiber with the parameters needed for the inboard suspension (Section 5.2) was prepared. As a first step a fiber with the parameters required for the inboard suspensions referring to the vertical resonance frequency, the length, and a fundamental violin-mode frequency as high as 740 Hz was welded in the monolithic double pendulum as the sample fiber. The $Q$'s and frequencies of the first two modes were measured prior to the application of a small amount of the damping material at two sections of the fiber. The application
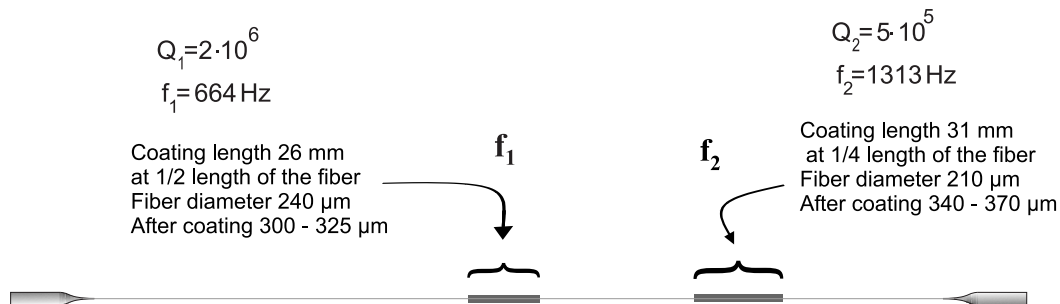


**Figure 5.4:** In an iterative process of coating and remeasuring eventually a reference fiber was produced. Since this fiber showed all parameters needed for the inboard suspensions, it was taken as a reference for the production of the required amount of fibers for the two suspensions.
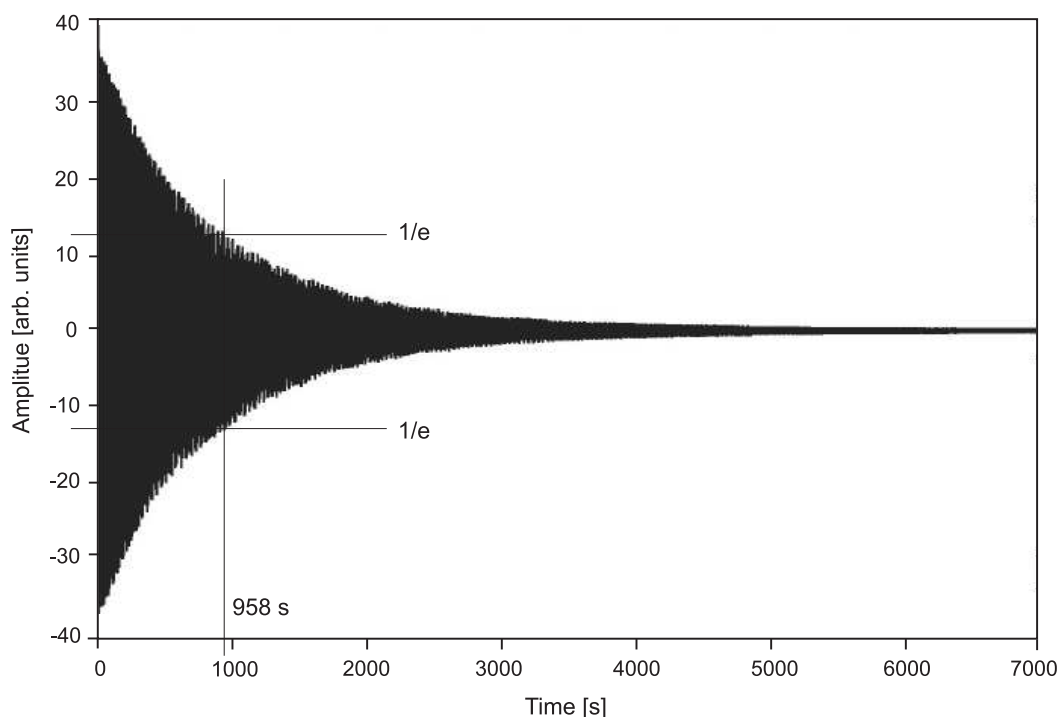
**Figure 5.5:** Ring-down time measurement of the fundamental violin mode of the reference fiber. The fiber was coated such that it had a $Q$ of $2 \cdot 10^6$ at $f_1$=664 Hz. Simultaneously the second order mode was damped to a $Q$ of $5 \cdot 10^5$ at $f_2$=1313 Hz.

was done by bending the upper stage of the double pendulum by $90°$ into a horizontal position and holding the lower fiber straight while a second person applies the coating. Measuring and remeasuring the $Q$'s and frequencies with gradual application of more Teflon® eventually led to a fiber with the properties aimed for (see Figure 5.4). The fiber showed quality factors of $Q_1 = 2 \cdot 10^6$ and $Q_2 = 5 \cdot 10^5$ at $f_1 = 664$ Hz and $f_2 = 1314$ Hz for the fundamental and the first harmonic mode, respectively. Figure 5.5 shows the ring-down time measurement of the fundamental violin mode of the reference fiber.

This fiber was taken as a reference for the production of the required number of fibers for the two inboard mirror suspensions. Since it is not possible to unweld a fiber and then use it for a further suspension, it is not possible to measure the violin-mode $Q$'s before the fiber is welded in and suspended in vacuum. However, it is possible to measure the frequencies and thus it is possible to reproduce fibers with a similar downward shift in frequency for the first two modes. If the coatings and fibers are of a similar geometry then comparable reductions in $Q$ are also to be expected.

### 5.4.4 Downward shift of the violin-mode frequencies

The downward shift of the violin-mode frequency originates from the mass added by the coating to the effective fiber mass (equations (5.26) and (5.27)). The added mass has to be weighted with its position when calculating the effectively added mass. In our case

the coated sections are short compared to the bending radii of the fiber and hence, can be treated as point like. Furthermore the coating was applied at sections where the first higher order mode $f_2$ has either a node or a maximum. Thus the effective mass for $f_2$ is simply the mass added at one fourth of the fiber length. For the fundamental mode $f_1$ the coating at the central section of the fiber counts fully, while the coating at one fourth of the length adds only weighted by a certain factor. This factor can be derived from the kinetic energy E stored in the coating. Referring to Equation (5.26) the kinetic energy for a mass at $z = L/4$ is given by

$$\mathrm{E} = \frac{m}{2}\,C^2\,\omega^2\sin^2\left(\frac{\pi}{4}\right) \; = \; \frac{1}{2}\,\frac{m}{2}\,C^2\,\omega^2 \tag{5.29}$$

Hence, the mass added at one fourth of the fiber length is weighed with a factor of 0.5 for the fundamental mode. The frequency shift due to the coating can be derived starting from

$$\omega = \sqrt{\frac{\kappa}{m}} \tag{5.30}$$

The derivative of the frequency with respect to the mass is given by

$$\frac{\partial\,\omega}{\partial m} = -\frac{1}{2}\,\sqrt{\kappa}\cdot m^{-3/2} = -\frac{1}{2\,m}\,\omega \tag{5.31}$$

The relation between the following derivatives allows for the backwards conclusion of the added mass from the observed frequency shift.

$$\frac{\partial m}{m} = -2\,\frac{\partial\omega}{\omega} \tag{5.32}$$

As described above, it is possible to tune the fundamental mode $f_1$ almost without influencing the first higher order mode $f_2$, since the latter one has a node at the center of the fiber. Tuning the first harmonic mode $f_2$ influences, however, the fundamental mode $f_1$, but less strongly then the first harmonic itself. Figure 5.6 illustrates the observed frequency shifts of a coating run (including 25 fibers) due to the individual application steps for the fundamental and the first higher order mode. The resulting spread for the fundamental violin mode was $\pm 2.75\,\mathrm{Hz}$. For the first higher order mode a spread of $\pm 6\,\mathrm{Hz}$ was achieved. Two examples of the tuning procedure, demonstrating the independence between the two modes are given in Table 5.1 .

From the average downward shift of about 50 fibers treated with the damping material the applied mass was calculated, using Formula (5.32). The derivation of the applied mass from the obtained frequency shift is based on the calculations of the effective fiber mass. This calculation is yet based on the fiber radius, which is known to vary along the fiber length by an individual amount for each fiber. The comparatively large error in the knowledge of the fiber mass, especially for the second mode, inhibits a precise determination of the absolute values of the added mass. Due to the uncertainty of the ratio of the effective mass for the first two modes, the ratio of the mass added to the two
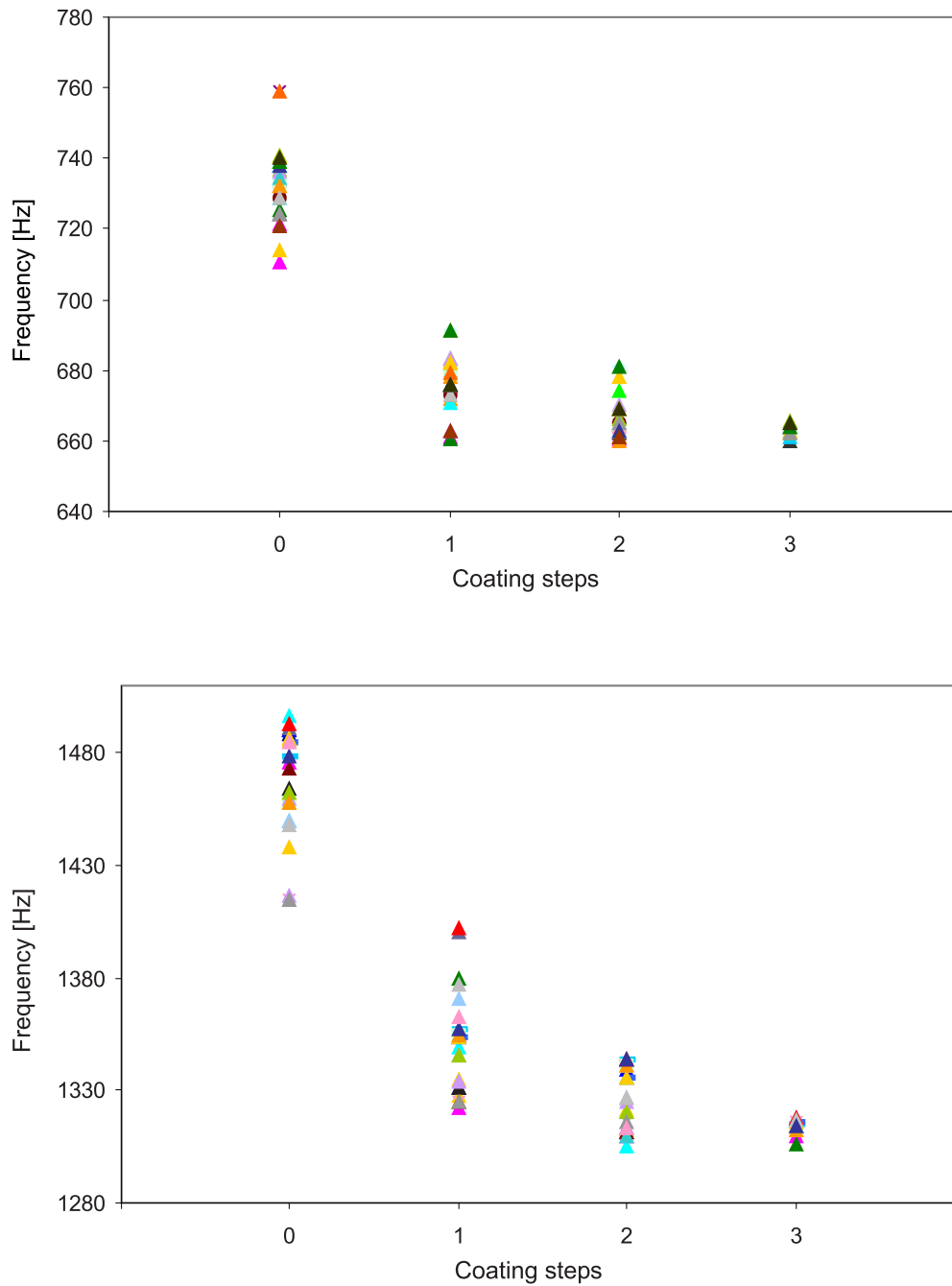
**Figure 5.6:** The development of the violin-mode frequencies due to the application of the damping material. The frequencies of the first two modes for the 25 fibers of one coating run are displayed. The upper graph shows the evolution of the fundamental mode with the stepwise application of the damping material. The lower graph shows the evolution of the first higher-order mode.

|          | Uncoated | After coating | After corr. coating | After 2nd corr. coating |
|----------|----------|---------------|---------------------|-------------------------|
| $f_1[Hz]$ | 741     | 691           | 678                 | 665                     |
| $f_2[Hz]$ | 1415    | 1325          | 1316                | 1316                    |
| $f_1[Hz]$ | 724     | 676           | 662                 | 660                     |
| $f_2[Hz]$ | 1490    | 1380          | 1353                | 1306                    |

**Table 5.1:** Two examples of the frequency tuning procedure. The coating was applied in an iteration to meet the requirements. In the first example the fundamental violin mode $f_1$ was still to high when the first harmonic $f_2$ was already in the target region. In the second example the fundamental mode $f_1$ of a different fiber was already in the target region when the first harmonic mode $f_2$ was still to high. Please note that in the latter case the coating at the central fiber section was not completely set within the measurement accuracy. Hence, an expected upward drift of a few Hz was most likely compensated by the downward shift due to the last corrective coating. The achieved results after the second correction demonstrate the independence between the modes.

coated regions can also be derived with only moderate accuracy. These uncertainties are accounted for when deriving the errors, stated in the next paragraph.

The observed average downward shift for the fundamental mode was 70.6 Hz, starting from 733.7 Hz. The effective mass of the coating is found to be $2.3 \pm 0.1$ mg for the fundamental mode. The average downward shift observed for the first harmonic mode is 153.1 Hz, starting from 1469.0 Hz. This results in an effective mass of the coating of $2.4 \pm 0.2$ mg for the first harmonic mode. Referring to the above considerations about the effective mass for the different modes (Section 5.3), the mass measured for the fundamental is composed of half the mass added to one forth of the length plus the mass added at the center of the fiber. The mass measured for the first harmonic mode is simply the mass added at one forth of the fiber length. Thus, the conclusion is that $(1.1 \pm 0.15)$ mg coating material was added to the central section of the fiber and $2.4 \pm 0.2$ mg at one quarter. The mass ratio of the two sections is $m_{center}/m_{quarter} = 0.46 \pm 0.1$. As was pointed out in Section 5.3, the effective mass of the mode $f_2$ was estimated too high. Hence, the derived mass ratio may require a small upward correction. This result is in agreement with the coating parameters, displayed in Figure 5.4. If the mean values of the displayed coating diameters are taken, the parameters suggest a mass ratio of $\sim 0.41$. However, when inspected with a microscope, the coatings were found to have relatively large peak-valley deviations (i.e., the coatings are not entirely smooth). This fact requires to account for relatively large errors in the coating parameters displayed in Figure 5.4.

In Section 5.8.5, measurements of the upward shift of the frequencies due to the residual outgassing of the damping material and its solvent, after being in vacuum for about one year, are presented. The analysis reveals the individual decrease of mass for the two section of the fiber. The obtained ratio between the two sections is $\sim 0.56$. The measurement of the mass decrease depends, however, also on the individual aspect ratio of

the coating layers at the two sections. Thus, it is expected to overestimate the outgassing of the central section, which has a greater surface to volume ratio. The required correction leads to a decrease of the measured ratio.

### 5.4.5 Treatment of the fibers before welding

Subsequent to the production, the fibers are evaluated as described in Section 4.2.2. The evaluation includes the measurement of the first two violin-mode frequencies for each fiber. Depending on the initial frequencies, each fiber is then treated individually with the damping material to obtain the target frequencies, set by the above described experiments. The fibers are preselected referring to their violin-mode frequencies to ensure that the required downshift is equivalent to a sufficient damping. The coating is applied to the selected fibers while they are clamped in the cutting jig (see Figure 4.7 for a picture of a fiber clamped in the cutting jig). The fibers are stored in the transportation box, which is used to transport the fibers from Hannover to the 25 km distant detector site. The transportation box has four removable frames, each carrying eight fibers. The fiber under treatment is taken from the frame, coated, and then inserted back to let the solvent evaporate. During this dry-out phase, the associated violin-mode frequency is subject to an upward drift of about 100 Hz. After about 30 minutes the evaporation has progressed enough to allow for reliable measurements. The violin-mode frequencies are measured as described in Section 4.2.2.3. A sturdy frame allows to suspend a fiber from a clamp. A lower clamp loads the fiber with the nominal weight of 1.4 kg. The violin modes are exited by tapping the remaining part of the silica rod, protruding from the clamp at the upper fiber end. The readout is done with a HeNe laser and a split photo diode (please see Figure 4.4 for the setup used). The signal is analyzed with an oscilloscope and a spectrum analyzer.

The fibers are consequently recoated and remeasured in an iterative process to eventually obtain the claimed frequencies for the first two modes (see Figure 5.6). Since it has not yet been demonstrated to remove some of the already applied coating material without damaging the fiber, the frequencies must converge from higher values to the target frequencies. More precisely, an over-coated fiber is irrecoverably damaged.

Before coating the fibers, frequencies of $f_1 = 738\,\mathrm{Hz} \pm 3.5\%$ and $f_2 = 1460\,\mathrm{Hz} \pm 4.2\%$ were obtained for the 25 fibers of one typical production run. By the application of the coating material the frequencies could be brought to $f_1 = 663\,\mathrm{Hz} \pm 0.4\%$ and $f_2 = 1314\,\mathrm{Hz} \pm 0.5\%$. The fact that the center frequencies of this set of coated fibers were only 1 Hz away from the target frequencies for both modes, demonstrates the remarkable accuracy of the method.

### 5.4.6 In situ tuning after the welding

Unfortunately, the frequency spread is very likely to be re-enlarged by the welding and by suspending the monolithic stage. This is caused by the fact that it is not possible to cut the four fibers, required for one suspension, exactly to the same length and weld them in under exactly the same tension. Welding slightly unequally with respect to the center of mass of the mirror, also causes a different tension of the fibers when the monolithic

stage is suspended. Thus, the violin-mode frequencies needed to be remeasured after the fibers were welded into the monolithic stage. This had to be done with the lower mass suspended.

The catcher, described in Section 4.3, is used to position the masses for the welding of the fibers. Directly after the welding, the new monolithic stage can be suspended inside the catcher, to confirm its strength, and to measure the violin-mode frequencies (Section 4.3.3). The violin-mode measurements are again done with a split photo diode and a HeNe laser. So far, tapping the remainder of the glass rod at the fiber end was used as the actuation to excite the modes. This is of course no longer possible, once the fibers are welded to the mirror and intermediate mass. Hence, a gentle wave with a sheet of tinfoil is applied to excite the fiber resonances. The induced air motion excites the violin-mode oscillations sufficiently strong to record a spectrum with a spectrum analyzer. The monolithic stage is clamped back into the catcher subsequent to this measurements. The catcher holds the two masses firmly enough in place to safely rotate the clamped suspension around all axes and to move it over long distances (e.g., from one end station of GEO 600 to the other). Hence, it can be laid on its sides, providing access to the fibers for the application of an additional amount of Teflon®, to reduce the frequencies where required. The spread of the fundamental mode for both suspensions was $\Delta f_1 = \pm 3.35\%$ after welding and suspending inside the catcher. A corrective coating was applied onto two of the eight fibers, further reducing the frequency spread of the fundamental mode to $\Delta f_1 = \pm 2.65\%$., including both suspensions.

As mentioned above, an additional re-enlargement of the spread can be expected from mounting the monolithic stages in the triple-pendulum suspensions. The origin of this extra spread is the coupling of both pitch and roll alignment to the fiber tensions via a shift of the center of mass (COM) of the lower mass. The COM is shifted since the bending point of the fibers is, for stability reasons, above the COM and hence the COM lies not on the axes of roll or pitch motion. This coupling causes any difference between the finally aligned suspension and the test setup to change the fiber tensions. Please see Section 3.11.1 for more details about this coupling and the consequences on the long-term alignment stability.

### 5.4.7 Influence on the pendulum $Q$

The influence of the violin-mode damping on the pendulum mode $Q$ can be evaluated by following a straightforward approximation of the occurring bending of the fiber sections where the coating is applied, due to the pendulum mode. The bending $B(z)$ of a fiber due to the pendulum mode decreases with the distance $z$ from the break-off point (which is in fact not a point but a region that is about 7 mm long in the case of the GEO 600 suspension fibers), following an exponential law

$$B(z) \propto \frac{\mathrm{d}^2}{\mathrm{d}z^2}\, e^{-z/\lambda} \tag{5.33}$$
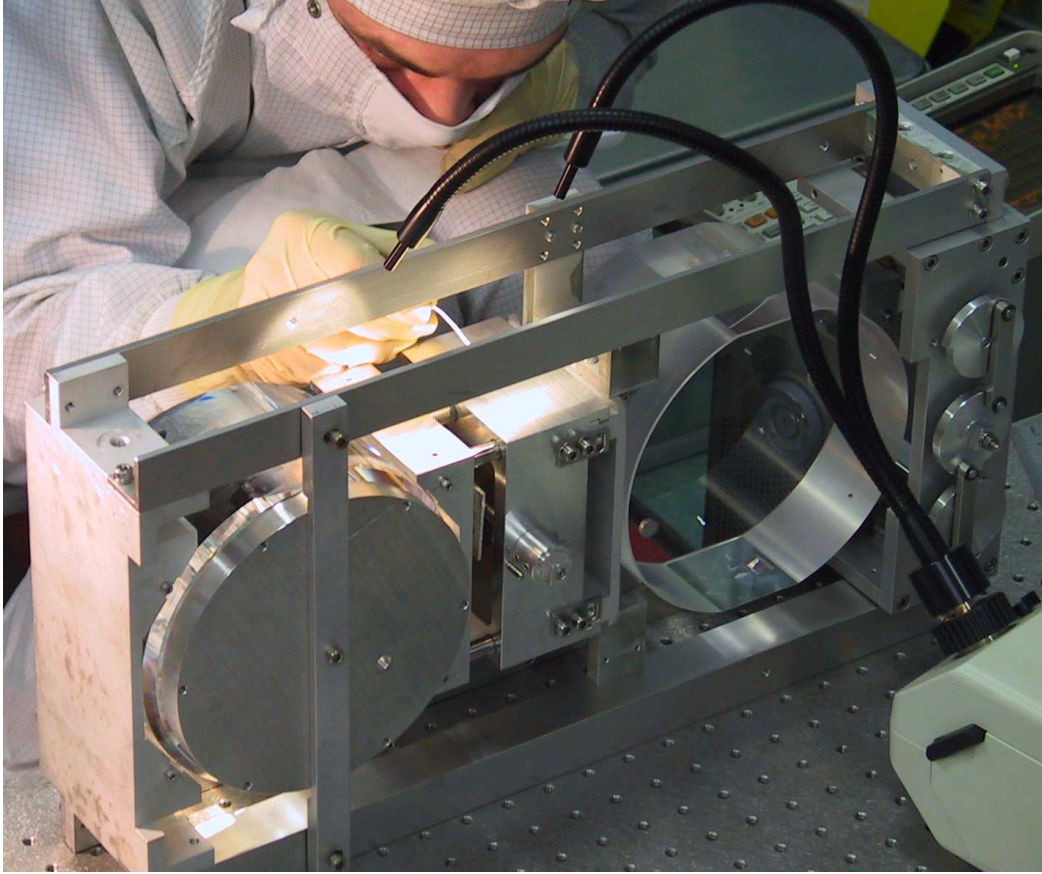
**Figure 5.7:** *In situ* application of the coating to a fiber of an already welded monolithic stage. After the welding of the fibers the frequency spread had increased such that one fiber of this suspension had to be tuned again. The two masses are reclamped such that the catcher can be laid flat on the side to allow for the work on the fiber.

with

$$\lambda = \sqrt{\frac{E_S \cdot I}{P}} \tag{5.34}$$

$E_S$ is the Young's modulus of fused silica ($E_S = 7.2 \cdot 10^{10}$ Pa), $P$ is the fiber tension, and $I = \frac{\pi}{4}R^4$ is the bending moment of inertia of the fiber. With $\lambda$ being of the order of about $10^{-3}$ m, the bending decreases rapidly with increasing distance from the break-off point. Thus, the fiber can be regarded as practically straight at the coated sections for the pendulum mode and hence the degradation of the pendulum mode $Q$ is negligible.

## 5.5 Measurements of the far north suspension fibers

In contrast to the inboard suspensions (Section 4.3.4.2), the far mirror suspensions have no feedback actuators besides the local-control actuators at the upper pendulum mass. Thus, the far mirror suspension's violin modes can only be excited by seismic events and only little damping is required.

Behind the far north mirror is a small electrostatic actuator mounted on a post (electrostatic actuator "on a stick", see Figure 4.9). The post is clamped to the bottom plate of the vacuum tank, holding a small block of Macor$^{\text{TM}}$. The electrostatic actuator itself consists of a copper ring attached to the Macor$^{\text{TM}}$ block. The copper ring is electrically connected to a pin of a feedthrough in the tank. Via this connection the copper ring can be charged with a modulated high voltage. The high voltage is supplied by an audio amplifier, which drives a transformer. The modulation frequency is provided by a spectrum analyzer. This setup was used to excite the violin modes of the far north suspension and with slight modifications also for the measurement of the internal $Q$'s of the test mass (**MFn**) (see Section 4.5).

One obstacle prior to the measurements of the violin modes is the determination of the exact frequencies, hampered by the very small line widths. The $Q$'s are, even after being degraded, still rather high. The line width of the natural frequency oscillation is given by

$$\text{FWHM} = \frac{f_1}{Q} \tag{5.35}$$

As a consequence, the line widths are of the order of $1\,\text{mHz}$ and hence the modes are difficult to detect. Due to the small line width, the employed drive must exactly meet the violin-mode frequency to guarantee a coherent excitation. A band-limited white noise with an amplitude of about $400\,\text{V}_{\text{pp}}$ was used for the search of the violin modes. Since the frequencies were not measured beforehand for the far suspensions, the search concentrated on the frequency range around the theoretical predictions. Due to some uncertainties (i.e., the predictions were based only on the fibers length and on the measurements of the uncoupled vertical mode frequency) the model was of limited accuracy. Due to the weak actuation force of the small electrostatic actuator and the small line width of the violin modes, long integration times are required if the band limitation of the white noise is broadened. Hence, the search had to be performed stepwise, mapping over the relevant frequency space. The GEO 600 data acquisition system was used to record an error-point spectrum of the interferometer length-control servo to search for peaks caused by the violin modes. Figure 5.8 shows some of the violin modes of the far north suspension. The frequencies lie at $666 - 702\,\text{Hz}$. The $Q$'s of the modes were derived from the ring-down times to be $Q = 2.5 \cdot 10^7 - 2.5 \cdot 10^8$. This well meets the requirements for the far mirror suspensions. For the inboard suspensions the requirements are, however, more stringently as is described in Section 5.2 .

The violin modes of the far east suspension could not be measured since there is no actuator in the far east tank. For the same reasons it is not possible to measure the internal eigenmodes of the test mass itself. Instead of an electrostatic actuator, a ring
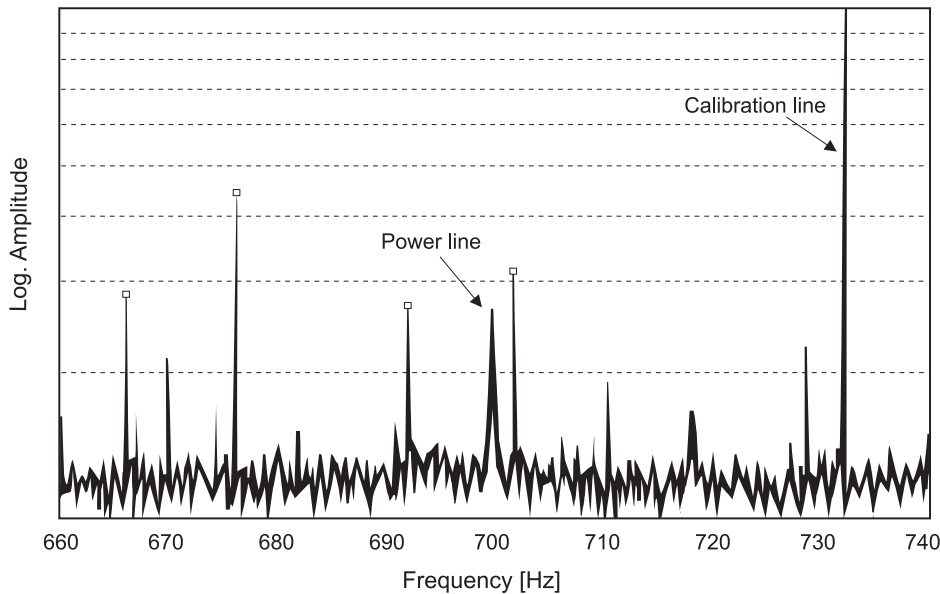
**Figure 5.8:** Error-point spectrum of the length-control servo. Some of the violin modes of the far north suspension were excited with a small electrostatic actuator behind the mirror. The marked peaks in the spectrum correspond to these modes.

heater, which is used for the adaption of the mirror's radius of curvature, is the mounted behind (**MFe**). Appendix B gives a description of the thermal adaption of the mirror's radius of curvature.

Since the sensitivity of the detector was substantially improved during the last months of 2003, latest measurements have revealed the violin-mode frequencies for each individual suspension. These measurements are presented in detail in Section 5.8. The obtained frequencies for the far east suspension are between 642 Hz and 686 Hz.

## 5.6 Measurements of the inboard suspension fibers

After installing the two monolithic stages as the last stages of the two inboard triple pendulums and evacuating the system, the violin modes were excited with the suspended electrostatic actuators. The sinusoidal modulation frequencies were provided by a waveform generator and were adjusted manually to the violin-mode frequencies. An error-point spectrum of the length-control servo was analyzed with a spectrum analyzer to find the frequencies and to adjust the modulation frequencies. The spectrum was then recorded with the data-acquisition system of GEO 600 [Kötter '02]. A snapshot of the error-point spectrum is displayed in Figure 5.9. The achieved frequencies and the spread of the violin modes of the two inboard suspensions is $f_1 = 645.5 \, \text{Hz} \pm 3.86 \, \%$ and $f_2 = 1287 \, \text{Hz} \pm 4.86\%$. The $Q$'s of the first two modes $f_1$ and $f_2$ were derived from the ring-down times to be $Q_1 = 5 \cdot 10^5 - 2.8 \cdot 10^6$ and $Q_2 = 5.4 \cdot 10^5 - 1.0 \cdot 10^6$.

With these frequencies, frequency spread and $Q$'s, the monolithic suspensions well meet the requirements, set by the length-control servo demands.
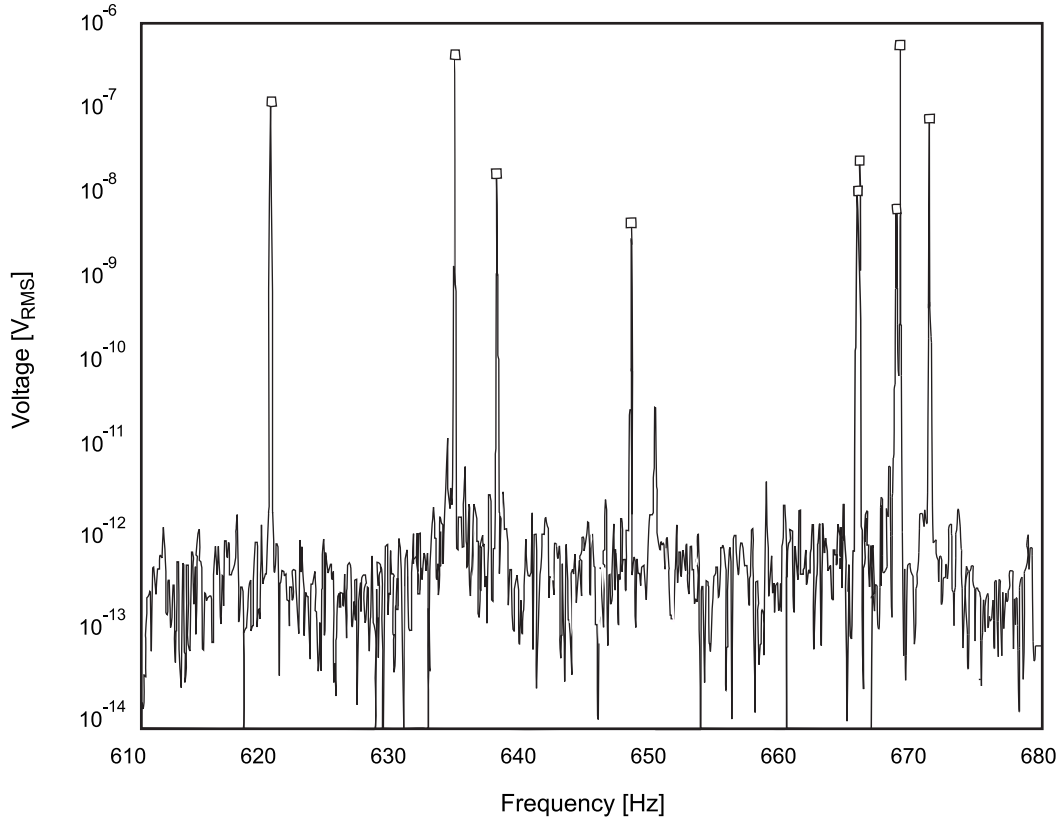
**Figure 5.9:** Error-point spectrum of the interferometer length-control servo. Nine of the sixteen violin-mode frequencies of the inboard suspensions are resolved. The fiber oscillations were exited before with the suspended electrostatic actuator.

## 5.6.1 Replacement of the north inboard suspension

During maintenance work inside the central cluster in July 2003, one fiber of the north inboard suspension broke. After extracting the monolithic stage from the vacuum tank, both fibers on the respective side of the monolithic stage were taken out and replaced before it was re-suspended in the tank. Due to the two new fibers and the re-suspension, the violin-mode frequencies had changed from the values given in the above Section 5.6 .

|          | $f_1$ [Hz] | $\Delta f_1$ | $Q_1$            | $f_2$ [Hz] | $\Delta f_2$ | $Q_2$            |
|----------|------------|--------------|------------------|------------|--------------|------------------|
| Target   | 650        | $\pm 5\%$    | $\leq 3 \cdot 10^6$ | 1300       | $\pm 5\%$    | $\leq 2 \cdot 10^6$ |
| Measured | 645.5      | $\pm 3.86\%$ | $\leq 2.8 \cdot 10^6$ | 1287       | $\pm 4.86\%$ | $\leq 1 \cdot 10^6$ |

**Table 5.2:** The target frequencies, spreads, and $Q$'s of the violin modes versus the values achieved before replacing the **MCn** suspension.

Table 5.3 provides the new frequencies and the new spread for the first two modes of the inboard suspensions along with targeted values.

The new frequencies were not measured by directly driving the resonances but instead derived from the data that were acquired during the S3II data run. The analysis is based on spectrograms of the error-point spectrum of the length-control servo. A detailed analysis of all observed violin-mode frequencies and a comparison with the frequencies measured prior to the replacement of the broken suspension revealed the violin-mode frequencies of the individual inboard mirror suspension. Due to a continuous excitement from residual seismic noise, from the feedback actuation on the suspension, and from thermal noise the violin-mode peaks will not vanish completely with time but rather remain with a certain signal to noise ratio in the error-point spectrum. By analyzing a spectrogram with a frequency resolution of $1\,\text{mHz}$ from a data set of $330\,\text{h}$ it was possible to track down 80 violin-mode frequencies, caused by different orders of violin-mode resonances.

|  | $f_1$ [Hz] | $\Delta f_1$ | $f_2$ [Hz] | $\Delta f_2$ |
|---|---|---|---|---|
| Target | 650 | $\pm 5\%$ | 1300 | $\pm 5\%$ |
| Measured | 650.2 | $\pm 3.49\%$ | 1296 | $\pm 4.02\%$ |

**Table 5.3:** The targeted violin-mode frequencies versus the values achieved after replacing the **MCn** suspension.

## 5.7 Treatment of the beamsplitter fibers

The situation for the fibers of the beamsplitter suspensions is comparable to that for the fibers of the far mirror suspensions. Besides the local-control signals, applied to the upper pendulum mass, there is no feedback applied further down the suspension chain. An excitation of the fiber resonances due to feedback actuation is thus not possible for these two suspension types and only the seismically induced noise has to be accounted for. However, a certain damping is required to avoid the aforementioned interferences with a sensitive detector operation after an accidental excitement of the fiber modes. In order to inhibit any significant excitation of the violin modes due to the seismic and to reduce the ring-down times, the modes were damped, but less strongly than the inboard suspension fibers. An exact tuning of the violin-mode frequencies is neither required for the beamsplitter suspension nor for the far suspensions. Nonetheless, it is desirable to have the violin-mode frequencies of all the interferometer suspensions in a narrow band.

## 5.8 Long-term analysis of the violin-mode frequencies

Altogether, 32 violin-mode frequencies due to the test-mass suspensions and eight frequencies due to the beamsplitter suspension appear per mode number. In order to get a better understanding of the performance of GEO 600, it is desirable to know all violin-mode frequencies, and their drifts, in the most sensitive frequency band of GEO 600. Hence, a search for the violin-mode frequencies was performed, based on the above mentioned spectrogram, derived from the error-point spectrum of the interferometer length-control servo. A spectrogram displays frequency (y-axis) versus time (x-axis). It is a powerful tool to detect oscillations and quantify their drift rates. The spectrogram that was used for the violin-mode frequency search is based on the data acquired during the 14 days long second participation phase of GEO 600 in the S3 run (S3II). The frequency resolution of the spectrogram is limited to 1 mHz due to the available computer power. The data set used to generate the spectrogram was computed on 16 nodes of the Cardiff Helix computer cluster with a computation duration of about five days [4]. It was derived from the error-point spectrum by a line detection algorithm (LineDetectMon GEO++ monitor), which selects oscillations of a given stability that exceed a certain amplitude threshold (or signal-to-noise ratio (SNR)). The threshold was set to the comparatively low limit of SNR $\geq 5$. This low threshold improves the chance to detect many of the violin modes, while on the other hand the total number of lines appearing in the spectrogram is dramatically increased. Figure 5.10 shows the full spectrogram (from 300 Hz to 3 kHz) that was used for the analysis.

The known facts were used to narrow the search for the violin-mode frequencies: The frequencies of some of the fundamental violin modes were measured earlier. The measurements performed in March 2003 revealed 14 of the 16 fundamental frequencies of the far north suspension. The measurements from April 2003 included nine of the 16 fundamental frequencies of the inboard suspensions. An assignment of the frequencies to an individual inboard suspension was, however, not possible.

Due to a broken suspension fiber, the north inboard suspension was replaced at the 1st of August in 2003 [5]. Thus, in the worst case scenario eight of the nine measured inboard frequencies could have changed. As a consequence, further hints were required to detect the lines caused by the violin modes among the variety of other lines in the spectrogram.

A method to distinguish the violin-mode frequencies from other lines in the spectrogram is to look for lines that drift in frequency. The violin-mode frequencies are subject to drifts for various reasons. The temperature dependence of the fiber material's Young's modulus, drift of the pitch and roll alignment, as well as residual outgassing of the material used for the damping and tuning procedure are possible reasons for a drift of the violin-mode frequencies. Both roll and pitch alignment drifts are caused by thermal effects via the temperature dependence of the Young's modulus of the cantilever springs

---

[4]With 323 Gflops at the LINPACK benchmark, the Helix cluster was ranked 378th in the 21st worldwide top500 supercomputer list, published in June 2003. The Helix cluster consists of a Beowulf cluster with 72 nodes. Each node contains two Xeon processors with 2.2 GHz, sharing 1.5 GB of RAM.

[5]In fact only two of the four fibers were replaced, but from previous experience it is known that replacing fibers and resuspending the monolithic stage is very likely to change all violin-mode frequencies of the particular suspension by a substantial amount (see, e.g., Section 5.4.6).
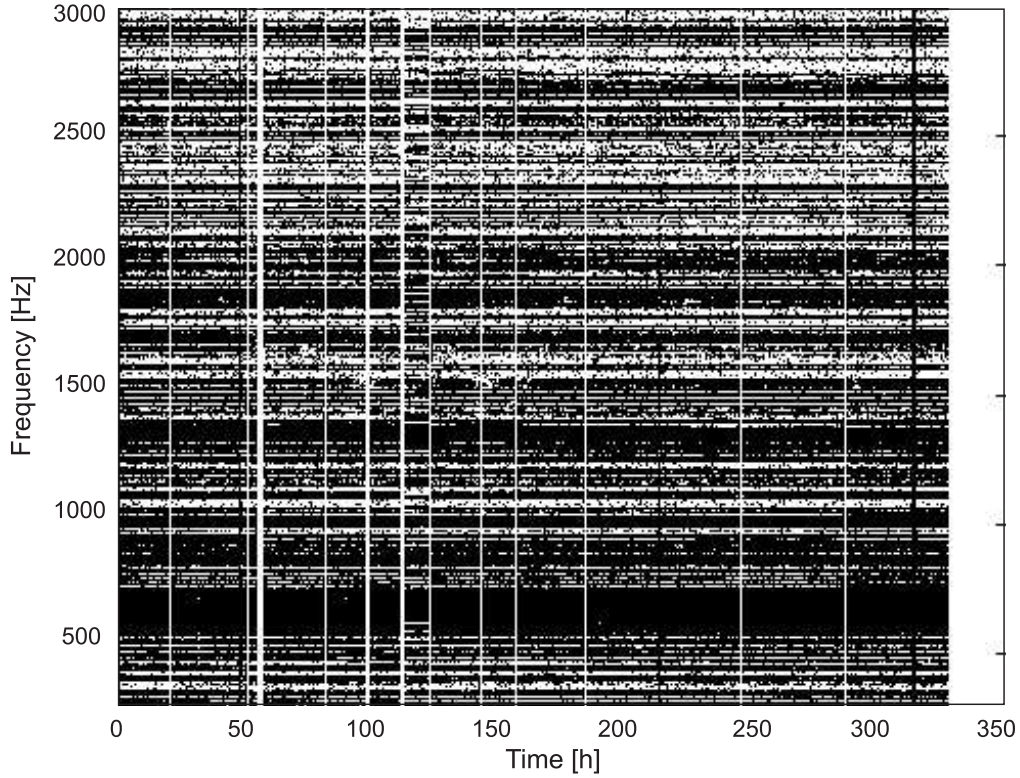
**Figure 5.10:** The full spectrogram from 300 Hz to 3 kHz, as was used for the violin-mode fre-
quency search and analysis. The enormous number of lines illustrates the need for
a reliable strategy to distinguish the violin-mode frequencies from other lines. The
fundamental violin-mode frequencies are centered around 650 Hz. The vertical white
lines are due to the fact that the algorithm was not run on data segments for which
the detector was out of lock. Hence, the spectrogram reflects the duty cycle of
GEO 600 during S3II.

(see Section 3.11.1). Hence, the former three of the four influences are dominated by
temperature changes while the latter one, the outgassing, should depend less strongly on
the temperature.

The relative change of the violin-mode frequencies with temperature due to the tem-
perature dependence of the fiber material's Young's modulus is given by [Willems '02]

$$\frac{(d\,f_n/dT)}{f_n} \simeq -\frac{1}{2}\left(\alpha - u_0\beta_{\mathrm{S}}\right) + \frac{1}{D_n}(\alpha + u_0\beta_{\mathrm{S}} + \beta_{\mathrm{S}}/2) \tag{5.36}$$

where $\alpha$ is the CTE of fused silica and $u_0$ denotes the static strain in the suspension fiber

$$u_0 = \frac{P}{A\,E_{\mathrm{S}}} \tag{5.37}$$

143

| | |
|---|---|
| $\alpha$ | $5.1 \cdot 10^{-7}\,\mathrm{K}^{-1}$ |
| $C_v$ | $1.64 \cdot 10^{6}\,\mathrm{J\,K^{-1}\,m^{-3}}$ |
| $E_\mathrm{S}$ | $7.2 \cdot 10^{10}\,\mathrm{Pa}$ |
| $\beta_\mathrm{S}$ | $\sim 2 \cdot 10^{-4}\,\mathrm{K}^{-1}$ |

**Table 5.4:** The relevant properties of fused silica.

$\beta_\mathrm{S}$ denotes the temperature dependence of the Young's modulus

$$\beta_\mathrm{S} = \frac{(dE_\mathrm{S}/dT)}{E_\mathrm{S}} \tag{5.38}$$

Table 5.4 provides the relevant material properties of fused silica. Using Formula (5.11) for the dilution factor $D_n$ and inserting into Equation (5.36) yields a drift of the fundamental violin-mode frequencies ($f_1 \simeq 650\,\mathrm{Hz}$) of

$$\frac{d\,f_1}{dT} \simeq 10^{-3}\,\mathrm{Hz\,K^{-1}} \tag{5.39}$$

It should be noted that this value not only strongly depends on the fiber radius, which is not well defined for the GEO 600 suspension fibers, but furthermore the reported values of $\beta$ differ by up to a factor of three.

Since the temperature drift in the central building was controlled to an accuracy better than $\pm 0.3\,\mathrm{K}$ during the S3II run, no temperature dependent drift of the violin-mode frequencies within the measurement precision can be expected. This does, however, not hold for the end stations, which are kept at room temperature by a combination of commercial heaters and commercial air conditioners. The measured temperature variations during the S3II run are displayed in Figure 5.11 . Based on the above considerations, these temperature characteristics were used to search for lines that drift with the expected temperature dependence. By doing this the violin-mode frequencies from the end stations could be identified. The differences in the temperature characteristics furthermore allow for an assignment of the frequencies to the individual suspensions. Figures 5.12 shows two clear matches of fiber frequencies, drifting with temperature. Each fiber is clearly correlated with the temperature of the respective end station.

Altogether 14 of the 16 violin-mode frequencies of the far suspensions could be found in the spectrogram by the temperature pattern matching. The missing two frequencies (700.42 Hz and 701.93 Hz) were found after a comparison with the measurements of the far north suspension from March 2003. Table 5.5 shows the results of the two measurements. The March 2003 measurement was found to be in perfect agreement with the assignment of the fibers to the according end stations (provided in Table 5.7), obtained by the temperature patterns.

In order to identify the violin-mode frequencies of the inboard suspensions, the measurements from April 2003 were used to firstly find one of these modes. The frequency
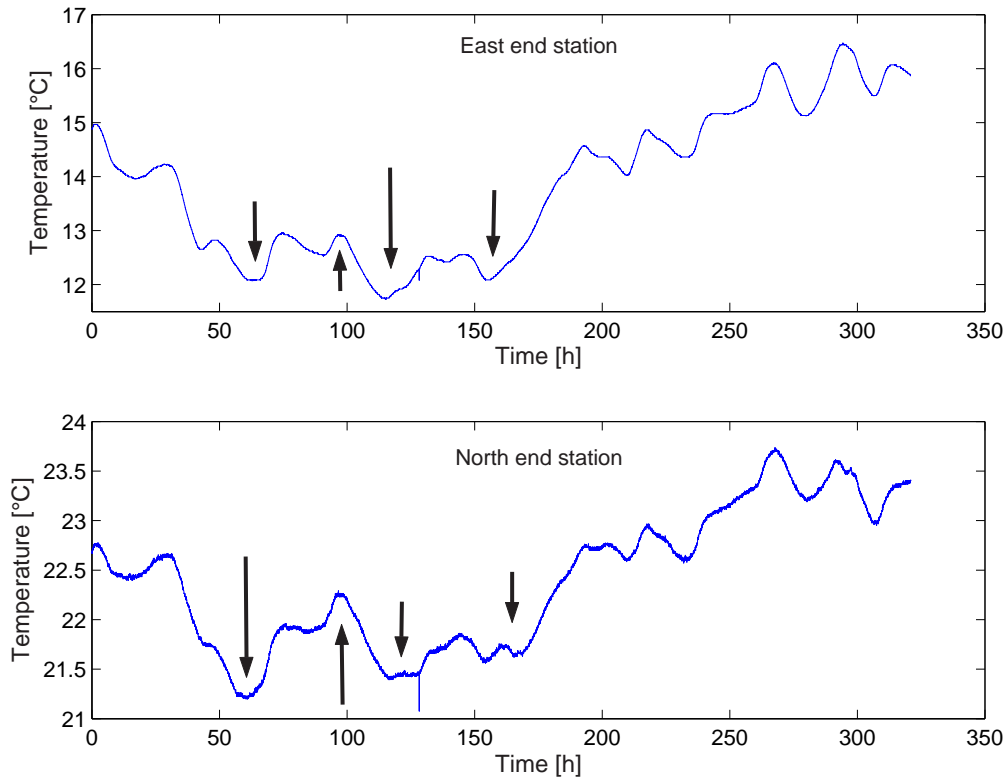
**Figure 5.11:** The temperature patterns from the two end stations during the S3II run. These patterns were used to search for lines with similar drift characteristics. The most prominent differences are marked by the arrows. The lengths of the arrow refer to the depth of the respective dip. These features were used to assign the violin-mode frequencies that were found in the spectrogram to their individual suspensions.

drift pattern of this particular fiber was then used to identify the frequencies of the other fibers (please see Section 5.8.3 for the analysis of the inboard violin-mode frequencies). Figure 5.13 shows the two fundamental violin-mode frequencies of an inboard fiber, close to a harmonic of the power line.

15 of the 16 violin-mode frequencies could be found by this method. The one missing frequency is very likely due to a fiber that is by chance oriented in coincidence with the optical axis such that only one of the two orthogonal modes couples significantly to the longitudinal motion of the mirror. Table 5.6 provides the results of the measurements performed in April 2003 and in January 2004. The comparison of the two measurements allows, due to the replacement of the north inboard suspension in August 2003, for the previously not possible assignment of the violin modes to individual suspensions.

Table 5.7 eventually provides the full list of the measured fundamental violin-mode frequencies of the GEO 600 test-mass suspensions. The frequency doublets belonging to the two orthogonal modes of one fiber are displayed in pairs.
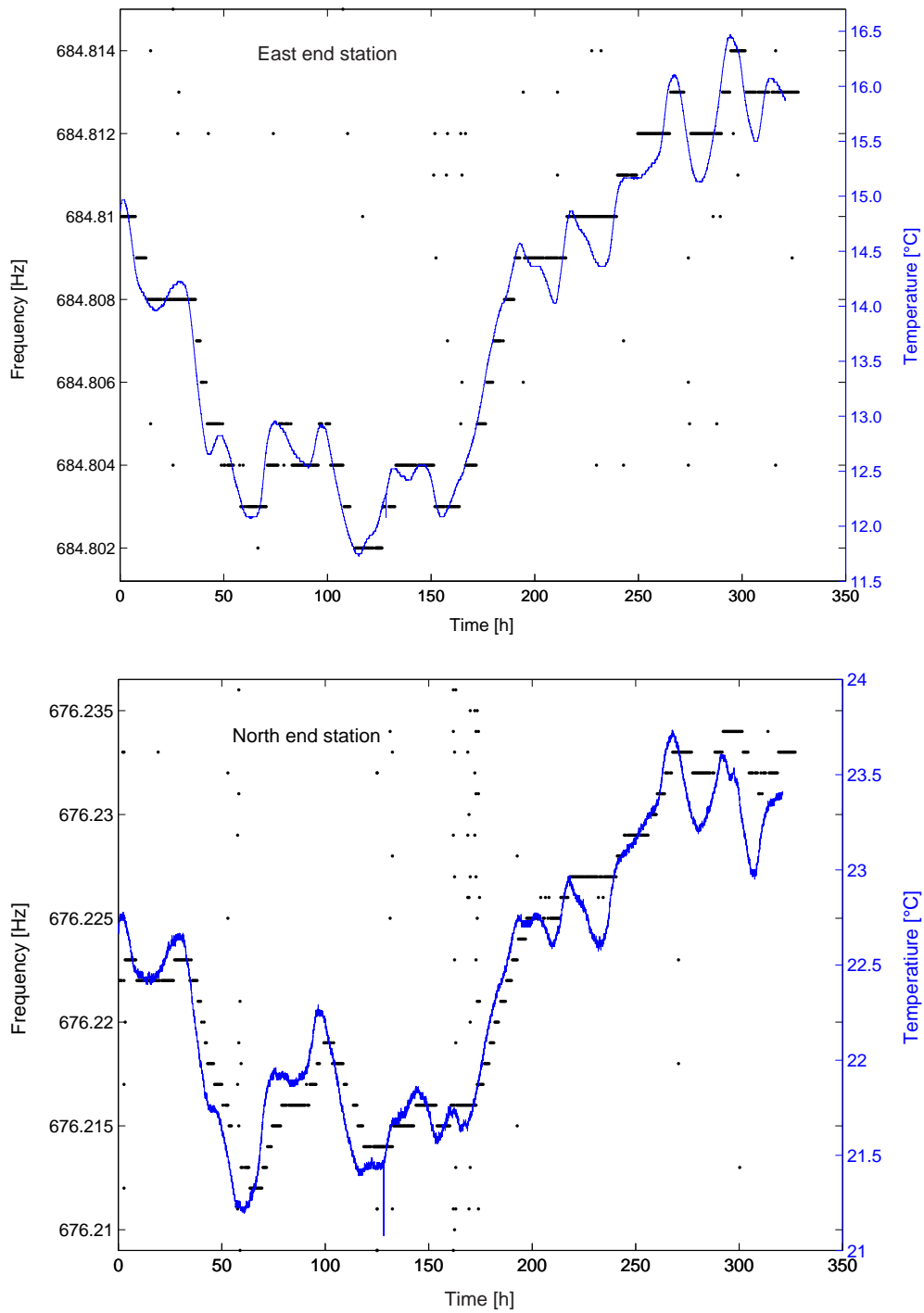
**Figure 5.12:** Violin-mode frequencies, evidently belonging to **MFn** or **MFe**, respectively, along with the respective temperature.

| MFn (March 2003) | MFn (January 2004) | MCe, MCn (April 2003) | MCe, MCn (January 2004) |
|---|---|---|---|
| Frequency [Hz] | Frequency [HZ] | Frequency [Hz] | Frequency [Hz] |
| — | 642.29 | 620.20 | — |
| — | 642.83 | 620.40 | — |
| — | 653.20 | — | 627.52 |
| — | 653.69 | — | 627.81 |
| 666.10 | 666.27 | — | 628.67 |
| — | 666.29 | — | 629.73 |
| 667.00 | 667.16 | 634.65 | 635.30 |
| — | 667.65 | 635.40 | 636.04 |
| — | 675.27 | 637.88 | — |
| 676.15 | 676.23 | 638.00 | — |
| 676.30 | 676.35 | 648.25 | 648.65 |
| 676.80 | 676.91 | 648.85 | 649.53 |
| — | 684.81 | 665.82 | 666.47 |
| — | 685.70 | 665.97 | 666.64 |
| 700.40 | 700.42 | — | 666.89 |
| 701.70 | 701.93 | — | 667.23 |
| | | 668.88 | — |
| | | 669.17 | — |
| | | 669.19 | — |
| | | — | 670.53 |
| | | 671.26 | 672.26 |
| | | — | 673.04 |

**Table 5.5:** Comparison of the fundamental violin-mode frequencies of the far suspensions, measured in March 2003 and January 2004. Since only the far north suspension could be measured in 2003, assigning the modes to the suspensions is possible. This assignment is in perfect agreement with the assignment achieved by the temperature pattern analysis.

**Table 5.6:** A comparison of the fundamental violin-mode frequencies of the inboard suspensions measured in April 2003 and in January 2004. The missing frequencies are due to the re-suspending of the north inboard suspension in August 2003. This allows to assign the violin modes to the respective suspension.
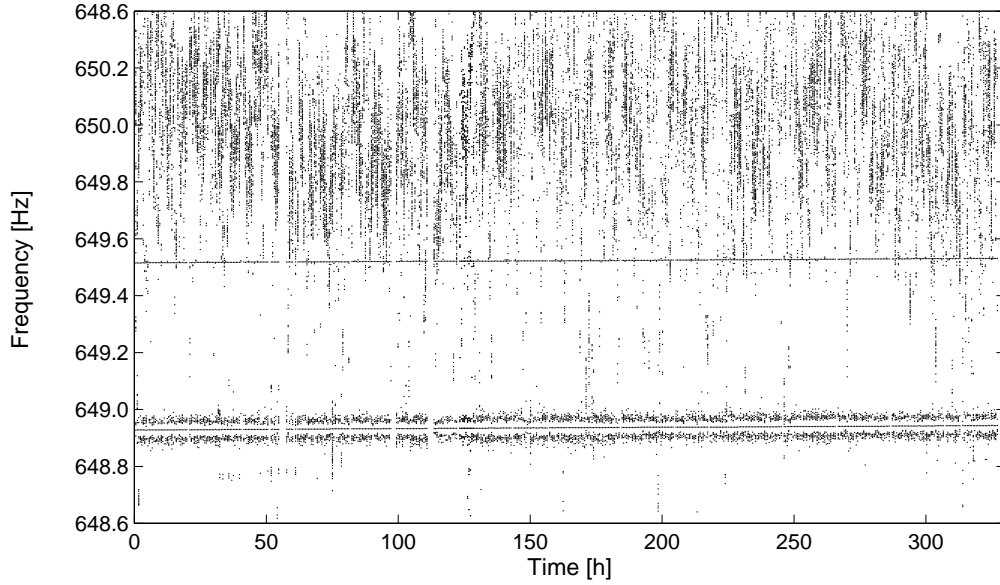
**Figure 5.13:** Two lines caused by violin modes (at 648.85 Hz and 649.53 Hz) in the vicinity of a harmonic of the power line (at 650 Hz). The two lines are caused by the orthogonal modes of one fiber from the east inboard suspension. One of the lines is accompanied by noisy sidebands at about 30 mHz. A peak at 30 mHz was found earlier in the seismic spectrum. It is, however, not clear why only one of the modes shows the sidebands.

| MCe | MCn | MFe | MFn |
|---|---|---|---|
| Frequency [Hz] | Frequency [Hz] | Frequency [Hz] | Frequency [Hz] |
| 635.30 | 627.52 | 642.29 | 666.27 |
| 636.04 | 627.81 | 642.83 | 667.16 |
| 648.85 | 628.67 | 653.20 | 675.27 |
| 649.53 | 629.73 | 653.69 | 676.35 |
| 666.47 | 666.89 | 666.29 | 676.22 |
| 666.64 | 667.23 | 667.65 | 676.91 |
| 672.26 | 670.53 | 684.81 | 700.42 |
| 673.04 | — | 685.70 | 703.93 |

**Table 5.7:** The frequencies of the fundamental violin modes. Due to the slightly elliptical cross section of the fibers, each one oscillates with slightly different frequencies at the two orthogonal fiber polarizations. The frequency doublets belonging to one fiber are displayed in pairs. The missing frequency of **MCn** indicates that the orthogonal modes of the according fiber are by chance oriented in coincidence with the optical axis such that only one of the modes couples significantly to the longitudinal motion of the test mass.

### 5.8.1 The far east suspension

Figure 5.14 displays the drift of the four fibers from the far east suspension. During the first 120 hours of the S3II run the downward drift was measured to be $6 - 8\,\mathrm{mHz}$. On average this leads to a drift rate of

$$\frac{\delta f_1}{\Delta T} = \frac{6.75 \pm 0.5\,\mathrm{mHz}}{3.25 \pm 0.05\,\mathrm{K}} \simeq 2.10 \pm 0.25\,\mathrm{mHz\,K^{-1}} \tag{5.40}$$

During the last 200 hours of the S3II run an upward drift of $8 - 13\,\mathrm{mHz}$ was observed. On average the drift rate in this period was

$$\frac{\delta f_1}{\Delta T} = \frac{9.75 \pm 0.5\,\mathrm{mHz}}{4.75 \pm 0.05\,\mathrm{K}} \simeq 2.05 \pm 0.15\,\mathrm{mHz\,K^{-1}} \tag{5.41}$$

In Section 5.8 a drift rate of $1\,\mathrm{mHz\,K^{-1}}$ was predicted. Although there is a considerable uncertainty in the calculated value due to the not well defined fiber radius, this uncertainty seems not suitable to explain a drift rate twice as strong.
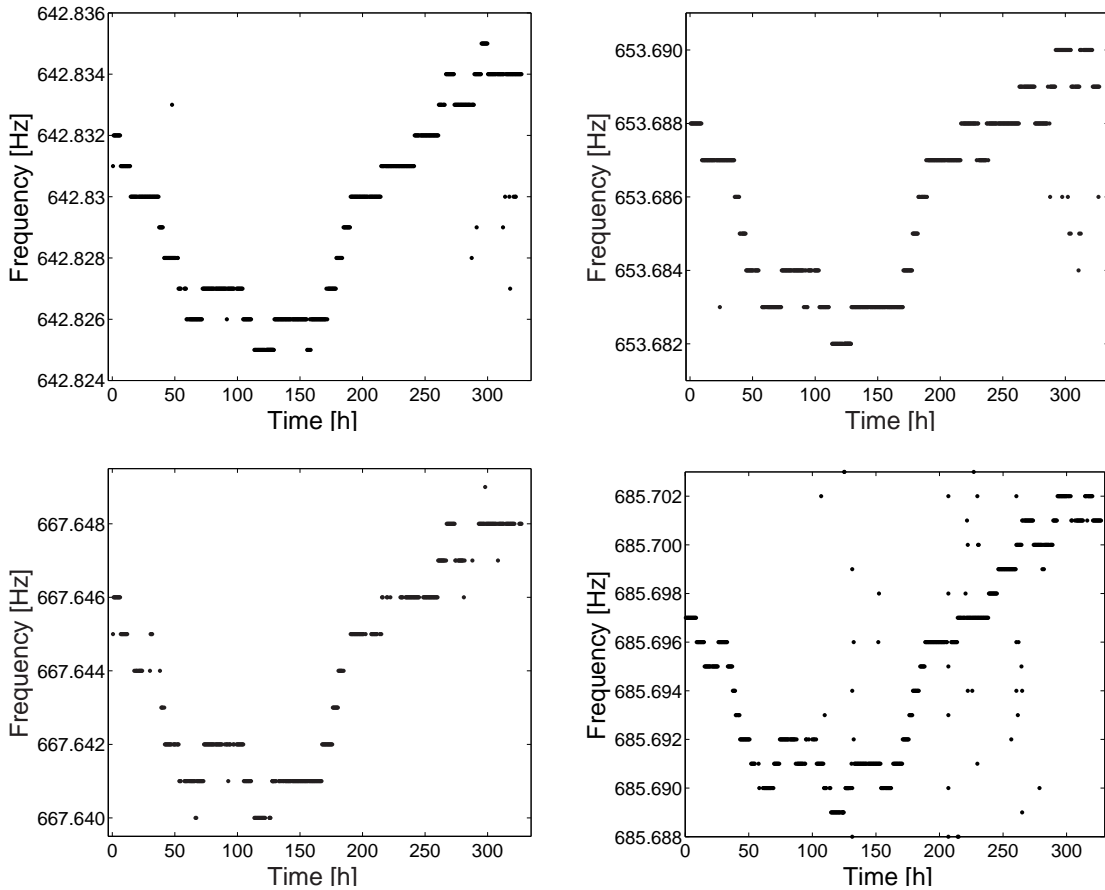


**Figure 5.14:** The drift of the violin-mode frequencies of all four fibers from the **MFe** suspension. The respective temperature characteristic is displayed in Figure 5.11 .

The required correction due to the outgassing of the damping material and its solvent can be derived from the measurements of the continuous upward drift due to this effect, presented in Section 5.8.3, to be smaller than 0.6 mHz. Since this upper limit is simply derived by averaging the continuous upward drift over 10 months, the upward drift from outgassing can safely be neglected for the far suspension fibers.

The greatest uncertainty in the measurement arises from the fiber temperature itself. The fibers can be expected to be in thermal equilibrium with the environment. The equilibrium is reached comparatively fast via radiation, since the fibers have a very large surface to volume ratio while having a low thermal conductance. A deviation of the actual fiber temperature from the measured value may arise from the way the temperature was monitored: The according sensor is attached to the outside of the vacuum tank [6]. However, the tank is not the only surface that has to be taken into account for the fiber temperature. A considerable fraction of the solid angle that can be seen from the fiber's position is occupied by the vacuum tube. Although the tube is thermally insulated by a layer of rock wool, it is basically exposed to the outside temperature and hence experiences greater temperature changes.

Again, this is not suitable to fully explain the observed deviation from the calculated value. Hence, it seems that the value for $\beta$ must be assumed higher than considered in the calculations. Clearly further investigation is required on this interesting effect.

### 5.8.2 The far north suspension

The temperature drift in the north end station was measured during the S3II run to be approximately half of that for the east end station.

Figure 5.15 shows two of the observed violin-mode frequencies from the far north suspension along with the temperature pattern from the north end station. Although the drift patterns match the pattern of the temperature quite well, the magnitude and for two of the four fibers even the sign, does not meet the prediction.

A possible explanation can be found in the pitch or roll alignment drift of the suspension. The drift in this degrees of freedom depends also on the temperature and leads to a change of the violin-mode frequencies, as will be explained in the following.

As described in Section 3.6.4, the spring constants of the cantilever springs are not perfectly matched with respect to each other. This mismatch leads to a temperature dependent differential deflection via the temperature dependence of the Young's modulus. While a mismatch of the springs at the front and rear side of the suspension leads to a pitch drift, a mismatch of the lateral springs leads to a roll alignment drift. Any alteration of the pitch or roll alignment leads in turn to a change of the associated violin-mode frequency via a change of the fiber tension. The origin of the tension change is a shift of the COM of the suspended mass with the alignment. The COM is shifted since for stability reasons the bending point of the fibers is above the COM and hence the COM lies neither on the axis of roll motion nor on the axis of pitch motion. The dependence of the tension on the pitch and roll alignment can be worked out from straightforward geometrical considerations. In the following the example of pitch misalignment is considered.

---

[6]The temperature sensor itself was calibrated repeatedly with different methods to safely exclude a miscalibration.
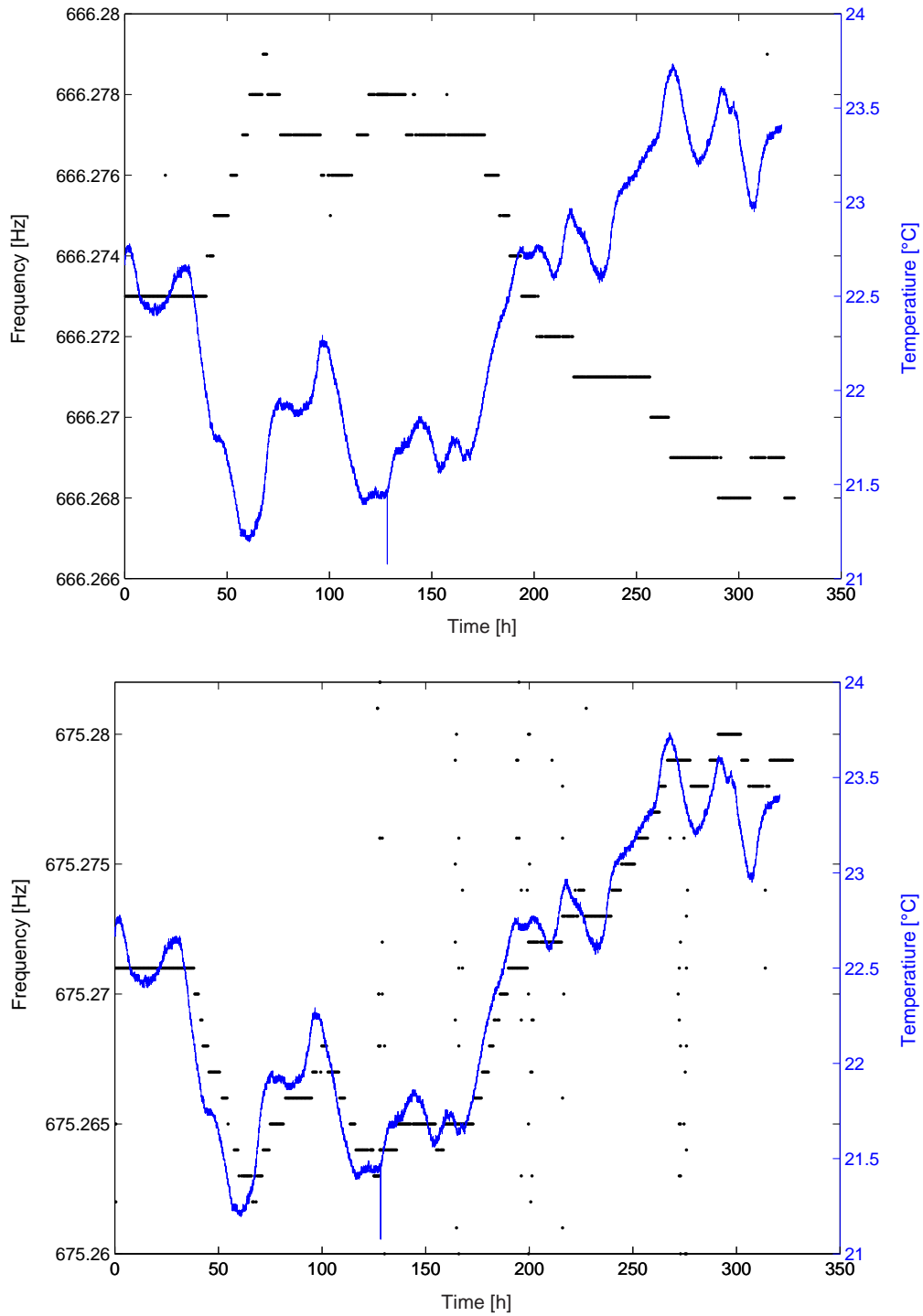
**Figure 5.15:** Two violin modes of **MFn**, drifting in different directions with temperature. Furthermore, the drift rate of the two modes has a large ratio of about 1.64 . The modes belong to fibers at opposite sides of the mirror, as is explained in the text.

The occurring shift of the COM toward the attachment point of the fibers at the rear side when the mass is pitched forward (i.e., such that a horizontal beam is reflected downwards) is given by

$$\delta x_{\text{COM}} = h_{\text{b}} \cdot \sin \gamma \tag{5.42}$$

with $\gamma$ being the angle of deviation from a perfectly balanced pitch alignment and $h_{\text{b}}$ is the height of the break-off position above the COM. In addition to the shift of the COM, the attachment point of the fiber is shifted toward the COM by

$$\delta x_{\text{fiber}} = d \cdot (1 - \cos \gamma) \tag{5.43}$$

where $d$ denotes half the separation of the fibers along the optical axes. The resulting change of distance $\Delta x$ between the COM and the fiber attachment point is given by the sum of the two contributions. The change of tension for a front fiber is

$$\frac{P_{\text{front}}(\gamma)}{P(\gamma = 0)} = \frac{d - \Delta x}{d} = \cos \gamma - \frac{h_{\text{b}}}{d} \cdot \sin \gamma \simeq 1 - \frac{h_{\text{b}}}{d} \cdot \gamma \tag{5.44}$$

The approximation made in the last step is justified by the small misalignment angles that are tolerable for the operation of GEO 600. The relative tension of the fibers is thus given by

$$\frac{P_{\text{front}}}{P_{\text{rear}}} = \frac{d - \Delta x}{d + \Delta x} = \frac{d \cdot \cos \gamma - h_{\text{b}} \cdot \sin \gamma}{2d + h_{\text{b}} \cdot \sin \gamma - d \cdot \cos \gamma} \simeq \frac{d - h_{\text{b}} \gamma}{d + h_{\text{b}} \gamma} \simeq 1 - 2 \frac{h_{\text{b}}}{d} \cdot \gamma \tag{5.45}$$

By inserting Equation (5.44) into Equation (5.8), the frequency change, depending on the pitch alignment is obtained.

The actual pitch alignment drift during the S3II run was derived from the permanent measurement of the laser beam position behind the inboard mirrors (see Figure 3.17). The position of the laser beam is permanently centered on quadrant photo diodes behind each interferometer mirror. The residual pitch alignment fluctuations during S3II were found to be $\pm 1\,\mu\text{rad}$, equivalent to a violin-mode frequency change of $\pm 5 \cdot 10^{-5}\,\text{Hz}$. Hence, no influence of the pitch alignment on the violin-mode frequencies within the measurement precision can be expected.

The situation differs substantially for the roll alignment. Although motion in this degree of freedom is damped via the local control actuators, long term drifts are not compensated for. On the one hand it is difficult to obtain a measure for the actual roll alignment (Section 3.11.3), while on the other hand the coupling of roll into the longitudinal degree of freedom is expected to be comparatively small. Hence, there is neither a direct measure nor a direct need for a control of the roll alignment drift. However, it will be shown in the following that one can obtain information about the actual roll alignment drift via the violin-mode frequencies. Furthermore, the drift of these frequencies is of direct influence on the detector sensitivity, when integrating over long periods of time.

Drift of the roll alignment causes a differential frequency change of the fibers attached to the lateral sides of the mirror. The occurring change of fiber tension is obtained

by using Equation (5.44) with modified arguments. The fiber separation $2d$ along the optical axis has to be replaced by the fiber separation $2D$ perpendicular to the optical axis ($\sim$ test mass diameter). Due to the greater separation of the fibers along this axis, the coupling coefficient of roll to tension is diminished by the factor $d/D$. Despite this weaker coupling a stronger effect on the violin-mode frequencies can be expected from this degree of freedom due to the lack of active alignment control.

Provided that the observed difference in the frequency drifts is caused by roll alignment drift, the fibers with different drift directions must be attached to opposite sides of the mirror. Using the above formulas reveals that a rotation of 0.19 mrad could explain the observed differential drift. A rotation of this magnitude can indeed be expected based on the observed relative mismatch between the cantilever springs, as is explained in detail in Section 3.11.3. The remaining common drift rate in the last 200 hours of the S3II run is on average

$$\frac{\delta f_1}{\Delta T} = \frac{4.3 \pm 0.5\,\mathrm{mHz}}{2.45 \pm 0.05\mathrm{K}} \simeq 1.75 \pm 0.25\,\mathrm{mHz\,K^{-1}} \tag{5.46}$$

Compared to the $2.05 \pm 0.15\,\mathrm{Hz\,K^{-1}}$ observed for the far east suspension, the results from the two end stations are found to be in agreement within the measurement precision.

### 5.8.3 The inboard suspensions

From the measurements of the far suspensions discussed in the above sections, it is conclusive that the violin-mode frequencies drift with a rate of the order of $2\,\mathrm{mHz\,K^{-1}}$. The temperature change in the central station rose during the last 200 hours of the S3II run by 0.25 K. Hence, a frequency drift of only 0.5 mHz can be expected for the inboard suspension fibers. Derived from the measurements of the far north suspension, a differential drift of the order of $\pm 0.5\,\mathrm{mHz}$ may result from a drift of the roll alignment with temperature. Both effects are hence not expected to show up for the inboard suspensions within the measurement precision.

In fact, all violin-mode frequencies of the inboard suspension were found to show an almost linear upward drift. No hypothetic alignment drift that can be thought of could explain this behavior. Moreover, no environmental influence shows a linear decrease or increase during the time of the measurement.

The observed upward drifts over S3II are of the order of $15 - 20\,\mathrm{mHz}$ for six of the eight fibers. Two fibers even show an upward drift of $43 - 49\,\mathrm{mHz}$. The upper graph in Figure 5.16 displays one of the two violin-mode frequencies close to the harmonic of the power line, displayed in Figure 5.13, but is zoomed in further to reveal the upward drift. The lower graph in Figure 5.16 shows a line caused by one of two fast drifting modes. The only reasonable explanation for the simultaneous upward drift of all fibers is residual outgassing of the material and its solvent that was used for the violin mode damping. Although the coating was applied more than one year ago and since then the fibers have always been in vacuum, the residual outgassing still produces this clearly visible effect. Table 5.8 shows the measured drifts along with the calculated decrease of the effective
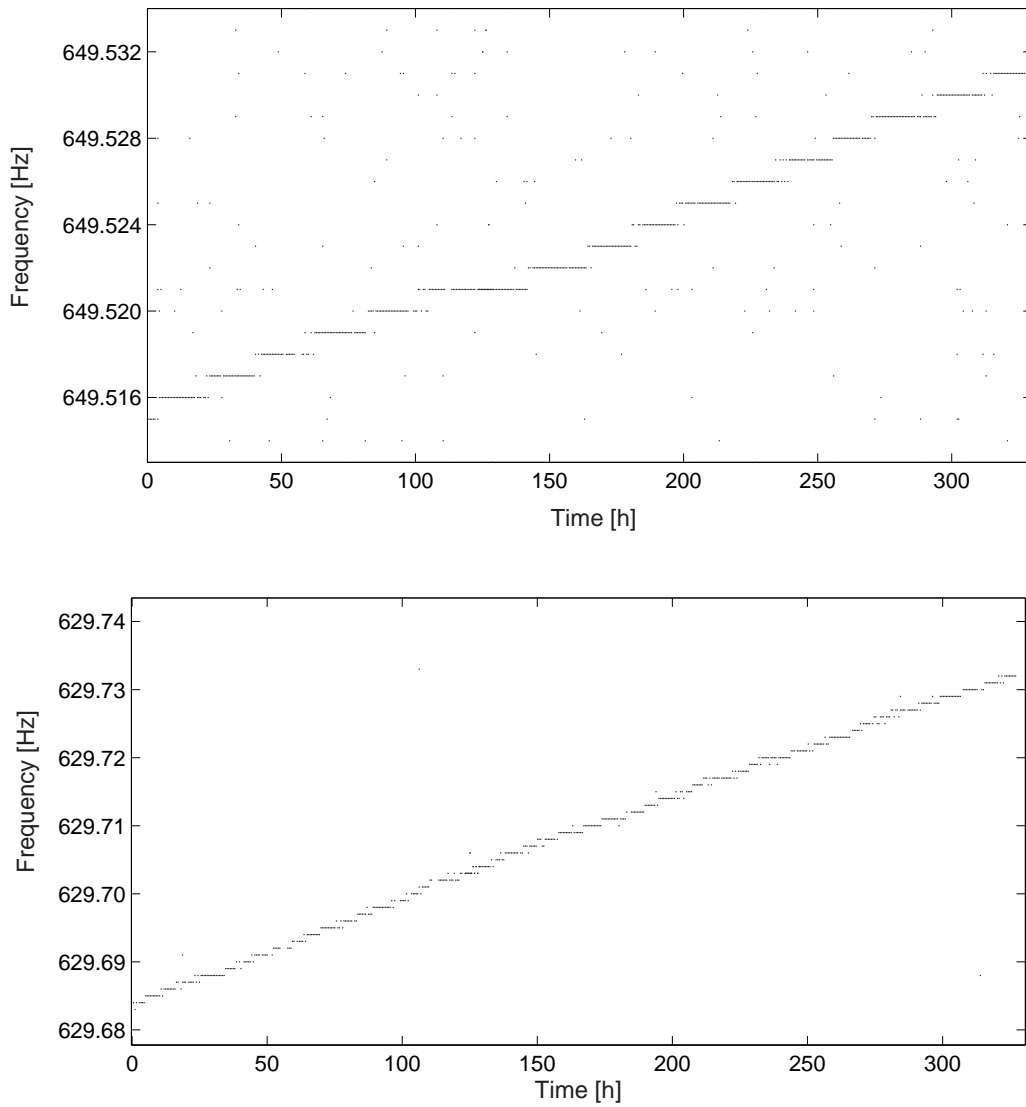
**Figure 5.16:** Two violin modes of **MCn**, drifting from outgassing. From the different drift rates of the two modes it is conclusive that the lower graph shows one of the two fibers which were replaced 5 months ago, while the upper graph shows one of the other two fibers, which are installed since 12 months. The upper graph is zoomed into the graph from Figure 5.13, showing the line close to the harmonic from the power line.

fiber mass. The mass reduction was calculated from the frequency drift by the formula

$$\frac{\partial m}{m} = -2\,\frac{\partial \omega}{\omega} \tag{5.47}$$

derived in Section 5.4.4. Here $m = 1/2 \cdot 23.4\,\mathrm{mg}$ is the effective mass of the fiber, calculated in Section 5.3.

In order to confirm the conclusions, the violin-mode frequencies of the far north sus-

| MCe | | | MCn | |
| --- | --- | --- | --- | --- |
| Upward drift [mHz] | Mass reduction [μg] | | Upward drift [mHz] | Mass reduction [μg] |
| 16 | 0.59 | | 18 | 0.67 |
| 16 | 0.59 | | 18 | 0.67 |
| 16 | 0.57 | | 49 | 1.80 |
| 15 | 0.54 | | 48 | 1.80 |
| 18 | 0.63 | | 17 | 0.59 |
| 17 | 0.59 | | 17 | 0.59 |
| 19 | 0.66 | | 43 | 1.50 |
| 20 | 0.69 | | — | — |

**Table 5.8:** The upward drifts over 330 h for the fundamental modes of the inboard suspension fibers along with the calculated mass reduction. The two fast drifting fibers of **MCn** are evidently the two fibers that were replaced five months before the measurement, while the other fibers were already installed for 12 months. The drifts are displayed in the same order as the frequencies given in Table 5.7 .

pension were reinspected whether or not a long-term upward drift was present. These fibers were installed in April 2001, almost 20 months before the inboard fibers. Furthermore, much less damping material was applied to the far suspension fibers. Hence, the expected upward drift is so small that it would be completely covered by the temperature drift during S3II. However, a noticeable upward drift of all four fibers of the far north suspension should show up on the relatively long time scale of ten months. Thus, the measurements performed at the 7th of March 2003 were again compared to the new results. The obtained frequency drifts can be found in Table 5.5 . All fibers were found to show the expected small upward drift, with an average value of about 13 mHz over ten months. This clearly sets an upper limit on the actual drift rate at January 2004, equivalent to 0.6 mHz over 330 h. Hence, a ratio of at least 30 is found on average for the drift of the strongly coated inboard fibers to the older and less strongly coated far suspension fibers.

From the fact that two fibers of the north inboard suspension drift much faster than all other fibers, it can be concluded that these are the two fibers of **MCn** that were replaced at the 1st of August 2003. These fibers were coated and installed five months ago, while all the other inboard fibers were coated and installed 12 months ago. The drift rate for the more recently installed fibers is about three times as high as for the other fibers. As a direct conclusion, the observed ratio between the far north fibers and the inboard fibers can not even nearly be explained by the longer evaporation time of the far fibers. Thus, it must be mostly due to the smaller amount of damping material applied to the far suspension fibers.

### 5.8.4 The beamsplitter suspension

Following the conclusions drawn in the above section, the upward drift of the beamsplitter fibers was measured. Table 5.9 provides all violin-mode frequencies of the beamsplitter suspension that could be revealed from the spectrogram. Since there is no feedback to the lower two pendulum stages, only little damping is required for the beamsplitter fibers. Thus, they were treated in a similar way as the far suspension fibers. Finding the violin-mode frequencies of the beamsplitter suspension is hence less straightforward than for the other suspensions: There is no actuator to drive the fiber oscillations on purpose, the temperature fluctuation should, referring to the above considerations, not show up within the measurement precision of 1 mHz. The same holds for alignment drifts. The pitch alignment of the beamsplitter is controlled as for the mirrors. The above estimate on the influence of roll can due to the greater diameter of the beamsplitter be regarded as an upper limit. Hence, the only drift can be expected from the outgassing. Based on these considerations and the above measurements, six of the eight frequencies were found. Since a certain frequency drift is required to safely identify a line caused by a fiber oscillation, the two orthogonal modes from one fiber could not be found.

| Beamsplitter | |
|---|---|
| Frequency [Hz] | Upward drift [mHz] |
| 683.61 | 3 |
| 668.44 | 5 |
| 688.66 | 2 |
| 688.99 | 2 |
| 710.15 | 2 |
| 710.98 | 2 |

**Table 5.9:** The violin-mode frequencies of three of the beamsplitter suspension fibers. The observed upward drift over 330 h well meets the expectations based on the amount of damping material applied and the drift measurements of the mirror suspension fibers.

The average drift rate of the beamsplitter violin-mode frequencies is 2 mHz over the 330 h period (assuming unresolvable drift for the forth fiber). This is approximately a factor of nine less than the inboard suspension fiber drift over the same period and hence in good agreement with the amount of damping material that was applied.

### 5.8.5 Second-order violin modes

The higher-order violin-mode frequencies of the different suspensions were found by the same methods as applied for the respective fundamental modes. Only the frequencies of three of the 16 inboard suspension fiber modes and none of the far suspension fiber modes

were measured before. Thus, an assignment of the fibers to their individual suspensions by comparison to previously measured values as was done for the fundamental modes is not possible. Nonetheless, the inboard fibers can easily be distinguished from the far suspension fibers and the temperature patterns from the end stations allow for the individual assignment of at least these fibers. Table 5.4.4 provides the frequencies of the second-order violin modes that were found in the spectrogram, along with the observed drift rates and calculated mass reduction for the inboard suspension fibers.

Knowing the reduction of the effective mass for both the $f_1$ and the $f_2$ mode of the inboard fibers, the individual contribution of each of the two coated sections to the decrease of mass can be revealed. Based on the considerations about the effective masses for the first and second violin modes, made in Section 5.4.4, the mass loss for the individual sections was calculated from the average of the measured values. The average had to be taken since a safe assignment of the higher order modes to the according fundamental modes is not possible. The two replaced fibers were excluded from the averaging.

The upward drift for the second-order mode was found to be on average 32 mHz over the 330 h period. This is equivalent to a loss of mass of 0.57 µg. The average mass loss for the fundamental modes is 0.61 µg. The resulting mass loss for the central section is hence 0.61 µg − 1/2 · 0.57 µg = 0.32 µg. The mass reduction for the second-order mode is simply the measured value. The resulting ratio is thus given by 0.32/0.57 = 0.56. A correction to this result arises from the fact that the outgassing rate depends on the surface to volume ratio of the coating. This ratio differs with the two coated sections, resulting in an underestimation of the mass at one forth of the fiber length. Hence, the

| **MCe, MCn** | | | **MFe** | **MFn** |
|---|---|---|---|---|
| Frequency [Hz] | Upward drift [mHz] | Mass reduction [µg] | Frequency [Hz] | Frequency [Hz] |
| 1243.90 | 40 | 0.75 | 1273.60 | 1291.60 |
| 1246.02 | 35 | 0.47 | 1274.90 | 1294.70 |
| 1251.10 | 95 | 1.78 | 1295.30 | 1296.25 |
| 1287.38 | 35 | 0.64 | 1296.55 | 1342.20 |
| 1288.90 | 30 | 0.55 | 1324.25 | 1344.20 |
| 1320.70 | 20 | 0.35 | 1328.00 | — |
| 1325.98 | 40 | 0.71 | 1356.15 | — |
| 1326.86 | 35 | 0.62 | 1358.50 | — |
| 1348.10 | 30 | 0.52 | | |

**Table 5.10:** The frequencies of the second-order violin modes of the inboard suspensions and of the far suspensions. The upward drifts over 330 h is provided for the inboard suspension fibers along with the calculated decrease of mass. The violin mode at 1251.10 Hz belongs obviously to one of the replaced **MCn** fibers.

result obtained requires a downward correction. The ratio calculated from the initial downward shift of the fiber frequencies due to the application of the coating material in Section 5.4.4, is about 0.46. As described, this value requires an upward correction.

### 5.8.6 Higher-order violin modes

Besides the 59 frequencies of the fundamental and first harmonic violin modes listed above, 21 frequencies of higher-order modes were found in the spectrogram. Table 5.11 provides a list of these higher-order modes of the inboard suspensions and of the far suspensions up to $f_6$.

|  | **MCe, MCn** | **MFe, MFn** |  |
|---|---|---|---|
|  | Frequency [Hz] | Frequency [Hz] |  |
| 3rd order: | 1818.95 | 1893.10 | (**MFn**) |
|  |  | 1850.55 | (**MFn**) |
|  |  | 1852.85 |  |
|  |  | 1855.15 |  |
|  |  | 1869.04 |  |
|  |  | 1874.60 | (**MFe**) |
|  |  | 1895.46 | (**MFn**) |
|  |  | 1898.55 | (**MFn**) |
|  |  | 1922.76 |  |
| 4th order: | 2051.26 | 2455.95 | (**MFe**) |
|  | 2053.05 | 2436.57 | (**MFn**) |
|  | 2054.84 | 2428.00 |  |
|  |  | 2501.05 |  |
| 5th order: | 2224.13 | — |  |
|  | 2395.20 |  |  |
| 6th order: | 2737.40 | — |  |
|  | 2908.50 |  |  |

**Table 5.11:** The frequencies of the higher-order violin modes up to $f_6$, as obtained from the spectrogram. The frequencies are assigned to individual suspensions where possible.

## 5.9 Calculation of the loss factor of Teflon

In the following the loss factor $\phi_c$ of the coating material itself is derived, starting from the definition

$$Q = 2\,\pi \cdot \frac{\text{Energy stored in the material}}{\text{Energy dissipated per cycle}} \tag{5.48}$$

The energy E stored in the fiber is calculated in Equation (5.26) to be

$$\text{E} = \frac{1}{2}\,A\,\rho\,C^2\,\omega^2 \int_0^L \sin^2\left(\frac{\pi}{\text{L}} \cdot z\right) dz \;=\; \frac{1}{4}\,A\,\rho\,L\,C^2\,\omega^2 \tag{5.49}$$

Since the $Q$'s were degraded by about two orders of magnitude by the damping, one can safely assume the loss is completely dominated by the damping material. The coating is longitudinally deformed when the fiber is bent during the violin-mode oscillation (see Figure 5.17). The elastic energy $\text{E}_{\text{Coating}}$ stored in the coating material is

$$\text{E}_{\text{Coating}} = \frac{1}{2}\text{E} \int_{\text{Volume}} \epsilon^2 \, dV \;=\; \frac{1}{2}\,I\,E_C \int_{\overline{z}-\frac{l}{2}}^{\overline{z}+\frac{l}{2}} \left(\frac{d^2}{dx^2}\,C \sin\left(\frac{n\,\pi}{L} \cdot z\right)\right)^2 \, dz \tag{5.50}$$

where $E_C$ is the Young's modulus of the coating material, $\overline{z}$ is the center of the coated section, $l$ is the coating length of this section, and $\epsilon = \Delta l/l$.

$$I_{\text{C}} = \frac{\pi}{4}\left((R+h)^4 - R^4\right) \tag{5.51}$$

is the bending moment of inertia of the coating, with $R$ being the fiber radius, and $h$ the thickness of the coating. Differentiating and then integrating of Equation (5.50) yields

$$\begin{aligned}
\text{E}_{\text{Coating}} &= \frac{1}{2}\,I\,E_C\,C^2 \left(\frac{n\pi}{L}\right)^4 \int_{\overline{z}-\frac{l}{2}}^{\overline{z}+\frac{l}{2}} \sin^2\left(\frac{n\,\pi}{L} \cdot z\right) \, dz \\
&= \frac{1}{2}\,I\,E_C\,C^2 \left(\frac{n\pi}{L}\right)^4 l \cdot \sin^2\left(\frac{n\,\pi}{L} \cdot \overline{z}\right)
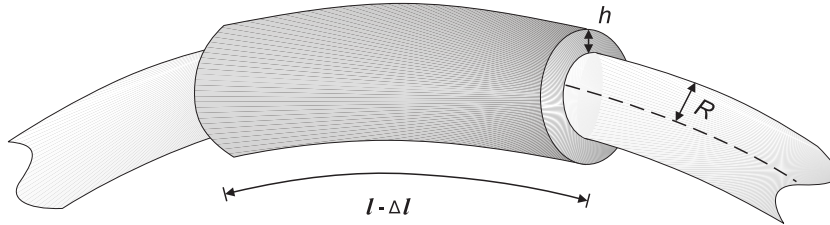\end{aligned} \tag{5.52}$$



**Figure 5.17:** Deformation of the coating when the fiber is bent due to violin mode oscillations.

The energy $E_{diss}$ dissipated per cycle is given by

$$E_{diss} = 2\pi \cdot \phi_C \cdot E_{Coating} \tag{5.53}$$

with $\phi_C$ being the loss function of the coating material. Thus, for the $Q$ of the $n$th violin mode of a fiber with one coated section follows

$$Q_n = \frac{\frac{1}{4} \rho A L \omega_n^2}{\left(\frac{n\pi}{L}\right)^4 \frac{1}{2} I E_C \cdot \phi_C \, l \cdot \sin^2\left(\frac{n\pi}{L} \cdot \overline{z}\right)} \tag{5.54}$$

For $m$ coated sections of different thickness at sections of the fiber with different radii the $Q$ of the $n$th violin mode is given by

$$Q_n = \frac{1}{2} \frac{\rho L \omega_n^2}{\left(\frac{n\pi}{L}\right)^4 E_C \cdot \phi_C} \sum_{i=1}^{m} \frac{A_i}{I_i \cdot l_i \cdot \sin^2\left(\frac{n\pi}{L} \cdot \overline{z}_i\right)} \tag{5.55}$$

All parameters of the fibers used in the inboard suspension are known, except for the Young's modulus $E_C$ and the loss function $\phi_C$ of the coating material. Hence, the $Q$ measurements can be used to deduce the imaginary part of the Young's modulus of the Teflon®. In the case of the GEO 600 inboard mirror suspensions two sections of each fiber (length $L$=280 mm, average cross section area $A = 3.9 \cdot 10^{-2}$ mm²) are coated (see Figure 5.4). The density of fused silica is $\rho = 2.2 \cdot 10^{-3}$ g mm⁻³. The relevant coating parameters referring to the index $i$ are given in Table 5.12. In Table 5.13 the measured relevant fiber parameters referring to index $n$ are given. Solving Equation (5.55) reveals the value of the product $E_C \cdot \phi_C$

$$E_C \cdot \phi_C = \frac{1}{2} \frac{\rho A L \omega_n^2}{Q \left(\frac{n\pi}{L}\right)^4 \sum\limits_{i=1}^{m} I_i \cdot l_i \cdot \sin^2\left(\frac{n\pi}{L} \cdot \overline{z}_i\right)} \tag{5.56}$$

| | $\overline{z}_i$ | $l_i$ | $I_i$ |
|---|---|---|---|
| i=1 | 140 mm | 26 mm | $3 \cdot 10^{-4} \pm 7 \cdot 10^{-5}$ mm⁴ |
| i=2 | 70 mm | 31 mm | $7 \cdot 10^{-4} \pm 1 \cdot 10^{-4}$ mm⁴ |

**Table 5.12:** The relevant parameters (index $i$) for the loss calculations of the two coated sections of the reference fiber. The center position of the coating $\overline{z}$, the coating length $l$ and the bending moment of inertia $I$ are given.

|       | $Q_n$          | $\omega_n$              |
|-------|----------------|-------------------------|
| n=1   | $2 \cdot 10^6$ | $2\pi \cdot 664\,\mathrm{Hz}$  |
| n=2   | $5 \cdot 10^5$ | $2\pi \cdot 1313\,\mathrm{Hz}$ |

**Table 5.13:** The relevant parameters (index $n$) for the loss calculations of the reference fiber. The measured $Q$'s and the frequencies for the first two violin modes are given.

Inserting the relevant values in Equation (5.56) yields for the first mode ($n$=1)

$$E_C \cdot \phi_{\mathrm{C}} = \frac{1}{2} \cdot \frac{2.2 \cdot 10^{-3} \cdot 3.9 \cdot 10^{-2} \cdot 280 \cdot (2\pi \cdot 664)^2 \left(\frac{\mathrm{g}}{\mathrm{mm \cdot s^2}}\right)}{2 \cdot 10^6 \cdot \left(\frac{\pi}{280}\right)^4 \cdot \left[3 \cdot 10^{-4} \cdot 26 \sin^2\left(\frac{\pi}{2}\right) + 7 \cdot 10^{-4} \cdot 31 \sin^2\left(\frac{\pi}{4}\right)\right]} \tag{5.57}$$

$$= (3.5 \pm 0.8) \cdot 10^8\,\mathrm{Pa}$$

and for the second mode ($n = 2$)

$$E_C \cdot \phi_{\mathrm{C}} = \frac{1}{2} \cdot \frac{2.2 \cdot 10^{-3} \cdot 3.9 \cdot 10^{-2} \cdot 280 \cdot (2\pi \cdot 1313)^2 \left(\frac{\mathrm{g}}{\mathrm{mm \cdot s^2}}\right)}{5 \cdot 10^5 \cdot \left(\frac{2\pi}{280}\right)^4 \cdot \left[3 \cdot 10^{-4} \cdot 26 \sin^2(\pi) + 7 \cdot 10^{-4} \cdot 31 \sin^2\left(\frac{\pi}{2}\right)\right]} \tag{5.58}$$

$$= (2.9 \pm 0.5) \cdot 10^8\,\mathrm{Pa}$$

Thus, the imaginary part of the Young's modulus of Teflon® could be worked out from the measurements of the violin-mode $Q$'s, to be about

$$E_{\mathrm{C}} \cdot \phi_{\mathrm{C}} \simeq 3 \cdot 10^8\,\mathrm{Pa} \tag{5.59}$$

This is the fundamental parameter for the approximation of the loss of the vertical mode, performed in the next section.

## 5.10 Calculation of the influence on the $Q$ of the vertical mode

Measurements showed that the vertical mode frequency is not affected by the damping of the first two violin modes. However, the $Q$ of the vertical mode is affected by the damping of the violin modes and hence an estimation of the introduced thermal noise has to be performed. An estimation for the $Q$ of the vertical mode can be derived from the loss of the violin modes.

First the resulting vertical spring constant of the fiber plus the coating has to be derived. The coated fiber can be treated as two springs in parallel (see Figure 5.18). One of these representing the fiber while the other represents the coating.
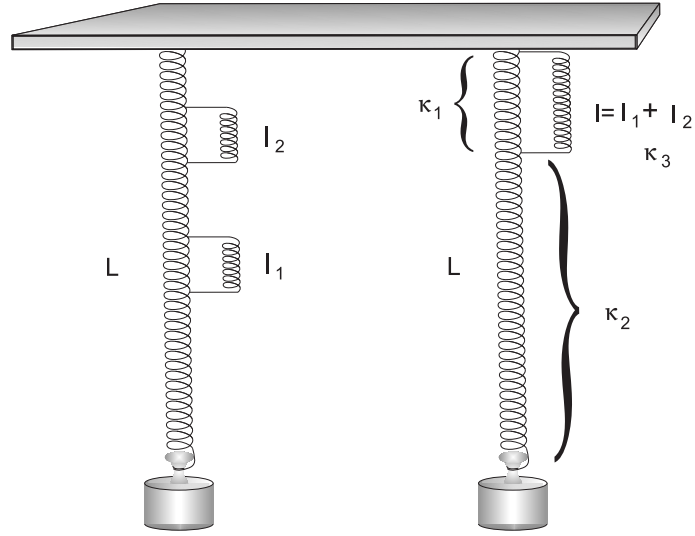
**Figure 5.18:** Two equivalent spring systems. **Left:** One large spring with two small springs in parallel. **Right:** An equivalent system consisting of a large spring with one medium spring, which has double the length and half the spring constant of one of the small springs. The effective spring constant $\kappa$ of such a system is characterized by the three spring constants $\kappa_1$, $\kappa_2$, and $\kappa_3$.

The composed spring constant is given by

$$\kappa = \left( \frac{1}{\kappa_2} + \frac{1}{\kappa_1 + \kappa_2} \right)^{-1} = \left( \frac{1}{E_S} \cdot \frac{A_S}{L - l} + \frac{1}{E_S \cdot \frac{S_S}{l} + E_C \cdot \frac{A_C}{l}} \right)^{-1} \tag{5.60}$$

where $A_S$ denotes the fiber cross section and $A_C$ gives the coating cross section.

$$\kappa = \left( \frac{L\,l}{E_S \cdot \pi R^2} + \frac{l}{\pi \left[ E_C \cdot (R + h)^2 + R^2 \cdot (E_S - E_C) \right]} \right)^{-1}$$

$$= E_S \cdot \frac{\pi R^2}{L} \cdot \left( \frac{L - l}{L} + \frac{l}{L \left( \frac{E_C}{E_S} \cdot \left[ \left( \frac{R+h}{R} \right)^2 - 1 \right] + 1 \right)} \right)^{-1} \tag{5.61}$$

With the approximation that $l \ll L$ and $E_C \ll E_S$ follows

$$\kappa \simeq E_S \frac{\pi R^2}{L} \cdot \left( 1 + \frac{l}{L} \frac{E_C}{E_S} \left[ \left( \frac{R+h}{R} \right)^2 - 1 \right] \right) \tag{5.62}$$

The loss factor $\phi_v$ for the vertical mode is

$$\phi_v = \frac{\operatorname{Im} \kappa}{|\kappa|} \simeq \phi_S + \frac{\phi_C \, E_C}{E_S} \frac{l}{L} \left[ \left( \frac{R+h}{R} \right)^2 - 1 \right] \tag{5.63}$$

where $\phi_S$ is the loss factor of fused silica ($\phi_S \in [10^{-7}, 10^{-6}]$). With the values for the fibers used for the inboard suspension one obtains an approximation for the $Q$ of the vertical mode.

$$\phi_v = \frac{\mathrm{Im}\,\kappa}{|\kappa|} \simeq \phi_S + \frac{1}{2}\frac{\rho\,\omega^2}{\left(\frac{n\pi}{L}\right)^4}\sum_{i=1}^{2}\frac{S_i}{Q_i\,I_i\,\sin^2\left(\frac{n\pi}{L}\,\overline{z}_i\right)}\left[\left(\frac{R_i+h_i}{R_i}\right)^2 - 1\right] \simeq 10^{-3} \quad (5.64)$$

Thus the vertical mode $Q$ can be approximated to be degraded to $Q_v \simeq 10^3$. However, measurements of the degradation of the vertical mode $Q_v$ could not be done with the described setup and hence, still need to be performed.

### 5.10.1 Coating induced vertical thermal noise

Figure 5.19 shows the increase of the suspension thermal noise due to the coating. The thermal noise induced by this "parasitic" damping of the vertical mode will not affect the sensitivity of GEO 600 in the most sensitive frequency band. Above 50 Hz the introduced
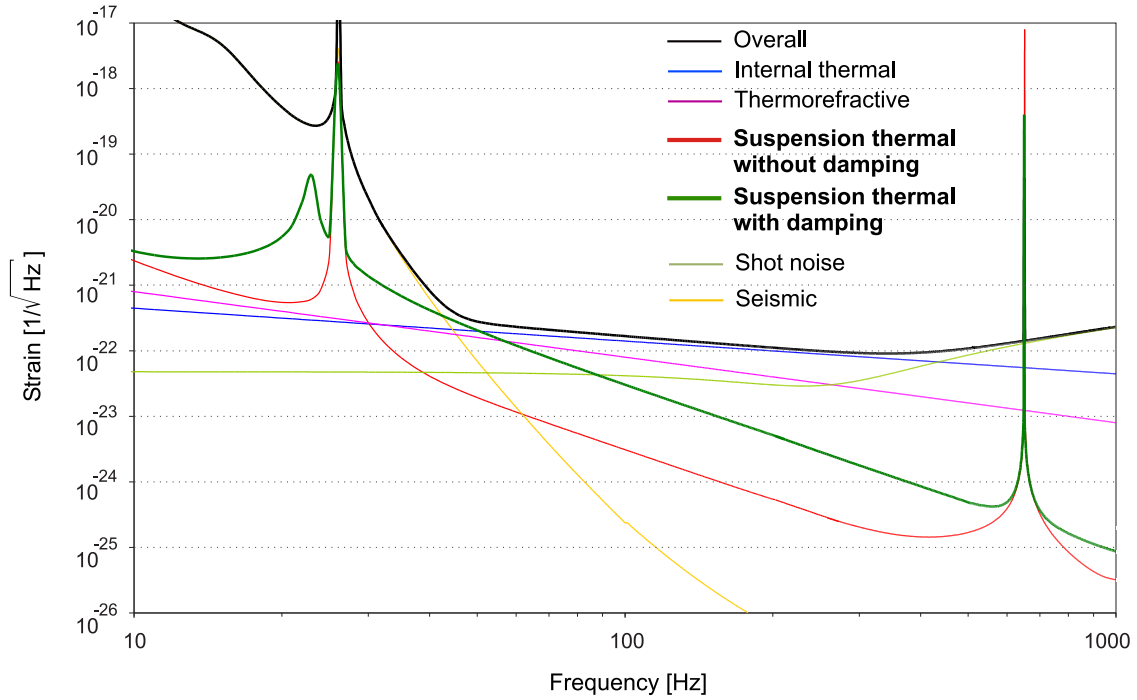


**Figure 5.19:** The GEO 600 design-sensitivity curve with the most relevant predicted noise contributions. Emphasized is the suspension thermal noise with and without violin-mode damping. The bump at 24 Hz is caused by the degradation of the vertical mode $Q$ of the inboard suspension fibers. The more sharp peak at 26 Hz is caused by the vertical mode of the far suspensions. The different frequencies are not a result of the damping but due to the fiber production as a trade-off in order to achieve the required set of parameters, given in Section 5.2. The "new" suspension thermal noise is limiting the sensitivity from $40 - 50$ Hz.

suspension thermal noise is below the internal thermal noise of the GEO 600 test masses. Above 60 Hz it is below the predicted thermo-refractive noise. Between 40 Hz and 50 Hz the increased suspension thermal noise sets, however, a limit to the sensitivity of GEO 600. Below this frequency the seismic noise dominates all other contributions.

## 5.11 Side experiments

In order to get a better understanding of the influence of the coating on different parameters, e.g., the higher order modes. a couple of side experiments were performed during the investigations of the coating properties. These are described in the following sections.

### 5.11.1 Influence on higher-order violin-mode frequencies and on the vertical-mode frequency

As the bending radii at the coated sections change with the mode number, the coating affects the frequencies and $Q$'s of the higher-order violin modes asymmetrically. Due to the fact that the third mode has nodes at both coated sections, this mode should hardly be affected by the damping. Hence, the frequency gap between the second and the third mode should be much larger than the gap between, e.g., the third and the fourth mode. In order to verify these considerations, the violin modes of a strongly damped fiber were measured up to $f_7$. The frequency separation of the modes, displayed in Table 5.14, shows the expected behavior. The degradation of the individual $Q$'s can be expected to be as asymmetric as the respective frequency step. This side experiment proved to be very useful for the search for higher-order violin modes in the spectrogram of the error-point spectrum of the interferometer length-control servo.

|  | $f_1$ | $f_2$ | $f_3$ | $f_4$ | $f_5$ | $f_6$ | $f_7$ |
|---|---|---|---|---|---|---|---|
| Frequency [Hz] | 461 | 979 | 1739 | 1954 | 2154 | 2548 | 2972 |
| Frequency step [Hz] | 461 | 518 | 760 | 215 | 200 | 396 | 434 |

**Table 5.14:** Frequency steps between the violin modes of a strongly coated fiber.

Even for this strongly damped fiber no influence on the vertical-mode frequency (14.9 Hz) could be observed within the measurement precision of 0.1 Hz. Nonetheless, a strong effect on the vertical mode $Q$ can be expected, referring to the calculations of the introduced loss for the vertical mode, given in Section 5.10 .

### 5.11.2 Coating of one long section

Since the handling of the fibers is very delicate and environmental influences like humidity weaken the fibers, a protective coating would be desirable. In an attempt to produce such

a protective coating, almost the entire length of a fiber was coated with a very thin layer of Teflon®. The end sections of the fiber remained uncoated to avoid a degradation of the pendulum mode. The violin modes of the fiber before and after coating are given in Table 5.15 .

|  | $f_1$ | $f_2$ | $f_3$ | $f_4$ |
|---|---|---|---|---|
| Before coating [Hz] | 682 | 1345 | 1909 | 2423 |
| After coating [Hz] | 671 | 1324 | 1885 | 2396 |

**Table 5.15:** Frequencies of the first four violin modes of a fiber with a coating over almost its entire length, before and after coating.

The such treated fiber showed a much greater tolerance to environmental influences. The protective coating kept the fiber from breaking when it was repeatedly touched with a glass rod while the fiber supported a load of 1.4 kg. Applying drops of water directly to the fiber did not degrade its strength. Such a protective layer can make the handling and storage of the fibers much more comfortable. The small frequency shifts indicate a small degradation of the violin-mode $Q$'s. The vertical mode $Q$ can, however, be expected to be much more strongly affected, since the loss originates from the extension of the coating instead of from the bending. For applications with strict requirements on the thermal noise at the vertical mode frequency (e.g., Advanced LIGO) such a treatment of the fibers seems not to be acceptable. However, the thickness of the layer could in principle be reduced by a substantial amount. Instead of the normal application method, one can let a drop of highly dissolved damping material run from one end of the fiber to the other a single time. The layer thickness can be further decreased by adding a greater amount of the solvent. Whether such thin coatings are still capable of providing a considerable protection and how big the influence on the different modes would be, needs still to be investigated.

### 5.11.3 Tuning a suspended fiber

In order to compensate for the additional frequency spread, introduced by suspending the monolithic stage, an *in vivo* coating would be desirable (see Section 5.4.6 for a description of the mechanism that leads to an enlargement of the frequency spread due to suspending the monolithic stage). The monolithic stage would need to be suspended and prealigned before measuring the violin-mode frequencies. Then a corrective coating has to be applied where required. The difficulty of doing this arises from the fact that the fiber is in a vertical position. The feasibility of coating a suspended fiber was demonstrated by tuning the fundamental mode of an already coated fiber, suspended with the nominal load of 1.4 kg, further down by 10 Hz. This additional tuning was done in three steps. The idea is to apply more Teflon® to an already coated section. This is possible because the already existing coating protects the fiber and thus allows to safely touch the section

with the application stick. Care has to be taken to prepare the right viscosity of the damping material, avoiding the possibility of an accidental application of a drop that could run down the fiber.

## 5.12 Future perspectives

The violin modes of the Advanced LIGO suspensions (expected around 400 Hz) will most likely also require damping. The experiences with the damping and tuning that was made in GEO 600 are currently being transfered to Advanced LIGO. Since the influence of the coating on the vertical mode $Q$ and thus on the thermal noise at the vertical-mode frequency may not be tolerable for Advanced LIGO, other damping techniques have to be explored in parallel.

### 5.12.1 Radiative cooling of the violin modes

As suggested by V. Mitrofanov, radiative cooling of certain fiber sections may be an alternative to the coating. The idea is to surround the relevant sections of the fiber with a cool environment to distract the thermal energy from these fiber sections. The high surface to volume ratio of the fiber and the low thermal conductivity of silica allow for an effective cooling of a well defined fiber section, while the rest of the fiber will be in a thermal equilibrium with the vacuum tank. The degradation of the violin-mode $Q$ results from an internal dissipation process, related to the flipping of the oxygen atoms between two isoenergetic positions between the two nearest Si atoms, that increases its effectiveness with decreasing temperature. As a free side effect the thermally-driven noise at the violin-mode frequencies is reduced due to the cooling. A tuning of the frequencies is, however, not possible with this damping scheme. Hence, it may be required to damp the violin modes more strongly than it is required for the GEO 600 inboard suspensions. Care must be taken when venting the vacuum system, avoiding any condensation of water vapor on the fiber surface, which would cause the fibers to break. The fibers need to thermalize to room temperature before coming into contact with humid air. Similar problems may arise from the condensation of molecules from the residual gas in the vacuum system. Experiments on this interesting idea still need to be performed.

### 5.12.2 Cooling the violin modes via anti-Stokes Raman conversion

Another interesting idea is the cooling of certain sections of the fibers via an anti-Stokes Raman process. Originally suggested to cool the break-off areas of the Virgo suspensions to obtain a reduction of the pendulum thermal noise, this scheme can be used for the violin modes as well. The idea is to add a dopant in the fiber material that can be used for an anti-Stokes Raman conversion via an incident laser beam. Thus, energy previously stored in the fiber could be distracted via the wave mixing process. The resulting degradation of the violin-mode $Q$'s and the reduction of the thermal noise follows the same mechanism as described in the above section. Again, experiments still need to be performed.

# Appendix A

# The output-optics suspensions

The preliminary output optics, described in Section 3.10, currently used to direct the light that leaves the interferometer via the output port toward the detection bench, will eventually be replaced by the final output optics. While the currently used beam steering mirror is simply mounted on a post at the bottom plate of the output tank (**TCOb**), the final output optics will be suspended by four single pendulums, each including one cantilever-spring stage, as described in the following sections.

As mentioned in Chapter 3.8.3, once the full laser power is used, the light power leaving the output port of GEO 600 will be dominated by light in higher order modes. The strong contribution of mainly $TEM_{02}$ modes will be caused by the mismatch of the interferometer arms, once the thermal lens in the beamsplitter substrate is fully developed. Even though the absorption inside the beamsplitter was measured to be smaller than $0.5 \, \mathrm{ppm \, cm^{-1}}$, a thermal lens is generated in the substrate by the residual absorption of laser light. The presence of this thermal lens reduces the spatial overlap of the beams recombining at the beamsplitter. The radius of the east beam at the beamsplitter is $10.8 \, \mathrm{mm}$ while the radius of the north beam is $10.2 \, \mathrm{mm}$. Hence, the phase difference between the two interfering beams has a spatial dependence with a radial symmetry.

Figure A.1 illustrates the optical layout of the final output optics. The suspension of **BDO2** will be located close beside the signal-recycling suspension in **TCOa** and is hence designed to be a "stand-alone" device. This design allows for a straightforward installation and leaves a certain freedom for the final positioning. The other three pendulums are located inside **TCOb** sharing a common top plate. Three mirrors are required to form the so-called output telescope since the mode matching into the output-modecleaner cavity ($w_0 = 120 \, \mu\mathrm{m}$) requires a folding of the beam path. The first mirror, **BDO1**, has a focal length of $f = 3.35 \, \mathrm{m}$ while the other two mirrors, **BDO2** and **BDO3**, are planar.

## A.1 The output modecleaner

In order to reject the excess light before the output photo diode **PDO**, the use of an output modecleaner is foreseen to complete the optical configuration of GEO 600. The output modecleaner was selected to be a triangular ring cavity based on a rigid spacer, having an optical round-trip length of $10 \, \mathrm{cm}$. A schematic drawing of the output modecleaner is displayed in Figure A.2. It consists of an ULE spacer with an on-bonded prism to support the two planar mirrors at the obtuse angle of the triangle. The curved mirror at
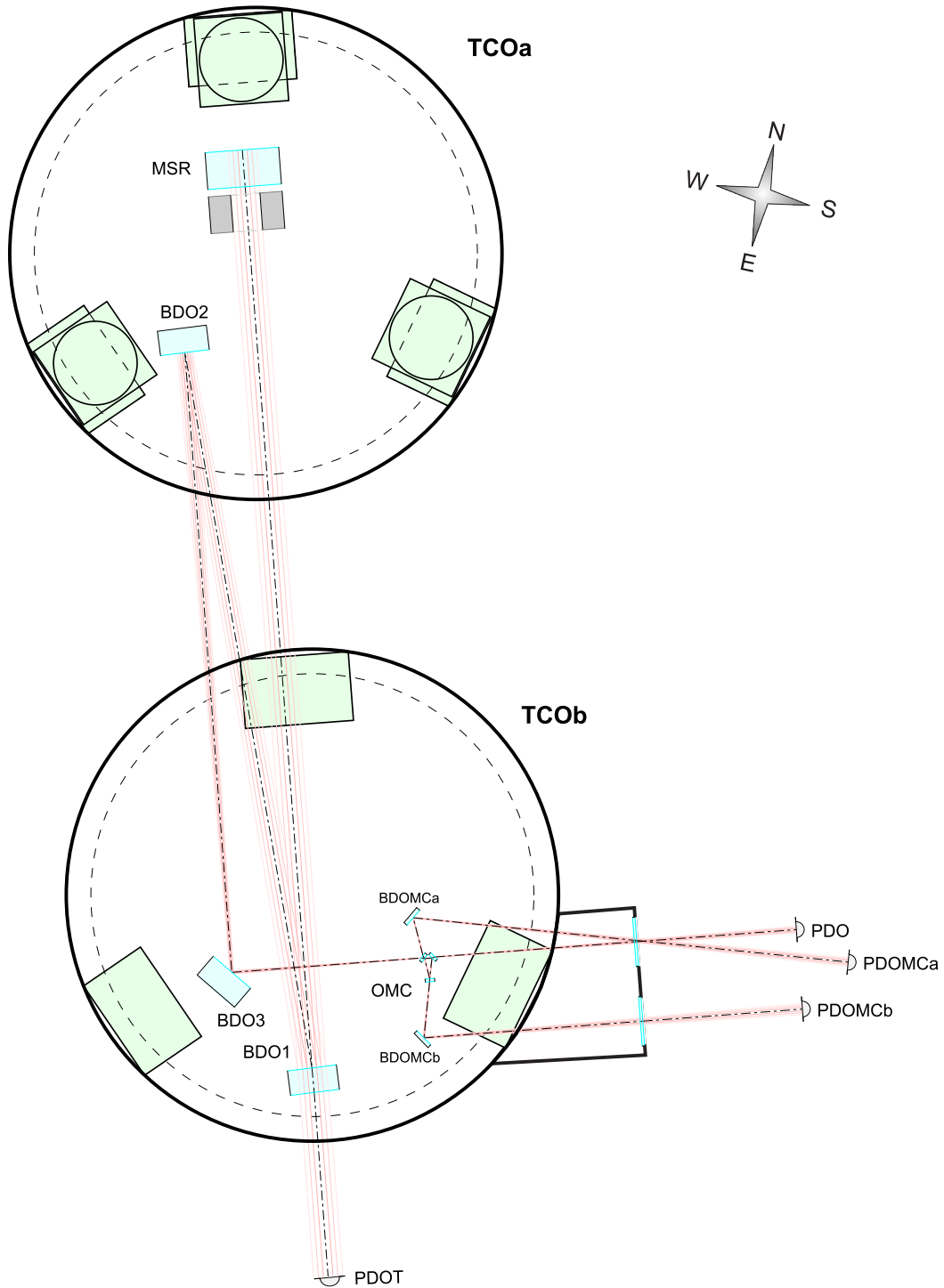
**Figure A.1:**  Optical layout for the output optics.  Three beam-steering mirrors (one focusing mirror, **BDO1**, and two planar mirrors, **BDO2** and **BDO3**,) form the output telescope. The output modecleaner **OMC** is the last optical element in the light path inside the vacuum system.  The beam north of the signal-recycling mirror **MSR** (i.e., inside the dual-recycled Michelson interferometer) has been omitted.
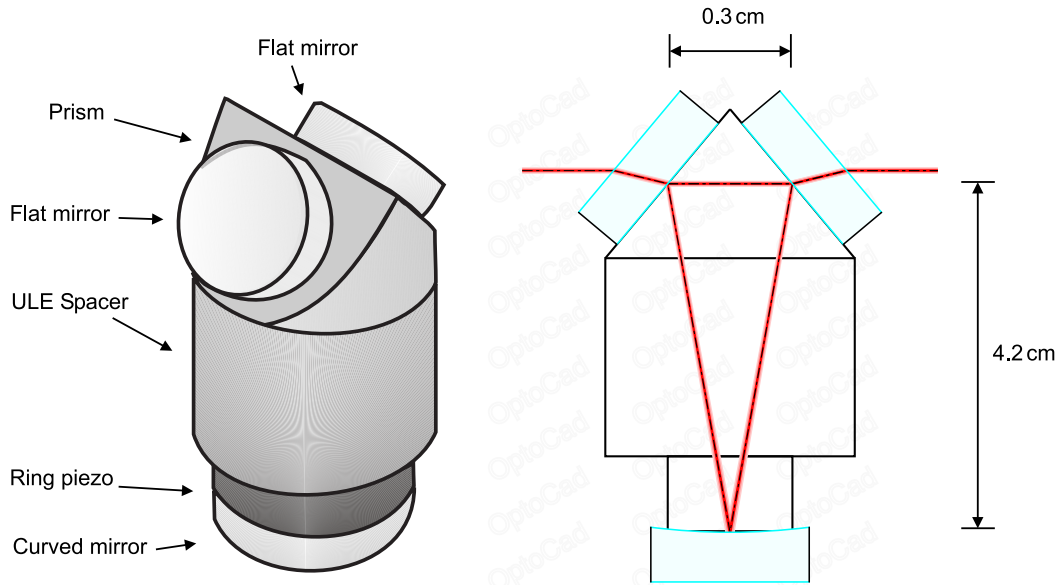
**Figure A.2:** The output modecleaner of GEO 600 is a triangular ring cavity supported by a rigid spacer. The optical round-trip length is 10 cm, the finesse will be around 30. A ring piezo allows for the length control of the cavity.

the acute angle is mounted on a ring piezo allowing for length control of the cavity. The finesse of the output modecleaner will be around 30.

The cavity itself will be clamped into an aluminum mass to allow for the appliance of the same suspension scheme as for the three output-telescope mirrors: The aluminum mass has the same outer dimensions and, together with the output modecleaner, the same weight as the mirrors.

## A.2  The suspensions

The requirements on the suspensions for the output-telescope mirrors in terms of seismic isolation are less stringent than for the other optics of GEO 600. This is due to the fact that these mirrors form no cavity and hence no dispersive effects can arise from the residual motion of the mirrors (dispersion could lead to a relative phase shift between the carrier light and both the control and signal sidebands). Thus, single pendulums including a cantilever-spring stage were chosen to realize a straightforward but nonetheless sufficiently effective design for the output-optics suspensions. Figure A.3 illustrates the suspension scheme for the output optics.

The output-telescope mirrors are of the same type as used for the input modecleaners. With a diameter of 100 mm and a thickness of 50 mm they weigh 860 g. Each mirror will lie in two steel wire loops, separated by 4 mm. Wire of 127 μm radius will be taken to realize the loops. Break-off-position defining bars are attached 2 mm above the COM to the sides of the mirrors. The wire ends will be attached via small titanium clamps to the tips of two cantilever springs. Eddy-current damping will be employed at the tips of the
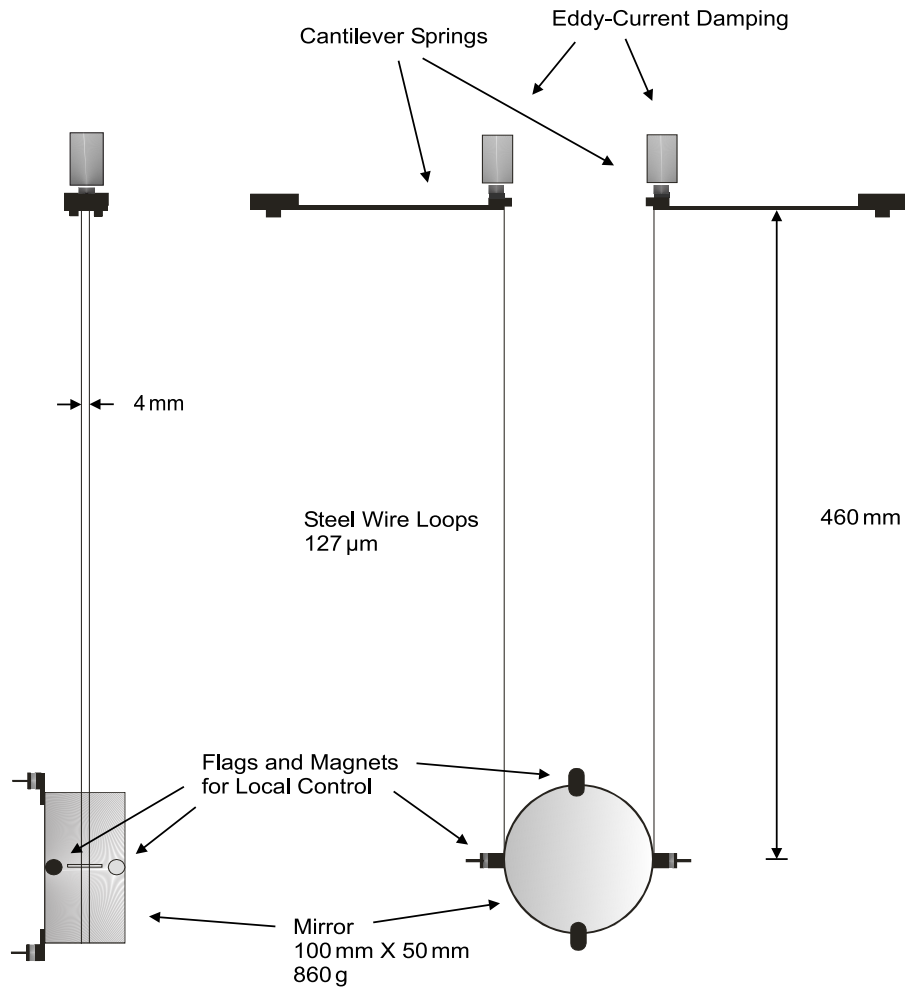
**Figure A.3:**  Schematic drawing of a pendulum as will be used for the output-optics suspensions. It consists of a single pendulums, suspended from a single cantilever-spring stage. Eddy-current damping is applied to damp the roll and vertical motion.  the other degrees of freedom as longitudinal motion, sideways, pitch, and yaw are actively controlled with four magnet-coil actuators at the mirror itself. Aluminum stand-off plates at the mirror support the flags and magnets for the local control.

cantilever springs in order to damp the vertical and roll motion of the optics. Therefore magnets of 10 mm diameter and 5 mm height will be bonded onto the titanium clamps. These magnets will be covered by copper tubes as for the Eddy-current damping of the upper cantilever springs of the main suspensions.  The copper tubes will extend from arms mounted to the support point of the suspensions.

The pendulum's eigenmodes in the remaining degrees of freedom (i.e., longitudinal, sideways, pitch, and yaw)will be damped in four degrees of freedom by active local control at the mirror itself. Small aluminum spacers will be bonded to the mirrors to support the magnets and flags for the position and orientation control. Glass encapsulated coils with co-located optical sensor as used for the input modecleaner suspensions will be employed

for the sensing and actuation. The coilholders for the local-control coils will be clamped to the bottom plate of the vacuum tank. A free aperture of 65 mm in the coilholders allows for a detection of the transmitted light outside the vacuum system. The transmitted beams contain information required for control reasons as for the automatic alignment of the signal-recycling cavity. In order to provide sufficient clearance for the transmittance of the beams the two pitch-control coils had to be separated by more than the diameter of the mirror. Hence, the corresponding magnets will be attached to the mirrors via extending stand-off plates. Vacseal® will be used for all bonds required for the output suspensions.

A speciality of the output-optics suspensions is the fact that each two wires will be attached to a common cantilever spring. This design is a concession to the limited space. Since the design allows to suspend each mirror from only two springs, the spring constants can be kept relatively high. Softer springs would simply be too long to fit in the output tanks at the desired positions.

The prealignment of the mirrors will be done via a leveled HeNe laser, positioned in **TCOa**, and a photo diode on the detection bench. The three pendulums in **TCOb** are individually suspended from revolvable support devices that will be used to obtain the yaw alignment of the optics. The clamping mechanism of the revolvable devices allows for a torque free clamping to the actual position after the prealignment. The pitch alignment will be done via the base clamps of the cantilever springs. The clamps allow the adjustment of the pitch angle under which the springs are mounted.

As already mentioned, mirror **BDO2** in tank **TCOa** is suspended from a stand-alone device. The yaw prealignment of this mirror will be done by positioning the whole device before clamping it to the bottom plate of the vacuum tank. The pitch alignment can be done as for the other three suspensions. The final alignment of all four suspensions will be achieved electronically via bias currents through the local-control coils.

# Appendix B

# Thermal adaption of the radii of curvature of the interferometer mirrors

In order to allow for an optically stable operation of the dual-recycled Michelson interferometer a combination of 600 m radius of curvature (ROC) for the inboard mirrors and 640 m for the far mirrors was chosen. After coating the mirror substrates the ROCs were found, however, to be $622 \pm 10$ m for **MCe**, $636 \pm 10$ m for **MCn**. $687 \pm 2$ m for **MFe**, and $666 \pm 2$ m for **MFn**. As a result of this mismatch the phase fronts of the beams returning from the north and east arm, respectively, have different ROCs and diameter at the beamsplitter. Hence, the interference contrast of the recombined beams is deteriorated. The thereby introduced loss is about 0.65%. A power build up of 300 inside the power-recycling cavity was observed with the test mirrors before the installation of the final mirrors. The loss due to the mismatch of the ROCs prevented, however, a power build up in exess of about 200. Furthermore, the error signal of the longitudinal control of the Michelson interferometer diminishes the more the closer to the impedance matched condition the power-recycling cavity is operated. As a consequence, any additional loss introduced by a misalignment of the cavity mirrors may cause the error signal to completely vanish. Thus, it was decided to employ an *in situ* correction for the observed deviations of the ROCs from the design values. Since the aim of this correction is to match the two interferometer arms with respect to each other, the compensation of the ROCs' mismatch for the different mirrors can be done at only one far mirror. As the small 'electrostatic actuator on a stick' is mounted behind the far north mirror **MFn**, the far east mirror **MFe** was selected for the compensation.

The initially considered utilization of a $CO_2$ laser would have required the replacement of at least one view port of the far east vacuum tank and furthermore a thorough testing of the heating scheme beforehand. Thus, it was decided to take the most straightforward action to achieve a thermal adaption of the ROCs by placing a radiation heater behind the mirror .

The heater consists of a Duran® [1] glass rod that was bent to a ring (similar to a pastoral staff) in a natural gas flame. The ring is wrapped with a ribbon of stainless-steel foil of 100 μm thickness. Figure B.1 shows a schematic drawing of the ring heater. The ends of the ribbon are held in position by a common clamp made from Macor®. The ends are connected to a power supply such that the ribbon can be heated by passing a bias

---

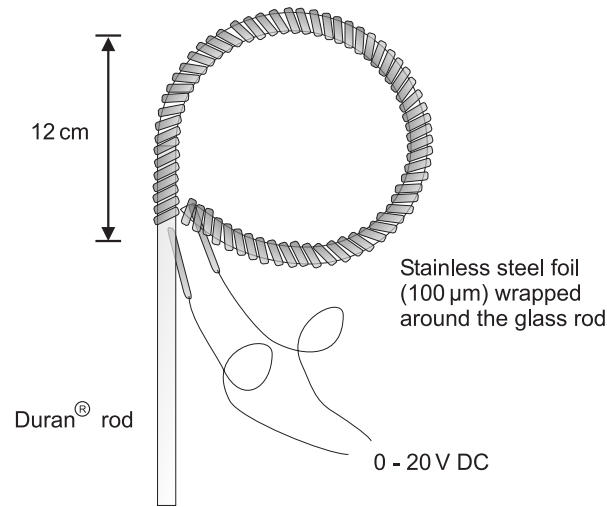[1] http://www.schott.com/labware/german/products/duran/

**Figure B.1:** Schematic drawing of the ring heater. It is based on a Duran® rod that is bent to form a ring. The ring is wrapped with a ribbon of stainless-steel foil of 100 μm thickness. The two ends of the ribbon are connected to a DC-power supply.

current of about 3 A through. Subsequent to the required UHV compatible cleaning the heater was given a vacuum bake at very high temperature (i.e., red glowing) before it was implemented in GEO 600. Figure B.2 shows a photograph of the ring heater positioned 5 cm behind the far east mirror **MFe**. The remaining end of the staff is used as an isolated post.

The heater generates a thermal gradient along the optical axis inside the mirror substrate due to the sufficiently low thermal conductance of the mirror's material. Due to the material's CTE, the rear side of the mirror substrate expands in turn more strongly than the front side. Thus, the ROC of the mirror is decreased. Figure B.3 illustrates the principle of the thermal adaption of the ROC.

The vertical component of the ROCs can be matched by setting the heater power to 67 W. At a heater power of 74 W eventually the horizontal component of the ROCs is found to be matched. In both cases a certain astigmatism remains, rotated by 90° in the respective cases. Possible reasons for astigmatic effects may lie in the nonuniform environment of the mirror or in a slightly non-planar beamsplitter. Figure B.4 shows a series of photographs of the mode shape of the light leaving the interferometer at the output port. By the use of a segmented heater such higher order effects could also be corrected for. However, so far this was not required for GEO 600 . The optimum heater power in terms of minimal dark-port power was found to be 71 W. At this heater power the dark-port power is diminished to be about 20 mW. Figure B.5 shows the measured dark-port power versus the light power inside the power-recycling cavity when changing the heater power.
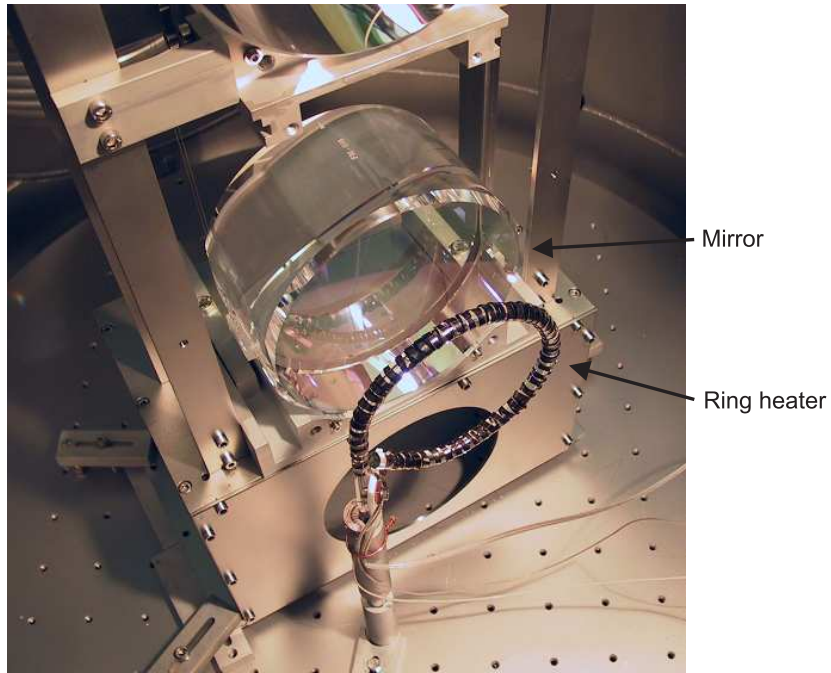
**Figure B.2:** The ring heater as mounted in the far east tank **TFe**. The distance to the mirror is 5 cm. Currently the heater is operated at 71 W.
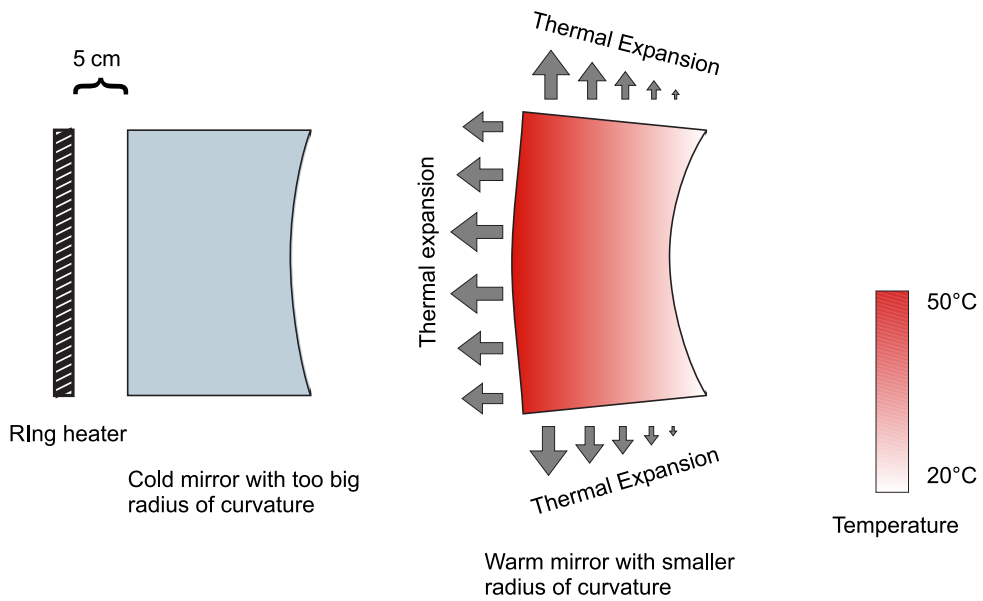


**Figure B.3:** The ring heater heats the mirror from the rear side in order to generate a thermal gradient in the substrate. The front side of the mirror remains cooler and therefore expands less strongly. Thus, the ROC of the mirror is decreased.
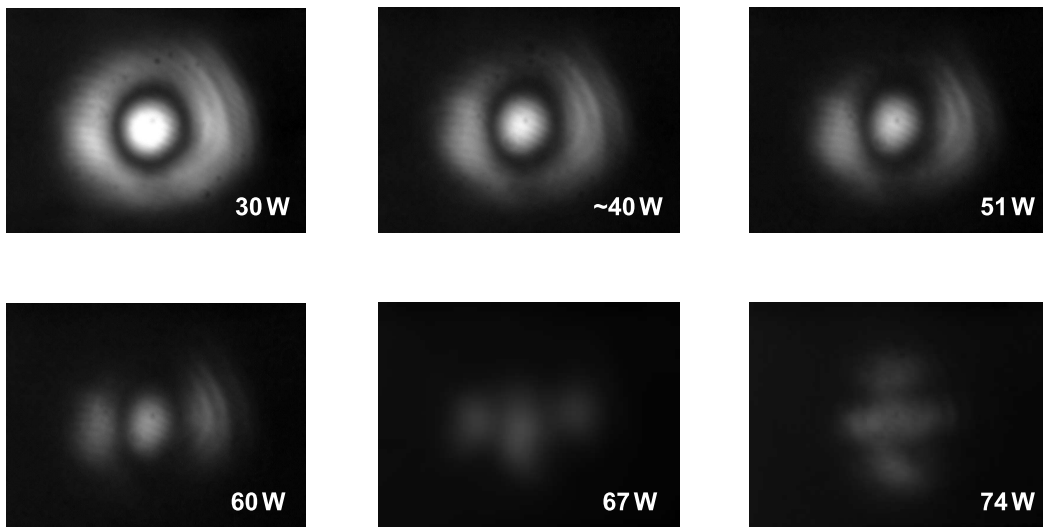
**Figure B.4:** The output port as recorded with a CCD camera. With increasing heater power the light power at the output port (dark-port power) is reduced. At 67 W the vertical component of the ROCs is compensated while the compensation of the horizontal component requires a heater power of 74 W. The optimum heater power was found to be 71 W.
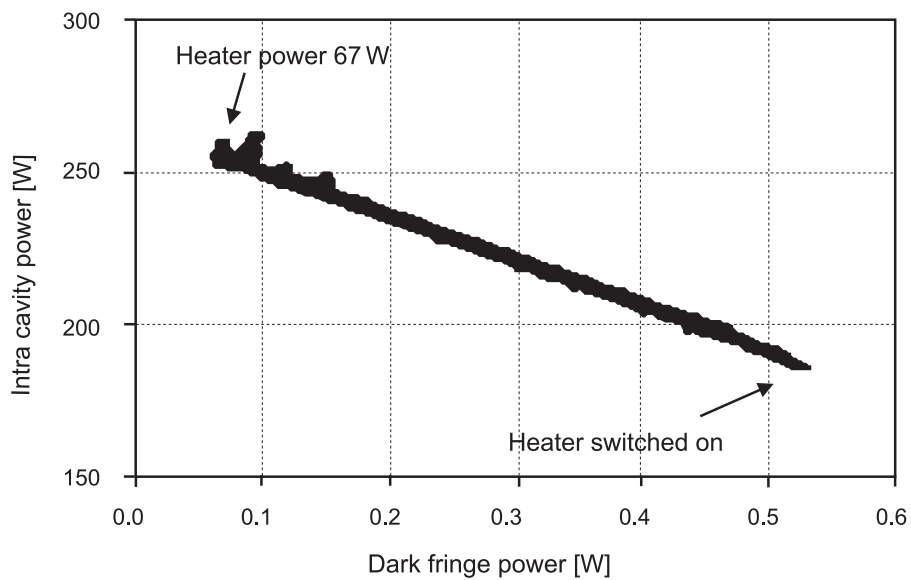


**Figure B.5:** The dark-port power versus the light power inside the power-recycling cavity when increasing the heater power.

# Appendix C

# Overview of the GEO 600 pendulums

The next two pages provide an overview of all types of suspensions that are currently installed inGEO 600. Although the output optics is planned to be installed within the next months in has been omitted here. In Table C.1 all relevant details of the different systems are given. These include the number of pendulum and cantilever spring stages of the respective suspension system, the length and suspension filament material of each stage, and the according suspended masses are listed in the table. The specialities of the individual systems, e.g., the employed actuators, are provided where indicated.

| | MC | MU | BDOMC2, BDIPR | MPR, MPRr |
|---|---|---|---|---|
| Quantity | 11 | 2 | 1, 1 | 1, 1 |
| Stack layers (active/passive) | $-/2$ | $-/2$ | $-/2$ | $-/2$ |
| Cantilever spring stages | $-$ | $-$ | $-$ | 1 |
| **1st stage:** wire diameter stage length stage weight | 2 steel wires 127 µm 290 mm 0.86 kg | 2 steel wires 290 mm | 2 steel wires 152 µm 290 mm 1.24 kg | 2 steel wires 300 µm 420 mm 2.9 kg |
| **2nd stage:** wire diameter stage length stage weight | 2 loops of steel wire 102 µm 460 mm 0.86 kg | 4 steel wires 460 mm | 2 loops of steel wire 127 µm 460 mm 1.24 kg | 2 loops of steel wire 162 µm 460 mm 2.9 kg |
| **3rd stage:** wire diameter stage length stage weight | $-$ | $-$ | $-$ | $-$ |
| Mirror | Ø=100 mm 50 mm thick | $-$ | Ø=120 mm 50 mm thick | Ø=150 mm 75 mm thick |
| Speciality: | Suspended magnet-coil actuators at 2 mirrors | | Magnet-coil actuators at the mirrors | Suspended magnet-coil actuators at the mirror |

**Table C.1:**  Properties of the GEO 600 double-pendulum suspensions.  The wire length, wire diameter, and the masses of the relevant stages are given for the different suspension types.  The table is continued overleaf.

| MCn, MCe | MFn, MFe | MCnr, MCer | BS | MSR, SRr |
|---|---|---|---|---|
| 1, 1 | 1, 1 | 1, 1 | 1 | 1, 1 |
| 2 / − | 2 / − | 2 / − | 2 / − | 2 / − |
| 2 | 2 | 2 | 2 | 2 |
| 2 steel wires | 2 steel wires | 2 steel wires | 2 steel wires | 2 steel wires |
| 550 µm | 550 µm | 550 µm | 600 µm | 360 µm |
| 420 mm | 420 mm | 420 mm | 420 mm | 420 mm |
| 5.6 kg | 5.6 kg | 5.6 kg | 9.34 kg | 2.9 kg |
| 2 loops of steel wire | 2 loops of steel wire | 2 loops of steel wire | 2 loops of steel wire | 2 loops of steel wire |
| 350 µm | 350 µm | 350 µm | 400 µm | 200 µm |
| 180 mm | 180 mm | 180 mm | 180 mm | 180 mm |
| 5.55 kg | 5.55 kg | 5.6 kg | 9.3 kg | 2.9 kg |
| 4 silica fibers | 4 silica fibers | 4 steel wires | 4 silica fibers | 2 loops of steel wire |
| 280 mm | 280 mm | 280 mm | 280 mm | 280 mm |
| 210 µm | 250 µm | 275 µm | 300 µm | 162 µm |
| 5.32 kg | 5.32 kg | 5.6 kg | 9.3 kg | 2.9 kg |
| Ø=180 mm | Ø=180 mm | − | Ø=260 mm | Ø=150 mm |
| 100 mm thick | 10 mm thick | | 75 mm thick | 150 mm thick |
| Suspended magnet-coil actuators at the penultimate mass | − | − | − | Suspended magnet-coil actuators at the mirrors |
| Suspended electrostatic actuators at the mirrors | | | | |

Continued from overleaf: Properties of the GEO 600 triple-pendulum suspensions.

# Appendix D

# The ultra-high vacuum system

All suspension systems of GEO 600 are enclosed in a common ultra-high vacuum (UHV) system to reduce both the acoustic coupling to the suspended optics and the air friction of the suspensions. Furthermore, a contamination of the optics is prevented and the influence of fluctuations of the refractive index are minimized. Figure D.1 illustrates the layout of the GEO 600 UHV system. Overall, it includes a volume of $400\,\mathrm{m}^3$, divided into seven sections (or cluster):

- The first section, with a volume of about $5\,\mathrm{m}^3$, houses the modecleaner system (**TCMa**, **TCMb**). It is pumped by a turbo-molecular pump with a pump rate of $180\,\mathrm{l/s}$. The residual gas pressure is $2.3 \cdot 10^{-6}\,\mathrm{Pa}$ ($2.3 \cdot 10^{-8}\,\mathrm{mbar}$), dominated by water vapor.

- The central cluster includes the telescope tube, the power-recycling tank **TCIb**, the beamsplitter tank **TCC**, and the two inboard tanks **TCn** and **TCe**. The overall volume of the central cluster is about $7\,\mathrm{m}^3$. Due to frequent installation and maintenance work in the last few month, the vacuum is limited to a residual gas pressure of $4.5 \cdot 10^{-6}\,\mathrm{Pa}$ ($4.5 \cdot 10^{-8}\,\mathrm{mbar}$).

- The output cluster, connected to the south side of the beamsplitter tank, consists of the signal-recycling tank **TCOa** and the output tank **TCOb**. It is pumped by a turbo-molecular pump like the one used for the modecleaner cluster.The output cluster has a volume of about $3\,\mathrm{m}^3$ at $4.3 \cdot 10^{-6}\,\mathrm{Pa}$ ($4.3 \cdot 10^{-8}\,\mathrm{mbar}$).

- Attached to the inboard tanks are the two tubes, each forming a section of the UHV system on its own. The $600\,\mathrm{m}$ long tubes have a diameter of $60\,\mathrm{cm}$ and hence, have a volume of $2 \cdot 192\,\mathrm{m}^3$.

- The two far tanks **TFn** and **TFe**, attached to the far ends of the tubes, complete the system. Each far tank encloses a volume of yet another $1.5\,\mathrm{m}^3$. The residual gas pressure in the far tanks is $1.3 \cdot 10^{-6}\,\mathrm{Pa}$ ($1.3 \cdot 10^{-8}\,\mathrm{mbar}$) for the far east tank (TFe) and $1.8 \cdot 10^{-6}\,\mathrm{Pa}$ ($1.8 \cdot 10^{-8}\,\mathrm{mbar}$) for the far north tank (TFn), respectively.

Whenever a suspension system is installed or maintained, the very section of the UHV system can be disconnected from the neighboring sections by closing the respective gate valves (see Figure D.1).

The far end of each tube and the attached far tank are pumped by a common turbo-molecular pump with a pump rate of 1000 l/s. The same type of pump is used at each inboard end of the tubes, simultaneously pumping the central cluster.

To ensure the UHV compatibility of all parts used to build the suspension systems (altogether a few thousand parts) had to pass a thorough cleaning process. The aluminum components were cleaned for about 30 min in an ultrasonic bath at about 75°C using demineralized water and the alkaline degreaser P3-Almeco 18®[1]. The stainless-steel, copper, and brass parts were cleaned in the ultrasonic bath at 80°C for 30 min using the alkaline agent Surtec [2]. Subsequent to the cleaning in the ultrasonic bath all parts were rinsed in a dishwater that is also fed with demineralized water. All tools required for the installation work had to be cleaned as well. Furthermore, the components and tools must not be handled without wearing clean abrasion proof gloves. In order to avoid contamination, the parts were solely handled in cleanroom environment.

The strong tendency of UHV compatible clean bolts to create cold welds due to the total lack of any lubricant, is a feature that has often been reported about. A way to tackle this problem is the use of oversized threads. Furthermore, it proved that the application of a few drops of Isopropanol may lubricate the respective thread for a short while when loosening a bolt. Combining both methods reliably prevents the frequent encounter of bolts, irrevocably stuck in a thread.

---

[1]http://www.henkel.de/
[2]http://www.surtec.com/
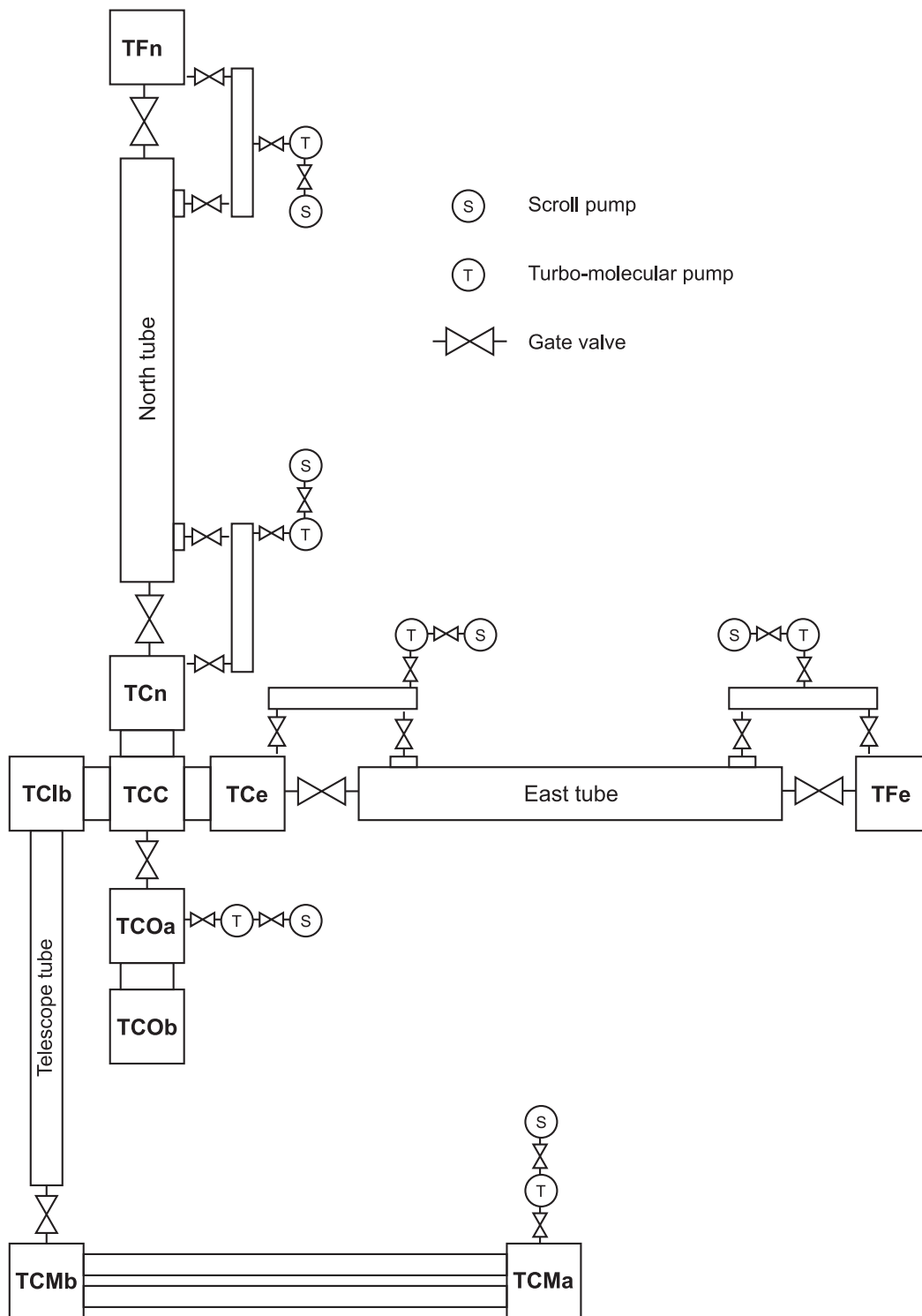
**Figure D.1:** Layout of the GEO 600 ultra-high vacuum system. The system consists of seven independent sections, that can be separated from each other by gate valves.

# Appendix E

# The optical layout of GEO 600

The complete optical layout of GEO 600 including all optical components, beams, beam dumps, and photo diodes at their precise positions is illustrated in Figure E.1. The drawing is based on the ray-tracing program OptoCad by R. Schilling. The input file used to generate the GEO 600 layout was as well written by R. Schilling who also maintains the file. Due to new developments and more precise computer simulations, the optical layout was subject to various changes in the last few years. As mentioned in Section 3.5, one of these changes was the shifting of the power-recycling mirror into the small vacuum tank **TCIb**. A further change was to omit the compensation plate (Section 3.8.3).

# GEO 600 optical layout
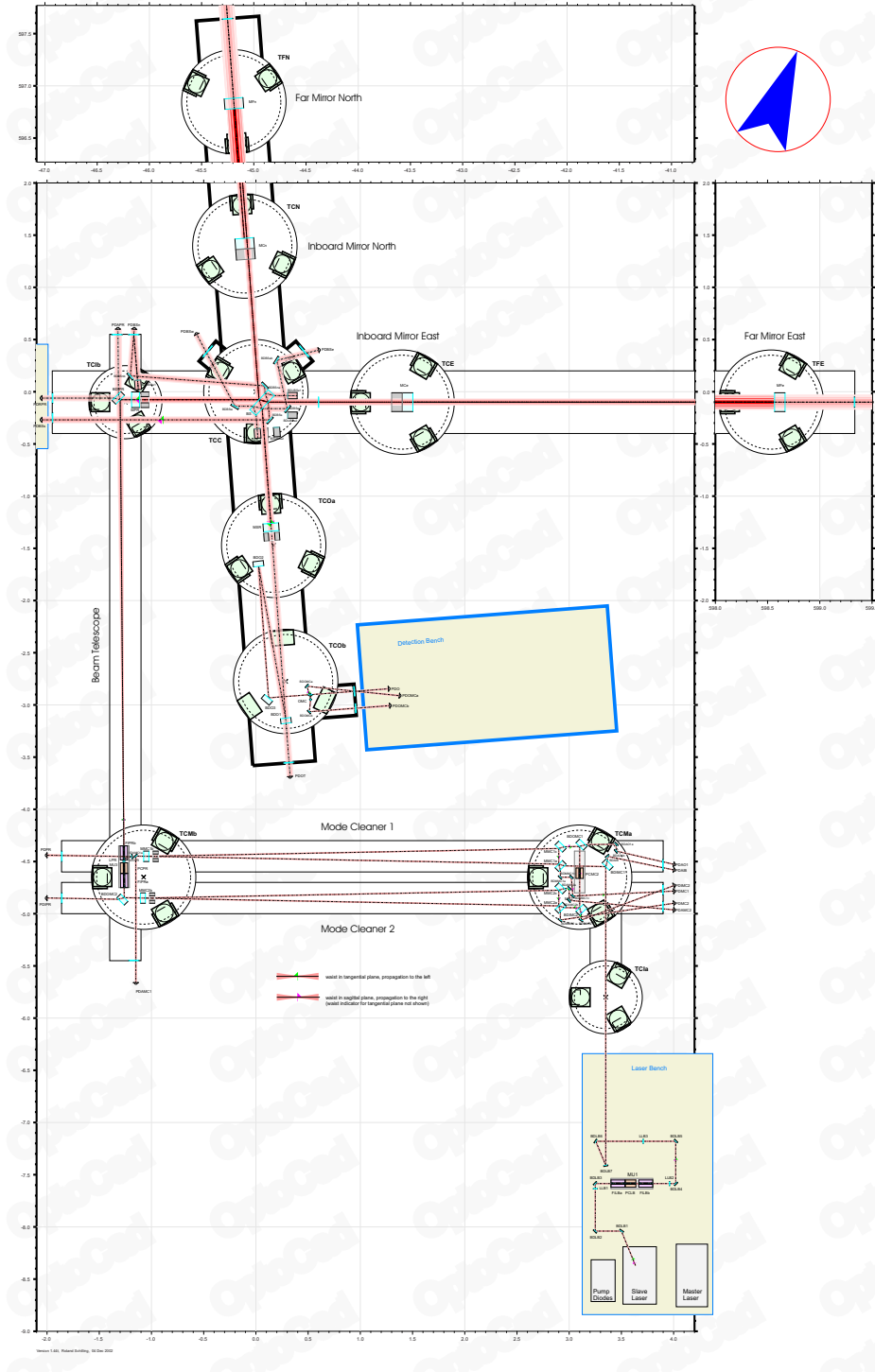
**Figure E.1:** Complete optical layout of GEO 600

# Bibliography

[Abbott '02]  R. Abbott, R. Adhikari, G. Allen, S. Cowley, E. Daw, D. DeBra, J. Giamie, G. Hammond, M. Hammond, C. Hardham, J. How, W. Hua, W. Johnson, B. Lantz, K. Mason, R. Mittleman, J. Nichol, S. Richman, J. Rollins, D. Shoemaker, G. Stapfer and R. Stebbins 2002 *Seismic isolation for Advanced LIGO* Class. Quantum Grav. **19** 1591–1598

[Acernese '04]  F. Acernese et al. 2004 *The status of VIRGO* Class. Quantum Grav. **21** 385–394

[Ageev '98]  A. Y. Ageev, I. A, Bilenko, V. B. Braginsky 1998 *Excess noise in the steel suspension wires for the laser gravitational wave detctor* Phys. Lett. A **246** 479–484

[Ageev '03]  A. Y. Ageev 2003 *Fused silica research for Advanced LIGO* LSC meeting, Hannover, Germany, http://www.ligo.caltech.edu/docs/G/G030509-00/G030509-00.pdf

[Aguiar '02]  O. D. Aguiar, L. A. Andrade, L. Camargo Filho, C. A. Costa, J. C. N. de Araújo, E. C. de Rey Neto, S. T. de Souza, A. C. Fauth, C. Frajuca, G. Frossati, S. R. Furtado, V. G. S. Furtado, N. S. Magalhães, R. M. Marinho Jr, E. S. Matos, M. T. Meliani, J. L. Melo, O. D. Miranda, M. F. Oliveira Jr, K. L. Ribeiro, K. B. M. Sallles, C. Stellatiand, W. F. Velloso Jr. 2002 *The status of the Brazilian spherical detector* Class. Quantum Grav. **19** 1949–1955

[Amico '02]  P. Amico, L. Bosi, L. Carbone, L. Gammaitoni, M. Punturo, F. Travasso and H. Vocca 2002 *Fused silica suspensioons for the VIRGO optics: status and perspectives* Class. Quantum Grav. **19** 1669–1675

[Arai]  K. Arai, personal communication

[Armandula]  H. Armandula, personal communication

[Astone '02]  P. Astone, M. Bassan, P. Bonifazi, P. Carelli, M. G. Castellano, G. Cavallari, E. Coccia, C. Cosmelli, S. D´Antonio, V. Favone, G. Federici, Y. Minenkov, G. Modestino, I. Modena, A. Moleti, G. Pizella, G. V. Pallottino, L. Quintieri, A. Rocchi, F. Ronga , R. Terenzi, G. Torrioli, and M. Visco 2002 *The EXPLORER gravitational wave antenna: recent improvements and performances* Class. Quantum Grav. **19** 1905–1911

[Astone '02]  P. Astone 2002 *Resonant mass detectors: present status* Class. Quantum Grav. **19** 1227–1235

[Barr '02] B. W. Barr, G. Cagnoli, M. M. Casey, D. Clubley, D. R. M. Crooks, K. Danzmann, E. J. Ellifi, S. Goßler, A. Grant, H. Grote, A. Heptonstall, J. Hough, O. Jennrich, H. Lück, S. A. McIntosh, G. P. Newton, D. A. Palmer, M. V. Plissi, D. I. Robertson, N. A. Robertson, S. Rowan, K. D. Skeldon, P. Sneddon, K. A. Strain, C. I. Torrie, H. Ward, P. A. Willems, B. Willke, W. Winkler *Silica Research in Glasgow* Class. Quantum Grav. **19** 1655 - 1662

[Bennett '04] C. L. Bennett, M. Halpern, G. Hinshaw, N. Jarosik, A. Kogut, M. Limon, S. S. Meyer, L. Page, D. N. Spergel, G. S. Tucker, E. Wollack, E. L. Wright, C. Barnes, M. R. Greason, R. S. Hill, E. Komatsu, M. R. Nolta, N. Odegard, H. V. Peiris, L. Verde, J. L. Weiland *First Year Wilkinson Microwave Anisotropy Probe (WMAP) Observations: Preliminary Maps and Basic Results* Astrophys. Journal, in press

[Bertolini '99] A. Bertolini, G. Cella, R. DeSalvo and V. Sannibale 1999 *Seismic noise filters, vertical resonance frequency reduction with geometric anti-springs: a feasibility study* Nucl. Instrum. Methods A **435** 475–483

[Bilenko '02] I. A. Bilenko, V. B. Braginsky and N. Y. Markova 2002 *Thermal and excess noise in suspension fibers* Class. Quantum Grav. **19** 2035–2038

[Bondu '98] F. Bondu, P. Hello, J-Y. Vinet 1998 *Thermal noise in mirrors of interferometric gravitational wave antennas* Phys. Lett. A **246** 227–236

[Braccini '00] S. Braccini, C. Casciano, F. Cordero, F. Corvace, M. De Santis, R. Franco, F. Frasconi, E. Majorana, G. Paparo, R. Passaquieti, P. rapagnani, F. Ricci, D. Righetti, A. Solina and R. Valentini 2000 *The maraging-steel blades for the Virgo super attenuator* Meas. Sci. Technol. **11** 467–476

[Braccini '02] S. Braccini 2002 *The VIRGO suspensions* Phys. Lett. A **175** 82–84

[Bradashia '90] C. Bradaschia et al. 1990 Nuclear Instruments and Methods in Physics Research A **289** 518–525.

[Braginsky '93] V. B. Braginsky, V. P. Mitrofanov and O. A. Okhrimenko 1993 *The isolation of test masses for gravitational wave antennae* Phys. Lett. A **175** 82–84

[Braginsky '94] V. B. Braginsky, V. P. Mitrofanov and V. K. Tokmakov 1994 *On the thermal noise from the violin modes of the test mass suspension in gravitational wave antennae* Phys. Lett. A **186** 18–20

[Braginsky '94] V. B. Braginsky, V. P. Mitrofanov and S. P. Vyatchanin 1994 *Isolation of test masses in the advanced laser interferometric gravitational wave antennae* Rev. Sci. Instr. **65** 3771–3774

[Braginsky '96] V. B. Braginsky, V. P. Mitrofanov and V. K. Tokmakov 1996 *Energy dissipation in the pendulum mode of the test mass suspension of gravitational wave antennae* Phys. Lett. A **218** 164–166

[Braginsky '99] V. B. Braginsky, M. L. Gorodetsky and S. P. Vyatchanin 1999 *Thermo-dynamical fluctuations and photo-thermal shot noise in gravitational wave antennae* Phys. Lett. A **218** 164–166

[Braginsky '00] V. B. Braginsky, M. L. Gorodetsky, S. P. Vyatchanin 2000 *Thermo-refractive noise in gravitational wave antennae* Phys. Lett. A **271** 303–307

[Braginsky '03] V. B. Braginsky, M. L. Gorodetsky and S. P. Vyatchanin 2003 *Thermo-dynamical fluctuations in optical mirror coatings* Phys. Lett. A **312** 244–255

[Cagnoli '96] G. Cagnoli, L. Gammaitoni, J. Kovalik, F. Marchesoni, M. Puntero 1996 *Suspension losses in low-frequency mechanical pendulums* Phys. Lett. A **213** 245–252

[Cagnoli '97] G. Cagnoli, L. Gammaitoni, J. Kovalik, F. Marchesoni, M. Puntero, S. Braccini, R. De Salvo, F. Fidecaro, G. Lourdo 1997 *Mechanical shot noise induced by creep in suspension devices* Phys. Lett. A **237** 21–27

[Cagnoli '99] G. Cagnoli, L. Gammaitoni, J. Kovalik, F. Marchesoni, M. Puntero 1999 *Low-frequency internal friction in clamped-free thin wires* Phys. Lett. A **255** 230–235

[Cagnoli '00] G. Cagnoli, J. Hough, D. DeBra, M. M. Fejer, E. Gustafson, S. Rowan, V. Mitrofanov 2000 *Damping dilution factor for a pendulum in an interferometric gravitaional waves detector* Phys. Lett. A **272** 39–45

[Cagnoli '02] G. Cagnoli and P. Willems 2002 *The Effects of Nonlinear Thermoelastic Damping in Highly Stressed Fibres* Phys. Rev. B **65 (17)** 174111 1–9

[Callen '51] H. B. Callen and T. A. Welton 1951 *Irreversibility and Generalized Noise* Phys. Rev. **83** 34–40

[Callen '52] H. B. Callen and G. F. Greene 1952 *On a Theorem of Irreversible Thermo-dynamics* Phys. Rev. **86** 702–710

[Casey '00] M. M. Casey, H. Ward and D. I. Robertson 2000 *Computer monitoring and control of the GEO 600 gravitational wave detector* Rev. Sci. Instrum. **71** 3910

[Cerdonio '01] M. cerdonio, L. Conti, A. Heidmann, M. Pinard 2001 *Thermoelastic effects at low temperatures and quatum limitis in displacement meaurements* Phys. Rev. D **63**

[Coward '02] D. Coward, D. G. Blair, R. Clay and G. Mazzitelli 2002 *Improved sensitivity of NIOBÉ in 2001 and the search for anomalous cosmic ray events* Class. Quantum Grav. **19** 1871–1877

[Crooks '04] D. R. M. Crooks, G. Cagnoli, M. M. Feijer, A. Gretarsson, G. Harry, N. Nakagawa, S. Penn, R. Route, S. Rowan, P. H. Sneddon 2004 *Experimental measurements of coating mechanical loss factors* Class. Quantum Grav. **21** 1059–1066

[Cutler '02]  C. Cutler and K. S. Thorne 2002 *An Overview of Gravitational-Wave Sources* Proc. GR16 eds. N. T. Bishop and S. D. Maharaj (Singapore: World Scientific) 72–111

[Danzmann '95]  K. Danzmann et al 1995 in *First Edoardo Amaldi Conference on Gravitational Wave Experiments* Frascati 1994, (World Scientific, Singapore) 100–111

[Danzmann '03]  K. Danzmann, A. Rüdiger *LISA technology – concept, status, prospects* Class. Quantum Grav. **20** 1–9

[Dawid '97]  D. Dawid, S. Kawamura 1997 *Investigation of violin mode Q for wires of various materials* Rev. Sci. Instrum. **68** 4600–4603

[DeSalvo '02]  R. DeSalvo 2002 *Path-finding towards a cryogenic interferometer for LIGO* Class. Quantum Grav. **19** 2021–2028

[Drever '83]  R. W. P. Drever, J. L. Hall, F. V. Kowalski, J. Hough, G. M. Ford, A. J. Munley, H. Ward 1983 *Laser Phase and Frequency Stabilization Using an Optical Resonator* Appl. Phys. B **31** 97–105

[Freise '02]  A. Freise, M. M. Casey, S. Goßler, H. Grote, G. Heinzel, H. Lück, D. I. Robertson, K. A. Strain, H. Ward, B. Willke, J. Hough, K. Danzmann 2002 *Performance of a 1200 m long suspended Fabry-Perot cavity* Class. Quantum Grav. **19** 1389–1397

[GEO]  http://www.geo600.uni-hannover.de/

[Gillespie '93]  A. Gillespie, F. Raab 1993 *Thermal noise in the test mass suspensions of a laser interferometer gravitational-wave detector prototype* Phys. Lett. A **190** 213–202

[Gillespie '94]  A. Gillespie, F. Raab 1994 *Suspension losses in the pendula of laser interferometer gravitational-wave detector prototype* Phys. Lett. A **178** 357–363

[Gillespie '95]  A. Gillespie, F. Raab 1995 *Thermally excited vibrations of the mirror of laser interferometer gravitational-wave detectors* Phys. Rev. D **52** 577–585

[Goßler '02]  S. Goßler, M. M. Casey, A. Freise, H. Grote, H. Lück, P. McNamara, M. V. Plissi, D. I. Robertson, N. A. Robertson, K. D. Skeldon, K. A. Strain, C. I. Torrie, H. Ward, B. Willke, J. Hough, K. Danzmann 2002 *The modecleaner system and suspension aspects of GEO 600* Class. Quantum Grav. **19** 1835–1842

[Goßler '03]  S. Goßler, M. M. Casey, A. Freise, A. Grant, H. Grote, G. Heinzel, M. Heurs, M. E. Husman, K. Kötter, V. Leonhardt, H. Lück, M. Malec, K. Mossavi, S. Nagano, P. W. McNamara, M. V. Plissi, V. Quetschke, D. I. Robertson, N. A. Robertson, A. Rüdiger, R. Schilling, K. D. Skeldon, K. A. Strain, C. I. Torrie, H. Ward, U. Weiland, B. Willke, W. Winkler, J. Hough and K. Danzmann 2003 *The mode-cleaning and injection optics of the gravitational-wave detector GEO 600* Rev. Sci. Instrum. **74** 3787

[Goßler '04] S. Goßler, G. Cagnoli, D. R. M. Crooks, J. R. Smith, H. Lück, J. Hough and K. Danzmann 2004 *Damping and tuning of the fibre violin modes in monolithic silica suspension* Class. Quantum Grav. **21** 923–933

[Gretarsson '99] A. M. Gretarsson and g. M. Harry 1999 *Dissipation of mechanical energy in fused silica fibers* Rev. Sci. Instrum. **70** 4081–4087

[Gretarsson '00] A. M. Gretarsson, G. M. Harry, S. D. Penn, P. R. Saulson, W. J. Startin, S. Rowan, G. Cagnoli, J. Hough 2000 *Pendulum mode thermal noise in advanced interferometers: acomparison of fused silica fibers and ribbons in the presence of surface loss* Phys. Lett. A **270** 108–114

[Grote '02] H. Grote, G. Heinzel, A. Freise, S. Goßler, B. Willke, H. Lück, H. Ward, M. M. Casey, K. A. Strain, D. I. Robertson, J. Hough, K. Danzmann2002 *The automatic alignment system of GEO 600* Class. Quantum. Grav. **19** 1849–1855.

[Grote '04] H. Grote, M. M. Casey, A. Freise, S. Goßler, G. Heinzel, M. Hewitson, H. Lück, H. Ward, B. Willke, J. Hough and K. Danzmann *Alignment control of GEO 600* Class. Quantum Grav. **21** 441–449

[Grote '04] H. Grote, A. Freise, M. Malec, G. Heinzel, B. Willke, H. Lück, K. A. Strain, J. Hough and K. Danzmann *Dual recycling for GEO 600* Class. Quantum Grav. **21** 441–449

[Grote] H. Grote, G. Heinzel, A. Freise, S. Goßler, B. Willke, H. Lück, H. Ward, M. M. Casey, K. A. Strain, D. I. Robertson, J. Hough and K. Danzmann *Automatic beam alignment for the modecleaner cavities of GEO 600* Applied Optics, in press

[Gwo '98] D. H. Gwo 1998 *Hydroxide-catalyzed ultra-precision bonding for optical materials in cryogenic applications* Proceedings of SPIE–The International Society for Optical Engineering **3435** 136–140

[Harry '02] G. M. Harry, A. M. Gretarsson, P. R. saulson, S. E. Kittelberger, S. D. Penn, W. J. Startin, S. Rowan, M. M. Fejer, D. R. M. Crooks, G. Cagnoli, J. Hough and N. Nakagawa 2002 *Thermal noise in interferometric gravitational wave detectors due to dielectric optical coatings* Class. Quantum Grav. **19** 897–917

[Heinzel '98] G. Heinzel, K. A. Strain, J. Mizuno, K. D. Skeldon, B. Willke, W. Winkler, R. Schilling, A. Rüdiger, and K. Danzmann 1998 *Experimental Demonstration of a Suspended Dual Recycling Interferometer for Gravitational Wave Detection* Phys. Rev. Lett. **81** 5493–5496.

[Heinzel '02] G. Heinzel, A. Freise, H. Grote, K. Strain, K. Danzmann 2002 *Dual recycling for GEO 600* Class. Quantum Grav. **19** 1547–1553

[Hewitson '03] M. Hewitson, P. Aufmuth, C. Aulbert, S. Babak, R. Balasubramanian, B. W. Barr, S. Berukoff, G. Cagnoli, C. A. Cantley, M. M. Casey, S. Chelkowski, D. Churches, C. N. Colacino, D. R. M. Crooks, C. Cutler, K. Danzmann, R. Davies,

191

R. Dupuis, E. Elliffe, C. Fallnich, A. Freise, S. Goßler, A. Grant, H. Grote, S. Grunewald, J. Harms, G. Heinzel, S. Heng, A. Heptonstall, M. Heurs, J. Hough, Y. Itoh, O. Jennrich, R. Jones, S. Hutter, K. Kawabe, C. Killow, K. Kötter, B. Krishnan, V. Leonhardt, H. Lück, B. Machneschalk, M. Malec, K. Mossavi, S. Mohanty, S. Mukherjee, S. Nagano, G. P. Newton, M. A. Papa, M. Perreur-Lloyd, M. Pitkin, M. V. Plissi, V. Quetschke, S. Reld, L. Ribichini, D. I. Robertson, N. A. Robertson, S. Rowan, A. Rüdiger, B. S. Sathyaprakash, R. Schilling, R. Schnabel, B. F. Schutz, F. Seifert, A. M. Sintes, J. Smith, P. Sneddon, K. A. Strain, I. Taylor, C. I. Torrie, A. Vecchio, H. Ward, U. Weiland, H. Welling, P. Willams, B. Willke, W. Winkler, G. Woan and I. Zawischa 2003 *A report on the status of the GEO 600 gravitational wave detector* Class. Quantum Grav. **20** 581–591

[Huang '98] Y. L. Huang and P. R. Saulson 1997 *Dissipation mechanisms in pendulums and their implications for gravitational wave detectors* Rev. Sci. Instrum. **69** 544–553

[Hulse '75] R. A. Hulse, J. H. Taylor 1975 *Discovery of a pulsar in a binary system* Astroph. Jour. (Letters) **195** (L59) 51–53

[Ju '02] L. Ju, D. G. Blair, J. Bilenko and D. Padget 2002 *Low loss niobium flexure suspension systems* Class. Quantum Grav. **19** 1703–1709

[Ju '04] L. Ju, P. Barriga, D. G. Blair, A. Brooks, R. Burman, R. Burston, X. T. Chin, E. J. Chin, C: Y. Lee, D. Coward, B. Cusack, G. de Vine, J. Degallaix, J. C. Dumas, F. Garoi, S. Gras, M. Gray, D. Hosken, E. Howell, J. S. Jacob, T. L. Kelly, B. Lee, K. T. Lee, T. Lun, D. McClelland, C. Mow-Lowry, D. Mudge, J. Munch, S. Schediwy, S. Scott, A. Searle, B. Sheard, B. Slagmolen, P. Veitch, J. Winterfloor, A. Wooley, Z. Yan, C. Zhao 2004 *ACIGA's high optical power test facility* Class. Quantum Grav. **21** 887–893

[Kane '85] T. J. Kane and R. L. Byer 1985 *Monolithic, unidirectional single-mode Nd:YAG ring laser* Opt. Lett. **10** 65–67

[Kötter '02] K. Kötter, C. Aulbert, S. Babak, R. Balasubramanian, S. Berukoff, S. Bose, D. Churches, C. N. Colacino, C. Cutler, K. Danzmann, R. Davies, R, Dupuis, A. Freise, H. Grote, G. Heinzel, M. Hewitson, J. Hough, M. Lück, M. Malec, S. D. Mohanty, S. Mukherjee, S. Nagano, M. A. Papa, D. Robertson, B. S. Sathyaprakash, B. F. Schutz, A. M. Sintes, K. A. Strain, I. J. Taylor, A. Vecchio, H. Ward, U. Weiland, B. Willke and G. Woan 2002 *Data acquisition and detector characterization of GEO 600* Class. Quantum Grav. **19** 1399–1409

[Kötter '04] K. Kötter, M. Hewitson and H. Ward 2004 *Timing accuracy of the GEO 600 data acquisition system* Class. Quantum Grav. **21** 493–500

[Kuroda '02] K. Kuroda et al. 2002 *Japanese large-scale interferometers* Class. Quantum Grav. **19** 1237–1245

[Lawrence '02] R. lawrence, M. Zucker, P. Fritschel, P. Marfuta and D. Shoemaker 2002 *Adaptive thermal compensation of test masses in advanced LIGO* Class. Quantum Grav. **19** 1803–1812

[Leonhardt '02]  V. Leonhardt, L. Ribichini, P. Klövekorn, B. Willke, H. Lück and K. Danzmann 2002 *Towards measuring the off-resonant thermal noise of a pendulum mirror* Class. Quantum Grav. **19** 1717–1722

[Levin '98]  Y. Levin 1998 *Internal thermal noise in the LIGO test masses: A direct approach* Phys. Rev. D **57** 659–663

[Logan '92]  J. E. Logan, N. A. Robertson, J. Hough 1992 Phys. Lett. A **170** 352

[Logan '93]  J. E. Logan, J. Hough and N. A. Robertson, 1993 *Aspects of the thermal motion of a mass suspended as a pendulum by wires* Phys. Lett. A **183** 145–152

[Lück '98]  H. Lück and the GEO 600 Team 1998 *The vacuum system of GEO 600* in E. Coccia, G. Veneziano, G. Pizzella (eds.) Gravitational Waves, Singapore 356–359

[Lück '00]  H. Lück 2000 *Correction of wavfront distortions by means of thermally adaptive optics* in: E. Coccia, G. Veneziano, G. Pizzella 1998 (eds.) Gravitational Waves. Singapore 356–359

[Lück]  H. Lück, S. Hild, S. Goßler, K. Kawabe, W. Winkler and K. Danzmann *Thermal compensation of the mismatch of the radii of curvature of GEO 600 mirrors* Class. Quantum Grav. **21** 985–989

[Abramovici]  A. Abramovici et al 1992 Science **256** 325–333

[LIGO]  http://www.ligo.caltech.edu

[Majorana '97]  E. Majorana, Y. Ogawa 1997 *Mechanical thermal noise in coupled oscillators* Phys. Lett. A **233** 162–168

[Màrka '02]  S. Màrka, A. Takamori, M. Ando, A. Bertolini, G. Cella, R. DeSalvo, M. Fukushima, Y. Iida, F. Jacquier, S. Kawamura, K. Numata, V. Sannibale, K. Somiya, R. Takahashi, H. Tariq, K. Tsubono, J. Ugas, N. Viboud, C. Wang, H. Yamamoto and T. Yoda 2002 *Anatomy of the TAMA SAS seismic attenuation system* Class. Quantum Grav. **19** 1605–1614

[Mitrofanov '02]  V. P. Mitrofanov, N. A. Styazhkina, K. V. Tokmakov 2002 *Test mass damping associated with electrostatic actuator* Class. Quantum Grav. **19** 2039–2043

[Meers '88]  B. J. Meers 1988 *Recycling in laser-interferometric gravitational-wave detectors* Phys. Rev. D **38** 2317–2326

[Numata '02]  K. Numata, S. Otsuka, M. Ando, K. Tsubono 2002 *Intrinsic losses of various kinds of fused silica* Class. Quantum Grav. **19** 1697–1702

[OptoCad]  R. Schilling 2002 *OptoCad, A Fortran 95 module for tracing Gaussian beams through an optical set-up, Version 0.74* internal note

[Penn]  S. Penn 2003 personal comunication

[Penn '01] S. D. Penn, G. M. Harry, A. M. Gretarson, S. C. Kittelberger, P. R. Saulson, J J. Schiller, J. R. Smith, S. O. Swords 2001 *High quality factor measured in fused silica* Rev. Sci. Instrum. **72** 3670–3673

[Penn '03] S. D. Penn, P. H. Sneddon, H. armandula, J. C. Betzwieser, G. Cagnoli, J. Camp, D. R. M. Crooks, M. M. Fejer, A. M. Gretarson, G. M. Harry, J. Hugh, S. C. Kittelberger, M. J. Mortonson, R. Route, S. Rowan and C. C. Vassiliou 2003 *Mechanical loss in tantala/silica dielectric mirror coatings* Class. Quantum Grav. **20** 2917–2928

[Plissi '98] M. V. Plissi, K. A. Strain, C. I. Torrie, N. A. Robertson, S. Killbourne, S. Rowan, S. M. Twyford, H. Ward, K. D. Skeldon and J. Hough 1998 *Aspects of the suspension system for GEO 600* Rev. Sci. Instrum. **69** 3055–3061

[Plissi '00] M. V. Plissi, C. I. Torrie, M. E. Husman, N. A. Robertson, K. A. Strain, H. Ward, H. Lück and J. Hough 2000 *GEO 600 triple pendulum suspension system: Seismic isolation and control* Rev. Sci. Instrum. **71** 2539–2545

[Reitze] D. Reitze, personal communication

[Romie] J. Romie, personal communication

[Rowan '97] S. Rowan, R. Hutchins, A. McLaren, N. A. Robertson, S. M. Twyford, J. Hough 1997 *The quality factor of natural fused quartz ribbons over a frequency range from 6 to 160 Hz* Phys. Lett. A **227** 153–158

[Rowan '00] S. Rowan, G. Cagnoli, P. Sneddon, J. Hough,, R. Route, E. K. Gustafson, M. M. Fejer, V. Mitrofanov 2000 *Investigations on mechanical loss factors of some candidate materials for the test masses of gravitational wave detectors* Phys. Lett. A **265** 5–11

[Rüdiger '81] A. Rüdiger, R. Schilling, L. Schnupp, W. Winkler, H. Billing, K. Maischberger 1981 *A mode selector to suppress fluctuations in laser beam geometry* Optica Acta **28** 641–658.

[Schnupp '88] L. Schnupp talk at the *European Collaboration Meeting on Interferometric Detection of Gravitational Waves* (Sorrento, 1988)

[Shoemaker '04] B. Abbott and the LIGO Scientific Collaboration 2004 *Detector Description and Performance for the First Coincidence Observations between LIGO and GEO* Nucl. Instr. Meth. Phys. Res. A **517** 154–179

[Sigg '04] D. Sigg 2004 *Commissioning of the LIGO detectors* Class. Quantum Grav. **21** 409–416

[Sintes '03] A. M. Sintes, P. Aufmuth, C. Aulbert, S. Babak, R. Balasubramanian, B. W. Barr, S. Berukoff, S. Borger, G. Cagnoli, C. A. Cantley, M. M. Casey, S. Chelkowski, D. Churches, C. N. Colacino, D. R. M. Crooks, C. Cutler, K. Danzmann, R. Davies, R. Dupuis, E. Elliffe, C. Fallnich, A. Freise, S. Goßler, A. Grant,

H. Grote, S. Grunewald, J. Harms, G. Heinzel, I. S. Heng, A. Hepstonstall, M. Heurs, M. Hewitson, J. Hough, R. Ingley, Y. Itoh, O. Jennrich, R. Jones, S. Hutter, K. Kawabe, C. Killow, K. Kotter, B. Krishnan, V. Leonhardt, H. Luck, B. Machenschalk, M. Malec, C. Messenger, K. Mossavi, S. Mohanty, S. Mukherjee, S. Nagano, G. P. Newton, M. A. Papa, M. Perreur-Lloyd, M. Pitkin, M. V. Plissi, V. Quetschke, S. Reid, L. Ribichini, D. I. Robertson, N. A. Robertson, S. Rowan, A. Rudiger, B. S. Sathyaprakash, R. Schilling, R. Schnabel, B. F. Schutz, F. Seifert, J. Smith, P. Sneddon, K. A. Strain, I. Taylor, C. I. Torrie, A. Vecchio, H. Ward, U. Weiland, H. Welling, P. Williams, B. Willke, W. Winkler, G. Woan, I. Zawischa 2003 *Detector characterization in GEO 600* Class. Quantum Grav. **20** 731–740

[Skeldon '96]  K. D. Skeldon, K. A. Strain, A. I. Grant and J. Hough 1996 *Test of an 18 m long suspended modecleaner cavity* Rev. Sci. Instrum. 2443–2448

[Smith '03]  J. R. Smith, G. M. Harry, J. C. Betzwieser, A. M. Gretarsson, D. A. Guild, S. E. Kittelberger, M. J. Mortonson, S. D. Penn and P. R. Saulson 2003 *Mechanical loss associated with silicate bonding of fused silica* Class. Quantum Grav. **20** 5039–5047

[Smith '04]  J. R. Smith, G. Cagnoli, D. R. M. Crooks, M. M. Fejer, S. Goßler, H. Lück, S. Rowan, J. Hough and K. Danzmann *Mechanical quality factor measurements of monolithically suspended fused silica test masses of the GEO 600 gravitational-wave detector* Class. Quantum Grav. **21** 1091–1098

[Sneddon '03]  P. H. Sneddon, S. Bull, G. Cagnoli, D. R. M. Crooks, E. J. Elliffe, J. E. Faller, M. M. Fejer, J. Hough and S. Rowan *The intrinsic mechanical loss factor of hxdroxy-catalysis bonds for use in the mirror suspensions of gravitational wave detectors* Class. Quantum Grav. in press

[Strain '91]  K. A. Strain, B. J. Meers 1991 *Experimental Demonstration of Dual Recycling for Interferometric Gravitational-Wave Detectors* Phys. Rev. Lett. **66** 1391–1394

[Takahashi '02]  R. Takahashi, K. Arai ant the TAMA collaboration 2002 *Improvement of the vibration isolation system for TAMA300* Class. Quantum Grav. **19** 1599–1604

[Takahashi '04]  R. Takahashi and the TAMA Collaboration 2004 *The status of TAMA300* Class. Quantum Grav. **21** 403–408

[Tsubono]  K. Tsubono et al., ibid., 112–114

[TAMA]  http://tamago.mtk.nao.ac.jp/

[Taylor '82]  J. H. Taylor, J. M. Weisberg *A new test of general relativity: Gravitational radiation and the binary pulsar PSR 1913 + 16* Astrophys. J. **253** 908–920.

[Torrie '00]  C. I. Torrie 2000 *Development of suspensions for the GEO 600 gravitational-wave detector* Ph.D. Thesis, University of Glasgow, Department of Physics and Astronomy

[Träger '97] S. Traeger, B. Willke, K. Danzmann 1997 *Monolithically suspended fused silica substrates with very high mechanical Q* Phys. Lett. A **225** 39–44

[Uchiyama '00] T. Uchiyama, T. Tomaru, D. Tatsumi, S. Miyoki, M. Ohashi, K. Kuroda, T. Suzuki, A. Yamamoto, T. Shintomi 2000 *Mechanical quality factor of a sapphire fiber at cryogenic temperatures* Phys. Lett. A **273** 310–315

[Uchiyama '04] T. Uchiyama et al. 2004 *Present status of large-scale cryogenic gravitational wave telescope* Class. Quantum Grav. **21** 1161–1172

[Vitale '02] S. Vitale, P. Bender, A. Brillet, S. Buchman, A. Cavalleri, M. Cerdonio, M. Cruise, C. Cutler, K. Danzmann, R. Dolesi, W. Folkner, A. Gianolio, Y. Jafry, G. Hasinger, G. Heinzel, C. Hogan, M. Hueller, J. Hough, S. Phinney, T. Prince, D. Richstone, D. Robertson, M. Rodrigues, A. Rüdiger, M. Sandford, R. Schilling, D. Shoemaker, B. Schutz, R. Stebbins, C. Stubbs, T. Sumner, K. Thorne, M. Tinto, P. Touboul, H. Ward, W. Weber, W. Winkler 2002 *LISA and its in-flight test precursor SMART-2* Nucl. Phys. B - Proc. Suppl. **110** 209–216

[VIRGO] http://www.virgo.infn.it

[Weinstein '04] A. Weinstein 2004 *Advanced LIGO optical configuration and prototyping effort* Class. Quantum Grav. **19** 1575–1584

[Willems '02] P. Willems, V. Sannibale, J. Weel, V. Mitrofanov 2002 *Investigations of the dynamics and mechanical dissipation of a fused silica suspension* Phys. Lett. A **297** 37–48

[Willems] P. Willems 2003 personal communication

[Willems '99] P. Willems, M. Thattai 1999 *Increased thermal noise in nonuniform fiber suspensions* Phys. Lett. A **253** 16–20

[Willems '03] P. Willems, C. Lamb, A. Heptonstall, J. Hough 2003 *Search for stress dependence in the internal friction of fused silica* Phys. Lett. A in press

[de Waard '02] A. de Waard, L. Gottardi and G. Frossati 2002 *MiniGRAIL progress report 2001: the first cooldown* Class. Quantum Grav. **19** 1935–1943

[Willke '04] B. Willke, P. Aufmuth, C. Aulbert, S. Babak, R. Balasubramanian, B. W. Barr, S. Berukoff, S. Bose, G. Cagnoli, M. M. Casey, D. Churches, D. Clubley, C. N. Colacino, D. R. M. Crooks, C. Cutler, K. Danzmann, R. Davies, R. Dupuis, E. Elliffe, C. Fallnich, A. Freise, S. Goßler, A. Grant, H. Grote, G. Heinzel, A. Heptonstall, M. Heurs, M. Hewitson, J. Hough, O. Jennrich, K. Kawabe, K. Kötter, V. Leonhardt, H. Lück, M. Malec, P. W. McNamara, S. A. McIntosh, K. Mossavi, S. Mohanty, S. Mukherjee, S. Nagano, G. P. Newton, B. J. Owen, D. Palmer, M. A. Papa, M. V. Plissi, V. Quetschke, D. I. Robertson, N. A. Robertson, S. Rowan, A. Rüdiger, B. S. Sathyaprakash, R. Schilling, B. F. Schutz, R. Senior, A. M. Sintes, K. D. Skeldon, P. Sneddon, F. Stief, K. A. Strain, I. Taylor, C. I. Torrie, A. Vecchio, H. Ward, U. Weiland, H. Welling, P. Willams, W. Winkler, G. Woan and I. Zawischa 2004 *Status of GEO 600* Class. Quantum Grav. **21** 417–424

[Winkler '91] W. Winkler, K. Danzmann, A. Rüdiger, R. Schilling: *Heating by optical absorption and the performance of interferometric gravitational-wave detectors*, Phys. Rev. A **44** (1991) 7022–7036.

[Yamamoto '01] K. Yamamoto, S. Otsuka, M. Ando, K. Kawabe, K. Tsubono 2001 *Experimental study of thermal noise caused by an inhomogeneously distributed loss* Phys. Lett. A **280** 289–296

[Zawischa '02] I. Zawischa, M. Brendel, K. Danzmann, C. Fallnich, M. Heurs, S. Nagano, V. Quetschke, H. Welling and B. Willke 2002 *The GEO 600 laser system* Class. Quantum Grav. **19** 1775–1782

[Zendri '02] J. P. Zendri, L. Baggio, M. Bignotto, M. Bonaldi, M. Cerdonio, L. Conti, M. De Rosa, P. Falferi, P. L. Fortini, M. Inguscio, A. Marin, F. Marin, R. Mezzena, A. Ortolan, G. A. Prodi, E. Rocco, F. Salemi, G. Soranzo, L. Taffarello, G. Vedovato, A. Vinante and S. Vitale 2002 *Status report and near future prospects for the gravitational wave detector AURIGA* Class. Quantum Grav. **19** 1925–1935

198

# Acknowledgements

# Curriculum vitae

**Personal data**

| | |
|---|---|
| Surname, Given name: | Goßler, Stefan |
| Adress: | Haltenhoffstraße 237 |
| Postcode/City | 30419 Hannover |
| Date/Place of birth: | 04.05.1968, Westerland/Sylt |
| Marital status: | Not married |
| Children: | None |
| Nationality/Citzenship: | German |

**University studies**

| | |
|---|---|
| 2000–to date | Doctoral studies in Physics, Universität Hannover Scientific Assistant, Universität Hannover, Institut für Atom- und Molekülphysik |
| 2000 | Diplom in Physics: Full marks and honours *Aufbau und Charakterisierung des GEO 600 Mode-cleanersystems* (*Assembly and characterization of the GEO 600 modecleaner system*) |
| 1992–2000 | Diploma studies in Physics, Universität Hannover |

**Alternative service (in lieu of military service)**

| | |
|---|---|
| 1991–1992 | Jugendpflege Stadt Springe |

**Education**

| | |
|---|---|
| 1990 | Abitur, Gymnasium Sarstedt |
| 1986–1990 | Gymnasium Sarstedt |
| 1984–1986 | Realschule Nordstemmen |
| 1982–1984 | Hauptschule Barnten |
| 1980–1982 | Gymnasium Sarstedt |
| 1978–1980 | Orientierungsstufe Nordstemmen |
| 1974–1978 | Grundschule Nordstemmen |

# Publications

1.      S. Goßler, G. Cagnoli, D. R. M. Crooks, H. Lück, S. Rowan, J. R. Smith, K. A. Smith, J. Hough and K. Danzmann 2004 *Damping and tuning of the fibre violin modes in monolithic silica suspensions*, Class. Quantum Grav. **21** 923–933

2.      S. Goßler, M. M. Casey, A. Freise, A. Grant, H. Grote, G. Heinzel, M. Heurs, M. E. Husman, K. Kötter, V. Leonhardt, H. Lück, M. Malec, K. Mossavi, S. Nagano, P. W. McNamara, M. V. Plissi, V. Quetschke, D. I. Robertson, N. A. Robertson, A. Rüdiger, R. Schilling, K. D. Skeldon, K. A. Strain, C. I. Torrie, H. Ward, U. Weiland, B. Willke, W. Winkler, J. Hough and K. Danzmann 2003 *Mode-cleaning and injection optics of the gravitational-wave detector GEO 600*, Rev. Sci. Instrum. **74** 3787–3795

3.      S. Goßler, M. M. Casey, A. Freise, H. Grote, H. Lück, P. McNamara, M.V. Plissi, D. I. Robertson, N. A. Robertson, K. Skeldon, K. A. Strain, C. I. Torrie, H. Ward, B. Willke, J. Hough and K. Danzmann 2002 *The modecleaner system and suspension aspects of GEO 600*, Class. Quantum Grav. **19** 1835–1842

**2004:**

4.      J. R. Smith, C. Cagnoli, D. R. M. Crooks, S. Goßler, H. Lück, S. Rowan, J. Hough and K. Danzmann 2004 *Mechanical quality factor measurements of monolithically-suspended test masses of the GEO 600 gravitational-wave detector*, Class. Quantum Grav. **21** 1091–1098

5.      H. Lück, S. Hild, S. Goßler, K. Kawabe, W. Winkler and K. Danzmann 2004 *Thermal compensation of the mismatch of the radii of curvature of GEO 600 mirrors*, Class. Quantum Grav. **21** 985–989

6.      H. Grote, M. M. Casey, A. Freise, S. Goßler, G. Heinzel, M. Hewitson, H. Lück, H. Ward, B. Willke, J. Hough and K. Danzmann 2004 *Alignment control of GEO 600*, Class. Quantum Grav. **21** 441–449

7.      A. Freise, M. M. Casey, S. Goßler, H. Grote, G. Heinzel, H. Lück, D. I. Robertson, K. A. Strain, H. Ward, B. Willke, J. Hough, K. Danzmann 2002 *Performance of a 1200 m long suspended Fabry-Perot cavity*, Class. Quantum Grav. **19** 1389–1397

8.      H. Grote, G. Heinzel, A. Freise, S. Goßler, B. Willke, H. Lück, H. Ward,
        M. M. Casey, K. A. Strain, D. I. Robertson, J. Hough and K. Danzmann
        *Automatic beam alignment for the modecleaner cavities of GEO 600*, Applied
        Optics, accepted

9.      B. Willke, P. Aufmuth, C. Aulbert, S. Babak, R. Balasubramanian,
        B. W. Barr, S. Berukoff, G. Cagnoli, C. A. Cantley, M. M. Casey,
        S. Chelkowski, D. Churches, C. N. Colacino, D. R. M. Crooks, C. Cut-
        ler, K. Danzmann, R. Davies, R. Dupuis, E. Elliffe, C. Fallnich, A. Freise,
        S. Goßler, A. Grant, H. Grote, S. Grunewald, J. Harms, G. Heinzel,
        I. S. Heng, A. Heptonstall, M. Heurs, M. Hewitson, S. Hild, J. Hough,
        R. Ingley, Y. Itoh, O. Jennrich, R. Jones, S. Hutter, K. Kawabe, C. Kil-
        low, K. Kötter, B. Krishnan, V. Leonhardt, H. Lück, B. Machneschalk,
        M. Malec, R. A. Mercer, C. Messenger, S. Mohanty, K. Mossavi, S. Mukher-
        jee, S. Nagano, G. P. Newton, M. A. Papa, M. Perreur-Lloyd, M. Pitkin,
        M. V. Plissi, V. Quetschke, V. Re, S. Reid, L. Ribichini, D. I. Robertson,
        N. A. Robertson, S. Rowan, A. Rüdiger, B. S. Sathyaprakash, R. Schilling,
        R. Schnabel, B. F. Schutz, F. Seifert, A. M. Sintes, J. R. Smith, P. Sned-
        don, K. A. Strain, I. Taylor, C. I. Torrie, C. Ungarelli, A. Vecchio, H. Ward,
        U. Weiland, H. Welling, P. Willams, W. Winkler, G. Woan and I. Zawischa
        2004 *Status of GEO 600*, Class. Quantum Grav. **21** 417–423

10.     M. Hewitson, P. Aufmuth, C. Aulbert, S. Babak, R. Balasubramanian,
        B. W. Barr, S. Berukoff, G. Cagnoli, C. A. Cantley, M. M. Casey,
        S. Chelkowski, D. Churches, C. N. Colacino, D. R. M. Crooks, C. Cut-
        ler, K. Danzmann, R. Davies, R. Dupuis, E. Elliffe, C. Fallnich, A. Freise,
        S. Goßler, A. Grant, H. Grote, S. Grunewald, J. Harms, G. Heinzel, S. Heng,
        A. Heptonstall, M. Heurs, J. Hough, Y. Itoh, O. Jennrich, R. Jones,
        S. Hutter, K. Kawabe, C. Killow, K. Kötter, B. Krishnan, V. Leon-
        hardt, H. Lück, B. Machneschalk, M. Malec, K. Mossavi, S. Mohanty,
        S. Mukherjee, S. Nagano, G. P. Newton, M. A. Papa, M. Perreur-Lloyd,
        M. Pitkin, M. V. Plissi, V. Quetschke, S. Reld, L. Ribichini, D. I. Robertson,
        N. A. Robertson, S. Rowan, A. Rüdiger, B. S. Sathyaprakash, R. Schilling,
        R. Schnabel, B. F. Schutz, F. Seifert, A. M. Sintes, J. Smith, P. Sneddon,
        K. A. Strain, I. Taylor, C. I. Torrie, A. Vecchio, H. Ward, U. Weiland,
        H. Welling, P. Willams, B. Willke, W. Winkler, G. Woan and I. Zawischa
        2003 *A report on the status of the GEO 600 gravitational wave detector*,
        Class. Quantum Grav. **20** 581–591

11.     A. M. Sintes, P. Aufmuth, C. Aulbert, S. Babak, R. Balasubramanian,
        B. W. Barr, S. Berukoff, S. Borger, G. Cagnoli, C. A. Cantley, M. M. Casey,
        S. Chelkowski, D. Churches, C. N. Colacino, D. R. M. Crooks, C. Cut-
        ler, K. Danzmann, R. Davies, R. Dupuis, E. Elliffe, C. Fallnich, A. Freise,
        S. Goßler, A. Grant, H. Grote, G. Heinzel, I. S. Heng, A. Heptonstall,
        M. Heurs, M. Hewitson, J. Hough, R. Ingley, Y. Itoh, O. Jennrich, R. Jones,

S. Hutter, K. Kawabe, C. Killow, K. Kötter, B. Krishnan, V. Leonhardt, H. Lück, B. Machneschalk, M. Malec, C. Messenger, K. Mossavi, S. Mohanty, S. Mukherjee, S. Nagano, G. P. Newton, M. A. Papa, M. Perreur-Lloyd, M. Pitkin, M. V. Plissi, V. Quetschke, S. Reid, L. Ribichini, D. I. Robertson, N.A. Robertson, S. Rowan, A. Rüdiger, B. S. Sathyaprakash, R. Schilling, R. Schnabel, B. F. Schutz, F. Seifert, J. Smith, P. Sneddon, K. A. Strain, I. Taylor, C. I. Torrie, A. Vecchio, H. Ward, U. Weiland, H. Welling, P. Willams, B. Willke, W. Winkler, G. Woan and I. Zawischa 2003 *Detector characterization in GEO 600*, Class. Quantum Grav. **20** 731–739

12.  B. Abbott and the LIGO Scientific Collaboration: B. Abbott, R. Abbott, R. Adhikari, A. Ageev, B. Allen, R. Amin, S. B. Anderson, W. G. Anderson, M. Araya, H. Armandula, F. Asiri, P. Aufmuth, C. Aulbert, S. Babak, R. Balasubramanian, S. Ballmer, B. C. Barish, D. Barker, C. Barker-Patton, M. Barnes, B. Barr, M. A. Barton, K. Bayer, R. Beausoleil, K. Belczynski, R. Bennett, S. J. Berukoff, J. Betzwieser, B. Bhawal, I. A. Bilenko, G. Billingsley, E. Black, K. Blackburn, B. Bland-Weaver, B. Bochner, L. Bogue, R. Bork, S. Bose, P. R. Brady, V. B. Braginsky, J. E. Brau, D. A. Brown, S. Brozek, A. Bullington, A. Buonanno, R. Burgess, D. Busby, W. E. Butler, R. L. Byer, L. Cadonati, G. Cagnoli, J. B. Camp, C. A. Cantley, L. Cardenas, K. Carter, M. M. Casey, J. Castiglione, A. Chandler, J. Chapsky, P. Charlton, S. Chatterji, Y. Chen, V. Chickarmane, D. Chin, N. Christensen, D. Churches, C. Colacino, R. Coldwell, M. Coles, D. Cook, T. Corbitt, D. Coyne, J. D. E. Creighton, T. D. Creighton, D. R. M. Crooks, P. Csatorday, B. J. Cusack, C. Cutler, E. D'Ambrosio, K. Danzmann, R. Davies, E. Daw, D. DeBra, T. Delker, R. DeSalvo, S. Dhurandhar, M. D´az, H. Ding, R. W. P. Drever, R. J. Dupuis, C. Ebeling, J. Edlund, P. Ehrens, E. J. Elliffe, T. Etzel, M. Evans, T. Evans, C. Fallnich, D. Farnham, M. M. Fejer, M. Fine, L. S. Finn, ´E. Flanagan, A. Freise, R. Frey, P. Fritschel, V. Frolov, M. Fyffe, K. S. Ganezer, J. A. Giaime, A. Gillespie, K. Goda, G. Gonzàlez, S. Goßler, P. Grandclèment, A. Grant, C. Gray, A. M. Gretarsson, D. Grimmett, H. Grote, S. Grunewald, M. Guenther, E. Gustafson, R. Gustafson, W. O. Hamilton, M. Hammond, J. Hanson, C. Hardham, G. Harry, A. Hartunian, J. Heefner, Y. Hefetz, G. Heinzel, I. S. Heng, M. Hennessy, N. Hepler, A. Heptonstall, M. Heurs, M. Hewitson, N. Hindman, P. Hoang, J. Hough, M. Hrynevych, W. Hua, R. Ingley, M. Ito, Y. Itoh, A. Ivanov, O. Jennrich, W. W. Johnson, W. Johnston, L. Jones, D. Jungwirth, V. Kalogera, E. Katsavounidis, K. Kawabe, S. Kawamura, W. Kells, J. Kern, A. Khan, S. Killbourn, C. J. Killow, C. Kim, C. King, P. King, S. Klimenko, P. Kloevekorn, S. Koranda, K. Kötter, J. Kovalik, D. Kozak, B. Krishnan, M. Landry, J. Langdale, B. Lantz, R. Lawrence, A. Lazzarini, M. Lei, V. Leonhardt, I. Leonor, K. Libbrecht, P. Lindquist, S. Liu, J. Logan, M. Lormand, M. Lubinski, H. Lück, T. T. Lyons, B. Machenschalk, M. MacInnis, M. Mageswaran, K. Mailand,

W. Majid, M. Malec, F. Mann, A. Marin, S. Màrka, E. Maros, J. Mason, K. Mason, O. Matherny, L. Matone, N. Mavalvala, R. McCarthy, D. E. Mc-Clelland M. McHugh, P. McNamara, G. Mendell, S. Meshkov, C. Messenger, V. P. Mitrofanov, G. Mitselmakher,35 R. Mittleman, O. Miyakawa, S. Miyoki„ v S. Mohanty, G. Moreno, K. Mossavi, B. Mours, G. Mueller, S. Mukherjee, J. Myers, S. Nagano, T. Nash, H. Naundorf, R. Nayak, G. Newton, F. Nocera, P. Nutzman, T. Olson, B. O'Reilly, D. J. Ottaway, A. Ottewill, D. Ouimette, H. Overmier, B. J. Owen, M. A. Papa, C. Parameswariah, V. Parameswariah, M. Pedraza, S. Penn, M. Pitkin, M. Plissi, M. Pratt, V. Quetschke, F. Raab, H. Radkins, R. Rahkola, M. Rakhmanov, S. R. Rao, D. Redding, M. W. Regehr, T. Regimbau, K. T. Reilly, K. Reithmaier, D. H. Reitze, S. Richman, R. Riesen, K. Riles, A. Rizzi, D. I. Robertson, N. A. Robertson, L. Robison, S. Roddy, J. Rollins, J. D. Romano, J. Romie, H. Rong, D. Rose, E. Rotthoff, S. Rowan, A. Rüdiger, P. Russell, K. Ryan, I. Salzman, G. H. Sanders, V. Sannibale, B. Sathyaprakash, P. R. Saulson, R. Savage, A. Sazonov, R. Schilling, K. Schlaufman, V. Schmidt, R. Schofield, M. Schrempel, B. F. Schutz, P. Schwinberg, S. M. Scott, A. C. Searle, B. Sears, S. Seel, A. S. Sengupta, C. A. Shapiro, P. Shawhan, D. H. Shoemaker, Q. Z. Shu, A. Sibley, X. Siemens, L. Sievers, D. Sigg, A. M. Sintes, K. Skeldon, J. R. Smith, M. Smith, M. R. Smith, P. Sneddon, R. Spero, G. Stapfer, K. A. Strain, D. Strom, A. Stuver, T. Summerscales, M. C. Sumner, P. J. Sutton, J. Sylvestre, A. Takamori, D. B. Tanner, H. Tariq, I. Taylor, R. Taylor, K. S. Thorne, M. Tibbits, S. Tilav, M. Tinto, K. V. Tokmakov, C. Torres, C. Torrie, S. Traeger, G. Traylor, W. Tyler, D. Ugolini, M. Vallisneri, M. van Putten, S. Vass, A. Vecchio, C. Vorvick, S. P. Vyachanin, L. Wallace, H. Walther, H. Ward, B. Ware, K. Watts, D. Webber, A. Weidner, U. Weiland, A. Weinstein, R. Weiss, H. Welling, L. Wen, S. Wen, J. T. Whelan, S. E. Whitcomb, B. F. Whiting, P. A. Willems, P. R. Williams, R. Williams, B. Willke, A. Wilson, B. J. Winjum, W. Winkler, S. Wise, A. G. Wiseman, G. Woan, R. Wooley, J. Worden, I. Yakushin, H. Yamamoto, S. Yoshida, I. Zawischa, L. Zhang, N. Zotov, M. Zucker, and J. Zweizig 2004 *Detector Description and Performance for the First Coincidence Observations between LIGO and GEO*, Nucl. Instr. Meth. Phys. Res. A **517** 154–179

13. B. Abbott and the LIGO Scientific Collaboration: (Please see the above publication No. 12. for the full LIGO Scientific Collaboration author list) *Setting upper limits on the strength of periodic gravitational waves from PSR J1939+2134 using the first science data from the GEO600 and LIGO detectors*, Phys. Rev. D, accepted

14. B. Abbott and the LIGO Scientific Collaboration: (Please see the above publication No. 12. for the full LIGO Scientific Collaboration author list) *First upper limits from LIGO on gravitational wave bursts*, Phys. Rev. D, accepted

15.   G. Gonzàlez and the LIGO Scientific Collaboration: (Please see the above publication No. 12. for the full LIGO Scientific Collaboration author list) 2004 *Search for inspiralling neutron stars in LIGO S1 data*, Class. Quantum. Grav. **21** 691–696

16.   J. T. Whelan and the LIGO Scientific Collaboration: (Please see the above publication No. 12. for the full LIGO Scientific Collaboration author list) 2004 *First upper limit analysis and results from LIGO science data: stochastic background*, Class. Quantum. Grav. **21** 685–690

17.   B. Allen, G. Woan and the LIGO Scientific Collaboration: (Please see the above publication No. 12. for the full LIGO Scientific Collaboration author list) 2004 *Upper limits on the strength of periodic gravitational waves from PSR J1939+2134*, Class. Quantum. Grav. **21** 671–676

18.   A. J. Weinstein and the LIGO Scientific Collaboration: (Please see the above publication No. 12. for the full LIGO Scientific Collaboration author list) 2004 *First upper limits from LIGO on gravitational wave bursts*, Class. Quantum. Grav. **21** 677–684

**2003:**

19.   G. Woan, P. Aufmuth, C. Aulbert, S. Babak, R. Balasubramanian, B. W. Barr, S. Berukoff, S. Bose, G. Cagnoli, M. M. Casey, D. Churches, C. N. Colacino, D. R. M. Crooks, C. Cutler, K. Danzmann, R. Davis, R. J. Dupuis E. Elliffe, C. Fallnich, A. Freise, S. Goßler, A. Grant, H. Grote, G. Heinzel, A. Hepstonstall, M. Heurs, M. Hewitson, J. Hough, O. Jennrich, K. Kawabe, K. Kötter, V. Leonhardt, H. Lück, M. Malec, P. McNamara, K. Mossavi, S. Mohanty, S. Mukherjee, S. Nagano, G. P. Newton, B. J. Owen, M. A. Papa, M. V. Plissi, V. Quetschke, D. I. Robertson, N. A. Robertson, S. Rowan, A. Rüdiger, B. S. Sathyaprakash, R. Schilling, B. F. Schutz, R. Senior, A. M. Sintes, K. D. Skeldon, P. Sneddon, F. Stief, K. A. Strain, I. Taylor, C. I. Torrie, A. Vecchio, H. Ward, U. Weiland, H. Welling, P. Williams, W. Winkler, B. Willke, I. Zawischa 2003 *The GEO 600 Gravitational Wave Detector Pulsar Prospects* in: M. Bailes, D. Nice, S. Thorsett (eds.) Radio Pulsars. ASP Conf. Ser. **302** 351–355

**2002:**

20.   N. A. Robertson, G. Cagnoli, D. R. M. Crooks, E. Elliffe, J. E. Faller, P. Fritschel, S. Goßler, A. Grant, A. Heptonstall, J. Hough, H. Lück, R. Mittleman, M. Perreur-Lloyd, M. V. Plissi, S. Rowan, D. H. Shoemaker, P. H. Sneddon, K. A. Strain, C. I. Torrie, H. Ward and P. Willems 2002 *Quadruple suspension design for Advanced LIGO*, Class. Quantum Grav. **19** 4043–4058

21. B. W. Barr, G. Cagnoli, M. M. Casey, D. Clubley, D. R. M. Crooks, K. Danzmann, E. J. Ellife, S. Goßler, A. Grant, H. Grote, A. Heptonstall, J. Hough, O. Jennrich, H. Lück, S. A. McIntosh, G. P. Newton, D. A. Palmer, M. V. Plissi, D. I. Robertson, N. A. Robertson, S. Rowan, K. D. Skeldon, P. Sneddon, K. A. Strain, C. I. Torrie, H. Ward, P. A. Willams, B. Willke, W. Winkler 2002 *Silica Research in Glasgow*, Class. Quantum Grav. **19** 1655–1662

22. H. Grote, G. Heinzel, A. Freise, S. Goßler, B. Willke, H. Lück, H. Ward, M. Casey, K.A. Strain, D. Robertson, J. Hough, K. Danzmann 2002 *The automatic alignment system of GEO 600*, Class. Quantum Grav. **19** 1849–1855

23. B. Willke, P. Aufmuth, C. Aulbert, S. Babak, R. Balasubramanian, B. W. Barr, S. Berukoff, S. Bose, G. Cagnoli, M. M. Casey, D. Churches, D. Clubley, C. N. Colacino, D. R. M. Crooks, C. Cutler, K. Danzmann, R. Davies, R. Dupuis, E. Elliffe, C. Fallnich, A. Freise, S. Goßler, A. Grant, H. Grote, G. Heinzel, A. Heptonstall, M. Heurs, M. Hewitson, J. Hough, O. Jennrich, K. Kawabe, K. Kötter, V. Leonhardt, H. Lück, M. Malec, P. W. McNamara, S. A. McIntosh, K. Mossavi, S. Mohanty, S. Mukherjee, S. Nagano, G. P. Newton, B. J. Owen, D. Palmer, M. A. Papa, M. V. Plissi, V. Quetschke, D. I. Robertson, N.A. Robertson, S. Rowan, A. Rüdiger, B. S. Sathyaprakash, R. Schilling, B. F. Schutz, R. Senior, A. M. Sintes, K. D. Skeldon, P. Sneddon, F. Stief, K. A. Strain, I. Taylor, C. I. Torrie, A. Vecchio, H. Ward, U. Weiland, H. Welling, P. Willams, W. Winkler, G. Woan and I. Zawischa 2002 *The GEO 600 gravitational wave detector*, Class. Quantum Grav. **19** 1377–1387

24. J. Hough, P. Aufmuth, R. Balasubramanian, B. W. Barr, O. S. Brozec, G. Cagnoli, M. Casey, E. Chassande-Mottin, D. Churches, D. Clubley, D. R. M. Crooks, C. Cutler, K. Danzmann, C. Fallnich, A. Freise, S. Goßler, A. Grado, A. Grant, H. Grote, M. Husman, K. Kawabe, M. Kirchner, P. Klövekorn, K. Kötter, V. Leonhardt, H. Lück, P. W. McNamara, S. A. McIntosh, K. Mossavi, S. Nagano, G. P. Newton, B. J. Owen, D. Palmer, M. A. Papa, M. Peterseim, M. V. Plissi, V. Quetschke, D. I. Robertson, N. A. Robertson, S. Rowan, A. Rüdiger, B. S. Sathyaprakash, R. Schilling, B. F. Schutz, A. M. Sintes, K. D. Skeldon, P. Sneddon, K. A. Strain, I. Taylor, C. I. Torrie, A. Vecchio, H. Ward, A. Weidner, H. Welling, P. Williams, B. Willke, W. Winkler, I. Zawischa 2002 *GEO 600 – Research, Progress and Prospects* in: R. T. Jantzen, V. Gurzadyan, R. Ruffini (eds.) Proceedings of the Ninth Marcel Grossmann Meeting on General Relativity. World Scientific, Singapore 2002, 1843–1844

**2000:**

25.      B. Willke, S. Brozek, K. Danzmann, V. Quetschke, S. Goßler 2000 *Frequency stabilization of a monolithic Nd:YAG ring laser by controlling the power of the laser-diode pump source*, Opt. Lett. **25** 1019–1021

26.      B. Willke, O. S. Brozek, K. Danzmann, C. Fallnich, S. Goßler, H. Lück, K. Mossavi, V. Quetschke, H. Welling, I. Zawischa 2000 *The GEO 600 Stabilized Laser System and the Current-Lock Technique* in: S. Meshkov (ed.) Gravitational waves AIP, Melville; AIP Conf. Proc. **523** 215–221

27.      A. Rüdiger for the GEO 600 Team 2000 *Detecting gravitational waves from quasi-continuous sources: the German-Britisch project GEO 600* in: M. Kramer, N. Wex, R. Wieblinski (eds.) Pulsar Astronomy - 2000 and Beyond, APS Conf. Ser. **202** 733–734

28.      B. Willke and the GEO 600 Team 2000 *The GEO 600 gravitational wave detector* in: S. Kawamura, N. Mio (eds.) Gravitational Wave Detection II. University Acadamy Press, Tokyo 25–34

29.      H. Lück, P. Aufmuth, O. S. Brozek, K. Danzmann, A. Freise, S. Goßler, A. Grado, H. Grote, K. Mossavi, V. Quetschke, B. Willke, K. Kawabe, A. Rüdiger, R. Schilling, W. Winkler, Ch. Zhao, K. A. Strain, G. Cagnoli, M. M. Casey, J. Hough, M. Husman, P. McNamara, G. P. Newton, M. V. Plissi, N. A. Robertson, S. Rowan, D. I. Robertson, K. D. Skeldon, C. I. Torrie, H. Ward, B. F. Schutz, I. Taylor, B. S. Sathyaprakash 2000 *The status of GEO 600* in: S. Meshkov (ed.) Gravitational waves AIP, Melville; AIP Conf. Proc. **523** 119–127

**1998:**

30.      H. Lück and the GEO 600 Team 1998 *The vacuum system of GEO 600* in: E. Coccia, G. Veneziano, G. Pizzella (eds.) Gravitational Waves. Singapore 356–359

Working in GEO 600